CRANFIELD UNIVERSITY

MARCO MESSINA

DESIGN AND OPTIMIZATION OF A NOVEL TRI-AXIAL MINIATURE EAR-PLUG PIEZORESISTIVE ACCELEROMETER WITH NANOSCALE PIEZORESISTORS

SCHOOL OF APPLIED SCIENCES

PhD THESIS

CRANFIELD UNIVERSITY

SCHOOL OF APPLIED SCIENCES

PhD THESIS

MARCO MESSINA

Design and optimization of a novel tri-axial miniature ear-plug piezoresistive accelerometer with nanoscale piezoresistors

Supervisor: Dr. James Njuguna

February 2013

Abstract

This work aims at the advancement of state-of-art accelerometer design and optimization methodology by developing an ear-plug accelerometer for race car drivers based on a novel mechanical principle. The accelerometer is used for the measurements of head acceleration when an injurious event occurs. Main requirements for such sensor are miniaturization (2×2 mm), because the device must be placed into the driver earpiece, and its measurement accuracy (i.e. high sensitivity, low crosstalk and low nonlinearity) since the device is used for safety monitoring purpose.

A micro-electro-mechanical system (MEMS)-based (bulk micromachined) piezoresistive accelerometer was selected as enabling technology for the development of the sensor. The primary accelerometer elements that can be manipulated during the design stage are: the sensing element (piezoresistors), the micromechanical structure and the measurements circuit. Each of these elements has been specifically designed in order to maximize the sensor performance and to achieve the miniaturization required for the studied application.

To achieve accelerometer high sensitivity and miniaturization silicon nanowires (SiNWs) as nanometer scale piezoresistors are adopted as sensing elements. Currently this technology is at an infancy stage, but very promising through the exploitation of the "Giant piezoresistance effect" of SiNWs. This work then measures the potential of the SiNWs as nanoscale piezoresistors by calculating the major performance indexes, both electrical and mechanical, of the novel accelerometer. The results clearly demonstrate that the use of nanoscale piezoresistors boosts the sensitivity by 30 times in comparison to conventional microscale

piezoresistors. A feasibility study on nanowires fabrication by both top-down and bottom-up approaches is also carried out.

The micromechanical structure used for the design of the accelerometer is an optimized highly symmetric geometry chosen for its self-cancelling property. This work, for the first time, presents an optimization process of the accelerometer micromechanical structure based on a novel mechanical principle, which simultaneously increases the sensitivity and reduces the cross-sensitivity progressively. In the open literature among highly symmetric geometries no other study has to date reported enhancement of the electrical sensitivity and reduction of the cross-talk at the same time. Moreover the novel mechanical principle represents advancement in the accelerometer design and optimization methodology by studying the influence of a uniform mass moment of inertia of the accelerometer proof mass on the sensor performance. Finally, an optimal accelerometer design is proposed and an optimized measurement circuit is also specifically designed to maximize the performance of the accelerometer.

The new proposed accelerometer design is capable of increasing the sensor sensitivity of all axes, in particular the Z-axis increases of almost 5 times in respect to the current state-of-art-technology in piezoresistive accelerometer. This occurs thanks to the particular newly developed approach of combination of beams, proof mass geometry and measurement circuit design, together with the use of silicon nanowires as nanoscale piezoresistors. Furthermore the cross-sensitivity is simultaneously minimized for a maximal performance. The sum of the cross-sensitivity of all axes is equal to 0.4%, well below the more than 5% of the state-of-art technology counterpart reported in the literature. Future work is finally outlined and includes the electro-mechanical characterization of the silicon nanowires and the fabrication of the proposed accelerometer prototype that embeds bottom up SiNWs as nanoscale piezoresistors.

III

Acknowledgement

Contents

List of Figures

List of Tables

Chapter 1

1 INTRODUCTION

1.1 Introduction

Since silicon devices have dominated IC chips for many decades, to date silicon is the most significant semiconductor currently available. Silicon nanowires devices can transport electrons and holes with enhanced opto-electro-mechanical properties, as known today due to the quantum confinement effect. Due to their enhanced features they could function as building blocks for nanoelectronics and advanced devices [1]. Furthermore, they present a very large piezoresistance effect [2-7], which is suitable for enhancing the mechanical sensors performance. Currently, other areas of study of this device are to improve silicon transistors [8, 9]. Silicon nanowires are also attractive for applications in the field-emission devices, photonics, chemical sensors and spintronics [10].

The piezoresistive effect is a simple way used for converting, for example, acceleration in an electrical output. After an inertial force is applied to the sensor the strain on the piezoresistive material (silicon) changes its electrical resistance proportionally, the correspondent voltage change is a measure of the acceleration by less than a constant of proportionality.

Currently, in the design and development of an accelerometer the main effort is to set the right trade-off between size and sensitivity that may satisfy the requirements of the device application. Conventional technology is limiting the fabrication of accelerometer below 1 square millimetre due to the drastic loss in sensitivity [11, 12]. Basically when the miniaturization is the main concern of the application, sensitivity is the main issue to address, since the smaller is the device the lower will be its sensitivity. Obviously reduced sensitivity will drastically affect the accuracy of the device since a low signal to noise ratio is obtained. Much of MEMS technology currently face this issue by simply introducing an amplifier at the output level, sometimes monolithically as in capacitive pick-off (the way the acceleration is converted to an electrical signal) or in a complete different device as in piezoresistive pick-off (hybrid system partitioning). Introducing an amplifier results into a relative signal noise that inevitably worsens the accuracy of the measurement.

This research intends to address this issue in a different way by avoiding the use of an amplifier. In particular, the study exploits a phenomenon observed when the dimension of a piezoresistor shrinks down to the nanoscale, called in the literature "Giant Piezoresistance" [3]. By implementing the accelerometer with nanoscale piezoresistors (i.e. nanowires or quantum wires) the traditional design trade-off explained earlier using conventional microscale piezoresistors is overcame, due to the high sensitivity and the minuscule size achievable (see Figure 1-1). This is demonstrated in this work by designing a novel tri-axial miniature accelerometer based on nanoscale piezoresistors for applications in head injury detection of race car drivers.
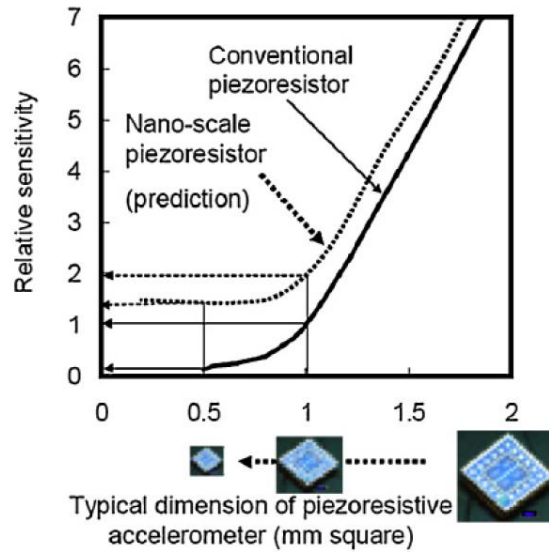
Figure 1-1. Relationship between relative sensitivity and typical dimension of a piezoresistive accelerometer [12]

1.2 Motivation

Traumatic brain injuries (TBI) due to impacts are common in helmeted sports, such as hockey, football and motorsport. Therefore, significant research effort has been made in the past decade in order to monitor and prevent head injuries in these sports, especially in motorsport where the high speeds and forces mean that crashes are inevitable. In the past there have been many deaths and injuries to race drivers, one of the most famous was Ayrton Senna on May 1, 1994 at the San Marino GP in Imola when he died for a fatal massive brain injury due to a high speed impact with the wall. The drivers were not monitored, therefore links between accelerations of specific body parts and injury could not be rigorously made.

The first solutions introduced in the late 90s were instrumented helmets, mounting sensors capable to measure the amplitude of a crash through accelerometers. These instrumented helmets may not accurately measure the actual acceleration experienced by the head due to

mainly helmet-to-head fit and helmet liner properties. In the latter case, the shell of the helmet distributes the impact force over a large surface area, and the helmet liner absorbs the acceleration forces, thereby reducing the acceleration of the head to non-concussive levels. [15, 16, 17, 18, 19, 20, 21]

Therefore, if the helmet shell or liner is instrumented, it is very difficult to estimate the amount of acceleration passed to the head. Helmets are designed to reduce the amount of acceleration experienced by the head; therefore, instrumented helmets may not reflect acceleration of the head [22, 23, 24], they overestimate the actual acceleration forces experienced by the head [22].

As accurate measuring of head accelerations is an important aspect in predicting head injury, it is important that the measuring sensor be well-coupled to the head. Therefore the instrumented helmet solution has been soon replaced in the new century, by a mouthpiece accelerometer in the football [25] and by attaching the accelerometer to an earpiece and not to the helmet in the motorsport [26, 27]. With these novel solutions the effects of the shell and liner properties are eliminated, allowing for the direct assessment of acceleration experienced by the head.

A version of these types of earpieces, the Delphi Earpiece Sensor System [28], was adopted by the Indy Racing League and Championship Auto Race Teams (CART) in 2003. In 2006, Begeman, Melvin, Troxel (Wayne State University) and Mellor (FIA Institute) [29] reported that signals from these earplugs mounted in post mortem human specimens (PMHS) showed a progressive phase lag from 50 to 100 Hz vibration when compared to skull measurement (rigidly mounted head accelerometers). These tests indicate less than perfect skull coupling for the earplugs mounted in the outer ear canal for high rate excitations. A step further has been made towards the improvement of the design of the ear-plug in order to obtain much

more accurate measurement at high rate and magnitude exposure by stiffening the coupling between the ear and the head.

One explored solution has been to developing a miniaturized tri-axial accelerometer that is small enough to be placed in the ear canal portion of the earpieces [30]. The sensor measurement was well correlated to the reference sensor and therefore, demonstrated improved coupling to the head over the Delphi version that were perceived too bulky [31]. Moreover other advices for improving the accuracy of the measurements is by improving the positioning technique and mounting material, a stiff material is recommended [30].

Currently there is still a need for research in this area of study in order to develop a more precise and reliable earplug accelerometer mainly used for biomechanics measurements, e.g. in helmeted sports. At the time of writing, no device on the market is available that is able to measure medium-g impact values with the size of few millimetres, because of the technical issues mentioned earlier. The only available micro-accelerometer on the market of the size of 2×2mm, e.g. from Bosch or ST, are low-g devices that incorporate an amplifier within it. Furthermore, the only attempt made so far in fabricating miniature prototypes with nanowires has been made for measuring low-g impacts with the sensitivity being of the same order of magnitude of the state-of-art sensors counterparts [6, 13, 14].

Other major applications of such novel sensors based on enhanced nanoscale piezoresistors are in the biomedical arena, such as implantable devices for motion/vibration sensing. Examples are in hearing aid systems (implantable sound sensor for cochlear implants [122]), heart wall motion measurement for cardiac artificial pacemakers (an adaptive control system that detects the human body activity level in order to adjust accordingly the pacemaker rate response [102]) and head injury monitoring of military soldiers in case of blast (the sensor is placed inside the helmet).

This study attempts a further improvement in the earplug sensor design by investigating possible ways of enhancing sensor performances and miniaturization, with the objective of achieving a more accurate response in case of medium-g impact crashes not achievable in state-of-art sensors. The data gathered from this new sensor would benefit all the stakeholders involved in the motorsports community.

First of all the race drivers that would wear the sensor would benefit from a more accurate safety system. When an injurious event occurs a better and fast diagnosis of the traumatic brain injury (TBI) would be possible to the medical personnel.

Medical, automotive researchers as well as engineers may use the data collected to evaluate how safety improvements like shoulder harnesses, helmets, seat belts and head and neck restraints commonly used in all forms of racing are helping prevent head injuries and eventually design better driver restraint systems and safety devices.

1.3 Thesis Aim and Objectives

The aim of this thesis is to advance current state-of-art knowledge of accelerometer design and optimization by developing a novel enhanced miniature accelerometer of 2×2 mm^2 characterized by improved sensitivity and cross-sensitivity.

The thesis objectives are:

- ➢ To conduct literature survey to establish current state-of-art earplug accelerometer and nanoscale piezoresistors technology.

- ➢ To design, model and optimize the novel accelerometer.

➤ To develop ear-plug accelerometer's circuits to enhance the performance of the devices.

➤ To evaluate the silicon nanowires as accelerometer sensing elements

1.4 Conclusion

The thesis aim is addressed by designing and modelling a novel accelerometer that embeds silicon nanowires as nanometer scale piezoresistors and by also designing a tailored measurement circuit that maximizes sensor performance. Accelerometer design has been addressed based on the flow chart presented in Figure 1-2. To start with, the accelerometer design is modelled based on highly symmetric geometries with four surrounding beams. These types of geometries have been chosen for their low cross-sensitivity due to their self-cancelled feature. Many geometries have been developed and analysed by finite element analysis technique, then the data have been collected and the design performances calculated (e.g., sensitivity, cross-sensitivity analysis, natural frequency). The design was set such that if the accelerometer performance is above or equal to the predefined technical specification for the device, the particular design is selected as a possible candidate, if not the design process is iterated. Furthermore, the possible candidate design is further modified based on an optimization method, where the mass moment of inertia of the proof mass becomes progressively uniform. The hypothesis demonstrated in this study is that with a uniform or even mass moment of inertia the performance of the accelerometer design is enhanced. Finally when the maximum performance is achieved a final new proposed design for the accelerometer is obtained otherwise the design is rejected, as illustrated in the schematic diagram on Figure 1-2.
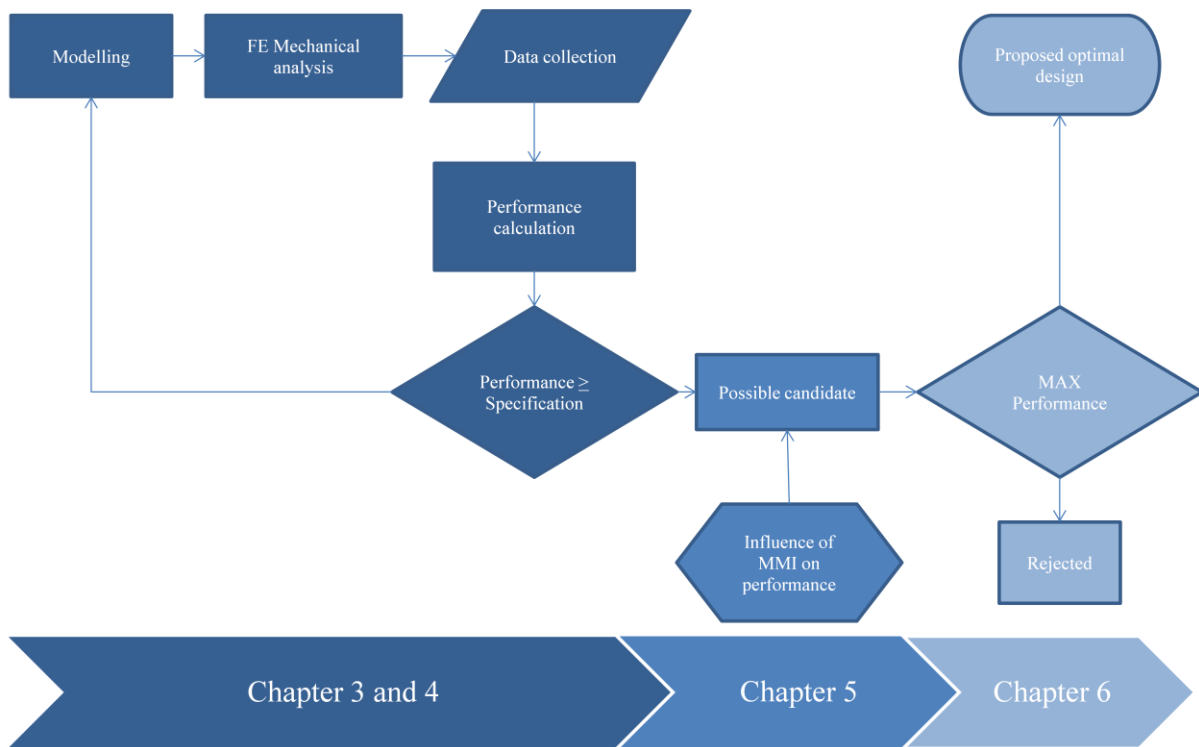
Figure 1-2. Schematic of the methodology adopted to address the thesis aim. As it can be seen the FEM of highly symmetric mechanical structures are first optimized by obtaining a possible candidate (Chapter 3 and 4) then a further optimization is attempted by a new optimization approach based on the influence of the mass moment of inertia (Chapter 5). Finally the device with maximum performance is obtained as output (Chapter 6).

1.5 Thesis structure

The thesis is structured in literature review in Chapter 2, where state-of-art earplug accelerometer, piezoresistive accelerometers, piezoresistance and giant piezoresistance are addressed, with identified gap in knowledge and conclusion. The design, modelling and optimization of the accelerometer is presented in chapter 3, where also the potential of silicon nanowires as nanoscale piezoresistors is evaluated based on previous experimental work on silicon nanowires. In Chapter 4, all major electrical and mechanical performance indexes of the device are calculated and a comparison between conventional microscale piezoresistors and novel nanoscale piezoresistors is presented. Then in Chapter 5, a further design step is undertaken in order to enhance the performance of the device. This optimization process is based on the mechanical principle that even mass moment of inertia determines even

electrical sensitivity and therefore improves measurement accuracy. The Chapter 6 presents the final geometry version of the device which represents the optimal solution output of the optimization process adopted. Chapter 7 deals with the experiments undertaken to verify the fabrication feasibility of silicon nanowires used in the simulation studies conducted in the thesis. Firstly, the nanowires processing made by focus ion bean direct milling is presented and then followed by self-assembled fabrication process. Finally the present work is completed by Chapter 8 on conclusion and future work.

Chapter 2

2 LITERATURE REVIEW

2.1 Introduction

This chapter addresses the latest scientific developments related to ear-plug accelerometer and then presents the different types of acceleration sensor currently available. The chapter then focuses on the piezoresistive accelerometer technology for the ear accelerometer design. Finally, piezoresistance developments followed by the recent giant piezoresistance discovery and fabrication processes of silicon nanowires are addressed, before completing the chapter with the identified gap in knowledge and conclusion of the literature review.

2.2 Overview of earplug accelerometer

The earplug accelerometer is a miniature sensor specifically designed to be inserted inside the ear by an earpiece. An ear plug accelerometer must be small enough to fit in the earpiece.

According to Sanders and McCormick (1993) [130], ergonomic product design refers to "designing for human beings." Accordingly, designing ergonomically ear-related products requires data on the dimensions and shapes of human ears. The anthropometric dimensions of outer ears, specifically the earhole length, the ear connection length, and the length of the pinna and the ear canal (see Figure 2-1 (a)), play a key development role in the design of our earpiece. However, human physical dimensions vary considerably with age, gender, race group, occupation, weight, height and so on [131] and the target users of our earpiece are different in gender, age, ethnicity, weight and height, therefore trying to accommodate all users is virtually impossible and costs increase proportionally with any effort to do so [132]. Therefore for cost effectiveness one needs to identify a typical target user at onset of the earplug accelerometer design.

(a)

(b)
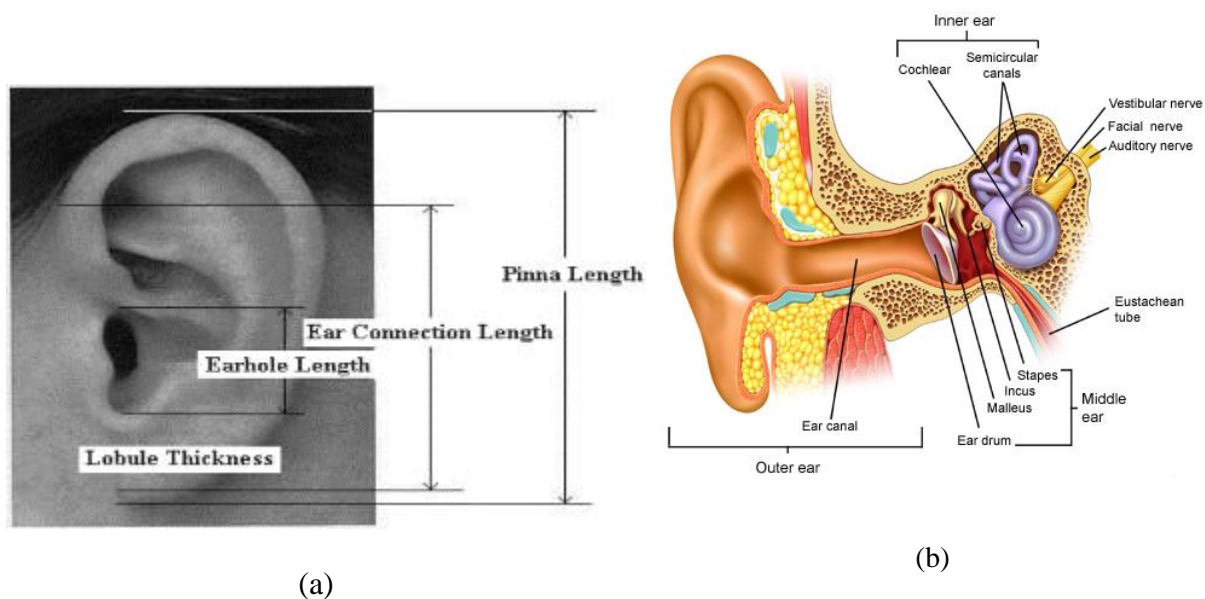
Figure 2-1. (a) Photo of outer ear that shows the length of different ear parts [133]; (b) Image of outer and inner ear [155].

Not many studies have been done to examine the correlation among the anthropometric dimension of the ear, the human physical dimension and age. Hwa S. Jung and Hyung-Shik Jung (2003) [133] selected six hundred male and female Korean subjects aged 17–89 for their

study, four different points of the outer ear (the lengths of the pinna, the ear connection point, the earhole and the lobule thickness) were measured and analyzed along with demographic data, including age, stature and weight. When they examine the correlation among each variable they found that age, regardless of gender difference, had a greater effect on the dimensions of ears than weight and height. As for the age group where the increase rate is highest, results show that the dimensions of ears increase in all age groups except the dimension of the earhole which decreases from the age of forty to fifty. Bor-Shong Liu (2008) [132] in his research of two hundred subjects aged 20–59 found that the coefficient of correlations between the three different dimensions of the outer ear (the earhole length, the ear connection length, the length of the pinna) and stature were very low (0.27, 0.27, and 0.29 respectively). In addition, the results showed that all ear dimensions had significant gender effects. From these studies seems that stature and weight play a minor role in the determination of the ear dimension. Age and sex are the most relevant variables that effect the growing of the ear. Concerning different ethnicity, Hwa S. Jung and Hyung-Shik Jung [133] in 2003, point out the shape and dimension dissimilarity of the ears between Koreans and Caucasians. Most of the Korean men have bigger ears with the shape of Disposition Nature, instead the ears of most Westerners had the shape of Bone Nature with few having Nutrition Nature or Disposition Nature (Figure 2-2).

(1) Nutrition Nature (2) Disposition Nature (3) Bone Nature
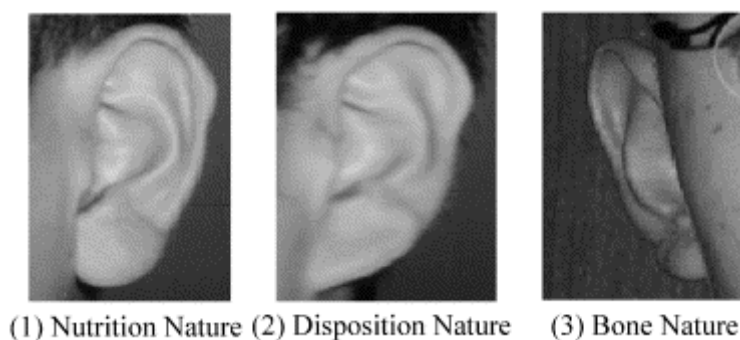
Figure 2-2. Ear shapes [133]

Based on the studies of the dimension and shape of the ears, we can apply the findings to the manufacturing of our ear plug accelerometer to ensure it fits properly. It is recommended that the length of the earhole be applied for designing our earpiece since it will resemble a earphone (see Figure 2-3). The main problem of many earphone users is that the earphone slips off, this was found especially to people in their 20s using a current model [133]. From this finding we concluded that in order to fit both big and small earholes, the earpiece should be made oblong and elongated inside the ear canal where the accelerometer would be placed (Figure 2-3).

Figure 2-3. Moulded earpiece [156]

We assume the race driver to be an adult male of an age from 20 to 50 years old. From this assumption we can identify the mean dimension of the earhole, considering that the human ear canal extends from the pinna to the eardrum and is about 26 mm in length and 7 mm in diameter in adults and it is slightly S-shaped (see Figure 2-1(b)). Below are listed the main results related to the earhole of the two studies examined above (Table 2-2 and Table 2-3) and the arithmetic mean obtained by merging the data from these studies (Table 2-4).

Table 2-1. Earhole dimension, age group and percentile (mm) [132]

			Percentile						
AGE	N	MEAN	5th	10th	25th	50th	75th	90th	95th
20	50	14.4	11.0	11.7	12.2	14.0	16.7	17.5	18.6
30	50	15.2	12.1	12.5	13.0	15.0	15.5	18.9	20.8
40	50	15.3	12.0	12.0	13.5	15.0	17.0	19.5	20.2
50	50	15.3	11.9	12.0	13.0	15.0	16.7	19.7	21.9

Table 2-2. Earhole dimension, age group and percentile (mm) [133]

			Percentile			
AGE	N	MEAN	5th	10th	25th	50th
20	50	16.3	12.5	13.0	15.0	16.0
30	50	17.2	14.7	14.7	15.8	17.4
40	50	17.9	15.8	16.2	16.8	18.2
50	50	18.3	16.6	17.0	17.5	18.4

Table 2-3. Arithmetic mean of the anthropometric data

AGE	N	MEAN Liu (2008)	MEAN Jung and Jung (2003)	MEAN
20	50	14.4	16.3	15.35
30	50	15.2	17.2	16.2
40	50	15.3	17.9	16.6
50	50	15.3	18.3	16.8

From the data above we obtain the arithmetic mean of the earhole dimensions of around 16.2 mm. This dimension is close to the 75th percentile for all males based on anthropometric data of the research of Liu and 50th percentile for people in their 20s, 25th percentile for people in their 30s, 10th for people in their 40s and 5th percentile for people in their 50s in the research

of Jung and Jung. In engineering design, percentiles are the most used anthropometric data. A percentile value for an anthropometric dimension represents the percentage of a population with a body dimension of a certain size or smaller [131]. From the percentiles obtained by Jung and Jung seems that an earpiece should be slightly bigger in order to cover a wider population. We can therefore recommend a 2-mm increment in earpiece diameter, with the length of the earhole applied to 50th percentile data of all males. However, earphones are made slightly bigger than the earholes to ensure a perfect fit. From this finding we can conclude that in order to fit both big and small earholes, the earpiece should be measuring around 18.2 mm×16.2 mm, based on the fact that an oval shape felt better, fitted more comfortably and without slip off.

2.3 Instrumented helmets

In the late 1990s for the first time in helmeted sports were introduced instrumented helmets mounting accelerometers to measure the severity of a head injury. The actual acceleration experienced by the head may not accurately be measured by these instrumented helmets due to mainly helmet-to-head fit and helmet liner properties. In the latter case, the impact force is distributed over a large surface area by the shell of the helmet, and the helmet liner absorbs the acceleration forces, thereby reducing the acceleration of the head to non-concussive levels [15, 16, 17, 18, 19, 20, 21]. Therefore, if the helmet shell or liner is instrumented, the measured acceleration would not be the actual acceleration passed to the head [22, 23, 24], basically they overestimate the actual acceleration forces experienced by the head [22].

It is important that the measuring sensor be well-coupled to the head as in predicting head injury accurate measuring of head accelerations represents a key aspect. Therefore in the new

century the instrumented helmet solution has been soon replaced, by a mouthpiece accelerometer in the football [25] and by attaching the accelerometer to an earpiece and not to the helmet in the motorsport [26, 27]. With these novel solutions the effects of the shell and liner properties are eliminated, allowing for the direct assessment of acceleration experienced by the head.

2.4 Earpiece accelerometer

In 2000, as the importance of the measurement accuracy was crucial the instrumented helmeted solution has been replaced by introducing the accelerometer in the ear together with an earpiece [26, 27]. Instrumented earplugs were first introduced in 2000 by the Air Force Research Lab (AFRL) as a means of measuring head accelerations in race car drivers after it was shown that instrumented helmets slipped on the head during impact events. The helmet moves relative to the head and it did not produce an accurate reading of head forces. A version of these earplugs, the Delphi Earpiece Sensor System (DESS), was adopted by the Indy Racing League and Championship Auto Race Teams (CART) in 2003 (Figure 2-4). For the first time researchers were able to collect data on the dynamic forces impacting a race car driver's head during an accident.

Figure 2-4. DESS and the smaller Endevco earplug [31]

The sensing system was consisting of 3 accelerometers (Analog Devices ADXL193), one for each axis and two circuit boards. The system had to fit inside the earpiece alongside the transducer for the radio receiver. The DESS is a variable-capacitance MEMS-based accelerometer. When the proof mass moves, with control provided by the springs, interleaving capacitive-sensing fingers detect minuscule changes in capacitance, which then get converted electronically to an acceleration reading. The following table summarizes the DESS specifications.

Table 2-4. DESS Specification

Measurement Range	±250g
Sensitivity	8mV/g
Filtering	400Hz 2 pole Bessel filter
Pre-filter headroom	1400g
Output Voltage Range	0.25 to 4.75V
Supply Current	3mA
Supply Voltage	+5V
Temperature Range	-40 to 125 degrees C
Weight	3 grams
Dimensions	9.9mm x 10.2mm x 6.6mm

In 2006, Begeman *et al.* [29] reported that signals from DESS earplugs mounted in cadavers showed a phase shift at 50 and 100 Hz vibration, indicating less than perfect coupling with the head. This led to the development of a new miniature tri-axial accelerometer that is small enough to be placed in the ear canal portion of communication earplugs (earpieces), thereby

improving the coupling and thus the reliability of the recordings from drivers undergoing multi-axial crash events.

Jesse Bonfeld in 2009 proposed to develop this mini-triaxis device. The AFRL/RHPA (Biomechanics Branch) team collaborated with Bonfeld to build the new sensors and provide the validation testing and comparison with the current operational sensors [31]. The new 7273GT sensors were mounted in molded earplugs and subjected to impacts as high as 300g with very short durations in multiple axes. They were also subjected to vibrations up to 100 Hz. The earplugs were mounted in artificial ears which were mounted on rigid blocks and on manikin heads. The sensors showed good correlation with reference sensors and demonstrated improved coupling to the head over the current generation of earplug accelerometers [31, 118] (Figure 2-5(a) and (b)).

(a)   (b)
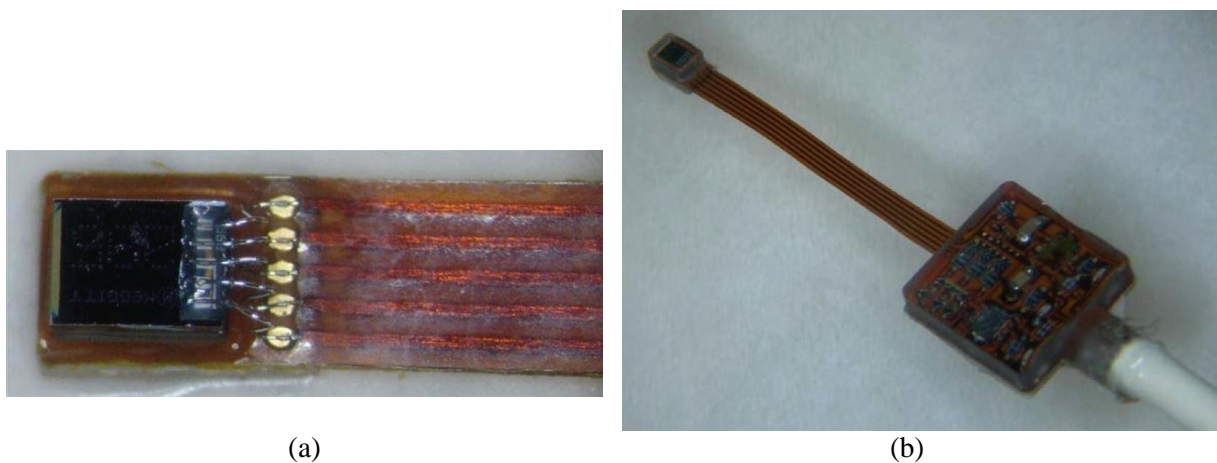
Figure 2-5. (a) Close-up of the 7273GT die mounted on a flex [118]. (b) Complete in-ear triaxial shock measurement system (Endevco) [118].

After the findings of Begeman (2006) [29] other studies have been undertaken in order to investigate the mechanical coupling between human head acceleration and a small tri-axial accelerometer package inserted into the ear bony canal. In 2009 Panzer *at al.* [107] used post mortem human specimens (PMHS) to carry out impact tests over a broad range of frequency inputs using moderate rate drop tests and high rate shock tube tests. The measurements

profile used were historically been used to quantify head injury risk. The result was a good agreement between sensors measurements due to an improvement of sensor positioning within the bony canal. Another work during the same period suggests to enhancing the measurement accuracy of the earplug by improving the position techniques and by using a stiff material for the mounting plug [30].

Recently, in 2012, a 3-axis acceleration switch of 3×3-mm specifically designed for traumatic brain injury was developed as an early warning capable to power up only when an injurious event occurs [108]. A novel three-axial biomechanic piezoresistive accelerometer enhanced by silicon nanowires as nanoscale piezoresistor as an implanted device for head injury g-loads detection for racecar drivers was also proposed in 2012 [134].

2.5 Acceleration Sensor

A *sensor* is a device that converts a physical phenomenon input into an electrical signal output. Acceleration sensors are sensing devices that provide an output proportional to acceleration, vibration, shock and seismic waves as input, measured in g-force. These sensors have found a wide variety of applications in both research and development arenas along with everyday use. In addition to the very technical test and measurement applications, such as modal analysis (the study of the dynamic properties of structures under vibrational excitation), NVH (noise, vibration and harshness - the study and modification of the noise and vibration characteristics of vehicles), and package testing, accelerometers are also used in everyday devices. They are widely used in automotive and space (airbag sensors and automotive security alarms, crash detection, stability control and navigation [88]), biomedical (activity monitoring [90, 91, 92], surgical instrument tracking [87]), consumer electronics

(portable computing, cameras lens stabilization, cellular phones), robotics (control and stability [89]), structural health monitoring, and military and sports applications (i.e. football, boxing, hockey and racing) for real-time health monitoring of traumatic brain injuries (TBI) due to impacts or blasts [32].

Currently there are three main different technologies of accelerometers and each has unique characteristics, advantages and disadvantages. These accelerometers are different regarding the output (integrated electronic piezoelectric - IEPE output, charge output, voltage output, 4-20mA output, velocity output), the design (shear type, flexural type, single ended compression type) and the technology (piezo-electric, capacitive, convection heat transfer, optical, piezo-resistive and servo). Many manufacturers use their own trade name to referring to sensor with built-in electronics, such as ICP® (PCB Piezotronics), Deltatron (Bruel & Kjaer), Piezotron (Kistler Instruments), Isotron [37], and LIVM (Low Impedance Voltage Mode), to name a few. IEPE sensors incorporate monolithically built signal conditioning electronics that convert the high-impedance signal output generated by the piezoelectric sensing element into a usable low-impedence voltage signal that can be easily transmitted, over ordinary cable, to any voltage readout or recording device. The charge output has also a high-impedance output because the electrical signal is generated directly by the piezoelectric sensing element. Therefore a signal conditioning is required in order to condition the signal to a low-impedance voltage [33]. Tribo-electric noise in the cable is a drawback determined by the high-impedance signal, therefore special treated cable should be used [32]. In industrial process control the analog 4-20 mA output is commonly used. The key advantage of this type of accelerometer output is that the signal accuracy is not affected by voltage drop in the line, and the loop can supply continuously operating power to the device [81]. Velocity output is commonly used to evaluate the health of a machine and the accelerometers with this type of output are typically used in condition monitoring applications. Velocity is also used in very

low frequency applications where the vibration amplitude is too small to measure and the velocity vibration is of higher and more meaningful value. Velocity output accelerometers are mainly effective if the vibration frequency is higher than 2 Hz and ideally 5Hz [34].

To perform the transduction principles of a piezoelectric accelerometer different mechanical configurations are currently available [33]. These configurations are different in the way the piezoelectric material is excited by the inertial forces of an accelerated mass. In the shear mode of operation under acceleration the mass applies a shear stress to the sensing crystals. Shear accelerometers excel in rejecting thermal transient and base strain sensitivity [33]. Furthermore, the shear geometry favours itself to a small size, which promotes high frequency response while minimizing mass loading effects on test structure [32]. Flexural mode designs utilize crystals shaped as beams that are supported to create strain on them when accelerated. This type of design is characterized by insensitivity to transverse motion, therefore they are well suited for low gravitational acceleration and low frequency applications such as structural testing [32]. The compression mode accelerometers represent the historical accelerometer design; they provide high rigidity combined to a simple structure. There are mainly three types of compression designs: upright, inverted and isolated.

2.5.1   Piezoresistive Accelerometers

In the piezoresistive accelerometers the piezoresistive effect describes the change of a material's electrical resistance caused by an applied mechanical stress proportional to the applied inertial forces. The piezoresistive effect determines a change in resistance of piezoresistors (gauges) connected electrically in a Wheatstone bridge circuit [85] (e.g., Z-axis piezoresistive accelerometer with four gages in a full-bridge configuration, see Figure 2-8) by the inertial force exerted by the seismic (or proof) mass (2 gages in tension, 2 gages in compression in the Figure 2-8) due to acceleration (see Appendix G). The unbalanced

Wheatstone bridge network detects the fractional resistance change producing a proportional output voltage; this is true in a full Wheatstone bridge because other types of bridge introduce nonlinearities (see Appendix G for details). This type of technology, differently from the piezoelectric one, allows for a response down to DC (i.e., they respond to steady-state accelerations).
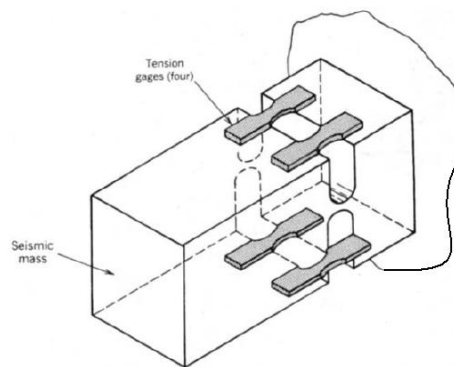
Figure 2-6. Z-axis Piezoresistive Accelerometer [32]

At frequencies close to 0 Hz, piezoelectric accelerometers cannot, when high accuracy is required, measure the acceleration an object is subject to. A static force results in a fixed amount of charges on the piezoelectric material and working with conventional electronics, not perfect insulating materials, and reduction in internal sensor resistance results in a constant loss of electrons, yielding an inaccurate signal [160]. When this slight inaccuracy is integrated in order to determine velocity, displacement and tilt, it becomes quite large. As a result, the velocity and displacement data are then inaccurate. For a static or quasi-static acceleration signal measurement, it is preferable to use either a piezoresistive or variable-capacitance accelerometer [37].

46

Many and diverse technologies are utilized in the piezoresistive accelerometer fabrication. Generally, in the bulk micromachining fabrication process the sequence of steps are: to grow the single crystal silicon; the ingot is trimmed, sliced, polished, and cleaned to obtain wafer; a mask layout on the wafer is patterned by a photoresist deposited film for diffusion or ion implantation of a dopant into a defined surface region; places defined by the mask are etched, followed by removal of the photoresist; and isotropic and/or anisotropic wet or plasma chemicals are used for releasing the structure by etching. The piezoresistive coefficients of the silicon are determined by the resultant stress distribution in the piezoresistors, the doping concentration and finally the orientation of the silicon wafer. The advantages of an accelerometer built in this way are: a high stiffness, resulting in a high resonant frequency (ω) which means a large usable frequency response. Other desirable features of such device fabrication are miniaturization, relatively large sensitivity (semiconductor strain gages have a gage factor 25 to 50 times that of metal), good linearity. Temperature compensation allows such devices to operate over a temperature range of -65 to +250ºF [32].

Roylance and Angell introduced the first fully integrated piezoresistive micromachined accelerometers in 1978 for biomedical applications [38, 39]. A comprehensive review on micromachined piezoresistive accelerometers was provided by Yazdi *et al.* [119]. Monolithic integration of piezoresistive accelerometers with CMOS circuitry that improves the output and compensates also temperature drift were developed in early 1990s [120, 121]. More recently a novel wafer-level package technique has been developed by encapsulating the die with a thick polysilicon epitaxial cup that protects the piezoresistors from dicing and plasma processing. Some devices that implement such novel encapsulation technique are the ones of Kwon and Park [123] which fabricated a three-axes piezoresistive accelerometer by using bulk micromachining and silicon direct bonding technology with a polysilicon layer. Also Partridge *et al.* [124] and Park *et al.* [125] for the piezoresistors used oblique ion-

implantation and deep reactive ion etching (DRIE) to fabricate devices designed for lateral acceleration sensing; moreover they adopted encapsulation technique in their devices. Park *et al.* developed a sub-mm single axis piezoresistive accelerometer as a sound sensor for a cochlear implant. This technology is a possible alternative for implantable hearing aids [122]. For wireless structural monitoring Lynch *et al.* [126] combined a planar piezoresistive accelerometer with wireless sensing unit.

Many different 3-DOF (degree of freedom) piezoresistive accelerometer designs with highly symmetric geometry have been developed in the past. Currently they can be divided in accelerometers with cross beams, cross-inset beams or surrounding beams designs.

Most of the structures with highly symmetric geometry present a cross [94, 96, 97, 98, 100, 101, 103] or a cross-inset beams [95, 99, 102, 105] due to the higher stress obtained during deformation. Even though surrounding beams design [2, 93, 104] presents a lower stress profile compared to the cross-inset beams counterpart, the surrounding beams design presents the advantage of reducing the beams deformation. Reduced deformation determines a lower nonlinearity and cross-sensitivity effect; therefore a higher accuracy of the measurement is expected at the expense of mechanical structure sensitivity. Another option for further sensitivity increasing of the mechanical structure is to combine the cross-inset beams design to the surrounding beams design as in the work of Amarasinghe *et al.* [106].

Regarding different types of pick-off in the piezoelectric accelerometers the piezoelectric effect of quartz or ceramic crystals triggers an electrical output when subject to compression, flexion or shear forces. A force applied to a quartz crystal lattice structure modifies alignment of positive and negative ions, determining an accumulation of these charged ions on an electrode. In an accelerometer, the stress on the crystals occurs by the seismic mass applying a force upon the crystal. On the usable frequency range, this structure obeys Newton's second

law of motion. Therefore, the total amount of charge accumulated is proportional to the applied force to the seismic mass, and the applied force is proportional to acceleration, therefore ultimately the voltage output is a measure of the applied acceleration [33].

The frequency response of the sensor is determined by the resonant frequency of the sensor, which occurs when the sensor is excited at his natural frequency (Figure 2-7). The resonant frequency (ω_o) of the sensor can be calculated by:

$$\omega_o = \sqrt{\frac{k}{m}}, \quad \text{where } k \text{ is the stiffness and } m \text{ the mass.}$$
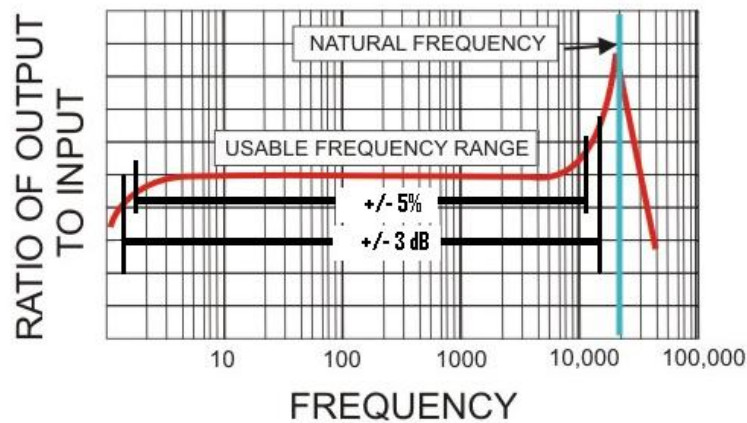
Figure 2-7. Typical frequency response of accelerometer [33]

The usable frequency response as depicted in the Figure 2-7 is the flat area of the frequency response curve and extends to approximately ⅓ to ½ of the natural frequency [34].

The natural frequency of an accelerometer is the frequency at its highest peak (Figure 2-7). From a frequency of around ⅓ to ½ of the natural frequency the ratio of output to input or transfer function becomes non-linear and therefore the measurement is difficult to be interpreted. A higher natural frequency of an accelerometer frequency response is preferable since it is wider the band of frequencies that can be measured. It can be seen from the formula of the resonant frequency that as the mass decreases the natural frequency increases

49

which is good for the measurement, but a small mass typically determine a lower sensitivity and this is true for most high frequency accelerometers [34].

In capacitive accelerometers the acceleration is a measure of an unbalanced bridge, measuring a change in capacitance. The pick-off element is formed by two parallel capacitors that work in a differential mode. These capacitors operate in a bridge configuration and are dependent on a carrier demodulator circuit to produce an electrical output proportional to acceleration. These types of accelerometer are built in a surface micromachining process [36] and typically a monolithically built electronic circuit is required for proper operation of a capacitive accelerometer. One of the major advantages of capacitive accelerometers is to measure low level (less than 2g), low frequency (down to DC) acceleration with high shock survivability, typically 5,000g or greater, and high accuracy [32].

In convectional heat transfer accelerometers a single heating element is centred in a substrate and suspended across a cavity with temperature sensors positioned in all four sides of the suspended heating element (Figure 2-8). Under zero acceleration the heat gradient will be symmetrical, which means that all the temperature sensors measure the same temperature. Due to convection heat transfer the acceleration in any direction causes the heat gradient to become asymmetrical and the unbalanced temperature sensors would represent a measure of the acceleration [35]. Simple electronics is typically used to converts the temperature measurements into signals.
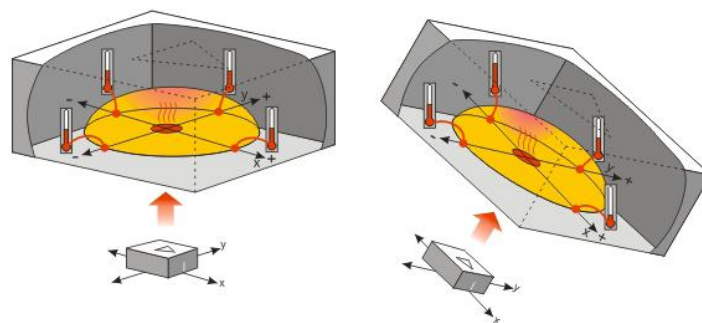
Figure 2-8. Convective Heat Transfer Accelerometer (MX2125) [128]

In the optical pick-off type of accelerometers the acceleration is converted in an electrical signal based on an optical intensity modulation techniques. There are two main categories of these devices. The first consist of two fibres attached to a substrate with supporting bars, one completely attached and the other one is a cantilever-like fibre beam. The other category is based on movable shutter fabricated by micromachined processes (MOEMS) [41]. An example is illustrated in the Figure 2-9.
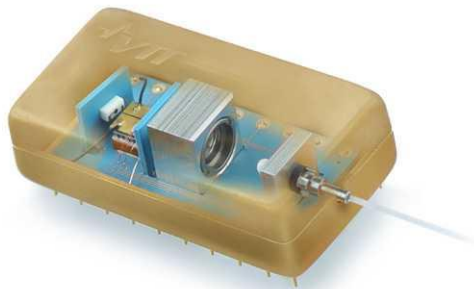
Figure 2-9. Silicon Micromachined MOEMS device [129]

The servo or force-rebalance type of accelerometer, which integrate a control system with feedback, is the most sensitive (capable of sensing distant earthquakes in micro-g's) and most precise (used in navigation of spacecraft) accelerometer. All type of open-loop sensors described so far may have a certain actuation system that works as force-rebalance. Typically the accelerometer that implements such system is the variable-capacitance accelerometer since the actuation is straightforward.

2.6 Piezoresistance

The piezoresistance effect can be described in a matrix form where each of the six fractional resistivity changes relates to each of the six stress components [40] (see Appendix H). Kanda [72] generalized the fractional resistivity change by [40]:

$$\frac{\Delta \rho_\omega}{\rho} = \sum_{\lambda=1}^{6} \pi_{\omega\lambda} \sigma_\lambda \tag{2.1}$$

where ω is a fixed voltage and current orientation and λ the stress orientation.

Mathematically this yields a matrix of 36 coefficients. By definition, the elements of this matrix are called piezoresistance coefficients, $\pi_{\omega\lambda}$, (ω, λ=1 to 6), expressed in Pa^{-1}.

Generally, two piezoresistors' contacts are formed by masked-ion implantation method, and lie on very thin surface layer, the beam [32]. Therefore, only two piezoresistance coefficients, i.e. π'_{11} and π'_{12} are relevant for calculation. π'_{11} corresponding to the case the stress parallel with the direction of electric field and current density, thus it is called the longitudinal piezoresistance coefficient, denoted by π_l. Similarly, π'_{12} relating to the case the applied stress perpendicular to the electrical field and current density, hence it is called transverse piezoresistance coefficient, π_t. The shearing stress is neglected since it is much smaller than the others. These two coefficients are expressed through three fundamental piezoresistance coefficients π_{11}, π_{12}, π_{44}, and directional cosines (l, m, n) for arbitrary crystal orientation by the general formulation for longitudinal ($\pi_l = \pi'_{11}$) and transversal ($\pi_t = \pi'_{12}$) piezoresistive coefficient by Mason and Thurston [70]:

$$\pi'_{11} = \pi_{11} - 2\pi_o(l_1^2 m_1^2 + l_1^2 n_1^2 + m_1^2 n_1^2) \tag{2.2}$$

$$\pi'_{21} = \pi_{12} - \pi_o(l_1^2 l_2^2 + m_1^2 m_2^2 + n_1^2 n_2^2) \tag{2.3}$$

$$(\pi_o = \pi_{11} - \pi_{12} - \pi_{44}) \quad \text{and} \quad \pi'_{12} = \pi'_{21} \tag{2.4}$$

Based on the theory and equation above, the resistance change can be calculated as a function of the beam stress. In the accelerometer the piezoresistors are located on the surface of a thin beam, therefore the material is stressed mainly in two dimensions at the surface plane. The mechanical stresses are considered constant over the piezoresistors; the fractional resistance change is simply given by:

$$\frac{\Delta R}{R} = \sigma_l \pi_l + \sigma_t \pi_t \tag{2.5}$$

where σ_l and σ_t are longitudinal and transversal stress, the shearing stress is neglected since very low respect to the others. It is noted that the above equation is only valid for uniform stress fields or if the piezoresistor dimensions are small compared to the beam size [71 , 40].

The first materials widely used as piezoresistors were single crystal germanium and silicon because with diamond lattice crystal structure. In 1954 in these semiconductor crystals Smith [48] reported the first measurements of large piezoresistive coefficients noting that this phenomenon could be explained by the work of Bardeen and Shockley [157], and later Herring [110, 111]. Smith measured the piezoresistive coefficients for (100) samples along the <100> and <110> crystal directions. Longitudinal and transverse coefficients for the fundamental crystal axes were determined directly. Shear piezoresistive coefficients were inferred. By these measurements and considering the crystal symmetry, Smith fully characterized the piezoresistive tensor of 7.8 Ω-cm at low p-Si concentration. At light concentrations (1.7×10^{15} cm^{-3}), Smith [48] found the p-type longitudinal piezoresistive coefficient in the [110] direction for bulk silicon to be relatively constant at 72×10^{-11} Pa^{-1} [$(\pi_{11} + \pi_{12} + \pi_{44})/2$]. His results have been showed graphically by Kanda [72] (see Appendix H). In other words, p-type piezoresistors must be oriented along the <110> directions to measure stress and thus should be either aligned or perpendicular to the wafer primary flat [73]. The

piezoresistance coefficient magnitude decreases significantly with the doping concentration and the temperature. The first systematic experimental study on piezoresistance over a broad temperature range (-90°C to 100°C) and doping concentration levels was carried out by Tufte and Stelzer [69] in the early 1960s. Subsequent studies by many investigators have generally confirmed the trend of their results. Kanda [72] has theoretically discussed the dependence of the piezoresistive coefficient on the impurity concentration and temperature. He concluded that the piezoresistive coefficient with a doping concentration of N at a temperature T, Π(N, T), can be generally expressed as:

$$\Pi(N,T) \ = \ P(N,T)\Pi(3OOK) \tag{2.6}$$

where Π(*300K*) is the piezoresistive coefficient at room temperature (300 K or 25°C) for low doped material of the same conductive type and $P(N,T)$ is a factor indicating the dependence of the piezoresistive coefficient on the doping level and temperature. Based on the multi-valley theory of semiconductor energy bands, the factor $P(N,T)$ has been calculated. The calculated values of the $P(N,T)$, agree well with the experimental values obtained by Mason [70] for doping concentrations less than 1×10^{17} cm^{-3}, over the temperature range of 50°C to 150°C, but differ by 21% at a concentration of 3×10^{19} cm^{-3} at room temperature. The error was attributed to dopant ions scattering for high dopant concentrations, whereas the calculation only considered lattice scattering. Harley and Kenny [53] later evaluated data from several researchers (see Figure 2-10) and provided an empirical fit of piezoresistance vs. concentration that better estimates the sensitivity for higher concentration devices.
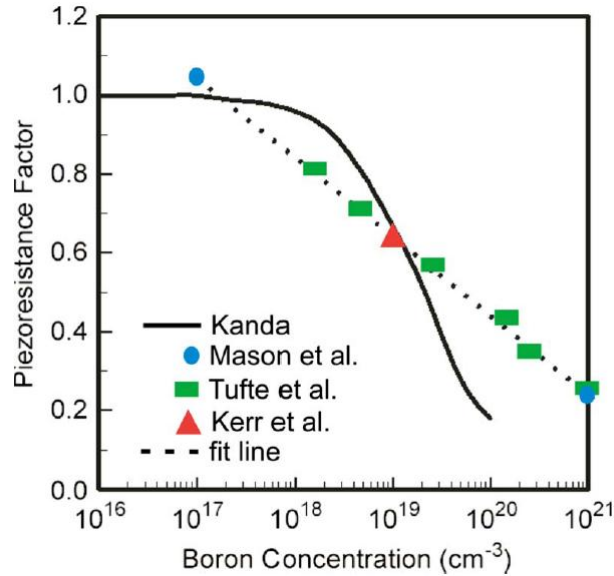
Figure 2-10. Piezoresistive Factor comparison at room temperature [53]

The theory underlying the physics of the piezoresistive effect of semiconductors are grounded in one-dimensional descriptions of electron and hole transport in crystalline structures under strain. During that period the existing theories were based on bandgap energies shifts, and the change in mobility with the lattice strain was explained as band warping or bending and the non-uniform density of states [109 − 112]. The many-valley model of Herring [110, 111] is the main model used for explaining the physics underlying the piezoresistive effect of n-type silicon. In 1988, Lin [113] explained the large mobility degradation at higher transverse electric field by the scattering mechanisms of quantized subbands at (100) silicon planes. The physics of p-type silicon piezoresistance has been almost unknown for decades due to the inherent complexity of valence band structure [114], most of the research and commercial piezoresistive devices had therefore been mainly based on experimental studies. However, only recently computational advances allowed improving the understanding of the p-type silicon piezoresistance effect [115 − 117].

2.6.1 Piezoresistance of p-type and n-type single crystal silicon

The doping concentration [69, 161], type of dopant [69, 161], and temperature of the substrate [69, 72] influence the piezoresistive coefficients of single-crystal silicon that are not constants. Different elements of the π matrix (π_{11}, π_{12} and π_{44}) are affected differently by temperature and doping concentrations. With increasing temperature and doping concentrations the value of the piezoresistive coefficient decreases for both p- and n-type silicon. The values of π_{11}, π_{12} and π_{44} for single-crystalline silicon under certain doping concentration and dopant types have been experimentally characterized. Several typical values for selected doping concentrations are listed in Table 2-5.

Table 2-5. Piezoresistivity components for single-crystal silicon under certain doping values.

Piezoresistive coefficient $(10^{-11}\,Pa^{-1})$	n-type (resistivity = 11.7 Ωcm)	p-type (resistivity = 7.8 Ωcm)
π_{11}	-102.2	6.6
π_{12}	53.4	-1.1
π_{44}	-13.6	138.1

However, all 36 of the coefficients in the coefficient matrix [π] may be nonzero when referring to a Cartesian system of arbitrary orientation relative to the crystallographic axes [162]. In the case of silicon, the components of the matrix change if the x-, y-, and z-axes are not aligned to <100> directions.

In the most commonly occurring cases, when the piezoresistor points in <100>, <110> or <111> directions [72, 163] the effective longitudinal and transverse piezoresistive coefficients are summarizes in Table 2-6.

Table 2-6. Formula for transverse and longitudinal piezoresistive coefficient for various commonly encountered resistor configurations.

Direction of strain	Direction of current	Configuration	Piezoresistive coefficient
<100>	<100>	Longitudinal	π_{11}
<100>	<010>	Transversal	π_{12}
<110>	<110>	Longitudinal	$(\pi_{11} + \pi_{12} + \pi_{44})/2$
<110>	<1$\bar{1}$0>	Transversal	$(\pi_{11} + \pi_{12} - \pi_{44})/2$
<111>	<111>	Longitudinal	$(\pi_{11} + 2\pi_{12} + 2\pi_{44})/2$

Combining the results in Table 2-5 and the formula of the piezoresistive coefficients in Table 2-6 it is possible to estimate the fractional resistance change (Eq. 2.5) for n-type and p-type piezoresistors in the <100> and <110> direction. N-type piezoresistors in the <100> direction with a resistivity of 11.7 Ωcm have a fractional resistance change equal to:

$$\frac{\Delta R}{R} = \sigma_l \pi_{11} + \sigma_t \pi_{12} = -\sigma_l \, 102.2 + \sigma_t \, 53.4 \approx \sigma_l \pi_{11} - \sigma_t \frac{\pi_{11}}{2} = \pi_{11} \left(\sigma_l - \frac{\sigma_t}{2} \right) \qquad (2.7)$$

Equation 2.7 shows the fractional resistance change as function of only the longitudinal piezoresistive coefficient and that the fractional resistance change is zero for a transversal stress twice the longitudinal stress. Therefore n-type piezoresistors in the <100> direction are suitable for measuring acceleration when the longitudinal stress is the main stress component as in uniaxial stress application. Clearly the p-type piezoresitors in this direction with a resistivity of 7.8 Ωcm are not suitable for measurements due to the very low piezoresistive coefficients.

In the <110> direction the n-type piezoresistors have a longitudinal coefficient of -31.2$\times$10^{-11} Pa^{-1} and a transversal coefficient of -17.6$\times$10^{-11} Pa^{-1}. This configuration is in general not prefered for measurements due to the low piezoresistive coefficents compared to the <100>

direction. P-type pezoresistors in the <110> direction with a resistivity of 7.8 Ωcm show a fractional resistance change given by:

$$\frac{\Delta R}{R} = \sigma_l \cdot \frac{\pi_{44}}{2} - \sigma_t \cdot \frac{\pi_{44}}{2} = \frac{\pi_{44}}{2} \cdot (\sigma_l - \sigma_t)$$ (2.8)

where π_{11} and π_{12} are considered zero due to their very low value compared to the π_{44}. This configuration is suitable for measurements and used in this study. P-type piezoresistors in the <110> direction are preferred in this work compared to the n-type in the <100> direction because is a convenient crystallographic orientation from a fabrication standpoint [53], moreover boron is the most common used dopant. In a (100)-oriented wafer the p-type piezoresistors in the <110> direction are orthogonal to each other, therefore fabricating the piezoresistors in the X and Y-axis pointing to the <110> direction it is possible to measure the in-plane acceleration by simple Wheatstone bridges circuits (see Appendix G and H for details).

2.6.2   Giant Piezoresistance in Silicon Nanowires

In the last decade experimental studies on piezoresistance effect of silicon nanowires agreed that SiNWs under uniaxial stress offers an enhanced piezoresistance effect respect to the bulk counterparts [2-7].

The origin and behaviour of this phenomenon called in the literature "Giant Piezoresistance" is currently not clearly understood. The origin of the giant piezoresistance effect was examined in numerous works [12, 45-47, 140-149]. Alongside with the quantum confinement [45, 137-139] the nature of the giant piezoresistance [3, 140] was explained by the following reasons: strong strain-dependence of effective masses of holes [46], strain modulation of the surface potential [47, 149], interface trapping of charged carriers [140] and stress concentration regions [150]. Existence of the giant piezoresistance in nanowires [3] was

contested in work [79]. To date, relatively few reports on the development of silicon nanowire-based sensors are available [42]. However, p-type single crystalline SiNWs have been studied for sensor applications [2, 13, 14, 43, 44, 134, 136].

Toriyama *et al.* studied silicon nanowire piezoresistors have been fabricated by separation by implanted oxygen (SIMOX), thermal diffusion, electron beam (EB) direct writing, and reactive ion etching (RIE) [43]. Longitudinal and transverse piezoresistive coefficients, π_l $_{<110>}$ and $\pi_{t <110>}$, are both dependant on the cross sectional area of the nanowires. The $\pi_{l <110>}$ of the nanowire piezoresistors increased (up to 60%) with a decrease in the cross sectional area, while $\pi_{t <110>}$ decreased with an increase in the aspect ratio of the cross sectional area. The enhancement behaviour of the $\pi_{l <110>}$ was explained qualitatively using 1-D hole transfer and hole conduction mass shift mechanisms. The decrease in the $\pi_{t <110>}$ with increase in the aspect ratio of the cross sectional area is explained due to decrease in the stress transmission from substrate to the nanowire. The maximum value, $\pi_{l <110>}$ of 48 x 10^{-11} Pa^{-1} at a surface concentration of 5 x 10^{19} cm^{-3}, suggests enough sensitivity for sensing applications (see Table II, [43]). Dao *et al.* incorporated these p-type silicon nanowires as piezoresistive elements in a miniaturized 3-degrees-of-freedom (3-DOF) accelerometer [2, 6]. Initial experimental studies undertaken by He and Yang [3] reported a very high piezoresistive effect (increased up to 3,776%) of self-assembled single crystal silicon nanowires in the <111> crystallographic orientation. Reck *et al.* later on used a lift-off and an electron beam lithography (EBL) technique to fabricate silicon test chips and study the piezoresistive properties of crystalline and polycrystalline nanowires as a function of stress and temperature [4]. They found that the piezoresistive effect in the <110> direction greatly increases as the silicon nanowire diameter decreases (up to 633%), consistent with the results from He and Yang [3]. Finally, Passi *et al.* [7] recently obtained an increase of piezoresistance of up to 2,140% respect to the bulk-Si in the same crystallographic direction, the <110>.

Some hypotheses have been speculated on the origin of such phenomenon, initially it was explained based on transconductance data as being due to enhanced strain modulation of carrier mobility in the p-type <111> and <110> SiNWs [3]. However, first-principle calculations later on point out surface states being the main culprit in p-type <111> silicon nanowires [46, 47]. But in 2009 first-principles results on piezoresistive effect in silicon nanowires in the <111>, <110> and <100> directions carried out by Nakamura *et al.* [12, 45, 137-139] were in contrast to the calculation by Cao *et al.*[46] that the hole transport occurs on the wire wall in p-type <111> SiNWs with dangling bond. Nakamura *et al.* [12, 45, 137-139] in their simulation model find out that the hole transport occurs stably in the interior of p-type <111> SiNWs without dangling bond. They conclude that the <100> direction is the most suitable one for integrating p-type SiNW without dangling bond as nanoscale piezoresistors and allege the origin of such Giant Piezoresistance in this direction ($\pi_{l<100>}= 588 \times 10^{-11}$ Pa^{-1}) can be explained in terms of orbital interactions theory [6, 12]. Finally in this study they obtained that the p-type <111> SiNWs without dangling bonds (H-terminated wire wall) have small piezoresistive coefficients, which is contradictory to the experimental results obtained by He and Yang [3] and in contrast to those in the case of p-type bare-walled <111> SiNW with dangling bonds, reported by Cao *et al.* [46]. Therefore Nakamura *et al.* [12, 45, 137-139] predict that <111>-oriented SiNWs will not be suitable candidate for nanoscale piezoresistors. In conclusion it may be asserted that conductivity of p-type <111> SiNW differs greatly between wire walls with or without dangling bonds and then it is natural for SiNW with a giant piezoresistance coefficient to be under an irregular wall-termination condition [45]. Finally, recently experimental findings adduced the giant effect of being a surface induces effect with {110} surfaces inducing much larger piezoresistance than {100} surfaces [5], showing a clear aspect ratio dependence of piezoresistance coefficient. This work supports the computational work of Cao *et al.* [46] and Rowe [47] pointing towards

surface states being the source of giant piezoresistance. In particular Rowe identifies the origin of this phenomenon in the partial depletion of the conduction channel.

Recently research by Milne *et al.* [79] claimed that this phenomenon may not exist after all The France-Switzerland research team claimed that the observations of giant piezoresistance were probably artefacts and caused by surface trapping of charges (also known as dielectric relaxation) that takes place in the Si/SiO_2 interface and induced by the voltage applied to measure the resistance. The charge trapping results in partial depletion of the nanowires determining the giant effect. The team by applying a heterodyne detection (an oscillating stress to its samples) were able to separate any non-stress-related drift in the resistance value from that caused by the applied stress. In this way the stress repeatedly increases and then decreases as function of time. According to Rowe [158], heterodyne techniques were never applied before to piezoresistance measurement before, so previous measurements revealed large (but not stress-related) resistance change in the silicon nanowires. Yang replied [158] to the results of Rowe [47, 79] by saying that they reported piezoresistance measurements on top-down micro and nanowires while in their measurements they used bottom-up grown nanowires. Since bottom-up synthetic bridging nanowires have quite different strain levels, surface states and dopant profiles from those of top-down fabricated ones the results obtained are of different nature. Moreover, the team of research guided by Yang [86] recently demonstrated the first resonator piezoresistively transduced with very high frequency (100 MHz) using silicon nanowire with on-chip electronic actuation at room temperature. Yang claimed that their resonator would not be possible without enhanced piezoresistance effect [86].

Another study undertaken by Koumela *et al.* [80] showed that top-down nanowires appear in general to have a gauge factors close to bulk, except for low doped suspended nanowires with

a gauge factor twice as high as the bulk. Top-down nanowires [5, 79] have shown much lower piezoresistive coefficients than the ones observed for bottom-up devices [3]. The results of this study support the work of Milne [79] and Barwicz [5] where no giant effect was observed. Table 2-7 summarizes the major experiments undertaken on p-type silicon nanowires under stress/strain.

The modelling of the silicon nanowires based on first principle simulation have revealed a piezoresistance effect higher than in the bulk counterparts in the <100> direction and similar to the bulk counterparts in the <111> [10, 12, 45, 46, 137-139]. These results are in contrast to the experimental work carried out so far. Therefore, future modelling and experimental work need to be conducted in conjunction in order to clarify the origin and to better describe the phenomenon under study.

Table 2-7. p-type silicon nanowires experiments

Researchers and date	Stress direction and Magnitude (MPa)	Crystallographic Orientations	Nanowires Size (W×T×L)	Aspect Ratio (T/W)	Doping Type	Doping Concentration (cm^{-3})	Sheet Resistance (R$_s$), Resistivity (ρ) or Resistance (R)	Piezoresistive Coefficients: longitudinal (π$_l$) and transverse (π$_t$) (MPa^{-1})	Resistance change vs. Stress response
Tufte and Stelzer (1963) [69]	N/A	<110>	Bulk	N/A	p-Type	N$_s$: 5x10^{19}	ρ(Ω-cm): 0.003	π$_l$: 31x10^{-5} π$_t$:-31x10^{-5}	Linear response
Toriyama et al. (2002) [43]	Tensile (0 to 80)	<110>	W: 53-333nm T:53-65nm L: 3μm	0.2 to 1.01	p-Type	N$_s$: 5x10^{19}	R$_s$(Ω/□): 809 R(kΩ): 9.1-105.8	π$_l$: 30 to 48x10^{-5} π$_t$:-4 to -20x10^{-5}	Linear response
Toriyama et al. (2003) [44]	Tensile (0 to 115)	<110>	W: 100nm T:53-nm L: 3μm	0.53	p-Type	N$_s$: 9x10^{19}	R$_s$(Ω/□): 604 R(kΩ): 61.2	π$_l$: 38.7x10^{-5} πt: 0	Linear response
Dao et al. (2004) [2]	Tensile (0 to 115)	<110>	W: 53nm T:53nm L: 3μm	1	p-Type	N$_s$: 5x10^{19}	R$_s$(Ω/□): 809 R(kΩ): 105.8	π$_l$: 30 to 48x10^{-5} π$_t$:-4 to -20x10^{-5}	Linear response
Okamura et al. (2005)* [13]	-0.7 to 0.7 (20G)	<110>	W: 100nm T:150nm L: 4μm	1.5	p-Type	N$_s$: 5x10^{19}	ρ(Ω-cm): 0.003	N/A	N/A
Sakai et al. (2006)* [14]	-0.9 to 0.6 (20G)	<110>	W: 300nm T:170nm	0.56	p-Type	N$_s$: 5x10^{19}	R(kΩ): 20	π$_l$: 35x10^{-5}	N/A
He and Yang (2006) [3]	-80 to 80	<111>, <110>	D$_{<111>}$: 50nm To 350nm (diameter) D$_{<110>}$: 73, 75nm (diameter) L: 1.5 μm	1	p-Type	N$_{s<111>}$: 1x10^{15} to 5x10^{19}; N$_{s<110>}$: 1.3x10^{14} and 6x10^{16}	ρ$_{<111>}$(Ω-cm): 0.003 to 10 ρ$_{<110>}$: 0.3, 100	π$_{l<111>}$: 35x10^{-5} to 3,550 x10^{-5} π$_{l<110>}$: 660 to 3100 x10^{-5}	Non Linear response
Reck et al. (2008) [4]	Compressive (0 to 90)	<110>	W: 50 to 350nm T:140 to 480nm L:1 to 7 μm	0.4 to 1.4	p-Type	N$_s$: 4x10^{16} and 3x10^{18}	ρ(Ω-cm): 0.02 and 0.4	π$_{l<110>}$: 70 to 455x10^{-5}	Linear response
Barwicz et al. 2010 [5]	Compressive (0 to 150) <110>-oriented	<110>, <100>	W: 5 to 113nm T:23 to 45nm L:400 nm	0.4 to 4.6	p-Type	N$_s$: 1x10^{15}	ρ(Ω-cm): 14	π$_{l<110>}$: 290x10^{-5}	Linear response
Dao et al. (2010) [6]	N/A	<110>	W: 35-480nm T: 35nm L: 2μm	0.07 to 1	p-Type	N$_s$: 1.28x10^{18}	N/A	π$_l$: 80 to 130x10^{-5}	N/A
Passi et al. (2010) [7]	Tensile (0 to 200)	<100>	W: 25-1000nm T: 50nm L: 0.3 to 2.4μm	0.05 to 2	p-Type	N$_s$: 6.55x10^{14} and 4.74x10^{18}	ρ(Ω-cm): 0.014 and 20	π$_l$: 1350 to 1538x10^{-5}	Non Linear response
Milne et al. (2010) [79]	-13.3 to 13.3	<110>	W: 50-3000nm T: 50-2000nm L: 1, 30 μm	0.1 to 2	n-Type p-Type	N/A	N/A	π$_l$: -99 to 205x10^{-5}	Non Linear response
Koumela et al. (2011) [80]	N/A	<110>	W: 36, 40 nm T: 38, 40 nm L: 350 nm to 5μm	~1	p-Type	N$_s$: 5x10^{17} to 2x10^{20}	ρ(Ω-cm): 0.0006 to 0.06	Gauge Factor: 235	Linear response

*SiNW embedded in an accelerometer

2.6.3   Fabrication processes of silicon nanowires

Currently there are two main technologies for the fabrication/growth of nanowires: self-assembly and top-down approach. The self-assembly technology is a growth mechanism. The more common growth mechanisms are vapour-liquid-solid (VLS) and oxide-assisted growth (OAG) mechanisms [10]. In the VLS model, the nanowire grows from a metal-catalyst droplet during silicon vapour deposition. The metal particles are present at the tips of the Si NWs. This mechanism is used by He and Yang [3] for growing their nanowires in the <111> and <110> direction using Pt as catalyst and $SiCl_4$ as precursor at 900°C. The oxide-assisted growth process produces metal-free SiNWs. The mechanism does not require metal catalyst and the oxide is continuously needed throughout the entire nucleation and growth process [10]. Main problem of the use of this technology is the integration of the silicon nanowires growth into the MEMS fabrications steps.

The top-down approach of fabrication of nanowires comprises mainly two different technologies: electron beam lithography (EBL) and nanoimprint lithography (NIL). These are currently part of standard industrial micro/nano fabrication. Both technologies have sub-10 nm resolution, a limit of 3-5nm resolution is achievable with both technologies [50, 51]. EBL consists of a focused electron beam with nanometre spot size that is scanned across the surface to be patterned. EBL is a maskless lithography, where the electron beam directly creates the fine patterns with random shapes in positive and negative electron beam sensitive resists [51]. Because of serial pattern generation EBL suffers from serious throughput limitations. It is typically ideal for research and development and small volume production. The EBL is followed by RIE etching or lift-off as pattern transfer. For industrial scale nanowire fabrication, NIL is a more suitable technology. Ultraviolet nanoimprint is a mechanical molding technique. A template made from quartz or a flexible elastomer with a

3D relief is brought into intimate contact with a UV-curable resist spin-coated on top of a substrate. Applying low imprint pressure at room temperature, features are filled within seconds due to the low viscosity of the imprint resist. Alignment of template and wafer is carried out with high precision and the resist is hardened via UV-light through the backside of the template. Finally substrate and template are separated. The replicated resist relief can further be transferred into the substrate via RIE-process or used as functional element [50]. These two technologies can be combined, in particular the EBL is used to fabricate efficient moulds for nanoimprinting structures with high density moulds [50, 51].

2.7 Gap in Knowledge

All of the studies reported in this study agreed that low doping and surface-to-volume ratio represent the main parameters that boost the piezoresistance effect of SiNWs. Some hypotheses have been speculated on the origin of such phenomenon [42]. Recently the major culprit has been indicated to be surface-state induced effect for nanowires smaller than 70 nm width, and enhanced strain modulation of carrier mobility for larger nanowires [43].

In this work the author intends to investigate experimentally the suitability of p-type SiNW in the <111> direction as nanoscale piezoresistors for mechanical sensors, by fabricating nanotechnology samples.

From the literature review outlined in the Table 2-5, the following summarized considerations have been made:

a. No experimental data are available for SiNWs with feature around 5 nm in any of the <111>, <110> and <100> directions.

Mainly because of technology difficulties in the downscale of SiNWs.

b. No experimental data are available for p-type SiNW in the <100> direction under only uniaxial stress

Because of the very low piezoresistive effect of the bulk piezoresistor counterparts in the <100> crystallographic direction

c. No experiment has been undertaken on bottom-up silicon nanowires applying an oscillating stress.

The surface charge trapping of SiNW was unknown before the study of Milne at al. [79]

d. Not clear explanation has been given on the giant effect origin (surface induced or carrier mobility modulation or orbital interaction) and two studies [79, 80] did not observe this phenomenon at all.

There are controversial results and explanations of previous theoretical and experimental studies.

The p-type <100>, <111> SiNW showed Giant effect in first-principles calculations [10, 12, 45, 46, 49],

BUT:

1   The p-type <100>, <111> SiNW are suitable as piezoresistor?

2 The bottom-up silicon nanowires under oscillating stress do they show an enhanced piezoresistance effect?

The experimental work undertaken in this study aims to answers part of the first question demonstrating the feasibility of fabricating silicon nanowires as nanoscale piezoresistors in the <111> direction.

2.8 Conclusion

The investigation carried out on silicon nanowires will ultimately allow the development of inertial sensors (e.g. accelerometer) with a very tiny footprint being characterized by high sensitivity not achievable before. Traditionally a trade-off between miniaturization and sensor sensitivity has limited the miniaturization and together the accuracy achievable. To date no tri-axis accelerometer are commercially available with a size below 2×2 mm capable to measure impacts events of >250g; besides, none of them can avoid amplification of the output signal, mainly because the relative high thermo-mechanical noise due to small proof mass size. The sensitivity achievable by the incorporation of quantum wires that benefits giant effect within the sensor (two orders of magnitude larger than that of bulk silicon, [6]) will permit to obtain an electrical sensitivity (static response) such that the device will not require any kind of amplification (high accuracy of measurements) and will allow to achieve a miniaturization level not permitted before. Obviously, sensors that avoid amplifier enjoy a much higher sensing accuracy. This study will predict the advent of a new class of electro-mechanical-system devices in the nanoscale dimension (NEMS) with a footprint less than 1 square millimetre with high sensitivity and accuracy.

Major applications of such novel sensor based on enhanced nanoscale piezoresistors are in the biomedical arena, such as implantable devices for motion/vibration sensing. Examples are in hearing aid systems (implantable sound sensor for cochlear implants [112]), heart wall motion measurement for cardiac artificial pacemakers (an adaptive control system that detects the human body activity level in order to adjust accordingly the pacemaker rate response [102]) and head injury monitoring of military soldiers and race car drivers in case of blast and crash respectively (an earplug sensor placed in the inner ear canal). It is presumed that such devices, with these amazing technical characteristics driven by nanotechnology, will spread also in the area of consumer products as can be observed already with conventional accelerometers.

Moreover, shrinking the miniaturization size in the sub-millimetre will pull the fabrication cost down due to the higher number of devices fabricated per silicon wafer (batch fabrication) and at the same time will increase the systems integration in a single chip allowing the development of increasingly intelligent sensors. Currently the most time and cost effective nanofabrication process of nanowires that seems more suitable for high volume manufacturing processes in the area of top-down fabrication technology is the nanoimprint lithography (NIL). The electron beam lithography (EBL) in comparison is much more time-consuming process and with higher cost obtaining similar or less resolution than NIL. Other option is to grow the nanowires as self-assemble devices, which is the technique used in this work. Currently most of the work on silicon nanowires as nanoscale piezoresistors has been carried out on top-down fabricated sensors, therefore the few study on bottom-up silicon nanowires are not exhaustive, and this work intends to progress the knowledge on this type of sensors.

All the historical findings since the experimental work of Smith [48], graphically described by Kanda [72] first and then improved by a fitting function of Harley and Kenny [53] that

perfectly describes the work of Mason *et al.* [70], Tufte *et al.* [69] and Kerr *et al.*[75] have been presented. The effort to explain the physics behind the piezoresistive phenomenon by Herring [110, 111] with his many-valley model and by Lin [113] with his scattering mechanism of subbands theory has been highlighted. The most recent advancement on the piezoresistive effect in the nanoscale dimension outlining all major experiments on p-type silicon nanowires and first-principle calculation by simulation models proposed by Nakamura *et al.* [12, 45, 137-139] have been addressed. The latest developments of Milne [79] and Koumela [80] on possible explanations of the giant effect as apparent phenomenon due to dielectric relaxation are also considered.   The work done so far on the giant piezoresistance effect is:

a. Limited to nanowires size above 5 nm in the <110> and <111> directions,

b. No experiments are currently available on bottom-up silicon nanowires applying oscillating stress.

c. The work carried out on explaining this phenomenon, if really exists, by first-principal simulations contradicts the results of various experimental studies.

The next chapter deals with the design and simulation of a novel accelerometer that embeds silicon nanowires as nanoscale piezoresistors. Moreover in order to highlight the potential of the nanowires, a comparison to conventional microscale piezoresistors is proposed.

Chapter 3

3 DESIGN, MODELLING AND OPTIMIZATION OF A BIO-MECHANIC PIEZORESISTIVE ACCELEROMETER WITH SILICON NANOWIRES

3.1 Introduction

This chapter aims at the design, modelling and optimization of a 3-axial single square millimeter bio-mechanic piezoresistive accelerometer and presents the simulation results. As accurate measuring of head accelerations is an important aspect in predicting head injury, it is important that the measuring sensor be well-coupled to the head [23]. Therefore, the main requirements of this application are miniaturization and medium-g measurement range to allow the accelerometer incorporation into an earpiece. In order to fulfil these requirements nanowires as nanoscale piezoresistive devices have been chosen as sensing element, due to their high sensitivity and potential in miniaturization [2-7, 43, 44]. The geometry structure has been selected based on sensitivity criteria by an optimization process using commercially available software ANSYS 12.1. Stress, deformation and modal analysis of nine different geometries has been undertaken with the common feature of being highly-symmetric (i.e. symmetry on the principal X and Y-axes, the respective diagonals and rotating of multiple of

90°). Moreover two new geometries not available in the literature have been developed in the study. These types of geometries are all single-mass and are divided in the literature in cross-beams [94, 96-98, 100, 101, 103], cross-inset beams [95, 99, 102, 105], surrounding beams [2, 93, 104] and surrounding cross-inset beams [106]; all of them allow the minimizing of the overall cross-sensitivity due to a self-cancelling feature typical of highly-symmetric geometry. In the literature only few piezoresistive accelerometers have been developed with silicon nanowires and surrounding beams [13, 14].

Section 3.2 introduces the main elements and considerations that have driven the accelerometer design and in section 3.3 follows the FE modelling. In section 3.4 the optimization process of nine different shapes is presented. Section 3.5 presents the results of the device performance calculation by comparing silicon nanowires to conventional microscale piezoresistors. Finally the optimization results are presented and the final optimal geometry is enhanced with the design of overload end stops.

3.2 Accelerometer design concept and considerations

The key design criteria are to develop a 'High Resolution - Low power 3-DOF Piezoresistive MEMS-based Accelerometer'. Low power consumption is mandatory for this device since it is placed inside the ear, hence, specific attention must be paid to power dissipation process in order to avoid discomfort during wear. This has a particular drawback in that it affects the signal to noise ratio due to the high resistance of the piezoresistors (high white noise).

The resolution will be maximized by reducing the noise level to the minimum possible. Moreover due to the miniaturization currently achievable by MEMS fabrication processes the

sensor is designed for this type of technology. This last choice will affect notably the design since a design for manufacturing and for packaging is required.

The basic ideas behind the design concept are driven by the required sensor technical specifications that are dependent on the particular sensor application (crash test) [32]. The target technical specifications of the accelerometer have been specifically designed to fulfil the application requirements that is to detect and measure high speed impacts of vehicles that have the typical characteristic of long duration transient (low frequency) and relatively high amplitude (medium-g impacts). The target sensor specifications are listed in the Table 3-1.

Table 3-1. Target sensor technical specifications

Range (g)	Sensitivity (mV/g)	Frequency Response (Hz)	Shock Limit (g)	Resolution (mg)	Non-linearity	Cross-Sensitivity	Dimension (mm^3)
±250	4	0 to 1,000	±1,000	<10	<1% FSO	<5%	<2×2×1

First of all the accelerometer was designed as a tri-axial one in order to measure all the linear components of the acceleration when an accident occurs (three-degree of freedom, 3-DOF). The device is a single sensing element and not a multiple sensing element, which means that only one sensor is developed for simultaneously detecting the linear acceleration on the three axis, instead of implementing three sensing elements one for each axis. This choice has been made after considering the two options in place (single or multiple sensing elements). The main advantage of developing one sensor for each axis (X, Y, Z), as the Delphi earplug [127], is the reduced cross-axis sensitivity on each axis that can disturb the principal signal. On the other hand, the implementation of three linear sensors for a given chip size implies an overall lower sensitivity, due to the smaller relative proof mass of each sensor than a single 3-axial sensor in a given space. Therefore it requires more complex read out circuitry in order to amplify the signal. Moreover the major electronic and mechanical complexity of the three

72

sensor chip choice increases the total noise and then it reduces the minimum detectable acceleration which means it reduces the sensor resolution. Thus the quality of measurement (accuracy and resolution) has driven this design decision.

Second, in order to overcome the cross-sensitivity issue of the single tri-axis accelerometer a highly symmetric geometry (i.e. symmetry on the principal X and Y-axes, the respective diagonals and rotating of multiple of 90°) is preferred, which means a proof mass suspended by four identical beams one for each side of the mass. This type of shape allows minimizing the overall cross-sensitivity of the device due to the self-cancelling feature that the highly symmetric geometry offers. Quad-beams sensing geometry is preferred because of its balanced structure stiffness and achievable sensitivity.

The measurement range of each axis has been set to 250g FS for detecting medium-g impacts because inertial forces of the head at 75 to 150g are common in racing accidents [28]. The sensitivity has been set to 4 mV/g in order to obtain an output voltage of at most 1 V at 250g, which in general does not require amplification. The upper limit of the sensor bandwidth is 1 kHz which is more than sufficient in case of shock measurement like crash observed via accident video footage, where by the driver's head move above 30 Hz [28]. It has been defined higher than necessary (the high frequency signals is also filtered) because it improves the dynamic response and the velocity of the response. A minimum of 0 Hz is required in order to detect a car impact, since generally a crash has a long duration transient of around hundreds of milliseconds (e.g., ≈ 0.5 sec or ≈ 2 Hz) [32]. The power and current supply, respectively 5 V and 10 mA, are supplied by the accident data recorder placed in the race car where the sensor is plugged in.

Shock survivability is set to 1000g which is a typical value for piezoresistive shock accelerometer. The resolution is set to a maximum of 10mg since the application does not require a higher resolution. This owes to the fact that the precision of the acceleration

measured is less relevant than the sensor accuracy for the medical personnel monitoring the race, since they are only alerted when an accident exceeds a severity threshold. The precision of the data collected may be additionally relevant for vehicle designers that can deploy the data in designing better driver restraint systems and safety devices. The usefulness of the sensor readings for designers is regarded as secondary in the design concept.

The overall sensor error, which is the sum of nonlinearity and cross-sensitivity in the dynamic working range, must be as small as possible in order to not affect the accuracy of the measurement. The target value of nonlinearity and cross-sensitivity are set to an acceptable limit (Table 3-1, <6%). Efforts are dedicated into designing a sensor with a smaller error (<2%).

Finally the physical dimension of the sensor must allow perfect fit inside the ear canal (part of the earpiece which is normally 7mm diameter) (see section 2.2.1 Dimension and Shape of Human Ears). The maximum dimension has been set to 2×2×1mm. In order to avoid mass loading, the device weight has been set following the common rule-of-thumb where the sensor weight is less than 10% of the test article [37] (Appendix A - *Physical Characteristics*). In this case the test article is an adult head which generally weights more than 4 kg, therefore there is a wide margin in the accelerometer weight to allow flexibility in the application.

The piezoresistive pick-off is selected due to the smaller size achievable and the opportunity of a hybrid system partitioning design due to the low impedance of the piezoresistive pick-off signal output. In other word, piezoresistive pick-off allows for integrating the signal conditioning far away from the sensing element, therefore main consequence is the opportunity of designing a larger seismic mass that enhance the sensor sensitivity. This type of system partitioning fits well for a moulded earpiece. Basically, the sensing element is

placed in the ear canal part of the earpiece and the necessary signal conditioning (amplifier and filter) can be placed in the outer part of it without affecting the accuracy of the measurement (see Figure 2-5 for an example). Furthermore the temperature drift, main concern of the piezoresistive pick-off, is restricted in the small temperature operation range of the device (+37°C to +40°C).

The fabrication process preferred for releasing the microstructure of the tri-axis accelerometer is one of the three MUMPs (Multi-User MEMS) processes: the SOI-MUMPS (silicon-on-insulator Multi-User MEMS) [82]. This process has been developed by the MEMSCAP Company in a standard fashion starting from a three layered SOI wafer with device thickness 10μm and silicon substrate thickness 400 μm. This standardized process allows a consistent cost cut.

3.3 Accelerometer model

3.3.1   Mathematical model

The mathematical modelling of the sensor is based on the classic configuration as second order mass-spring-damper mechanical system. Figure 3-1-(a) shows a schematic diagram of an accelerometer of one-degree of freedom. The spring constant (k) defines the stiffness of the entire structure. For the Hooke's law the deformation of a spring is directly proportional to the load applied, provided the limit of proportionality is not exceeded.

The damping element (B) is the representation of all source of damping inside this structure including mechanical damping in the springs and support, airflow and acoustic radiation.
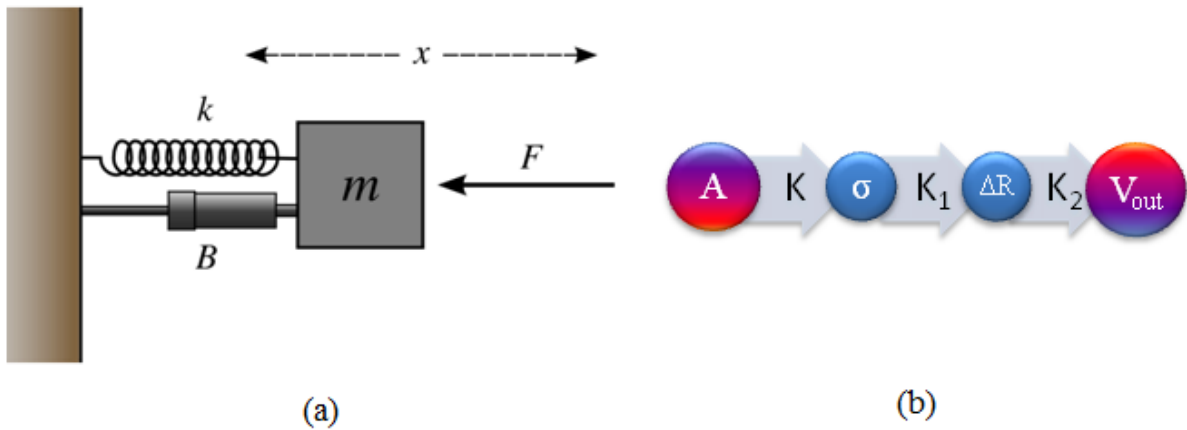
Figure 3-1. (a) Mass-spring-damper system; (b) Graphical representation of the electromechanical physical model involved in the sensing (K, K1, K2 are the constants)

A model example of the sensing chip is shown in Figure 3-2. The proof mass in the centre area is suspended by a single beam that resembles a spring, while the damper is air in the model. The beam is clamped to an external fix frame (not showed in the figure). When acceleration is applied to the die, the proof mass is displaced due to inertial forces, resulting to beam deformation.

The structure in Figure 3-2 is equivalent to the mechanical schematic diagram in Figure 3-1-(a) with only a key difference: the spring in Figure 3-1-(a) is subject to axial load (compressive or tensile stress), whereas the beam in Figure 3-2 is subject to a transversal load (bending).
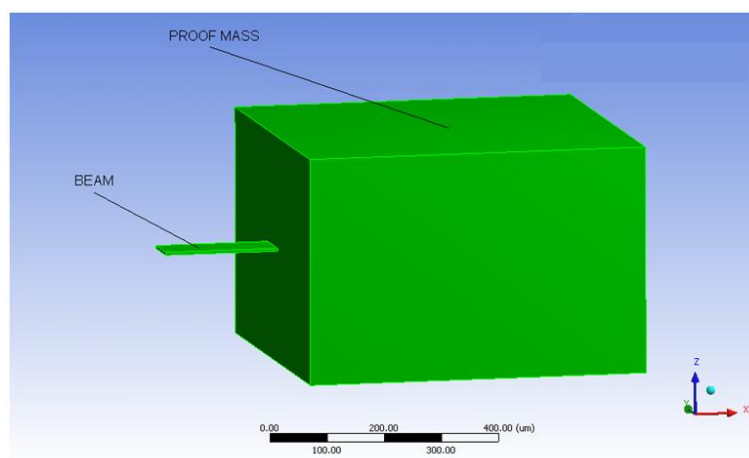
Figure 3-2. Simple 1-DOF accelerometer with a beam and suspended proof mass.

Under acceleration on the Z-axis the beam deflects proportionally determining stress and strain on its surfaces.

In the case of free-vibration without damping, the proof mass will oscillate with simple harmonic motion with frequency of f_n (undamped natural frequency). For the simple mass–spring system, f_n is defined as:

$$\omega_n = 2\pi f_n \tag{3.1}$$

where ω_n is the angular natural frequency

$$f_n = \frac{1}{2\pi}\sqrt{\frac{k}{m}} \tag{3.2}$$

where f_n is the natural frequency, k is the stiffness and m is the mass.

The mechanical sensitivity (S) of the structure is related to the angular frequency as:

$$S = \frac{1}{\omega_n{}^2} \tag{3.3}$$

This equation clarifies the trade-off to be achieved between sensitivity and natural frequency in designing the accelerometer mechanical structure.

The beam deformation, due to the applied stress (σ) (see Figure 3-1-(b)), leads to a change in resistance (ΔR) of piezoresistors proportional to the applied acceleration (A). The fractional resistance change ($\Delta R/R$) in the measurement circuit is proportional to the output voltage drop V_{out}, therefore representing a measure of the acceleration; as demonstrated in Figure 3-1-(b).

3.3.2 Finite element modelling

FE analysis of nine mechanical structures (Table 3-3), both static (under 250g in X or Y-axis and Z-axis direction) and modal analysis (free vibration, only the first three mode of operation are obtained) is conducted under simplified conditions (undamped structure, isotropic silicon material properties, tetrahedron meshing elements at maximum 30,000

nodes) since the first step of the optimization process represents just a qualitative study (only the shape is evaluated, not the geometry size). The boundary conditions for the static analysis (stress and deformation) are a vector of acceleration with amplitude of 250g and the beams clamped in one extreme to a fixed frame. Regarding the modal analysis set-up, the beams are clamped to a fixed frame in order to allow a free vibration of the proof mass in different mode shapes.
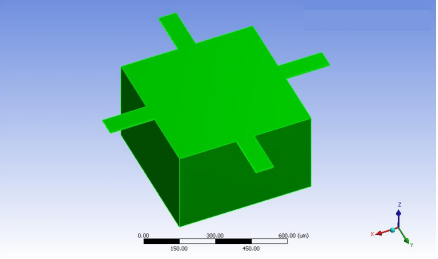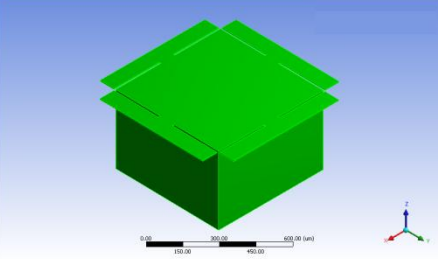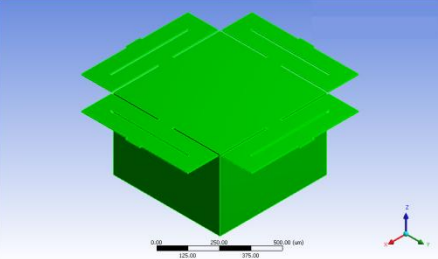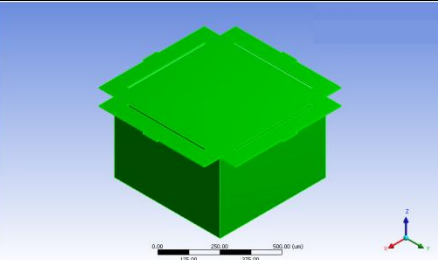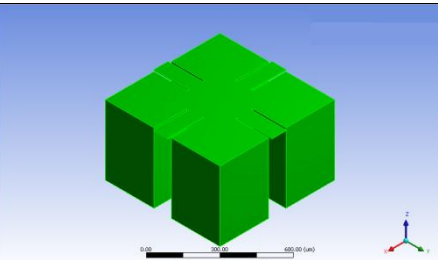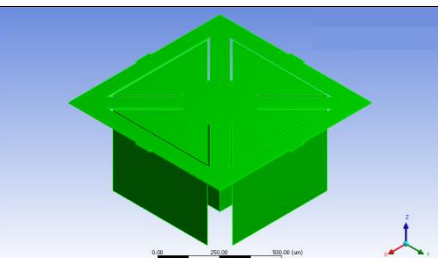
The finite element analysis sets the following initial values for each of the nine structures under analysis, for structural shape comparison purpose (Table 3-2):

Table 3-2. FEM analysis set up

Initial proof mass volume (V)	144×10^{-12} m^3
Beam Thickness (t)	5 μm
Silicon (single-crystal) density (ρ)	2330 kg/m^3
Young's modulus of silicon (E)	185 GPa
Poisson's ratio of silicon (ν)	0.28
Acceleration applied (a)	250g (around 2450 m/s^2)
Mass of the proof mass (m)	335520×10^{-12} kg (or 0.33 mg)

Notice that all the structures under study have identical proof mass volume therefore since they are all under the same loading condition the inertial forces applied to the beams of each structure are comparable.

Table 3-3. Highly symmetric shapes selected for the analysis

SHAPE 1. Cross-beams The proof mass is suspended by four beams connected in the middle of each of the four sides of the proof mass perpendicularly.	
SHAPE 2. Surrounded-beams Picture-frame type 1 The proof mass is suspended by four beams connected in the middle of each of the four sides of the proof mass surrounding it.	
SHAPE 3. Surrounded-beams Picture-frame type 2 The proof mass is suspended by four beams connected in the middle of each of the four sides of the proof mass surrounding it. Moreover each beam form a closed shape.	
SHAPE 4. Surrounded-beams Picture-frame type 3 The proof mass is suspended by four beams connected in the corner of each of the four sides of the proof mass surrounding it.	
SHAPE 5. Cross-inset beams The proof mass is suspended by four beams connected in the middle of each of the four sides of the proof mass perpendicularly and crossing inside the proof mass.	
SHAPE 6. Surrounded-cross inset beams Picture-frame type 1 The proof mass is suspended by four beams connected in the corner of each of the four sides of the proof mass surrounding it and crossing inside the proof mass.	
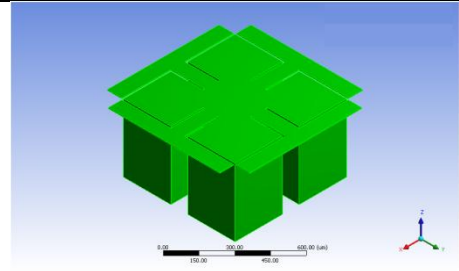
SHAPE 7. Surrounded-cross inset beams Picture-frame type 2 The proof mass is suspended by four beams connected in the middle of each of the four sides of the proof mass surrounding it and crossing inside the proof mass**.**	
SHAPE 8. Surrounded-cross inset beams Picture-frame type 3 The proof mass is suspended by four beams connected in the middle of each of the four sides of the proof mass surrounding it and crossing inside the proof mass. Moreover each beams for a closed shape.	
SHAPE 9. Surrounded beams Picture-frame type 4 The proof mass is suspended by four beams connected in the corner of each of the four sides of the proof mass surrounding it. Moreover each beam form an open shape.	
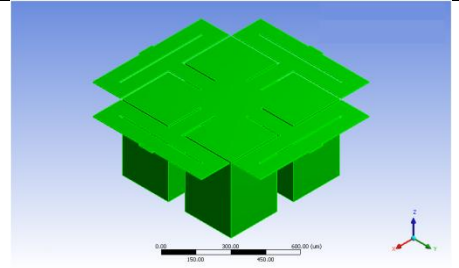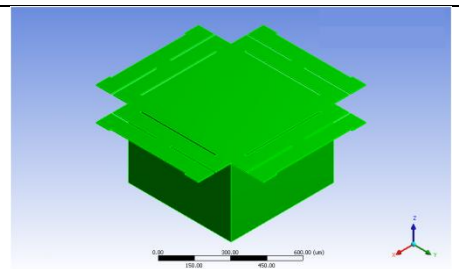
3.4 Accelerometer Geometry Optimization

This section addresses the decision making process of the device geometry design, which covers first the shape design and then the size design and optimization.

The geometry structure, selected on sensitivity criteria, has been identified by an optimization process using commercially available software, ANSYS 12.1. This process consisted of an extensive stress/strain, deformation and modal analysis (undamped free vibration) of nine different highly-symmetric geometries (Table 3-3) divided in the literature as cross-beams [94, 96, 97, 98, 100, 101, 103], cross-inset beams [95, 99, 102, 105], surrounding beams [2, 93, 104] and surrounding cross-inset beams [106]. All selected shapes are available in the literature except shapes no. 6 and 9 that are completely new (see Table 3-3). Shape no. 6 is designed as an evolution of shape no. 4 and 5, in fact is a combination of surrounding and

cross-inset beams. Shape no. 9 is designed as an evolution of shape no. 4, where the surrounding beams are extended.

The design of the geometry of the micromechanical structure of the sensing element is divided in various steps as follows:

1. Qualitative and comparative analysis of various types of structure shapes (shape design)

2. Selection of possible shape candidates for the final structure

3. Size optimization of the candidate shapes (size design and optimization – design for packaging)

4. Selection of the best microstructure geometry

5. Selection of a manufacturing process and adjustment of the geometry accordingly (design for manufacturing)

6. Overload end stops design

3.4.1   Accelerometer shape optimization

In order to minimize the total chip size for a given sensor sensitivity and bandwidth this study selects the shape that maximize the stress and the natural frequency, that is, the one with the highest sensitivity and bandwidth. The sensor sensitivity and bandwidth are inversely proportional therefore a trade-off must be achieved, see equation (3.3).

Since the piezoresistor changes resistance proportionally with the stress applied, for example in a tensile condition the resistance of the piezoresistor increases proportionally with the tensile stress, if the piezoresistor is placed where the maximal stress is located on the device beams the highest sensor sensitivity is then obtained. Therefore, if it is chosen a device shape

with the highest stress value, for a given proof mass volume and under the same load and boundary conditions, the device that offers the highest sensitivity can be identified.

The FEM static analysis allows determining the device mechanical stress under load, while the modal analysis reveals the natural frequency at different modes of operation of the device under no load (free-vibration without damping). For both analyses the external frame of the mechanical structure is kept fixed in order to allow the movement of the suspended proof mass. The higher the natural frequency, which is the frequency at which the device resonates, the larger the usable bandwidth of the device. Typically, the usable bandwidth (linear dynamic response) is five times smaller (20%) than the natural frequency [34], see Figure 2-7. The shape optimization identifies the five best shapes out of the nine shapes under study (see Figure 3.3).

3.4.2 Size optimization of the candidate shapes

The next step is to define the size of beams and proof mass given a minimum natural frequency of five kilohertz as hard constraint, in order to obtain a bandwidth at least of one kilohertz (see specifications in Table 3-1).

The optimization problem has as objective function to maximize the equivalent stress, in order to improve sensitivity, and as constraints the natural frequency of at least 5 kHz, and the die body size of at most 1.5×1.5-mm. This last constraint depends on the packaging decision. Since a chip-scale packaging is chosen for the sensing element, with a maximum packaging footprint of 2×2-mm the die body size may be at most 1.5×1.5-mm (i.e. packaging area = 1.2 × die body size). This last constraint accounts for the design for packaging.

For all five shapes selected from the initial nine (shape optimization) the size optimization is carried out by design of experiments (DOE) approach (the size parameters are changed progressively to create many new designs), finally the stress analysis will indicate the

geometry with the highest performance (see Appendix C for the complete optimization study).

3.4.3 Overload End Stops Design

The final geometry output of the optimization process, is furthermore improved with the introduction of overload end stop in order to stop the proof mass movement when the device is subject to an acceleration of over 500g on either the X- or Y-axis. This feature will prevent both the device to resonate and potential fracture of the silicon (break of the beams) that occurs at the acceleration of around 1000g. At 1000g acceleration the structure achieves the maximum fracture stress of the silicon (set to 300 MPa which is an experimental conservative failure stress value for anisotropically etched diaphragms [83]). The actual fracture strength of silicon is given by Petersen [84] as being 7000 MPa, more than 20 times larger than the value set for the shock survivability.

3.5 Results and discussion

3.5.1 Shape optimization

The various shapes addressed in this study are cross, surrounded, folded and inset beams with single mass (Table 3-3). Since the highly symmetric geometry selected, for in-plane acceleration only a single axis acceleration is simulated (X-axis acceleration), the results of the other axis is similar (see Appendix B for the complete study results). Note that the best five shapes out of the total initial nine are selected after the qualitative analysis that compares their performance. The optimization function used to select the five remaining shapes is maximization of stress and natural frequency (first mode of operation) in order to have

further chances to increase their performance in the next size optimization stage (Table 3-4 for a summary).

The five shapes selected as possible candidates for further optimization are depicted in Figure 3-3, showing the beams deformation and stress under Z-axis acceleration. Notice that the number of each shape is correspondent to the order in the complete shape study, available in the Appendix B (see also Table 3-4).
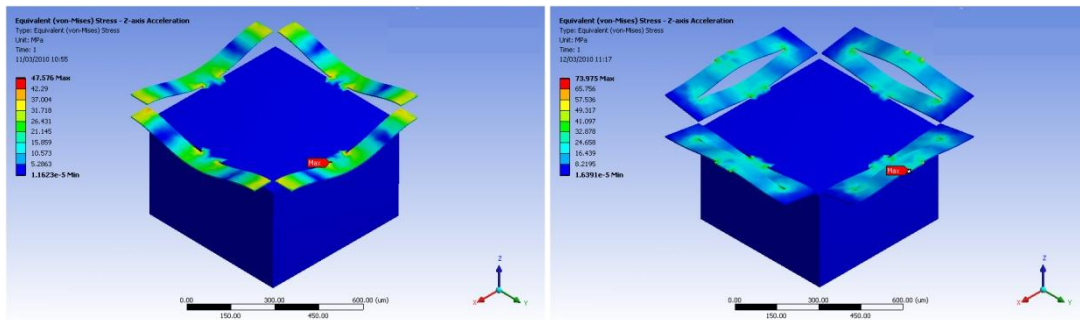
Shape n. 2   Shape n. 3
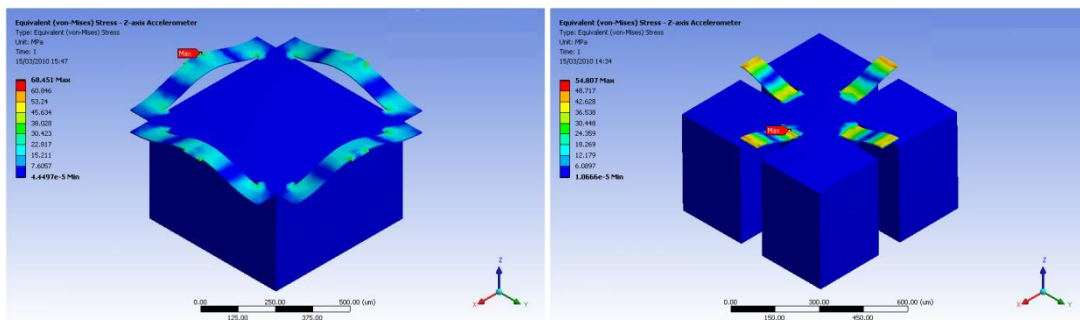
Shape n. 4   Shape n. 5
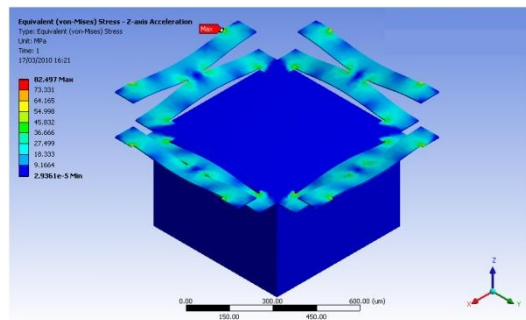
Shape n. 9

Figure 3-3. Five shapes selected as possible candidates for further optimization. The beams are deformed under Z-axis acceleration.

The surrounded picture-frame beams type of accelerometers have demonstrated improved sensitivity at more than acceptable natural frequency (see Table 3-4).

At the moment since the proof mass and beams size is an invariant for all shapes, the shape that offers the best performance is the number 9 (1st) with the highest values of stress, strain and deformation, followed in order by shape no. 3, 4, 5, and 2 respectively. Considering the higher natural frequency of shape no. 2 and no. 4 it follows that this two shapes have room for improving their performance at the size optimization stage, because reducing their natural frequency to the specified limit (5kHz) will inevitably increasing their sensitivity (see Eq. 3.3). Finally shape number 4 for its sensitivity and wide frequency response looks promising from this analysis.

Table 3-4. Performance comparison of shapes selected

Shape N°	Accel. Axis Load: 250g	Equivalent Stress (MPa)	Maximum Principal Stress (MPa)	Maximum Shear Stress (MPa)	Equivalent Elastic Strain (Dimensionless)	Maximum Principal Elastic Strain (Dimensionless)	Total Deformation (µm)	Natural Frequency 1st mode (kHz)	Order based on the optimization function (1st best – 5th worst)
2	Z	53.46	52.42	29.04	2.89E-04	2.84E-04	1.20	6.95	5th
	X, Y	48.69	50.73	26.91	2.63E-04	2.64E-04	1.52		
	Tot.	**102.15**	**103.16**	**55.95**	**5.52E-04**	**5.48E-04**	**2.72**		
3	Z	77.12	109.30	42.74	4.17E-04	4.80E-04	1.86	5.78	2nd
	X, Y	61.04	86.58	32.44	3.30E-04	3.89E-04	1.98		
	Tot.	**138.16**	**195.88**	**75.19**	**7.47E-04**	**8.69E-04**	**3.84**		
4	Z	71.30	97.82	38.43	3.85E-04	4.46E-04	0.70	8.93	3rd
	X, Y	62.94	74.00	34.02	3.40E-04	3.52E-04	0.92		
	Tot.	**134.24**	**171.83**	**72.46**	**7.26E-04**	**7.98E-04**	**1.62**		
5	Z	51.40	69.32	28.71	2.78E-04	2.96E-04	0.85	5.28	4th
	X, Y	85.52	85.41	47.68	4.62E-04	4.37E-04	2.44		
	Tot.	**136.92**	**154.74**	**76.39**	**7.40E-04**	**7.32E-04**	**3.30**		
9	Z	82.49	122.41	44.95	4.46E-04	5.40E-04	1.93	5.70	1st
	X, Y	65.13	92.66	35.02	3.52E-04	4.16E-04	2.00		
	Tot.	**147.62**	**215.07**	**79.98**	**7.98E-04**	**9.56E-04**	**3.94**		

A slight problem occurs if we consider the total deformation of the five structures selected. In the case of large deformation the nonlinearity may affect the static response of the accelerometer. Large deflections are present as a rule of thumb if the transverse displacements in a slender structure are more than 10% of the thickness. Therefore the shape with small total deformation would be preferred (shape no. 4 and 2) due to lower nonlinearity error.

Next the size of the five selected shapes will be optimized by a design of experiments approach.

3.5.2 Size optimization

Figure 3-4(a) and (b) show the optimization results of the mechanical structure shape n. 2 under Z-axis acceleration and X- or Y-axis acceleration respectively (DOE optimization). As it can be seen from the figures, all feasible points are above ~5 kHz, in order to get a bandwidth set in the specification of approximately 1 kHz. Moreover a Pareto frontier curve is drawn to highlight the boundary of the feasible points region (see Figure 3-4(a)). For all five shapes selected, under Z-axis and X- or Y-axis acceleration, the design points at higher equivalent stress are selected as optimal designs (see Appendix C for the complete study results).

(a)   (b)
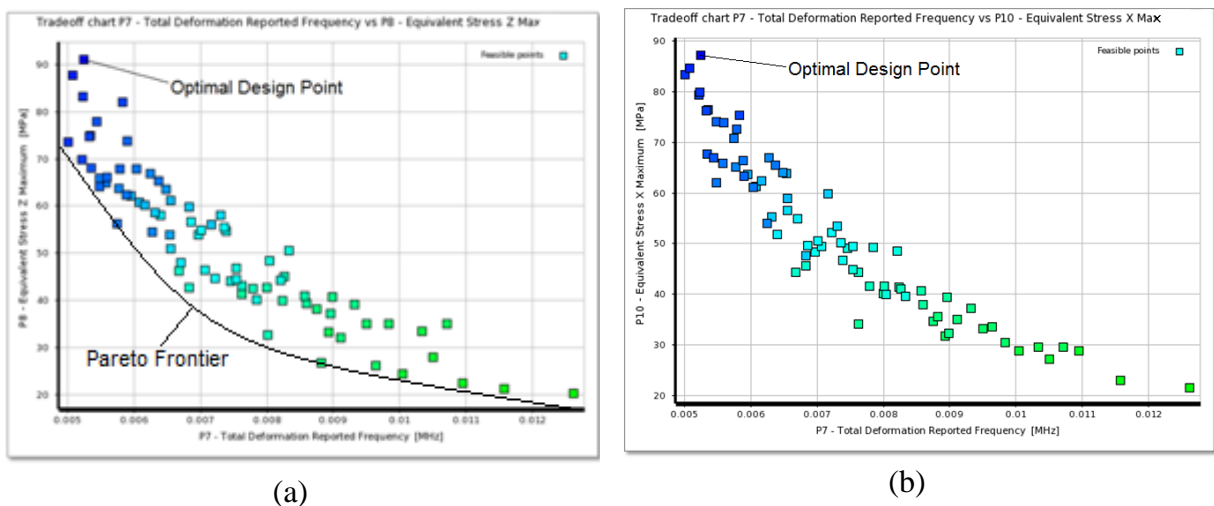
Figure 3-4. (a) Graph that shows the results of the DOE optimization process under Z-axis acceleration. All points above 5 KHz are feasible design points. Notice the Pareto frontier in the graph that is the boundary of the feasible points region. (b) Graph that shows the results of the optimization process under X-axis acceleration. Similar results are obtained for Y-axis acceleration

For example, the optimal design point for shape no. 2 is as follows: 1st mode (ω_{oz}) of 5,251 Hz (bending on Z-axis), the maximum equivalent stress (σ_{eq}) at 250g acceleration in the X or Y-axis are 87 MPa and 128 MPa in the microscale and nanoscale piezoresistors respectively.

In the Z-axis σ_{eq} at 250g acceleration is 91 MPa and 134 MPa in the microscale and nanoscale piezoresistors respectively (Table 3-5).

By taking advantage of structure symmetry only the equivalent stress under X-axis acceleration has been analysed. The results for the Y-axis acceleration are equivalent.

Nanoscale piezoresistors, due to stress concentration region (i.e. the width is 10 times smaller than conventional piezoresistors), show an equivalent stress that is 47% higher than the conventional counterparts under 250g. This increase represents an initial sensitivity enhancement for geometrical reasons. Clearly progressively reducing the piezoresistors dimension will increase the stress concentration effect. The 1st mode shape of the structure is a Z-axis bending at more than 5 kHz. This value defines the bandwidth of the device frequency response. Under an optimal damping design the upper frequency limit is of approximately 1 kHz, as set in the specifications (Table 3-1).

Three potential design candidates are selected for each of the five shapes using DOE, Therefore from a total of fifteen design points (see Appendix C) the best five geometries are identified (see Table 3-5).

Table 3-5. Best geometry design candidates

Shape	Candidate	Beam_Width (μm)	Mass_Width (μm)	Mass_Thickness (μm)	Beams_Thickness (μm)	Total Deformation Reported Frequency (kHz)	Equivalent Stress Z Maximum (MPa)	Total Deformation Z Maximum (μm)	Equivalent Stress X Maximum (MPa)	Total Deformation X Maximum (μm)
2	A	60	550	400	5	5.25	91	1.8	87.	2.7
3	B	60	650	400	7	5.19	95	2.4	82.3	2.4
4	C	70	650	500	6	5.24	103.5	1.6	112	2.8
5	D	50	250	500	6	5.12	49.5	0.6	110	3
9	E	70	550	500	8	5.36	65	2.	55	2.8

Candidate A (shape no. 2) and candidate C (shape no. 4) represent the best geometries both optimized in order to maximize sensitivity given the resonant frequency as a hard constrain (>5kHz) (see Appendix C for the complete optimization study).

The main difference of these two geometries is the overall size, since candidate A has a die size of 550×550×400 μm (considering the surface for the bond pads overall the size is 1210×1210×400 μm) and the candidate C has a die size of 650×650×500 μm (overall 1330×1330×500 μm).

The overall geometry dimensions of the two microstructures are available in the Figures 3-5 (a) and (b).

(a)   (b)
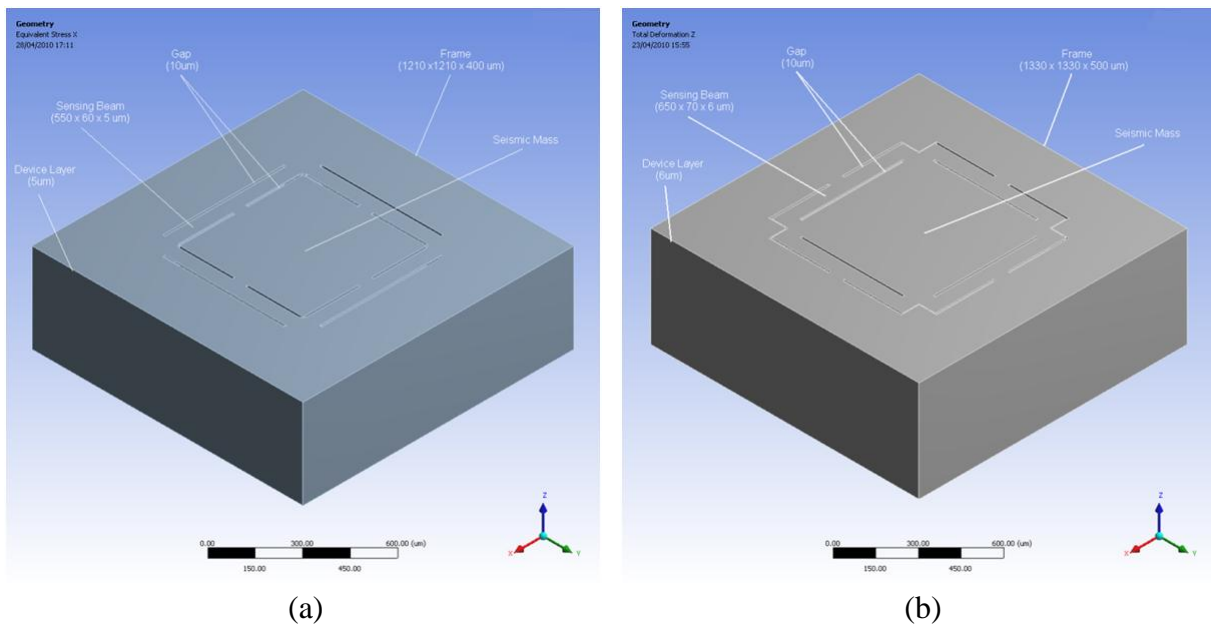
Figure 3-5. (a) Geometry Dimensions Shape no. 2. (b) Geometry Dimensions Shape no. 4

Final consideration for a decision to be made between the two best geometries selected is the design of overload end stops. Overload end stops are required for two main reasons: first to prevent the accelerometer from resonating (at resonant frequency the structure could break) and second to limit the acceleration when the structure is subject to very high-g shock (when g-force > device shock survivability there could be a failure of the structure – breakage of the beams). For this purpose shape no. 2 allows for easily design of overload end stops necessary

for taking account of the reliability of the device and thus has been selected as final candidate.

3.6 Conclusion

The geometry design development of the micro-mechanical structure presented in this chapter optimizes the mechanical structure by improving the performance under the predefined constrains stated in the target specifications (Table 3-1). The shock survivability of 1000g is met thanks to the design of proper overload and stops for the three axes. Shape and size optimization (DOE) of various geometries has been conducted and the best structure has been selected and redesigned for manufacturing purpose. Finally the overload end stops have been added to the selected structure. The final structure presents the highest mechanical sensitivity and the required frequency bandwidth.

The next chapter deals with the results calculations of the electrical design part of the accelerometer with sensitivity and cross-sensitivity estimation of conventional microscale piezoresistors vs. nanoscale piezoresistors. Moreover calculation of nonlinearity, damping, bandwidth, noise and resolution are presented.

Chapter 4

4 ELECTRICAL PERFORMACE OF NANOSCALE PIEZORESISTORS COMPARED TO CONVENTIONAL MICROSCALE PIEZORESISTORS

4.1 Introduction

This chapter aims to evaluate silicon nanowires as nanoscale piezoresistors for a piezoresistive accelerometer and to develop the accelerometer measurement circuit to enhance the performance of the devices. All main accelerometer performance indexes are covered. Sensitivity, cross-axis sensitivity, nonlinearity, damping, bandwidth, noise and resolution are calculated with the objective of comparing the results obtained between conventional microscale piezoresistors and nanoscale piezoresistors. All major signal errors are considered. The signal sensor error is a combination of different errors sources (i.e. mechanical, thermal and electrical origin) such as sensor cross-talk, nonlinearity and various types of noise (e.g. white, pink and brown). The precision of a measurement reflects how exactly the result is determined without reference to what the result means and is identified by the sensor resolution. The accuracy represents how the data recorded (sensor voltage

output) comes close to the true value measured (sensor acceleration input) and indicates the correctness of the result.

Nanowires as nanoscale piezoresistive devices have been chosen as a sensing element, due to their enhanced piezoresistance effect under uniaxial stress (high sensitivity) and miniaturization achievable compared to the conventional microscale counterparts [2-7]. The origin and behaviour of so called "Giant Piezoresistance" was examined in numerous works [12, 45-47, 140-149] but few reports are available on the development of silicon nanowire-based sensors [42]. However, several studies have been conducted on p-type single crystalline SiNWs for sensor applications [2, 13, 14, 43, 44, 134, 136].

The results of the calculation presented in this chapter show that by exploiting the electromechanical features of nanowires as nanoscale piezoresistors, the nominal sensor sensitivity is overall boosted by more than 30 times compared to the conventional microscale piezoresistors. This approach allows significantly higher accuracy and resolution to be obtained with smaller sensing elements in comparison with conventional devices without the need of signal amplification. This achievement opens up new developments in the area of implanted devices where the high-level of miniaturization and sensitivity is essential.

Next sections present the performance calculations of the accelerometer under a maximum of 250g of acceleration and discuss each of the performance indexes calculated. Notice that a comparison between microscale and nanoscale piezoresistors is proposed and that all results are based on FE stress distribution analysis.

4.2 Methodology

4.2.1 FEM model

The output of the previous chapter that is the highly-symmetric mechanical structure with four surrounding beams (Figure 3-6) is the input of this chapter. This structure is the result of a thorough optimization process started from selecting five shapes out of nine highly symmetric structures by a shape optimization function (higher stress and natural frequency) and then each of the five shapes selected have been further investigated by a size optimization process (max. stress under the hard constraint of a natural frequency higher than 5kHz). Then the structure geometry with optimal size and shape is identified.

The optimized mechanical structure presents a square proof mass and four surrounding beams clamped-clamped to the fixed frame and connected to the suspended proof mass in the middle. The structure is here enhanced by designing overload end stops in the four corners of the frame able to stop the in-plane movements of the structure in case of acceleration higher than 500g. Moreover the optimized structure is further modified in order to comply with the fabrication process preferred for the device.

For the performance calculation presented in this chapter the material selected for the mechanical structure of the sensing element is anisotropic single crystal silicon (SCS), which has been chosen for its mechanical properties (good stress tensile strength and high gauge factor) [73] and its wide adoption in MEMS fabrication processes (Table 4-1). The matrix of stiffness coefficients of SCS used in the FEM developed is [52] (further details available in Appendix J):

$$C = \begin{bmatrix} 1.66 & 0.64 & 0.64 & 0 & 0 & 0 \\ 0.64 & 1.66 & 0.64 & 0 & 0 & 0 \\ 0.64 & 0.64 & 1.66 & 0 & 0 & 0 \\ 0 & 0 & 0 & 0.80 & 0 & 0 \\ 0 & 0 & 0 & 0 & 0.80 & 0 \\ 0 & 0 & 0 & 0 & 0 & 0.80 \end{bmatrix} \cdot 10^{11} \text{Pa} \qquad (4.1)$$

In order to validate the sensitivity obtained in output from the FEM simulation, the model was compared to a similar model based on the mechanical structure and measurement circuit readily available in the literature [6, 93] (Figure 4-1-(a)) with length × width × thickness of 2×2×0.45-mm and beams length × width × thickness of 1×0.06×0.01-mm. The longitudinal piezoresistive coefficient of each piezoresistor is 35×10^{-11} Pa^{-1}.
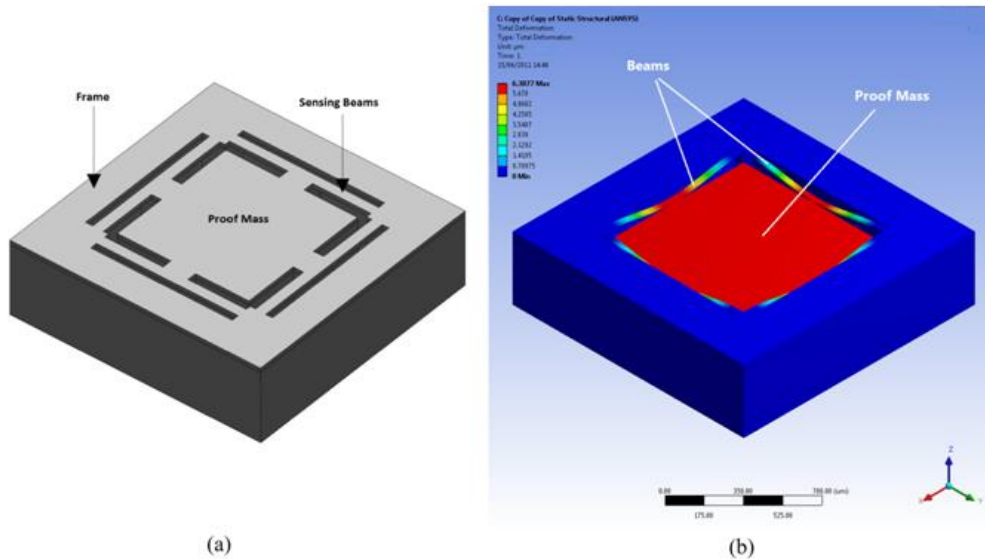
Figure 4-1. (a) Current state-of-art accelerometer mechanical structure [6, 93]; (b) Typical accelerometer under stress due to external forces (Z-axis acceleration and blue frame fixed). The red colour corresponds to the maximum displacement of the proof mass. In blue is the surrounding frame which is undeformed.

See Table 4-1 and 4-2 for the inputs material and geometry parameters respectively, used in the developed FEM for sensitivity validation.

Table 4-1. Inputs material parameters used in the developed FEM

Mechanical Structure material	Single Crystal Silicon Anisotropic
Density (kg/m^3)	2330
Matrix of stiffness	Eq. 4.1

Table 4-2. Input geometry parameters used in the developed FEM for sensitivity validation.

Piezoresistive coefficient	35×10^{-11} Pa^{-1}
Device length $\times$ width $\times$ thickness	$2\times2\times0.45$-mm
Beams length $\times$ width $\times$ thickness	$1\times0.06\times0.01$-mm

The tetrahedron elements were used for the FE modelling due to a better meshing of the model and 250,000 nodes characterise the model mesh. Proximity meshing option was used because it allows a finer meshing on accelerometer beams to accurately capture the stress. The bottom side of the external frame of the mechanical structure (in blue in Figure 4-1-(b)) is fixed. The load has been applied by a gravitational force vector of 250g of magnitude, for each of the three axes.

4.2.2   Measurement circuit

The electrical circuit used to measure the acceleration in each axis is the classical Wheatstone bridge [85] that consists of four resistors connected to form a quadrilateral, a source of excitation (voltage or current) connected across one of the diagonals, and a voltage detector connected across the other diagonal. The difference between the outputs of two voltage dividers connected across the excitation was measured by the detector [32] (see Appendix G for details). The *full-bridge* configuration was adopted in the measurements due to the

inherent linearity and higher sensitivity. In this configuration the voltage output is equal to the source of voltage multiplied the fractional resistance change.

A total of 16 nanoscale piezoresistors were placed in strategic locations on the top surface of the mechanical structure (Figure 4-2(a)). In order to maximize the device electrical sensitivity, the piezoresistors were placed where the highest stress regions were identified by FE stress distribution analysis (see Appendix D for the analysis results). The stress analysis was conducted on the model presented in Figure 4-1(b), which is the mechanical structure obtained from the previous optimization process (see also Figure 3-6).
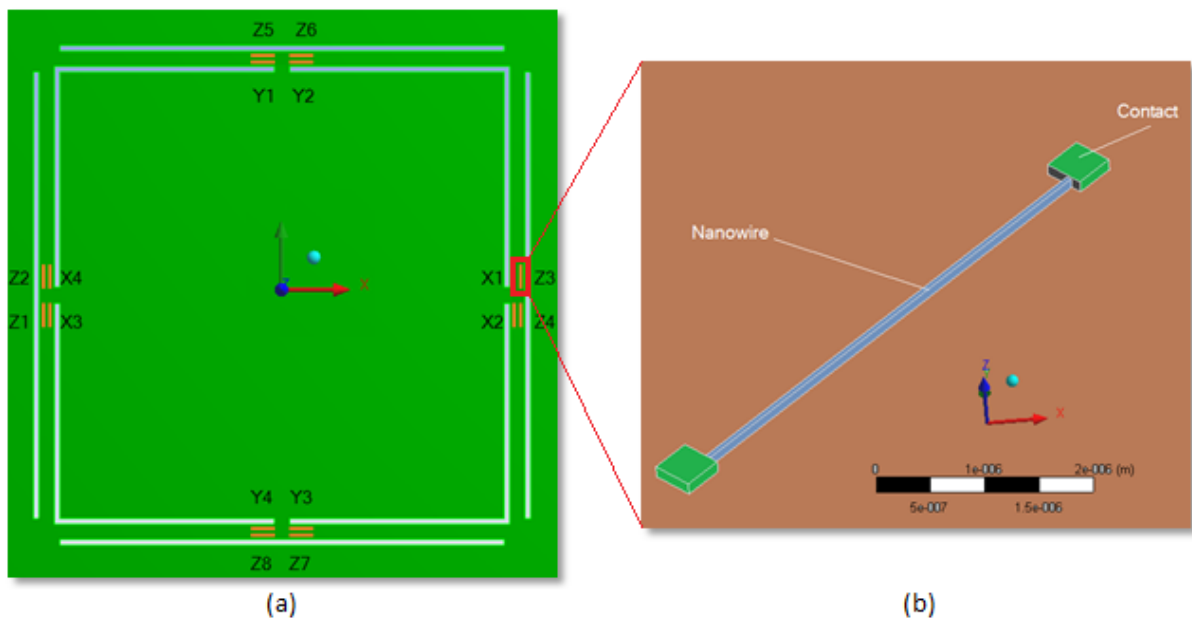
Figure 4-2. (a) Piezoresistors location.16 nanoscale piezoresistors, in orange, are placed in strategic locations where the maximum stress is present in order to maximize the sensitivity and minimize the cross-sensitivity (top view). (b) Nanoscale Piezoresistor model. In blue is the nanowire and in green are the contacts

A detailed image of a nanoscale piezoresistor placed on one of the four beams is presented in Figure 4-2(b). Each piezoresistor is geometrically identical with a length of 3 micrometers and a width of 100 nanometers.

The measurement circuit is formed by three different full Wheatstone Bridges, one for each axis-sensing (Figure 4-3). Hence, the change in resistance of the piezoresistors is measured as the output voltage drop by these bridges. The advantage of using a bridge is that as the four

resistors are identical, the effect of the temperature coefficient can be cancelled out by the balanced configuration and moreover, the highly symmetric geometry chosen for the structure allows a self-cancellation of part of the cross-axis acceleration (the piezoresistors are intentionally positioned symmetrically for this reason).
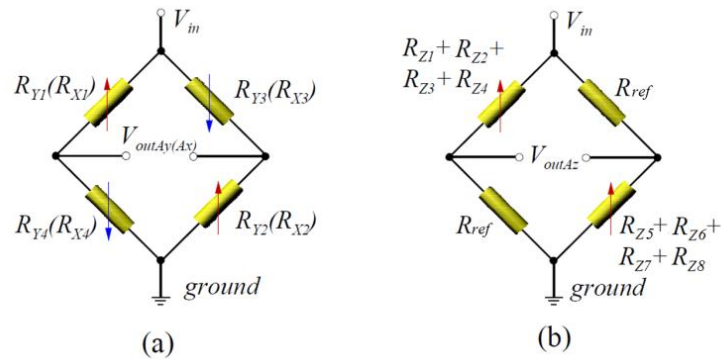
Figure 4-3. Measurement circuit design type A. (a) Ax-, Ay-bridge and (b) Az- Wheatstone Bridge measurement circuit

There is a compensation effect when there is acceleration on the X- and Y-axis. For X-axis acceleration the A_x-bridge becomes unbalanced and detects the acceleration at is output, the A_y-bridge remains balanced since, on each arm, one resistance decreases and the other one increases by the same amount. Therefore overall the resistance on each arm remains unchanged. Simultaneously the total resistance in the A_z-bridge remain unchanged since hypothetically, one resistance increases and the other one decreases by the same amount. This also gives a voltage drop of zero output since it remains balanced.

For Y-axis acceleration the A_y-bridge becomes unbalanced and detects the acceleration while the A_x-bridge remains balanced giving, theoretically, a differential output voltage (voltage drop) zero; therefore the cross-talk is nearly zero. The A_z-bridge, due to Y-axis acceleration behaves as follows, $R_{z1}+R_{z2}+R_{z3}+R_{z4}$ and $R_{z5}+R_{z6}+R_{z7}+R_{z8}$ remain unchanged, therefore the output remains zero.

Finally as in the case of Z-axis acceleration, the resistance decrement of A_x, A_y-bridge is theoretically equal since the geometrical symmetry is of identically designed resistance, and the two bridges remain balanced at zero volt output. In contrast, the A_z-bridge, due to Z-axis acceleration becomes unbalanced and the output voltage is the measure of acceleration. Table 4-3 summarizes the values of the resistance change, + is an increment, - is a reduction and 0 unchanged.

Table 4-3. Resistance change due to unbalanced bridge

	R_{x1}	R_{x2}	R_{x3}	R_{x4}	R_{y1}	R_{y2}	R_{y3}	R_{y4}	$R_{z1}+R_{z2}$ $+R_{z3}+R_{z4}$	$R_{z5}+R_{z6}$ $+R_{z7}+R_{z8}$
A_x	-	-	+	+	+	-	-	+	0	0
A_y	-	+	+	-	-	-	+	+	0	0
A_z	-	-	-	-	-	-	-	-	-	-

In reality the 16 piezoresistors will not be of equal resistance and nor of perfect geometrical symmetry because of fabrication errors and non-linearities. Therefore some cross-talk on the output signal is expected.

4.2.3 Electrical Sensitivity and cross-axis sensitivity

The electrical sensitivity S of the accelerometer can be defined as the ratio between the output voltage and the applied acceleration. In the case of in-plane acceleration (X- or Y-axis), the longitudinal stress on the beams that are perpendicular to the direction of the applied acceleration is larger than that distributed on the beam which are parallel to the acceleration orientation. Therefore, the piezoresistors to measure A_x are arranged on the Y-oriented beams, and vice versa.

For example, in the case of X-axis acceleration, the electrical sensitivity for the A_x-bridge is [93]:

$$S_{A_x} = S_{A_y} = \frac{V_{out_{A_x}}}{A_x} = \frac{1}{A_x} \times \frac{\Delta R_x}{R_x} \times V_{in} \tag{4.2}$$

where V_{out} is the output voltage, V_{in} is the bias voltage applied to the piezoresistor (5V), and

$\frac{\Delta R_x}{R_x}$ is the fractional resistance change of A_x-bridge that is equal to [71, 40]:

$$\frac{\Delta R_x}{R_x} = \pi_l \cdot \sigma_l^y + \pi_t \cdot (\sigma_t^x + \sigma_t^z) \tag{4.3}$$

where π_l and π_t are longitudinal and transverse piezoresistive coefficients respectively. $\sigma_l^y, \sigma_t^x,$ σ_t^z are respectively longitudinal stress in the Y-axis in case of acceleration along the X-axis, and transverse stress in the X- and Z-axis directions. The shearing stress is negligible and, therefore, neglected. It should be noted that the aforementioned equation is only valid for uniform stress fields or if the piezoresistor dimensions are small compared to the beam size [56].

Since the common approximation is valid in the <110> silicon crystallographic direction, i.e., $\pi_l = -\pi_t$, the fractional resistance change becomes

$$\frac{\Delta R_x}{R_x} = \pi_l \cdot \left[\sigma_l^y - (\sigma_t^x + \sigma_t^z) \right] \tag{4.4}$$

The electrical sensitivity in the other directions is similarly calculated. The longitudinal piezoresistive coefficient at room temperature used for the conventional piezoresistor was 72×10^{-11} Pa^{-1} as reported by Smith [48], while the correspondent nanoscale value was, 1527×10^{-11} Pa^{-1} , obtained by Passi *et al.*. [7].

The cross-axis acceleration is an error of measurements related to different factors: the mechanical structure of the sensor and fabrication errors that affect its symmetry, the piezoresistors location on the top surface and the measurement circuit. Its sensitivity is calculated in percentage and it is the absolute value of the fraction of the voltage output of each axis other than the one under stress and the axis under stress. For example, the cross-

axis sensitivities under the X-axis acceleration $S_{(Ax-Ay)\%}$ and $S_{(Ax-Az)\%}$ are detected, respectively, in the output of the A_y, A_z-bridge for the nanoscale piezoresistors as follows:

$$S_{(Ax-Ay)\%} = S_{(Ay-Ax)\%} = \left|\frac{V_{out_{Ay}}}{V_{out_{Ax}}}\right| \% \qquad (4.5)$$

$$S_{(Ax-Az)\%} = \left|\frac{V_{out_{Az}}}{V_{out_{Ax}}}\right| \% \qquad (4.6)$$

4.2.4 Nonlinearity

The static response of the sensor (input/output relationship) is usually not perfectly linear. Nonlinearities are mainly related to nonperfect Ohmic contact of the piezoresistors at high bias voltage (> 0.2V), and/or due to large deflection (structure stiffness changes). The former causes the *I-V* characteristic to become nonlinear, the latter is typically present for slender structures. An Ohmic contact can be obtained by a high boron doping concentration localized in the contact pad. Instead, large deflection cannot be controlled in an open loop device. A controlled feedback is required (actuation) as in a servo or force-balanced accelerometer. Typically, the accelerometer that implements such system is the variable-capacitance accelerometer since the actuation is straightforward.

The easier solution for piezoresistive accelerometers is to correct this nonlinearity electronically during calibration if necessary. A rule of thumb is that large deflection occurs if the transverse displacements in a slender structure are more than 10% of the thickness. This last condition occurs in the proposed device for acceleration over 100g and it has been taken into account in the FE analysis.

Due to the inherent linearity of the response obtained, the nonlinearity is calculated using the end point linearity method, instead of the more common best fit straight line method (BFSL) or Least Squares BFSL Method [135]. This can be expressed as a percentage of either Full-

Scale Output (FSO = 500g) or ± Full Scale (±FS = ±250g) in g's (g is the gravitational acceleration, i.e. = 9.8ms^{-2}).

The method for calculating the device nonlinearity (*NL*) is [56]:

$$NL = \frac{\frac{MD}{S}}{FSO}\% = \%FSO \qquad (4.7)$$

The *NL* is calculated as the percentage of the fraction between the maximum deviation (*MD*) and the sensitivity (*S*) based on the *FSO* or *FS*.

4.2.5 Damping

Optimal damping design of the structure (damping ratio ζ=0.7) offers the widest bandwidth in the amplitude-frequency relationship (flat dynamic response). Therefore, the gaps between top/bottom cap and proof mass of the accelerometer have been designed to work in this regime.

For the vibration in the vertical direction (first mode shape), there are two main types of damping acting on the seismic mass, i.e., viscous damping and squeeze-film air damping [93]. The latter occurs when the proof mass moves up and down, the air films trapped between the bottom/top surfaces of the seismic mass and the bottom/top caps are squeezed. This damping type is more dominant than the viscous damping [93]. The damping ratio, caused by double sided squeezed-film air damping, is defined by eq. (4.8), assuming that the air films have the same thickness *d* [58, 93]:

$$\zeta = \frac{\beta \mu W^2}{H \rho g^3 \omega_{oz}} \rightarrow d = \sqrt[3]{\frac{\beta \mu W^2}{H \rho \zeta \omega_{oz}}} \qquad (4.8)$$

where *β* is correction factor depending on the ratio between the width *W* and the length of seismic mass, *ρ* is mass density of silicon (2330 kg/m^3), *μ* is viscosity of the air (1.81×10^{-5} Pa-s), ω_{oz} is undamped natural radian frequency in the first shape mode (bending on Z-axis).

4.2.6   Bandwidth

The usable frequency response of the proposed accelerometer is calculated and is defined as the flat area of its frequency response curve. To do this, it is necessary to know the behaviour of the spring-mass-damper model when a harmonic force is added. A force of this type could, for example, be generated by a rotating imbalance. The applied sinusoidal acceleration with circular frequency ω is

$$a = a_o \cdot \cos(\omega t) \tag{4.9}$$

adding the acceleration on the mass, the ordinary differential equation of the entire system becomes:

$$\ddot{x} + \frac{c}{m}\dot{x} + \frac{k}{m}x = a_o \cdot \cos(\omega t) \tag{4.10}$$

The steady-state deflection of the spring is of the form

$$x = x_o \cdot \cos(\omega t + \phi) \tag{4.11}$$

The result states that the mass will oscillate at the same angular frequency (ω) of the applied acceleration, but with a phase shift ϕ.

The deflection magnitude x_o, which is also the amplitude of the vibration, is related to the magnitude of the applied acceleration a_o by

$$x_o(\omega) = \frac{a_o}{(\omega_n)^2} \cdot \frac{1}{\sqrt{\left[1 - \left(\frac{\omega}{\omega_n}\right)^2\right]^2 + \left(2\zeta\frac{\omega}{\omega_n}\right)^2}} \tag{4.12}$$

where $\frac{\omega}{\omega_n}$ is defined as the ratio of the harmonic force frequency over the undamped natural frequency of the mass-spring-damper model.

As indicated by the notation, x_o depends on the driving angular frequency ω. In particular, x_o becomes diminishingly small when ω is sufficiently large, and the accelerometer will cease to be useful for accelerations at such a frequency. In practice, the useful bandwidth within

which the accelerometer is used is given by the *upper cutoff frequency* ω_c. This frequency is the maximum frequency at which the relative amplitude remains constant and the accelerometer sensitivity remains uniform, this is true when the second term of eq. (4.12) is equal to 1 and it is defined conservatively as

$$\frac{x_o(\omega_c)}{x_o(0)} = 1 \tag{4.13}$$

and is given by

$$\omega_c = \gamma \cdot \omega_n \tag{4.14}$$

where

$$\gamma = \sqrt{2(1 - 2\,\zeta^{\,2})} \tag{4.15}$$

4.2.7 Noise and resolution

Noise is any output voltage that occurs when there is no acceleration applied to the sensor. There are three typical noise sources existing in all piezoresistive sensors, including the Johnson noise (noise floor or white noise), Hooge's noise (or $1/f$ noise, also called pink noise), and the thermo-mechanical noise (brown noise or Brownian noise).

The first two noises are easily distinguishable on a typical noise versus frequency spectrum, as shown in Figure 4-4. At low frequencies, all resistors suffer from conductance fluctuations, usually called 1/f noise because the noise power density [V^2/Hz] decreases as one over the frequency. Added to this is Johnson noise, which is independent of frequency. Johnson noise is fundamental, due to thermal energy in a resistor, and is well understood [59].
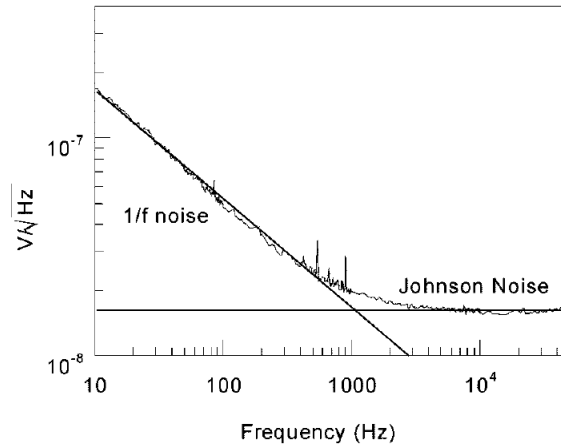
Figure 4-4. Typical cantilever noise spectrum showing Johnson and *1/f* noise [53].

Hooge noise is a natural property of all resistors and dominates over Johnson noise at lower frequencies. It is theoretically determined that Hooge noise is equal to Johnson noise at approximately 40 Hz. Both Johnson and Hooge noise levels represent asymptotes for the accelerometer noise [60] (Figure 4-4).

Improvements in fabrication can drive the noise levels of the current piezoresistive accelerometer closer to the theoretical Johnson and Hooge asymptotes. Figure 4-5 clearly shows the frequency dependence of noise in a piezoresistive accelerometer, with theoretical noise asymptotes also shown by Lynch *et al.* [60].
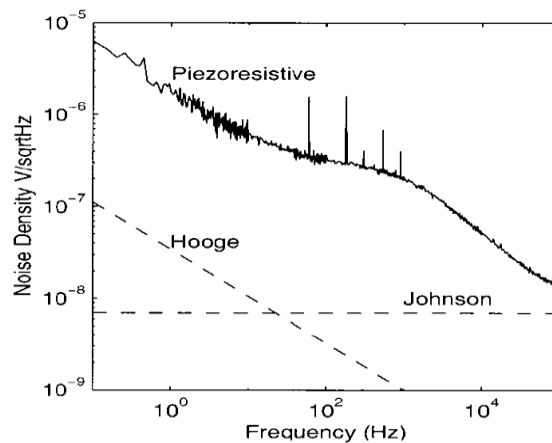
Figure 4-5. Noise spectral density of piezoresistive accelerometer [60]

Johnson noise is due to random motion (thermal agitation) of carriers in any electrical conductor. In a piezoresistor, Johnson noise can be described as [59, 93]:

$$V_{Jn(rms)} = \sqrt{4k_B T R \Delta f} \tag{4.16}$$

where k_B is Boltzmann's constant (1.38×10^{-23} J/K), T is temperature (310 K or 37°C), R is the resistance of the piezoresistor at low carrier density (1×10^{17} cm^{-3}), and Δf is the measurement bandwidth.

1/f noise is empirically determined noise, and can be estimated by the equation [53, 61, 93]:

$$V_{1/f(rms)} = \sqrt{\frac{\alpha V_{in}^2}{N} ln\left(\frac{f_{max}}{f_{min}}\right) \cdot \frac{1}{\Delta f}} \tag{4.17}$$

where V_{in} is bias voltage across a piezoresistor with total number of carriers N, and f_{max} and f_{min} are upper and lower limit of measurement frequency, respectively. α is a dimensionless parameter called Hooge parameter which, for an implanted resistor, has been found to vary depending on the anneal [62]. For semiconductors, α was found to be 10^{-7} [63, 64]. Several publications have shown that it is possible to decrease the value of α down to 3e^{-6} [62, 65-68]. For a constant doping concentration, the number of carriers $N = p \cdot l_p \cdot w_p \cdot t_p$, where p, l_p, w_p and t_p are, respectively, doping concentration, doping concentration length, width and depth of piezoresistor. Because other noise sources are independent of the frequency range, it is necessary to specify the 1/f noise for a specific bandwidth; this is done by dividing the 1/f noise by Δf.

Thermo-mechanical noise is mechanical analog of Johnson noise, and consists of physical oscillations due to thermal agitation in the sensing structure. The thermo-mechanical noise equivalent acceleration can be written as [58, 93]

$$A_{TM} = \sqrt{\frac{8K_B T \omega_n \zeta}{m}} \qquad \left(\frac{m}{s^2} / \sqrt{Hz}\right) \tag{4.18}$$

where m is the mass of the seismic mass and T is the surrounding temperature. The total noise voltage is calculated for each bridge as the square root of the sum among the square power of each noise, as

$$V_{Noise} = \sqrt{\left(V_{Jn}\right)^2 + \left(V_{1/f}\right)^2 + (V_{TM})^2} \qquad (4.19)$$

The resolution of an accelerometer determines the minimum acceleration that can be measured. Resolution is defined as the noise divided by the sensitivity; therefore, the resolution of the accelerometer is defined by [93]

$$R_{A_z} = \frac{V_{Noise}^{A_z}}{S_{Az}}, \qquad R_{A_{x,y}} = \frac{V_{Noise}^{A_{x,y}}}{S_{Az}} \qquad (4.20)$$

4.3 Results and discussion

4.3.1 Structural analysis

The mechanical structure geometry identified in the previous chapter requires a last step in the entire geometry design, which is to take into account the sensor fabrication process and make the necessary adjustments to the structure size (device thickness 10 μm and silicon substrate thickness 400 μm). Therefore, the final optimized geometry was modified in order to comply with the manufacturing constrains of the MEMSCAP fabrication process (device thickness 10 μm and silicon substrate thickness 400 μm), and a final optimization process was undertaken to maximizing the device mechanical performance (max. sensitivity at the bandwidth required). The final geometry is presented in the Figure 4-6.
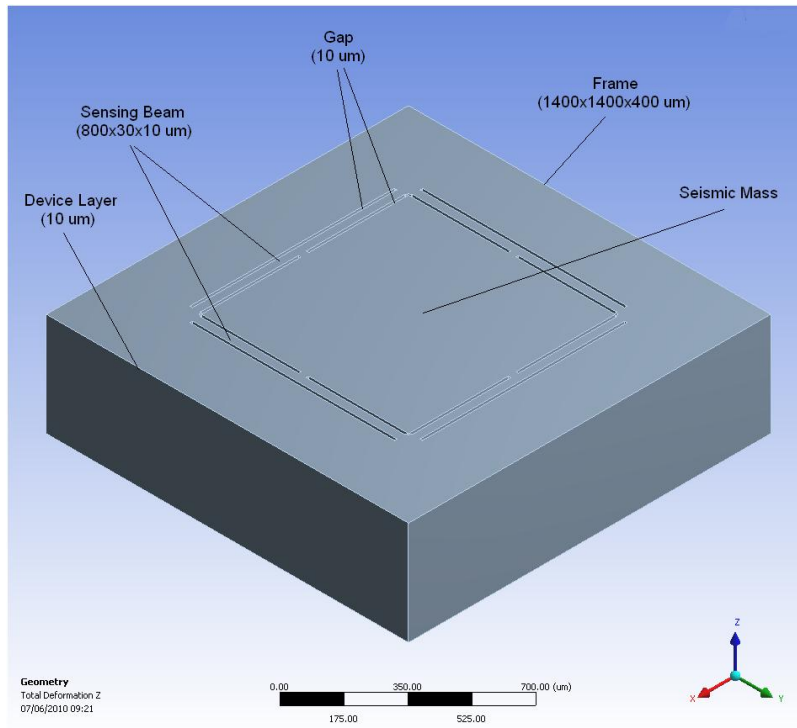
Figure 4-6. Optimized mechanical structure geometry

Table 4-4 summarizes the final geometry size with the correspondent mechanical performance and compares it to the geometry before manufacturing process decision. The overall die body size passes from 1210×1210×400 μm to 1400×1400×400 μm, the cross section area of the beam and the natural frequency remain the same but the new design improves significantly the nonlinearity due to large deflection. This occurs because the total deformation in both design remain almost invariant but the beam thickness doubles. Finally, consideration is given to the maximum equivalent stress under X-, Y-axis acceleration that is mainly reduced in the new design due to the mass and beam width change.

Table 4-4. Final geometry size and performance

	Mass Width (μm)	Mass Thickness (μm)	Beam Width (μm)	Beams Thickness (μm)	Natural Frequency -1st Mode (Hz)	Equivalent Stress Z Maximum (Mpa)	Total Deformation Z Maximum (um)	Equivalent Stress X Maximum (Mpa)	Total Deformation X Maximum (μm)
MEMSCAP design	800	400	30	10	5270	87	2.3	61.6	2.1
Best design	550	400	60	5	5250	91	1.8	87.1	2.7

Therefore the new constraints introduced by the manufacturing process selected don't negatively affect the overall performance of the accelerometer; rather improve accuracy and reliability except for a lower sensitivity contribution for in-plane accelerations.

The final geometry is then enhanced with overload end stops as depicted on Figure 4-7 (a) and (b). As shown on the figure the four end stops, one for each corner, are designed to cross all the silicon substrate. The gap between the proof mass and the end stops is set to 5 μm, which correspond to an axial translation of the proof mass caused by around 500g of in-plane acceleration.

(a) **(b)**
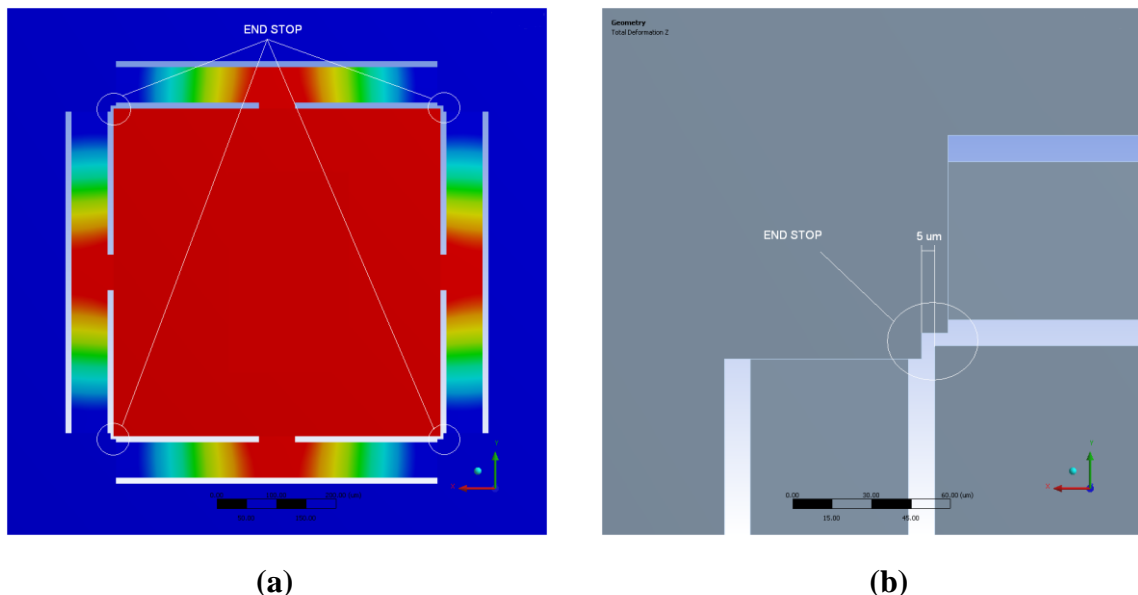
Figure 4-7. (a) Overload End Stop (Top view). The colour defines the total deformation of the structure under Z-axis acceleration. In red the maximum deformation and in blue the undeformed section. (b) Overload End Stop (Detail). The gap of 5 microns for in-plane acceleration allows a movement of the proof mass under a maximum of 500g of acceleration.

With respect to the overload end stop design for out-of-plane acceleration (Z-axis), this step is passed to the wafer level packaging design, since it concerns the bottom and top cap bonded to the die. It is anticipated that for obtaining optimal damping of the sensor the gap between the caps and the proof mass must be more than 5 μm, therefore breakage of the beams can occurs. To overcome this issue, bumpers of 3 μm of radius have been introduced in the caps, since the gap has been calculated to be totally around 8 μm.

The designs' sensitivity is validated by comparing the sensitivity results to the demonstrator developed by Dao et al. [93]. The value of piezoresistive coefficient used for the sensitivity calculation is 35×10^{-11} Pa^{-1}, which is the value adopted by Dao et al. [93]. The simulation results of this study are on the same order of magnitude of the value of sensitivity obtained in the demonstrator device of Dao et al. [93]. Sensitivity under X-axis acceleration is 0.2 mV/g vs. 0.48 mV/g [93]; a similar value is obtained under Y-axis acceleration. Under Z-axis acceleration the sensitivity is 0.314 mV/g vs. 0.56 mV/g [93]. Figure 4-8 compares the two studies.
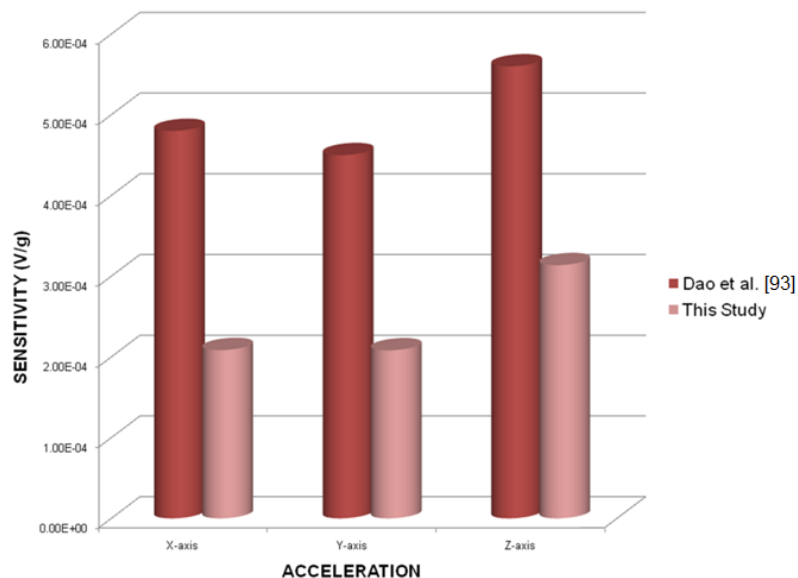
Figure 4-8. Validation of the model sensitivity by comparing to the demonstrator performance of Dao et al. [19].

4.3.2 Electrical sensitivity and cross-sensitivity

In the calculation of the electrical sensitivity the temperature drift has been considered (temperature coefficient of sensitivity, TCS = 0.25 %/°C) since the device is meant to be inserted inside the ear canal (~37°C). Therefore, a further calculation of the sensitivity at the temperature of 37°C and 40°C has been undertaken (see Figure 4-9). The latter temperature has been identified conservatively as the maximum temperature before a dermal injury of the ear skin occurs [57].

The temperature increase, as can be seen from Figure 4-9, significantly reduces the sensitivity of the device. The linearity is not affected since the resistors are hypothetically identical and in a Wheatstone bridge configuration.
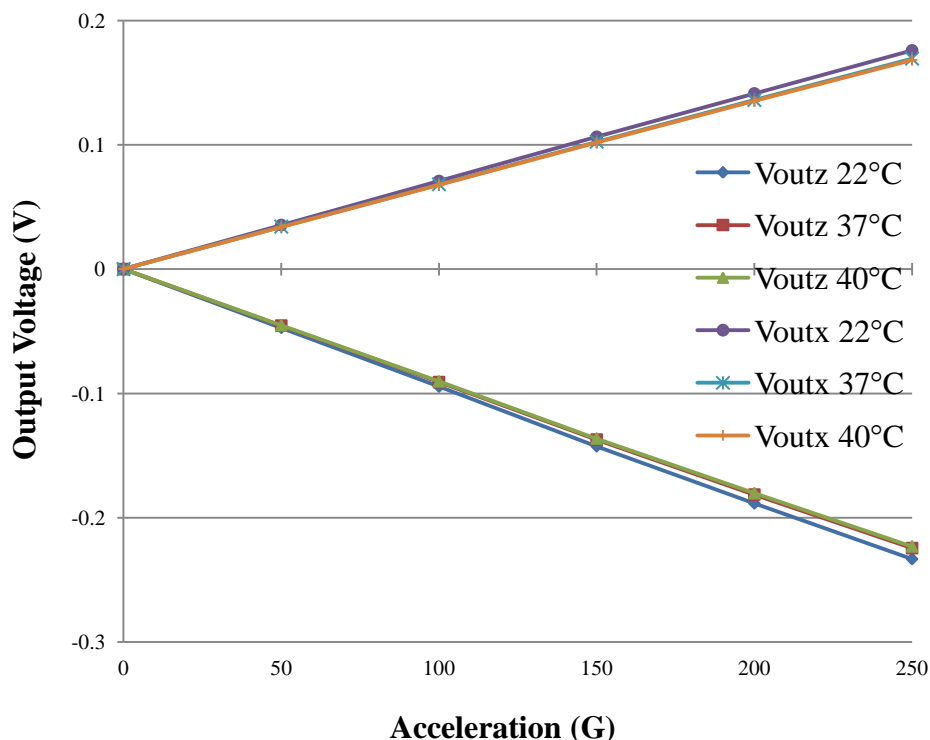
Figure 4-9. Temperature drift – Output Voltage vs. X- or Y-axis and Z-axis Acceleration. It was observed that the sensitivity is progressively reduced due to temperature increase.

Table 4-5 summarizes the sensitivity change due to the temperature drift for the microscale piezoresistors. As can be seen in Table 4-5 the sensitivity is overall reduced by around 4% by an increment of almost 18°C. This occurs because the increase of temperature reduces the value of piezoresistive coefficient corrected by the TCS. Similar results are obtained for the nanoscale piezoresistors.

Table 4-5. Temperature drift - sensitivity

Temperature (°C)	Ax, Ay (mV/g)	Az (mV/g)
22	0.684	0.907
37	0.677	0.898
40	0.655	0.868

However, the temperature drift calculated takes into account the piezoresistive coefficient variation only but ignores the variation of the resistance value, which is considered invariant, due to the small temperature range. Therefore, if we consider the resistance temperature dependence overall the total effect is deteriorated.

The calculated electrical sensitivity of nanoscale piezoresistors in the <110> direction at low boron concentration at 37°C, increases by approximately 3000% in comparison to the conventional ones (see Table 4-6).

Table 4-6. Voltage Noise – Sensitivity – Resolution

	Microscale		*Nanoscale*		*Ratio*	
	Ax, Ay	*Az*	*Ax, Ay*	*Az*	*Ax, Ay*	*Az*
V_{jn} (µV)	1.01	1.42	3.2	4.52	3.1	3.2
$V_{1/f}$ (µV)	0.4	0.28	13.14	9.29	32	33
V_{Noise} (µV)	1.2	1.97	13.53	10.41	11	5.3
Sensitivity (mV/g)	0.67	0.9	20.9	28.9	30	32
Resolution (mg)	1.78	2.2	0.64	0.36	0.36	0.16

Cross-sensitivity is below 5% for all axes due to the highly symmetric geometry selected.

$$S_{(Ax-Ay)\%} = S_{(Ay-Ax)\%} = \left|\frac{V_{out_{Ay}}}{V_{out_{Ax}}}\right| \% = 0.06\% \qquad (4.21)$$

$$S_{(Ax-Az)\%} = \left|\frac{V_{out_{Az}}}{V_{out_{Ax}}}\right| \% = 2.78\% \qquad (4.22)$$

As can be seen, the value obtained for Y-axis is the same as X-axis due to the geometrical symmetry. The cross-axis sensitivity related to the Z-axis acceleration is as follows:

$$S_{(Az-Ax)\%} = \left|\frac{V_{out_{Ax}}}{V_{out_{Az}}}\right| \% = 0.006\% \qquad (4.23)$$

$$S_{(Az-Ay)\%} = \left|\frac{V_{out_{Ay}}}{V_{out_{Az}}}\right| \% = 0.014\% \qquad (4.24)$$

These values are a consequence of the highly symmetric geometry selected, the symmetric localizations of the piezoresistors on the top surface of the device, and the measurement circuit (see Figures 4-2(a) and 4-3). Similar results are obtained for the microscale piezoresistors.

4.3.3 Nonlinearity, damping and bandwidth

The result of nonlinearity for both microscale and nanoscale piezoresistors is less than 1%FSO for all three axes.

Considering an optimal damping condition the gap between the top and bottom caps for the proposed accelerometer is calculated (Eq. 4.8) with $W = 800$ μm, $\beta = 1$, $H = 400$ μm, and $\omega_{oz} = 2\pi f_z = 33 \times 10^3$ rad/s. The value of d is found to be 8.12 μm with optimal damping condition ($\zeta = 0.7$). Since this value endangers the beams performance for acceleration over 1000g, bumpers are incorporated in the top/bottom cap (see section 3.4.5 Overload end stop design in the Z-axis). For the second and third mode shapes (rotation around X- or Y-axis), the gaps between the two side walls of the seismic mass and the two inner side walls of the frame have not be designed for an optimal damping. Priority has been given to the design of

an optimized sensing chip structure (beam width). This gap is 50 μm. In this case, squeezed-film air damping effect is much smaller than viscous damping. The damping ratio is therefore smaller than 0.7 (underdumped), and optimal damping is not achieved.

The measurement bandwidth is calculated (Eq 4.15) in the case of optimal damping (ζ = 0.7) , where $\gamma = 0.2$ and the cutoff frequency, which determines the measurement bandwidth, is 1054 Hz ($f_n = 5270$ Hz), as set in the specification (Table 3-1).

4.3.4   Noise and resolution

The calculated Johnson noises corresponding to nanoscale and microscale piezoresistors are shown on the Table 4-6. This type of noise in the nanoscale piezoresistors is increased by around 300% mainly due to one order of magnitude higher resistance than conventional microscale ones. The resistance of the nanoscale piezoresistors is much higher than the conventional counterparts because of the reduced dimentison by keeping similar resistivity value (see Eq. 7.8). The total 1/f noise voltage corresponding to each measurement bridge is calculated to be approximately 30 times higher in the nanoscale devices due to the very low number of charge carriers, as clearly summarized on Table 4-6. For a constant doping concentration between nanoscale and conventional microscale piezoresistors, the number of carriers ($N = p \cdot l_p \cdot w_p \cdot t_p$, where p, l_p, w_p and t_p are, respectively, doping concentration, doping concentration length, width and depth of piezoresistor) are dependent only on the piezoresistor dimension. The thermo-mechanical noises corresponding to each component of acceleration at 37°C with the bandwidths for X or Y bending (mode 2 and 3) of 5,539 Hz are in the order of few μg. $A_{TM}^{x,y}$ is the noise related to X- and Y-axis and A_{TM}^{z} is the value related to Z-axis as follows:

$$A_{TM}^{x,y} = 25.7\ \mu g,\ A_{TM}^{z} = 46.9\ \mu g \tag{4.25}$$

Equivalent thermo-mechanical noise voltage can be obtained by:

$$V_{TM}^{x,y} = S_{A_{x,y}} \cdot A_{TM}^{x,y} = 20.9 \times 10^{-3} \cdot 25.7 \times 10^{-6} = 0.53 \ \mu V \qquad (4.26)$$

$$V_{TM}^{z} = S_{Az} \cdot A_{TM}^{z} = 28.9 \times 10^{-3} \cdot 46.9 \times 10^{-6} = 1.35 \ \mu V \qquad (4.27)$$

As can be seen from the eq. (4.18), the thermo-mechanical noise is inversely proportional to the square root of the mass. Therefore, an increase of the mass can reduce the thermo-mechanical noise. Notice that this type of noise remains unchanged between microscale nanoscale piezoresistors. Noise analysis indicates that the total voltage noise in the accelerometer is increased by ten times in the X and Y-axis, and five times in the Z-axis, see Table 4-6. The main contributor to the total noise signal is the Hooge noise due to very low number of carriers in the nanoscale piezoresistors.

The resolution of the accelerometer with nanoscale piezoresistors is improved compared to the conventional microscale one of around 60-80% in all axes, due to their much higher sensitivity (see Table 4-6). However, the noise level of the nanoscale piezoresistors is worse than the conventional microscale ones because Johnson and Hooge noises are dependent on the resistance value and numbers of carriers respectively. Therefore, given the doping concentration, smaller size means higher resistance and lower number of carriers.

Scaling down the device size will affect all three types of noise. In particular the Johnson noise will increase due to a larger frequency bandwidth (see Eq. 3.2), the Hooge noise will reduce for the same reason and the thermo-mechanical noise will increase is value based on the ratio between natural frequency and mass. In this last case, scaling down the device size the natural frequency will increase and the mass value will reduce, therefore the overall effect on the thermo-mechanical noise will be much worst then in the other noise types.

4.3.5 Discussion

The results obtained from the combined FE modeling, simulation of the mechanical structure and performance calculation of both MEMS and nanostructure are interesting for this field of study. Input values used as piezoresistive coefficients for calculating the sensitivity and cross-sensitivity are obtained from experiments of Passi *et al.* [7] for the nanostructure and Smith [48] for the microstructure. This study raises the attention on SiNWs as devices being embedded into mechanical sensors as piezoresistors. The improved resolution of the designed accelerometer (less than 1mg on all axes) compared to the conventional microscale ones with 60-80% increase (see Table 4-5) suggests that nanowires have the credential to be the sensing element of the future NEMS. This level of accuracy and precision of measurement is comparable to the capacitive counterparts' sensors.

To date only few laboratory prototypes have been fabricated with silicon nanowire as nanoscale piezoresistors, as reported by Dao *et al.* [2] suitable for low-G measurements. However, their device [2] sensitivity for each axis is only about 400 μVg^{-1}, and the resolution of 14 mg which requires further signal conditioning, see Table 4-7.

This work instead presents a sensor with higher sensitivity obtained by calculations (20.9 mVg^{-1}), mainly due to a higher stress on the nanowires compared to the work of Dao *et al.* [2]. This is thanks to the optimization process undertaken that maximizes the stress on the beams of the mechanical structure, under the constraints listed in the specification (see Table 3-1). The resolution in this study is improved considerably compared to the work of Dao *et al.* [2] (see Table 4-6) given that the sensor of Dao *et al.* is significantly smaller.

Table 4-7. Sensor performance comparison

	Microscale		Nanoscale	
	This work	**Dao et al. [6]**	**This work**	**Dao et al. [2]**
Range	Medium-g	Low-g	Medium-g	Low-g
Sensitivity (µV/g)	677	30	20,900	400
Resolution (mg)	1.78	-	0.64	14
Cross-Sensitivity (%)	2.78	5.5	2.78	-
Dimension (mm^3)	1.3×1.3×0.4	1×1×0.45	1.3×1.3×0.4	0.5×0.5×0.35

The performance calculated of the sensor met the sensor specifications. Cross-sensitivity, nonlinearity and resolution are under the constraints set for this type of application; therefore, the designed sensor results suitable for the biomechanical application of head injuries monitoring. Finally, the total noise of nanoscale piezoresistors results are much higher than the conventional microscale ones; however, since in the nanoscale structures the sensitivity grows faster than the noise level, the overall resolution is significantly improved. It is worthwhile to point out that this work is based on previous published experimental work on nanowires structures used as piezoresistors [7, 48].

4.4 Conclusion

This chapter presented the electro-mechanical performance of a motion sensor for biomechanical measurement within a space-constrained environment developed in Chapter 3. Due to the exploitation of electro-mechanical features of nanowires as nanoscale piezoresistors the nominal sensor sensitivity is boosted overall by more than 3,000%. This technology avoids the need of signal amplification but allows a higher resolution with the advantage of a smaller sensing element. Therefore, in comparison with conventional devices, the measured accuracy is considerably improved.

This achievement opens up new developments in the area of implanted devices where the high-level of miniaturization and sensitivity is often essential. Example applications are in hearing aid systems (implantable sound sensor for cochlear implants [122]), heart wall motion measurement for cardiac artificial pacemakers [102] and head injury monitoring [134], amongst others. This study represents a valuable guideline for the development of future biomotion sensing devices.

The next chapter deals with a novel electro-mechanical parametric study that intends to further enhance the electrical and mechanical performance of the accelerometer under study.

Chapter 5

5 INFLUENCE OF VARIATIONS IN THE MASS MOMENT OF INERTIA INTO THE PERFORMANCE OF A TRI-AXIAL PIEZORESISTIVE ACCELEROMETER

5.1 Introduction

This chapter aims to introduce a further optimization of the piezoresistive accelerometer selected as a possible candidate in the Chapter 4, by exploring the influence of the variation in the mass moment of inertia of the accelerometer proof mass. In the literature no study is available on this new design optimization method.

When the miniaturization is the main concern of the application, sensitivity becomes the main drawback, since the smaller the device is the lower is its sensitivity. Reduced sensitivity affects drastically the device accuracy, determining low signal to noise ratio. MEMS technology currently faces this issue by simply introducing an amplifier at the output level, sometimes monolithically as in capacitive pick-off or in a complete different device as in piezoresistive pick-off (hybrid system partitioning). Introducing an amplifier introduces a relative signal noise that inevitably worsens the measurement accuracy. The work developed

in this chapter intends to address this issue in a different way by avoiding the use of an amplifier by exploiting the "Giant Piezoresistance" phenomenon observed when the dimension of a piezoresistor shrinks down to the nanoscale dimension [2-7, 13, 14, 43, 44]. Moreover, the study proposes a new design approach and compares different measurement circuits with the intention of increasing the accelerometer performance. By implementing the accelerometer with nanoscale piezoresistors (i.e. nanowires or quantum wires) connected in a particular measurement circuit and enhancing the geometry with an optimization study that progressively improves the sensor performance, the traditional design trade-off that must be addressed by designers using conventional microscale piezoresistors is overcome [93], due to the high sensitivity and the minuscule size achievable.

The accelerometer design and optimization method proposed in this chapter creates a new solution (design) by changing the mass moment of inertia *(MMI)* of accelerometer proof mass to current solution. If the new solution is better, search proceeds utilizing the new solution, if not the older solution is retained. The objective function that guides the optimization process and generates feasible alternatives is that the mass moment of inertia (*MMI*) of the proof mass becomes constant for X-Y plane accelerations and therefore improving the accelerometer performance. The evaluation criterion is based on the performance calculation of sensitivity and cross-sensitivity.

For this study, the initial design used in the design optimization method is the piezoresistive accelerometer studied in the previous chapters (see Figure 4-6). The objective function is defined from the hypothesis that even *MMI* of the accelerometer proof mass improves the device measurement accuracy. *MMI* is a property of a distribution of mass in space that measures its resistance to rotational acceleration about an axis and it is a purely geometric characteristic of the object, as it depends only on its shape and the position of the rotational axis.

A numerical model has been developed to assess the performances of six different new sensor design solutions of type A and B. Notice that only sensitivity and cross-sensitivity are evaluated here, mainly because the other performance indexes are purely dependent on the piezoresistor design which is a common variable for the different design addressed in this study.

The study evolves from an uneven (or not constant) *MMI* to an even (or constant) *MMI* of the accelerometer proof mass in order to understand the effect of *MMI* changes on the sensor performance. The results reflect on advances in present state-of-art sensor performance. The study demonstrates that an even *MMI* does not always improve measurement accuracy, instead this improvement occurs only under particular circumstances dependent on type of measurement circuit, level of sensitivity of the sensing element and accelerometer beam geometry.

Section 5.2 describes the numerical model adopted and validates the input of the FEM against a previous experimental work. Section 5.3 explains the design optimization approach applied for addressing the hypothesis formulated for this study. Section 5.4 presents the results of two different design types. Moreover the section deals with the measurement circuits design comparison, where two different measurement circuits are compared in terms of performance. The simulation results of the study are then discussed in section 5.5, formulating a thesis and providing future advice on possible further enhancement of the accelerometer design. Section 5.6 presents a conclusion section.

5.2 FE Modelling and input validation

The input parameters used in the developed FEM for the material are available in chapter 4 in Table 4-1 and the geometry parameters are summarized in Table 4-4.

The modelled geometries are analysed using 350,000 meshing nodes and tetrahedron elements with the use of ANSYS 12.1 commercial software. Moreover the modelled geometries are all highly symmetric micromechanical structure surrounded by four beams (Figures 5-1(a) and (b)) [2, 93, 104]. The initial designs, A1 and B1 (also available in Figure 4-6), of the two different types of design evolution (curved and straight beams), have the same geometry also available in the literature [6, 93]. The other four designs (A2, A3, B2, B3) obtained after applying the design optimization method are completely new.

(a)   (b)
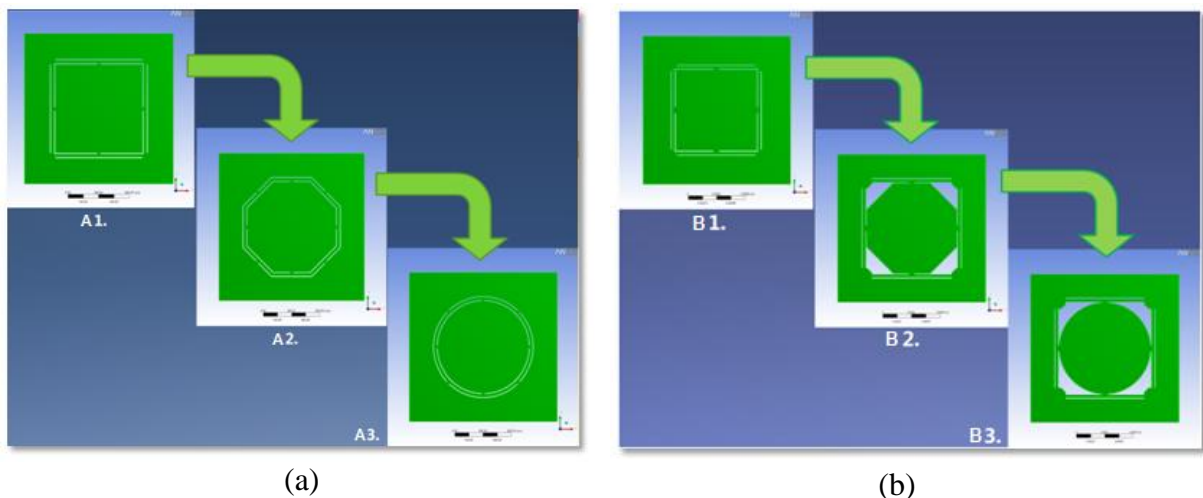
Figure 5-1. (a) Evolutionary design approach of mechanical structures type A (curved beams). Design A1: square, Design A2: octagon, Design A3: circle. (b) Evolutionary design approach of mechanical structures type B (straight beams). Design B1: square, Design B2: octagon, Design B3: circle.

The meshing option used for the meshing size is proximity, in order to increase the number of elements in the geometries areas of reduced size. This type of meshing, proximity, allows for a deeper meshing on the beams of the accelerometer mechanical structure, where good stress analysis is required. Boundary conditions are applied by fixing the bottom side of the external

frame of the mechanical structures. The load applied is a gravitational force vector of 500g of magnitude because it represents the maximum value reachable by the structure due to overload endstops. Notice that in order to effectively compare the performance results of these different geometries, they are all designed with the same proof mass volume.

The designs' inputs are validated by comparing the sensitivity results of the initial design (A1 or B1) to the demonstrator developed by Dao et al. [93]. The geometry parameters of Dao et al. demonstrator are available in Table 4.2. Moreover, the value of piezoresistive coefficient used for the sensitivity calculation is 35×10^{-11} Pa^{-1}, which is the value adopted by Dao et al. [93]. The simulation results of this study are on the same order of magnitude of the value of sensitivity obtained in the demonstrator device of Dao et al. [93], therefore the inputs of the simulation are considered valid (see Figure 4-9 for the results details).

After validation of the device against a real demonstrator [93] further investigation on the design optimization of the model is carried out, which is the main purpose of this chapter. The optimization is a parametric one, where some parameters are changed individually and the performance calculated accordingly, in order to understand the effect of that particular parameter on the design performance. The parameters that are varied in this study are the piezoresistive coefficient of the sensing elements (i.e. 72×10^{-11} Pa^{-1} for conventional microscale piezoresistors [48] vs. 1527×10^{-11} Pa^{-1} for nanoscale piezoresistors [7]), the measurement circuit, the beams and proof mass geometry. The changes and combination of these parameters are made according to a design optimization approach that intends to increase the sensor performance progressively based on the hypothesis that an even mass moment of inertia (*MMI*) of the accelerometer proof mass under in-plane acceleration improves measurement accuracy.

5.3 Design optimization approach

This section presents the design optimization approach that allows progressive reduction of the cross-axis sensitivity of our NEMS-based piezoresistive accelerometer by exploring new sensor designs. The study starts from a highly-symmetric micro-mechanical structure with square proof mass (design A1 or B1), studied in the previous chapters (Figure 4-6), and evolve this structure design based on a mechanical study with the objective of obtaining a much more even *MMI* on the X-Y plane when in-plane acceleration occurs, because in-plane acceleration determines mainly torsion on an axis of rotation. In principle an even, or constant, *MMI* on the X-Y plane should results in a corresponding even sensitivity under in-plane acceleration (both uniaxial and biaxial), that results in a more accurate measurement of the acceleration and a reduced noise due to cross-sensitivity. This is true since both structural sensitivity (S_{Ax}) and *MMI* increase when the mass increases (both quantities are proportional to the mass, Eqs. 5.1 and 5.2), therefore *MMI* and sensitivity are proportionally related (Eq. 5.3).

$$MMI = \sum_{i=1}^{N} m_i r_i^2 \qquad (5.1)$$

where r_i here is the distance from a point to the axis of rotation q.

$$S_{Ax} = \frac{\sigma_l^{Ax}}{Ax} = \frac{\sigma_l^{Ax} \cdot m}{Fx} \qquad (5.2)$$

where σ_l^{Ax} is the longitudinal stress at the piezoresistor R_x due to the application of the acceleration, A_x. Applying Newton's second law of motion ($F_x = m \cdot A_x$), the proportional relationship of the structural sensitivity, S_{Ax}, and mass, *m,* is revealed. Therefore,

$$S_{Ax} \propto MMI \qquad (5.3)$$

By keeping the *MMI* constant, which is obtained by designing the accelerometer proof mass with a uniform mass distribution in relation to the axis of rotation r, the structural sensitivity is kept constant as well (Eq. 5.3).Figure 5.2 shows the two steps of optimization, wherein the vector of biaxial acceleration (X-Y axis acceleration) is applied to the proof mass. Under these inertial forces the proof mass will rotate around the *q* axis, determining a *MMI* dependent on the distribution of masses. In the square proof mass the *MMI* due to uniaxial acceleration is different from the *MMI* due to biaxial acceleration, therefore is uneven. Moving forward towards the circular proof mass the *MMI* become the same for both uniaxial and biaxial acceleration, therefore similarly, the structural sensitivity will be the same for both uniaxial and biaxial acceleration, improving the overall measurement accuracy.
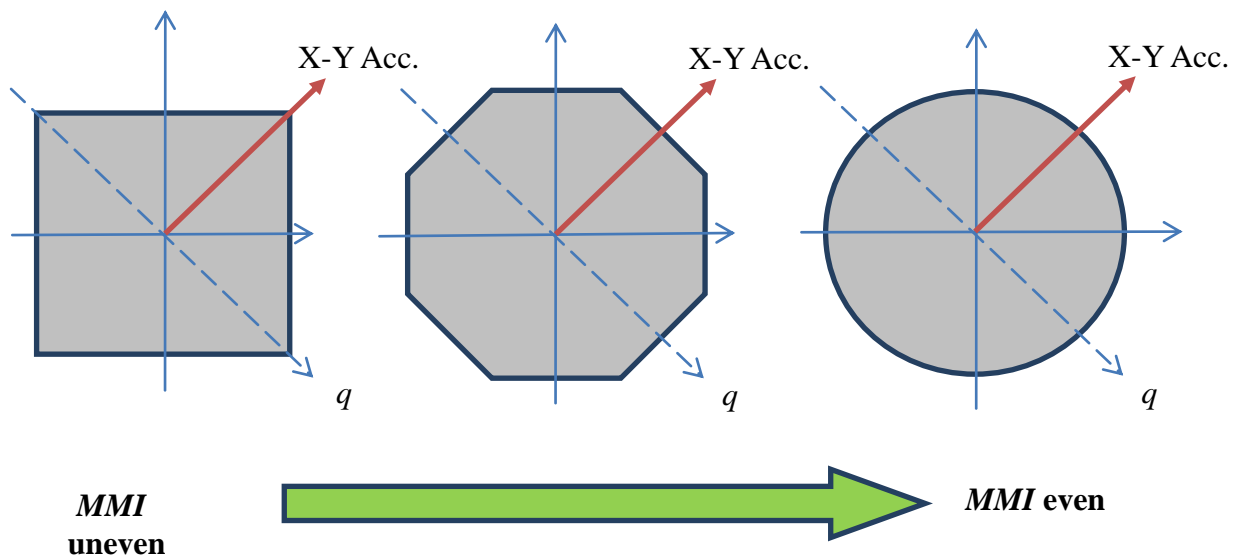
Figure 5-2. Evolutionary design approach. The *MMI* under biaxial acceleration at each step of optimization become more and more similar to the *MMI* under uniaxial acceleration. Therefore the sensitivity, since it is proportional to the *MMI*, in the last step of optimization is the same for uniaxial and biaxial acceleration improving the measurement accuracy.

The electrical sensitivity, S_{Elec}^{Ax}, is itself proportional to the structural sensitivity (Eq. 5.4), therefore constant structural sensitivity implies constant electrical sensitivity [93].

$$S_{Elec}^{Ax} = \frac{V_{outX}}{Ax} = \frac{1}{Ax} \cdot \frac{\Delta R_x}{R_x} \cdot V_{in} = \pi_l \cdot S_{Ax} \cdot V_{in} \qquad (5.4)$$

where $\dfrac{\Delta R_x}{R_x}$ is the functional resistance change, π_l is the longitudinal piezoresistive

coefficient and V_{in} is the input voltage. Finally, this last relationship implies higher

measurement accuracy, because the input/output relationship of the sensor (the acceleration

applied, A_x, versus the output voltage of the accelerometer, V_{out}) remains the same for any in-

plane acceleration (both uniaxial and biaxial), determining a linear transfer function, which

means that the device responds in the same way for acceleration of different directions on the

X-Y plane.

Next sections present the performance calculation of the electrical sensitivity and cross-

sensitivity of the two different types of design concept developed (design concept A: curved

beams, and design concept B: straight beams, Figures 5-1 (a) and (b)).

5.4 Results

5.4.1 Design Concept Type A: Curved beams

The performance calculation of each structure has been made considering the use of

nanoscale piezoresistors made of silicon nanowires. The values of piezoresistive coefficients

used in the calculation are obtained from previous experimental work on silicon nanowires

[7]. In order to compare the microstructures under study a common measurement circuit is

developed and an equivalent value for all proof masses is considered. Three microstructures

are modelled (Figure 5-1(a)) and the approach adopted in order to reduce the cross-axis

sensitivity is that the structures are improved and analysed progressively. The design

optimization approach applied in the development of the mechanical structures is based on the principle of making the mass moment of inertia even on the X-Y plane for each step of optimization. Figure 5-1 shows the three steps of optimization from a micromechanical structure on the X-Y plane with square proof mass (Design A1) to a micromechanical structure with circular proof mass (Design A3). Intermediate micromechanical structure is made up of an octagonal proof mass on the X-Y plane (Design A2).

The method reported here differs from previous work [6] in the specific measurement circuit, since the measurement circuit adopted previously cannot be applied in the new designs geometries due to the use of curved beams. See Figures 4-6, 4-2(a) and 4-3 for the model, the piezoresistors location on the top surface of the chip and the measurement circuit of the starting design respectively.

The performances of these three structures have been analysed, electrical sensitivity and cross-sensitivity have been calculated based on stress/strain analysis obtained by FEA. In order to be comparable all proof masses of the structures have identical volume (3×10^8 μm^3), moreover the piezoresistors are all placed in the same locations on the top surface of the chip (Figure 4-2(a)) and the measurement circuits are identical for all designs (Figure 4-3). The electrical sensitivity is calculated as the Wheatstone bridge voltage output divided by the g-force applied, as in Eq. 5.4; the cross-axis sensitivity is calculated as fraction, where the denominator is the output voltage of the axis where the acceleration is applied and the numerator is the output voltage of the remaining axis, in percentage (Eqs. 4.4 and 4.5). The results are illustrated graphically in Figure 5-3 and 5-4 (see also Table I-1 in Appendix I).
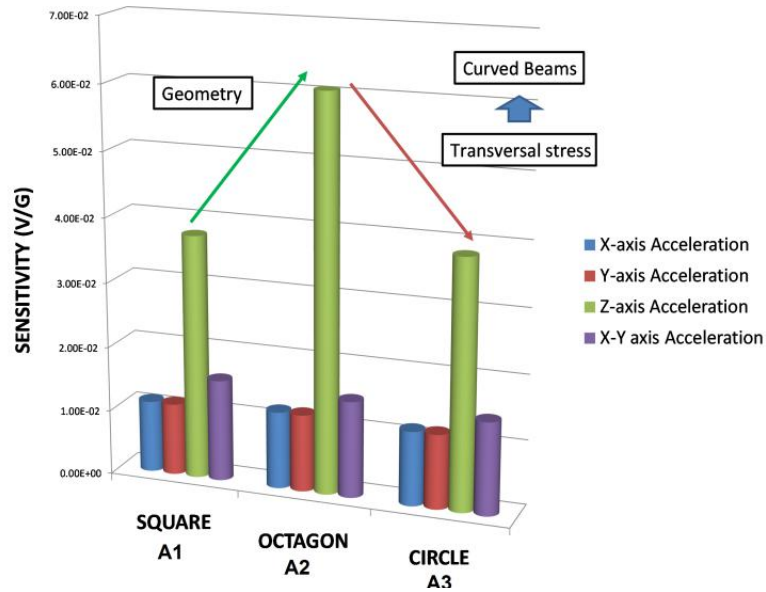
Figure 5-3. Sensitivity comparison of three designs using silicon nanowires as nanoscale piezoresistors. Due to geometry effect the octagon design (A2) presents higher sensitivity under Z-axis acceleration. The circle design (A3) due to curved beams presents higher transversal stress than the octagon geometry A2; therefore the sensitivity under Z-axis acceleration is reduced.
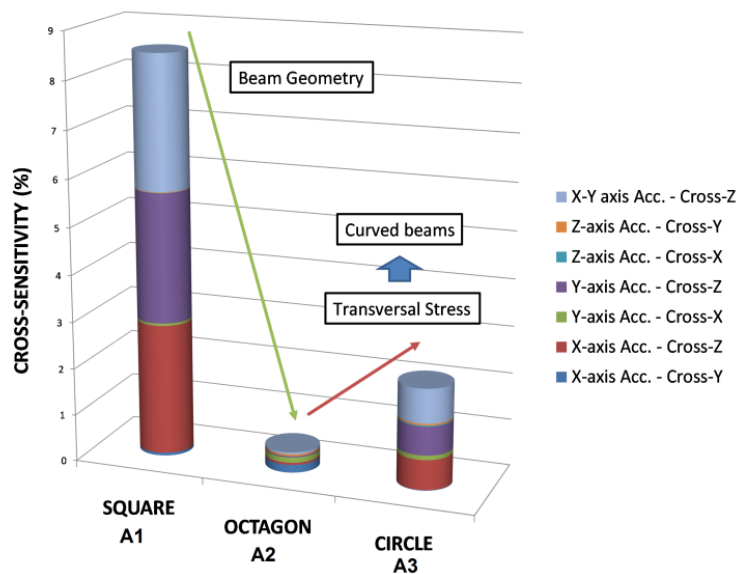
Figure 5-4. Cross-axis sensitivity of three designs using silicon nanowires as nanoscale piezoresistors. Beam geometry determines the superior performance of the octagon geometry (A2) with the lower cross-talk. The circle design (A3) due to curved beams (higher transversal stress) presents higher cross-talk than the octagon geometry (A2).

The octagonal design (Design A2) shows the minimum cross-sensitivity and the higher Z-axis sensitivity compared to the other designs. This is explained mainly by the advantageous geometry effect of the design optimization. In other words the much more even distribution

of masses in the octagonal design offers a better performance. This trend does not continue to the circular geometry (Design A3) because of the adverse effect of curved beams. The higher cross-sensitivity in the Design A3 (circle) respect to the Design A2 (octagon) is due to the effect of transversal stress, which is more relevant in Design A3 respect to Design A2 because of curved beams, therefore reduces the effect of longitudinal stress and determines higher cross-talk (Figure 5-4). For the same reason the Z-axis sensitivity results reduced respect to the Design A2. Design A1 presents a very high cross-talk in the Z-axis output, this is mainly a consequence of geometric effects, due to a non-even distribution of masses on the X-Y plane. The Design A2 is stiffer with higher stress and sensitivity at higher natural frequency (5,412 Hz against 5,355 Hz of Design A3 and 4,453 Hz of Design A1, 1st mode shape - bending on Z-axis), therefore, this shape overcome the classic trade-off between sensitivity and size of the sensor and offer a higher usable bandwidth. This is explained due to a better distribution of masses related to the geometry of the sensor, but is not so evident in the shape A3 (circle) because of much more transversal stress acting against the sensitivity. Finally, at equal mass value the octagonal geometry (A2) gives higher natural frequency and higher sensitivity. Therefore this shape allows for extreme miniaturization due to the improved overall performance.

The effect of deformation in the square geometry (A1) follows the Hook law where higher deformation determines lower natural frequency (Eq. 3.3). In the octagonal geometry (A2) smaller deformation increases the natural frequency more than the other geometries. The same thing occurs in the circular geometry (A3) but with less effect. The design optimization approach reaches its limit with the octagonal geometry and does not improve progressively when it comes to the circular geometry. This is because the transversal forces are more evident in the curved beams of the circular geometry, acting against the sensitivity and therefore reducing the performance.

The octagonal sensor due to its higher performance is a possible candidate for fabrication (see Figure 5-5), thanks to its optimized geometry and the enhancement offered by the use of nanowires as nanoscale piezoresistor. Overall the sensor meets the requirements for the application for which has been designed initially by the target specifications (Table 3-1).
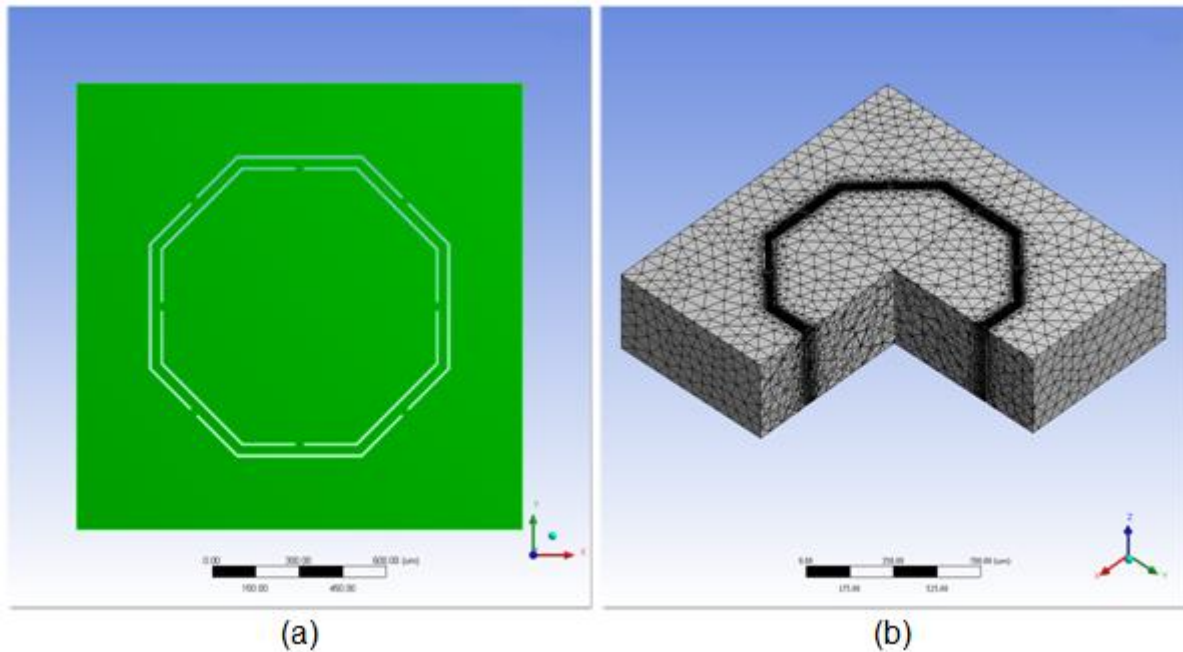
Figure 5-5. (a) Octagonal geometry sensor (top view). (b) Octagonal geometry sensor (isometric view with mesh).

5.4.2 Design Concept Type B: Straight beams

Other two types of mechanical structure have been investigated with different measurement circuit that offers higher sensitivity. As before an optimization approach has been applied starting from the square design (Design B1), also available in the literature [6, 93], see Figure 5-1(b).

The main difference with the previous geometries type A is that the beams are left straight in order to minimize transversal stress that is relevant mainly in the circle design. The

measurement circuit is also different (see Figure 5-7(a) for the piezoresistors locations on the top surface of the accelerometer and Figure 5-7(b) for the Wheatstone bridges circuit).
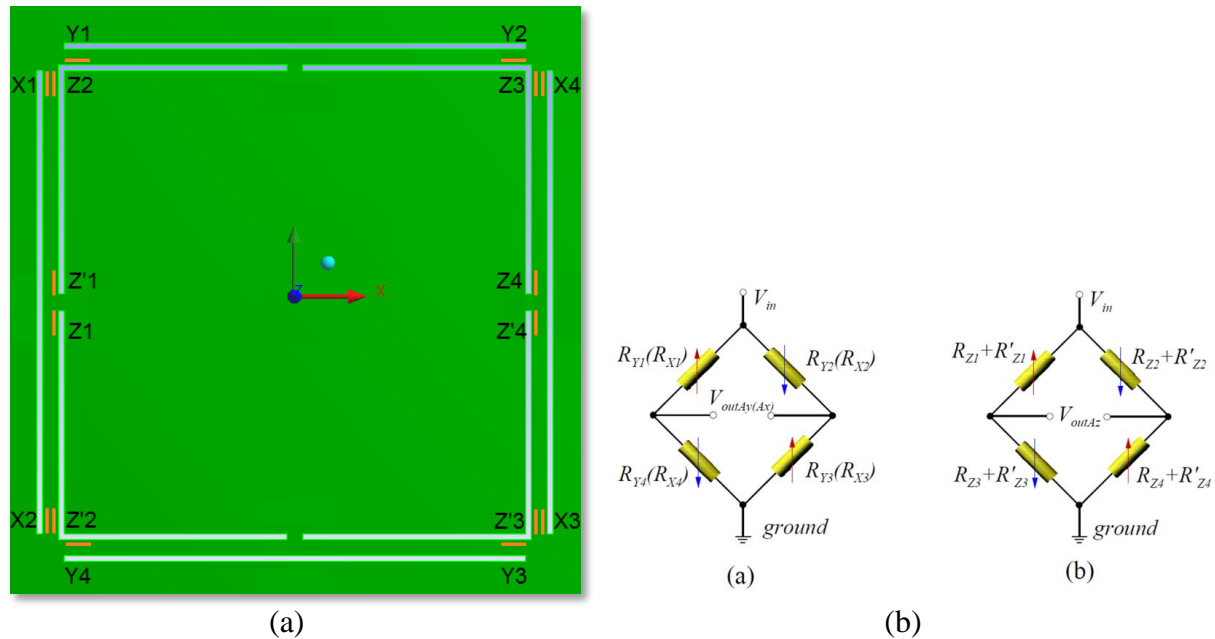
Figure 5-6. (a) Piezoresistors locations on the top surface of the chip (Design B1). (b) Measurement circuit type B. - (a) X, Y-axis Wheatstone bridge; (b) Z-axis Wheatstone bridge.

As in the previous analysis the performance calculations are based on previous experimental work, in particular the longitudinal piezoresistive coefficient used for both nanoscale piezoresistors [7] and conventional microscale piezoresistors [48]. Again, in order to be comparable all proof masses of the structures have identical volume (3×10^8 μm^3), moreover the piezoresistors are placed all in the same locations on the top surface of the chip (Figure 5-6(a)) and the measurement circuits are identical for all designs (Figure 5-6(b)). Table 5-1 summarizes the electrical sensitivity and correspondent cross-axis sensitivity of the three designs type B under study with conventional piezoresistors.

Table 5-1. Sensitivity and cross-sensitivity of three designs type B with conventional piezoresistors

	X-axis ACCELERATION (500g)			Y-axis ACCELERATION (500g)			Z-axis ACCELERATION (500g)			X, Y-axis ACCELERATION (500g)		
	X-axis (V/G)	Cross -Y (%)	Cross -Z (%)	Y-axis (V/G)	Cross -X (%)	Cross -Z (%)	Z-axis (V/G)	Cross -X (%)	Cross -Y (%)	X-axis (V/G)	Y-axis (V/G)	Cross -Z (%)
SQUARE	5.66E-04	0.104	0.191	5.65E-04	0.055	0.003	8.37E-04	0.031	0.165	5.61E-04	5.60E-04	0.011
OCTAGON	5.41E-04	0.002	0.322	5.41E-04	0.011	0.157	8.32E-04	0.257	0.326	5.40E-04	5.39E-04	0.339
CIRCLE	5.37E-04	0.001	0.311	5.37E-04	0.001	0.107	8.34E-04	0.032	0.156	5.36E-04	5.36E-04	0.285

The cross-sensitivity does not improve with the straight beams because the combination of measurement circuit and shapes is not electromechanically advantageous; nevertheless it is reduced from the Design B2 to the Design B3 due the use of a circular proof mass. The cross-sensitivity is less than 1% for square and circle geometries, respectively Design B1 and B3. The data of cross-sensitivity calculated with the use of nanowires as nanoscale piezoresistors are illustrated in the Figure 5-7. Regarding the sensitivity, it remains almost unchanged for each of the three different design of type B (see Table I-2 in Appendix I).
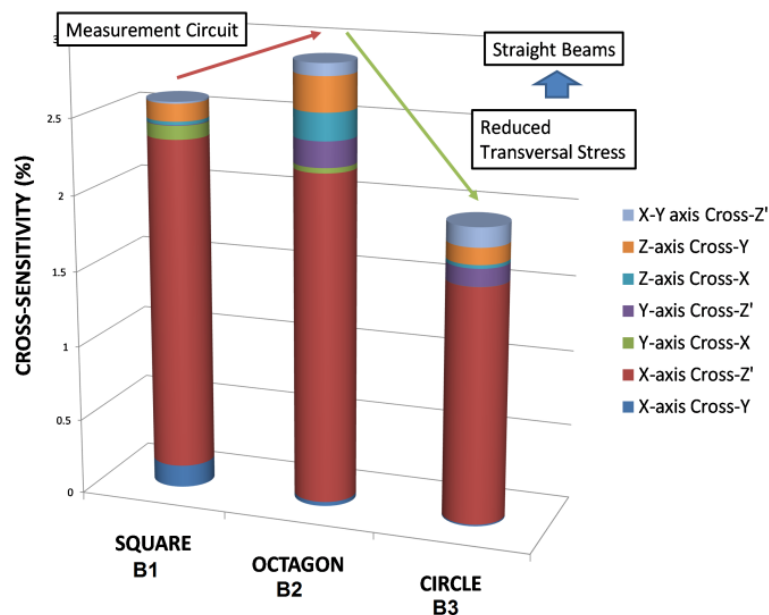
Figure 5-7. Cross-axis sensitivity of three designs type B with nanowires. As it can be seen optimization process not improves the performance from geometry B1 to geometry B2 but improves in B3 due to circular proof mass and straight beams.

The high sensitivity of nanowires increases the cross-sensitivity as well but is overall reduced in the last design (B3, circle) due to the favourable effect of distribution of masses in the circular proof mass. The sensitivity, even if it is improved due to the use of nanowires it is less even for biaxial acceleration than in the previous results on conventional piezoresistors (Table 5-1). Moreover the cross-sensitivity deteriorates respect to the designs type A using nanoscale piezoresistors, mainly due to the output of the Z-bridge under X-axis acceleration (Figure 5-7). One can ascribe this effect of the cross-sensitivity to the use of the nanowires due to their higher sensitivity combined to the particular measurement circuit used in this case (Figure 5-6(a) and 5-6(b)).

Finally, for higher sensitivity by using nanowires, the circle design (B3) is preferable on the other designs due to lower cross-sensitivity, less than 2%. Notice that the three geometries use the same type of beams (straight beams) and the same measurement circuit therefore the change in cross-sensitivity is attributed only to the proof mass geometry effect. Given this performance results the circle design (B3) is also a possible candidate for fabrication (see Figure 5-8).
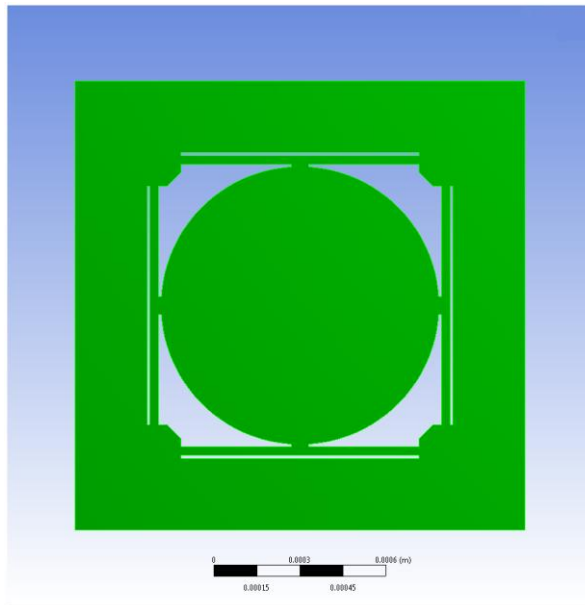
Figure 5-8. Circle design with straight beams (Top view)

5.4.3 Effect on performance of beam geometry

The performance results presented in the section 5.4.1 and 5.4.2 highlight the different effect of straight, octagonal and circular beams on device sensitivity and cross-sensitivity.

Figure 5-9 compares the sensitivity of all geometries under study. As can be seen the much higher sensitivity under Z-axis acceleration for the type A geometries compared to the type B geometries is related mainly to the different measurement circuit deployed. The sensitivity levels under X- and Y-axis acceleration change slightly among different geometries. The two designs with square proof mass and straight beams (A1 and B1) are identical except for the use of a different measurement circuit, therefore the sensivity change under Z-axis acceleration is down to it. The deisgn with octagonal mass and octagonal beams (A2) compared to the design with octagonal mass and straight beams (B2) present improved sensitivity for all axes, again the very high sensitivity under Z-axis acceleration is due to the measurement circuit used and the particular beam geometry. Similar results as the geometries

A2 and B2 are obtained comparing the design with circular proof mass and circular beams (A3) to the design with circular proof mass and straight beams (B3).
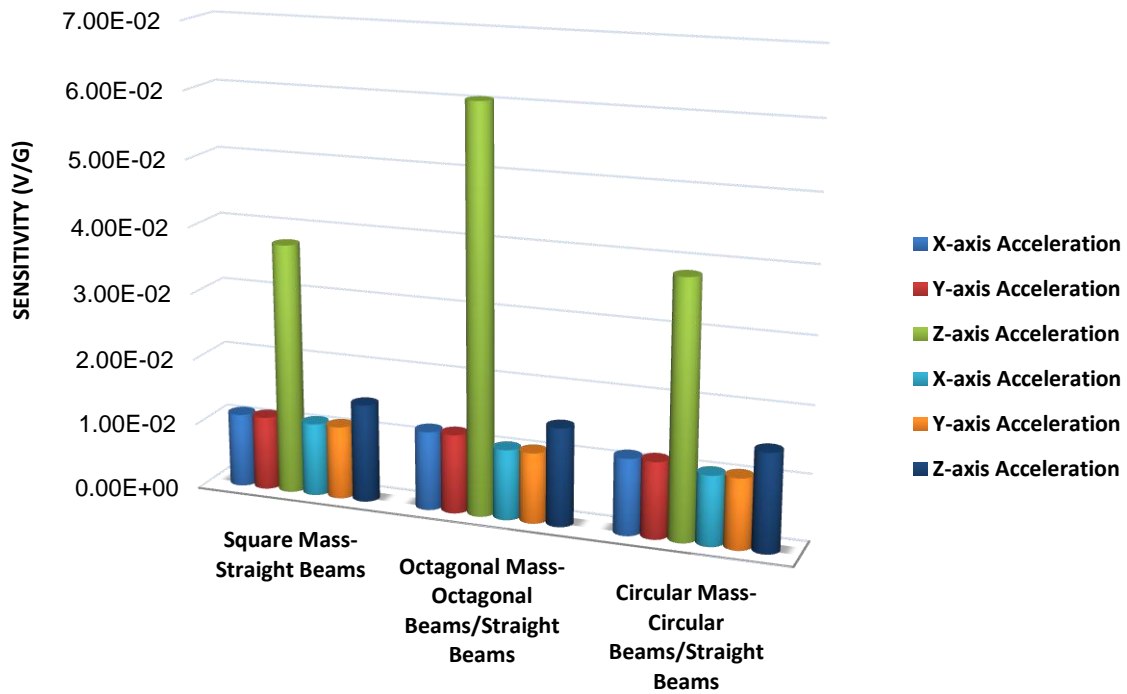
Figure 5-9. Sensitivity comparison among the various geometries analysed in the study. As can be seen square mass with straight beams gives similar sensitivity performance except under Z-axis acceleration due to the different measurement circuit used. The octagonal proof mass geometry with octagonal beams compared to straight beams is superior under all different acceleration directions, again the high improvement under Z-axis acceleration is related to the measurement circuit used and also the bend angle. Finally, the geometry with circular proof mass and circular beams shows slightly higher sensitivity levels than the geometry with circular proof mass and straight beams.

Overall the results obtained shows that octagonal beam geometry compared to the straight one regardless of the proof mass geometry present higher sensitivity levels for out-of-plane acceleration and similar sensitivity levels for in-palne acceleration. This improvement of the sensitivity is related mainly to the particular measurement circuit used that enhance the sensitivity under Z-axis acceleration and also related to a higher stress available at the piezoresistors location, close to the attachments. This type of beam geometry presents higher stress at the attachments to the proof mass or frame because of the bend angle (45°) at the middle of the beam. The change in direction of the beam determines a slight increase of stress

134

compared to the straight beam. Note that the beam length is slightly reduced in the octagonal geometry compared to the straight one.

Regarding the comparison between circular and octagonal beams, the sensitivity change is very little when it come to in-plane acceleration. Therefore in these particular cases the stress distribution on the beams is not much affected by the different geometry. Note that for these two types of beam geometries the beam length is similar.

Under out-of-plane acceleration the sensitivity is notably different between octagonal and circular beam geometry. This difference is related to the distribution of transversal stress on the piezoresistor locations. The transversal stress affects negatively the sensitivity, therefore circular beams determine higher transversal stress than octagonal beams on the piezoresistors location. Under in-plane acceleration the change in transversal stress distribution between octagonal and circular beam geometry is compansated by the measurement circuit, this compensation is not occurring under Z-axis acceleration because of the particular measurement circuit used (see section 5.5 for details).

The effect of transversal stress at the piezoresistor location is affected by the angle of curvature of the circular beam geometry. The higher is this angle the lower would be the effect of transversal stress on the sensitivity.

Finally the octagonal beam geometry offer an enhanced sensitivity compared to the straight beam geometry due to a slightly increased stress at the piezoresistors location due to the bend angle and an enhanced sensitivity compared to the circular beam geometry due to a lower transversal stress at the piezoresistors location (improved sensitivity under out-of-plane acceleration). Measurement circuit comparison

From the performance calculations undertaken so far it is possible to evaluate the impact of the different measurement circuits deployed in the two types of geometries. Notice that the type of measurement circuit depends on the particular beam geometry (curved or straight) where the piezoresistors are placed (compare Figures 4-2 to 5-8). Therefore, the type of circuit is a consequence of the type of beams. In particular, notice that the starting geometry of the evolutionary design approach study (square geometry - Design A1 or B1) is identical for both types of geometries developed in this work; therefore the obtained values of sensitivity and cross-sensitivity are comparable based on the exclusive measurement circuit design. Table 5-2 compares the two measurement circuits deployed in this study.

Table 5-2. Measurement circuit performance comparison between Square geometry type A1 and Square geometry type B1

	X-axis ACCELERATION (500g)			Y-axis ACCELERATION (500g)			Z-axis ACCELERATION (500g)			X, Y-axis ACCELERATION (500g)		
	X-axis (V/G)	Cross -Y (%)	Cross -Z (%)	Y-axis (V/G)	Cross -X (%)	Cross -Z (%)	Z-axis (V/G)	Cross -X (%)	Cross -Y (%)	X-axis (V/G)	Y-axis (V/G)	Cross -Z (%)
Square type A1	1.11E-02	0.06	2.78	1.11E-02	0.052	2.76	3.77E-02	0.005	0.013	1.57E-02	1.57E-02	2.842
Square type B1	1.10E-02	0.15	2.2	1.10E-02	0.090	0.004	1.48E-02	0.022	0.115	1.22E-02	1.22E-02	0.011

As it can be seen from Table 5-2 the outputs obtained from the two measurement circuit under X-axis acceleration are comparable, similar results under Y-axis acceleration except for the output of the Z-bridge (cross-Z). These results are easily explained due to the symmetric location of the piezoresistors on the top surface of the sensor beams for X and Y-bridge in both types of design. When X-axis acceleration occurs the piezoresistors of the measurement circuit type A are compressed, meanwhile the correspondent piezoresistors of the

measurement circuit type B are tensed. Therefore, the absolute value of output voltage is similar.

When it comes to the Z-bridge the values of the output voltage (cross-Z) are of the same order of magnitude under X-axis acceleration (2.78% and 2.2%), but very different under Y-axis acceleration (type B is two order of magnitude smaller, 2.76% vs. 0.004% – lower cross-talk, Table 5-2). This occurs because the type B Z-bridge circuit is unbalanced under the X-axis acceleration and balanced under Y-axis acceleration, due to different piezoresistors locations. Under Z-axis acceleration the performance of the measurement circuit type A is much better than type B (37.7 mV/g vs 14.8 mV/g), this is down to the higher sensitivity obtained from the circuit design due to a higher number of piezoresistors under the same stress condition. In conclusion it was found out that the circuit type A has higher performance than type B, except for the output of Z-bridge under Y-axis acceleration (cross-Z) due to measurement circuit design. It could be possible to combine both types of measurement circuit for the Z-bridge and improve the measurement accuracy. This is currently reasonable only for the geometry type B with straight beams, due to the use of piezoresistors on the <110> direction. In the case of the type A geometries with no-straight beams, the feasibility of the measurement circuit should be tested since the use of piezoresistors on the <100> direction. If the nanowires built on the <100> direction give the expected sensitivity under stress [6, 12, 45] it could be possible to apply the improved measurement circuit to the new geometries developed in this study.

5.5 Optimum design selection

By comparing the results obtained from the design optimization approach of geometry types A and B with the use of nanowires it can be concluded that the design A2 (octagon) and the design B3 (circle) are the favourite geometries for fabrication. Table 5-3 compares closely the performance results of the two geometries; clearly the octagon type A geometry (A2) presents higher performance in terms of sensitivity and cross-sensitivity, due to the combined geometry and measurement circuit effect. As can be seen from the Table 5-3, the octagonal geometry type A considerably improves the cross-talk of the Z-bridge under in-plane acceleration and more than double the sensitivity under Z-axis acceleration. On the other hand, the circle geometry type B (B3) presents worst cross-sensitivity on the Z-bridge output under X-axis acceleration due to the measurement circuit effect (1.553% vs. 0.046%), but presents much more even sensitivity for in-plane acceleration (the sensitivity for biaxial acceleration is much closer to the uniaxial one, 11.5 mV/g vs. 14.9 mV/g for biaxial and 10.5 mV/g vs. 11.9 mV/g, for uniaxial one - Table 5-3).

Table 5-3. Sensor performance comparison of Octagon geometry type A2 and Circle geometry type B3

	X-axis ACCELERATION (500g)			Y-axis ACCELERATION (500g)			Z-axis ACCELERATION (500g)			X, Y-axis ACCELERATION (500g)		
	X-axis (V/G)	Cross-Y (%)	Cross-Z (%)	Y-axis (V/G)	Cross-X (%)	Cross-Z (%)	Z-axis (V/G)	Cross-X (%)	Cross-Y (%)	X-axis (V/G)	Y-axis (V/G)	Cross-Z (%)
Octagon type A2	1.19E-02	0.169	0.046	1.19E-02	0.115	0.029	6.06E-02	0.001	0.037	1.49E-02	1.49E-02	0.040
Circle type B3	1.05E-02	0.010	1.553	1.06E-02	0.0005	0.115	1.48E-02	0.022	0.109	1.15E-02	1.15E-02	0.128

From those results, it could be interesting to exploit the potential of both designs combining them in a single design with circle geometry, plus beams and measurement circuit of the

octagon geometry type A (A2), in order to maximize the advantages coming from both design types. In this new design it may even possible to uses the potential of the improved measurement circuit explained earlier (section 5.4) that exploit nanowires on the <100> direction. This new design is addressed in the next chapter.

The design optimization approach demonstrates that even sensitivity, due to geometry and measurement circuit, for biaxial in-plane acceleration reduces cross-sensitivity on the remaining axis (Z-axis); see the value change of the cross-Z under X-axis acceleration in Figure 5-7. The reason for this can be easily explained, because if we have higher sensitivity for biaxial in-plane acceleration (overall uneven), the correspondent cross-talk (Z-axis) would be higher as well for a proportional quantity. This is down to the relationship of piezoresistors in the measurement circuit (common location). This phenomenon can be much more appreciated with high sensitivity devices such as nanowires (see Figure 5-7).

The study points out the possibility of developing a design that combines nanowires on the <110> and <100> direction. It should be noted that such design needs further investigation beyond present study due to the unknown behaviour of nanowires in the <100> direction under 5 nanometer size, and therefore, performance calculation are unavailable at this stage. The design performance at present can be calculated only with the use of <110> nanowires direction, therefore only a particular measurement circuit can be used, e.g. the two types investigated in this study, that limits the chances to maximize the sensor performance.

5.6 Conclusion

In summary, the hypothesis of this study is that an even mass moment of inertia would improve measurement accuracy. The hypothesis has been proved with a design optimization

approach (from uneven to even mass moment of inertia) and performance comparison (sensitivity and cross-sensitivity) of two types of design. Finally, the thesis obtained from the analysis of the calculations results is that even mass moment of inertia not always improve measurement accuracy, but it depends on the measurement circuit, the level of sensitivity of the sensing element (piezoresistors) and on the beams geometry (straight or curved). The electro-mechanical study developed is a valuable tool for enhancing the performance of any piezoresistive accelerometer that adopts four surrounding beams and a highly-symmetric geometry.

Chapter 6

6 PROPOSED OPTIMAL ACCELEROMETER DESIGN

6.1 Introduction

This chapter presents the performance results of the optimal accelerometer design obtained as a final output of a design optimization approach developed in Chapter 5. The design optimization strategy adopted basically creates a new solution (design) by changing the mass moment of inertia *(MMI)* to current solution. If the new solution is better, search proceeds utilizing the new solution, if not the prior solution is retained. The final design is the result of three steps of design optimization that starts from a state-of-art design readily available in the literature [93] that is configured with straight beams and square proof mass. The optimization process is guided by an objective function that generates feasible alternatives. The objective function is based on changes of the *MMI* of the proof mass, which becomes more and more even at each step of design evolution for any biaxial acceleration (acceleration of X-Y plane). In the first step of optimization the square proof mass of the accelerometer becomes octagonal with two different designs, one with straight beams and one with curved beams. In the second step of optimization the octagonal proof mass of the accelerometer becomes

circular in two different designs, one with straight beams and one with curved beams. In the third and last step of optimization the final design is obtained. Notice that except for the first accelerometer geometry with square proof mass and straight beams, all designs obtained from the optimization process are completely new (not available in the literature). Therefore this work presents new device geometries achieved through adoption of an optimization process based on a novel design optimization approach (changes of the proof mass *MMI*).

As expected the accelerometer geometry obtained as the final output of the design optimization approach has superior performance in term of sensitivity and cross-sensitivity in respect to the previous geometries. This new and final design increases the sensitivity but simultaneously reduces the cross-talk, a phenomenon not reported in the literature. Typically, an increase in sensitivity results to a proportional increase in the cross-sensitivity.

This chapter work represents a further and final step in the enhancement of the accelerometer design performance. The aim is to maximize the performance of the accelerometer, thus sensitivity and cross-sensitivity are investigated, in order to improve the device measurement accuracy.

6.2 Optimization strategy

Figure 6-1 shows the entire design optimization process adopted for the study. As it can be seen, the approach starts from a state-of-art design and then evolves into two different designs types based on distinct beams geometry (curved beams type A and straight beams type B). Each step of evolution has common proof mass geometry that changes in the first step of evolution from square to octagon and in the second step changes into circle. Following a thorough performance analysis undertaken in Chapter 5 (section 5.4) two

geometries are selected (octagon type A – Design A2, and circle type B – Design B3, see the Figure 6-1) for their higher performance (higher sensitivity and lower cross-sensitivity - see results in Figure 5-3, 5-4 and Figure 5-7 in Chapter 5). The final design is obtained from a combination of these two geometries (Figure 6-1) that utilises the measurement circuit type A (Figure 4-2(a) and 4-3) due to the use of octagonal beams geometry.
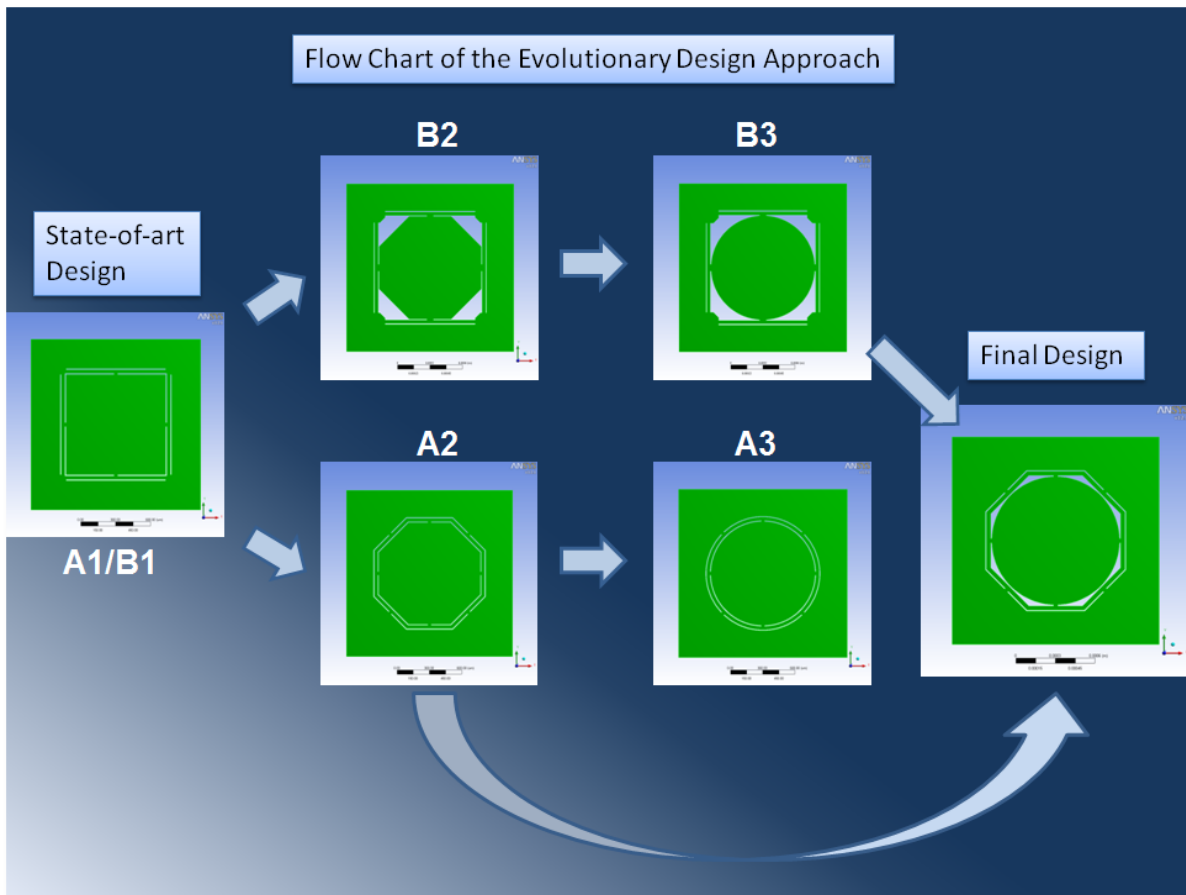
Figure 6-1. Flow chart of the design optimization approach. As it can be seen the geometry optimization starts with a square proof mass (Design A1/B1) and then it becomes octagonal (Design A2 and B2) and finally a circle (Design A3 and B3). Two types of beams are used straight and curved. The final design is obtained after a performance analysis that indicates the superior geometries (Design A2 and B3).

6.3 FE Modelling

The modelled geometry in Figure 6-2, which is the proposed optimal accelerometer design, is analysed with the use of ANSYS 12.1 commercial software by using 350,000 meshing nodes and tetrahedron elements and proximity meshing option for improved accuracy in the geometry areas of reduced size, such as the beams, where good stress analysis is required (see Figure 6-2(b)).

(a)

(b)
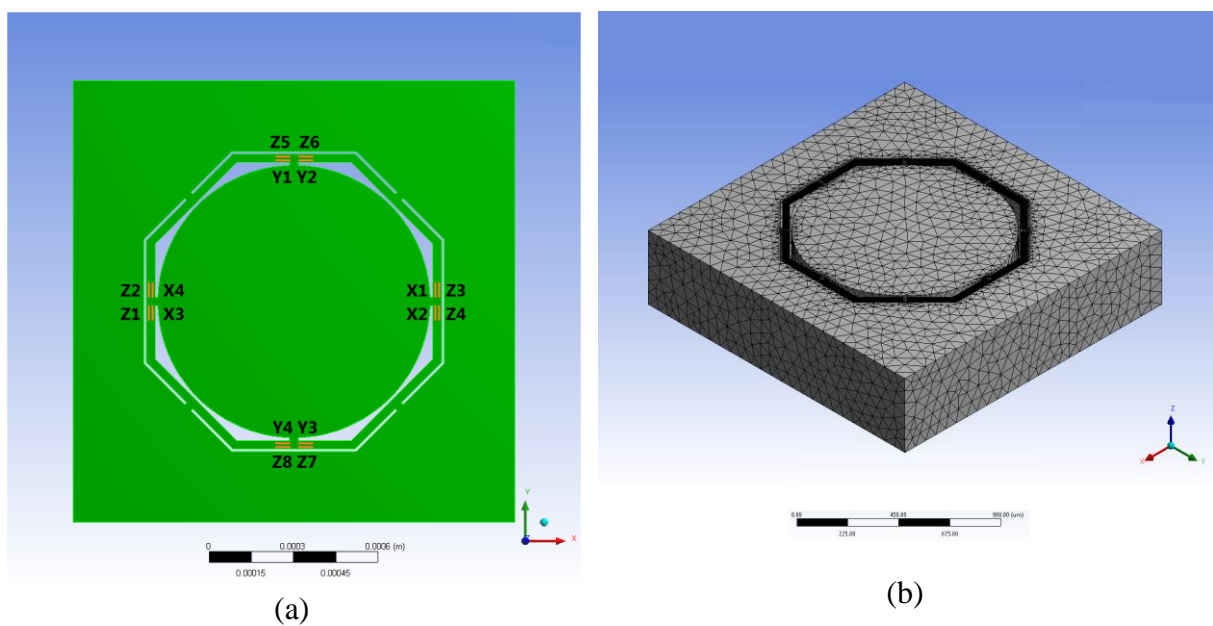
Figure 6-2. (a) Optimal design (top view). The design is obtained from the combination of the octagon geometry type A and circle geometry type B and utilizing the measurement circuit of type A. (b) Meshed optimal design (isometric view). As it can be seen the beams have a much more dense mesh for accuracy enhancement.

Boundary conditions are applied by fixing the bottom side of the external frame of the mechanical structures and then leaving the proof mass free to move. The load applied is a gravitational force vector of 500g of magnitude, one for each of the three principal axes. The material properties of the model are provided in Table 6-1. To allow comparison among the different geometries studied, all structures' proof masses have identical volume (3×10^8 μm^3).

Table 6-1. Model material and geometrical properties

Mechanical Structure material	Single Crystal Silicon Anisotropic
Density (kg/m^3)	2330
Matrix of stiffness	see Eq. 4.1
Proof Mass volume	3×10^8 µm^3
Proof mass radius	488.60 µm
Proof mass thickness	400 µm

In order to better understand the effect of beam and proof mass geometry on the sensor mechanical performance (sensitivity and cross-sensitivity) three different types of geometries have been developed (see Figures 6-3) with distinct curved beams (Design curved+circle and curved+circle 2, Figure 6-3(a) and (b) respectiveley) and with a doughnut proof mass (Figure 6-3(c)) using the same measurement circuit type A.

(a) (b) (c)
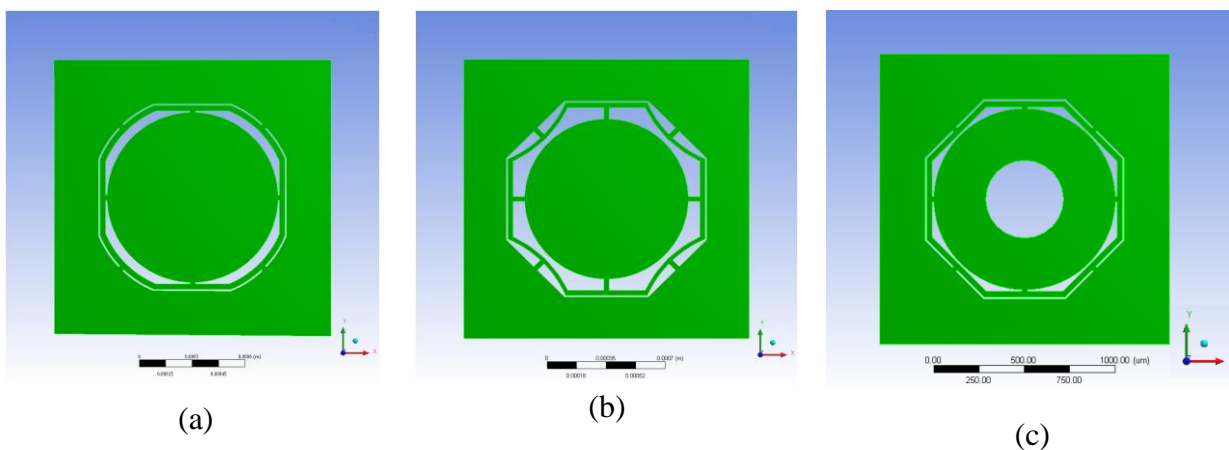
Figure 6-3. (a) Curved+circle geometry. The beams have a concave geometry. (b) Curved+circle2 geometry. The beams have convex geometry. (c) Doughnut geometry. The proof mass is empty in the middle.

6.4 Results and discussion

6.4.1 FEA results - nanowires as piezoresistors

Figures 6-5 shows comparison of the sensitivity performance results for the final design to the three designs type A using similar measurement circuit (type A) and nanowires (the longitudinal piezoresistive coefficient at room temperature used for the nanoscale value is 1527×10^{-11} Pa^{-1}, obtained from Passi *et al.* [7] experimental work). Detailed results are provided in Table I-3 (Appendix I). As can be seen from Figure 6-6, the final optimal design presents under X or Y-axis acceleration a maximum increase in sensitivity of 16.2% (final vs. square A1), while under biaxial acceleration (X and Y-axis acceleration) an increase of 19.5%. When it comes to the sensitivity under Z-axis acceleration the maximum increment of the final design is four times larger (proposed optimal design vs. square A1) and the minimum increment is of 216% (proposed optimal design vs. octagon A2), this is achieved thanks to the use of octagonal beams, circular proof mass, type of measurement circuit and nanowires. The final design presents the maximum performance in term of sensitivity.
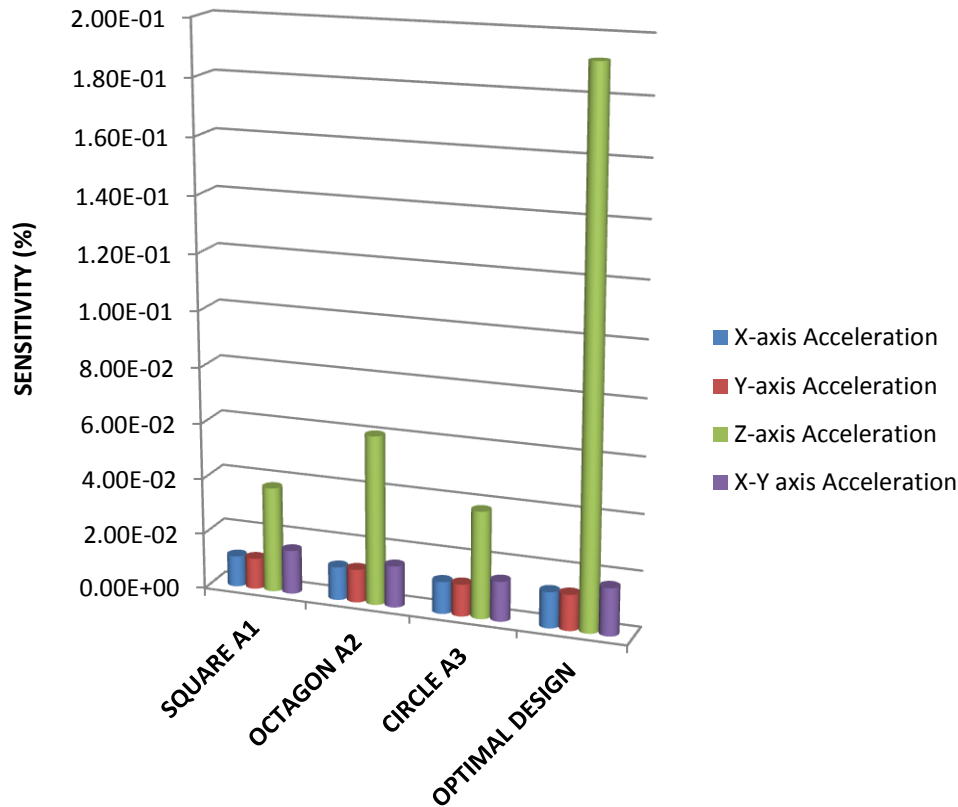
Figure 6-4. Sensitivity comparison of different design. The proposed optimal design due to combination of parameters, such as octagonal beams, circular proof mass, measurement circuit type A and the use of nanowires determines the maximum performance.

Figure 6-6 shows the cross-sensitivity of the different designs. As expected, the proposed design is superior with respect to the other studied accelerometer designs. The sum of the cross-sensitivity of all axes is minimized and equal to 0.4%. This result is attributed to the combination of different parameters selected after a thorough analysis, i.e. octagonal beams, circular proof mass, measurement circuit type A and nanowires. For the first time a design is capable of increasing the sensitivity and meanwhile minimizing the cross-sensitivity. This is in contrast to the design available in the literature [94 – 106] whereby any increase in sensitivity was reported to lead to a correspondent increase in the cross-sensitivity.
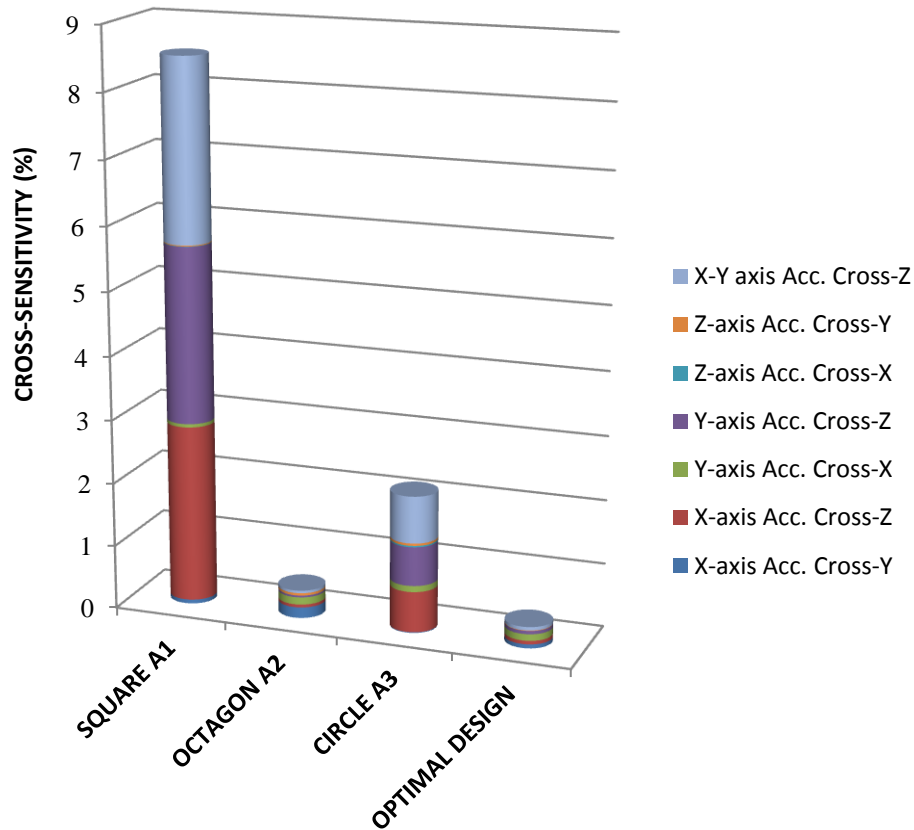
Figure 6-5. Cross-sensitivity comparison. The proposed optimal design presents lower cross-sensitivity.

6.4.2 FEA results - conventional microscale piezoresistors

With the use of conventional microscale piezoresistors (the longitudinal piezoresistive coefficient at room temperature used for the conventional piezoresistor is 72×10^{-11} Pa^{-1} as reported by Smith [48] experimental work), the proposed design also presents the highest performance mainly in term of cross-sensitivity (Figure 6-6 and 6-7). Therefore, in this particular case the effect of nanowires that increases cross-sensitivity especially on the Z-bridges under X-axis acceleration observed previously (Figure 5-7) is not present, mainly because the measurement circuit used (type A).

Other three different geometries types (curved+circle, curved+circle2 and doughnut) have been designed and the performance has been calculated with the use of conventional

piezoresistors. The new geometries due to the curved beams (concave and convex) present higher sensitivity because the beams are relatively longer and determine higher deformation and stress (see Figure 6-6), but at the cost of higher cross-talk (Figure 6-7). This is the main drawback in the state-of-art design [94 – 106], the proposed optimal design developed in this study overcome this effect. It is able to increase the sensitivity but not at the cost of the cross-sensitivity, in fact the cross-sensitivity is reduced.
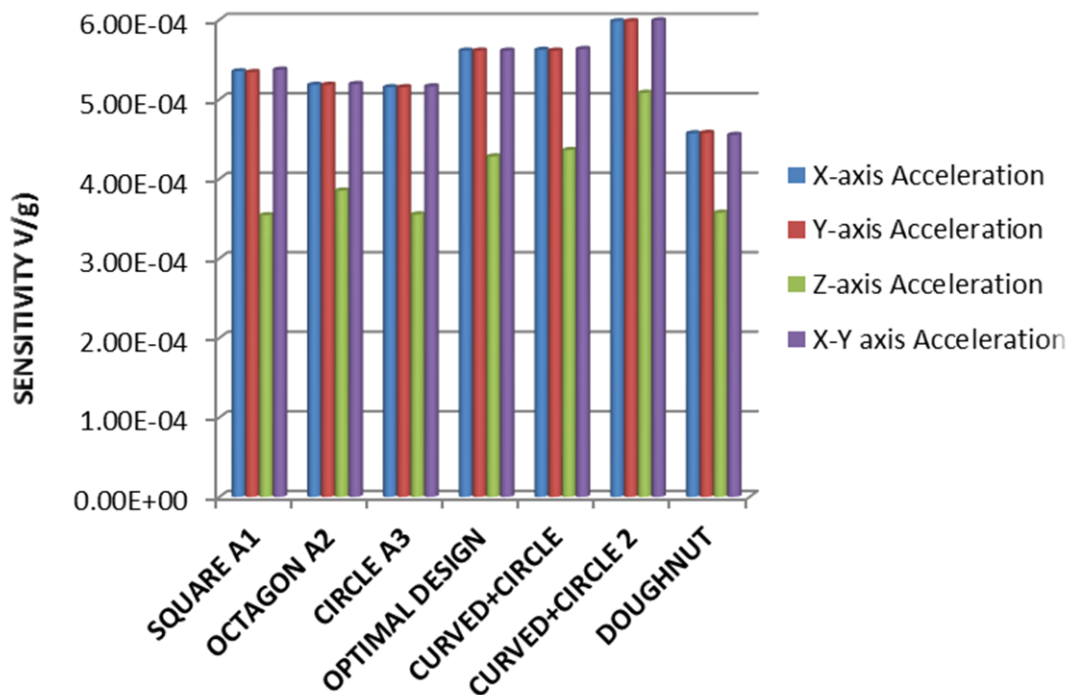
Figure 6-6. Sensitivity comparison with conventional microscale piezoresistors. The final optimal design and the new beam geometries (curved+circle and curve+circle2) present higher sensitivity. The doughnut geometry presents the lower sensitivity compared to the other geoemtries.

The use of nanowires in this study has its main impact on boosting the sensitivity under Z-axis acceleration (Figure 6-5) mainly due to the measurement circuit used. The two geometries, curved+circle and curved+circle2, provide higher sensitivity due to curved beams used (Figure 6-6) but this effect does not prevent increases of cross-talk (Figure 6-7). As it can be seen in Figure 6-7, the cross-sensitivity of curved+circle and curved+circle2 geometries is worst than the octagonal A2 design because the beams are much longer

determining higher deformation and stress and therefore higher cross-talk. The circle A3 design compared to the curved+circle and curved+circle2 presents higher cross-talk due to the use of circular beams that reduces the effect of longitudinal stress compared to the transversal one on the piezoresistors. The doughnut geometry compared to the other geometries presents the lowest sensitivity in all axes of measurements. The concentration of mass on the edge of the proof mass does not improve the mechanical behaviour of the device instead the sensitivity get worst because of the reduced stress on the piezoresistors locations. This is more evident under X and Y-axis acceleration where rotation occurs under the axis perpendicular to the vector of the applied acceleration. Therefore the effect of a lower mass moment of inertia influences the in-plane sensitivity. For out-of plane acceleration the sensitivity is comparable to the state of art design (design Squate A1). Similar results are obtained with the doughnut geometry for the cross-sensitivity, which is not improved by a distribution of mass on the edge of the proof mass (Figure 6-7).

Table I-4 (Appendix I) compares the results of sensitivity and cross-sensitivity of three type A designs, such as the proposed optimal geometry and the three new geometries (curved+circle, curved+circle2 and doughnut) with conventional microscale piezoresistors.
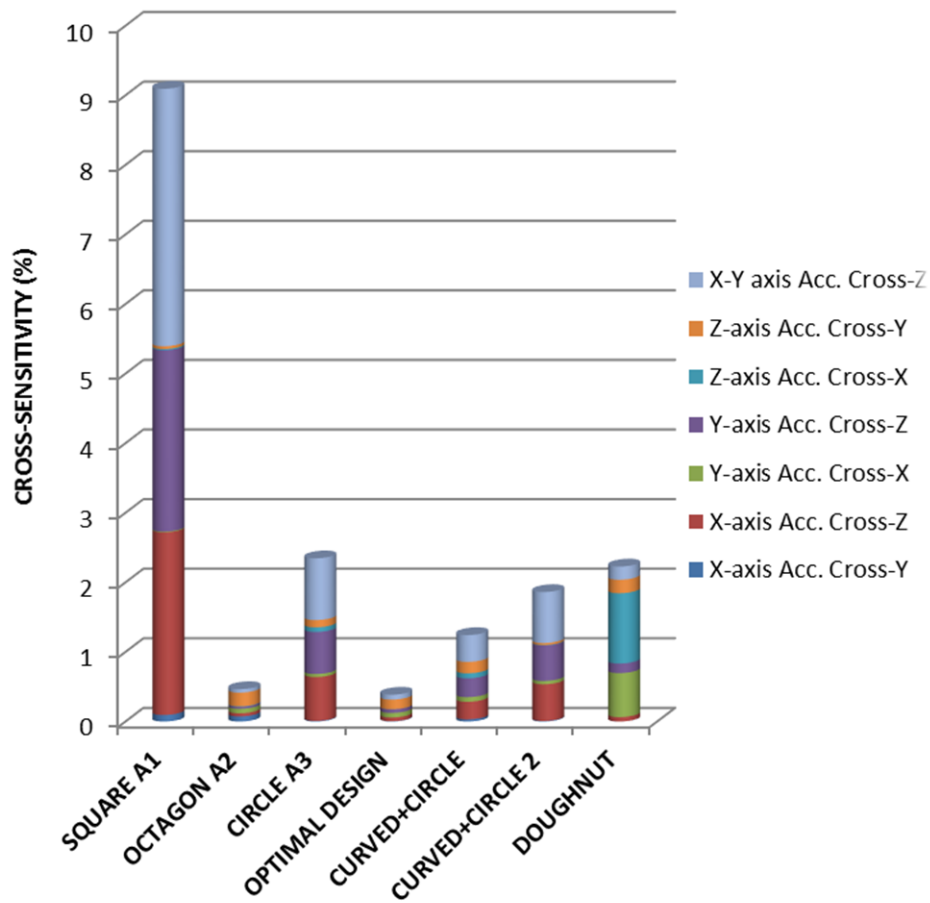
Figure 6-7. Cross-sensitivity comparison with conventional microscale piezoresistors. The new geometries (curved+circle,curved+circle2 and doughnut) present higher cross-talk. The final design results superior to all geometries studied.

6.5 Conclusion

In conclusion, from all the geometries studied and the performance comparison of each of them, it can be asserted that the proposed optimal design of this study with measurement circuit type A, octagonal beams, circular proof mass and with or without the use of nanowires is electromechanically superior to all the other geometries studied or available in the literature. With the use of nanowires, the optimal design presents under X or Y-axis acceleration a maximum increase in sensitivity of 16.2% (optimal design vs. square A1), while under biaxial acceleration (X and Y-axis acceleration) an increase of 19.5% is

observed. The sensitivity under Z-axis acceleration in the proposed optimal design has a maximum increment up to four fold (optimal design vs. square A1) and a minimum increment of 216% (optimal design vs. octagon A2). Therefore the implementation of this electromechanical design would determine higher measurement accuracy with respect to the current state-of-art designs of the same type of accelerometer (bulk micromachined piezoresistive). The improvements of the proposed optimal design are related to a combinations of factors that have been studied throughout this work, and in particular the beams and proof mass geometry and the measurement circuit deployed. The beams with octagonal geometry showed higher performance when in combination to the circular proof mass (see Figure 6-6) due to the beams bending angle of 45 degree and the circular proof mass that incease the stress at the piezoresistors locations. This particular combination presents also the minimum cross-sensitivity for the same reason. If we consider the beam length it is observed an increase of sensitivity with the increase of beam length (see curved+circle and curved+circle2 geometries in Figure 6-6). This sensitivity improvement due to only the beam length determines a worsening of the cross-sensitivity (Figure 6-7) which was not observed by shorter beams with octagonal shape.

Higher measurement accuracy of an earplug accelerometer means reliable data in case of an accident in predicting head injury; therefore, a much more accurate safety system would be in place. Future research on experimental work is required to develop the proposed optimal accelerometer design.

Chapter 7

7 A FEASIBILITY STUDY ON THE FABRICATION OF SILICON NANOWIRES FOR NANOSCALE PIEZORESISTORS

7.1 Introduction

This chapter describes the set-up of the silicon nanowire experiments and the results obtained. Two different types of fabrication process are under study: Focus Ion Beam (FIB) direct milling and self-assembled nanowires. The former process is not a common practice in the silicon industry because of the long time and cost related to the fabrication of a single nanowire. The nanowire was fabricated by top-down approach by direct milling of the structure sidewalls. Amarasinge et al. [71] in their study demonstrate the feasibility of sensitivity enhancement of conventional piezoresistors with FIB tool through a nanometer stress concentration region. The latter fabrication process considered in this study is the self-assembly technology which is a growth mechanism. The more common growth mechanisms are vapour-liquid-solid (VLS) and oxide-assisted growth (OAG) mechanisms [10]. In the VLS model, the nanowire grows from a metal-catalyst droplet during silicon vapour deposition. This mechanism is used by He and Yang [3] that observed an enhanced

piezoresistance effect in their nanowires grown in the <111> and <110> direction using Pt as catalyst and SiCl$_4$ as precursor at 900°C. The main problem of the use of this technology is the integration of the silicon nanowires growth into the MEMS fabrications steps.

The experiment undertaken in this study for fabricating silicon nanowires focuses on demonstrating our capability of fabricating their mechanical structure. Regarding the bottom-up approach the fabrication process comprises the microfabrication of the samples with contacts and then the growing of the nanowires between them. This study is not intended to characterize electromechanically the fabricated nanowires. Potential future work would be to characterize the nanowires by applying an oscillating stress in order to avoid an apparent and time dependent giant piezoresistance effect caused by surface trapping of charges (also known as dielectric relaxation) [79].

7.2 Design of samples

The samples for the bottom-up approach have been designed taking into account the size required for the samples to be placed into the characterization station (Figure K-2(a)). Figure 7-1 below shows the sample design with the nanowires devices.
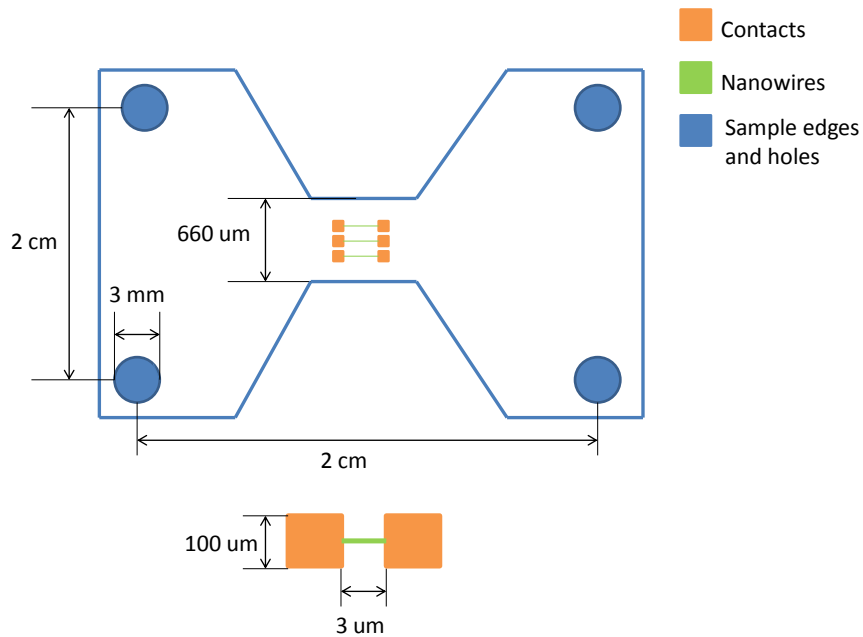
Figure 7-1. Sample and nanowires design. The samples are specifically designed to fit in the characterization station (see Appendix K). The nanowires grown to be 3 microns with contacts of 100 square microns. As it can be seen a set of three pairs of nanowires are placed into the middle of the sample microstructure in order to have with 20 N a maximum of 100MPa of stress.

As can be seen from Figure 7-1 the sample comprises 4 holes from which the sample is secured to the station for tensile test. The nanowires were designed to be placed in the middle of the sample where a concentration region is designed in order to increase the stress applied to the nanowires. The concentration region is designed in order to apply a maximum of around 100 MPa under 20 N of force, which is the maximum force the micro-tensile equipment can apply. The contacts size of the nanowires devices is set to 100×100 μm because a wire bonding will be necessary for electrical measurements. The length of the nanowires is set to 3 μm in order to have a solid structure.

Figure 7-2 shows a front mask sketch of a SOI (110)-oriented wafer with the principal flat perpendicular to the [111] direction and two other flats placed in order to be able to rotate the

mask of the required angular degree and obtain samples on the other two remaining principal

directions (see Figure 7-2).
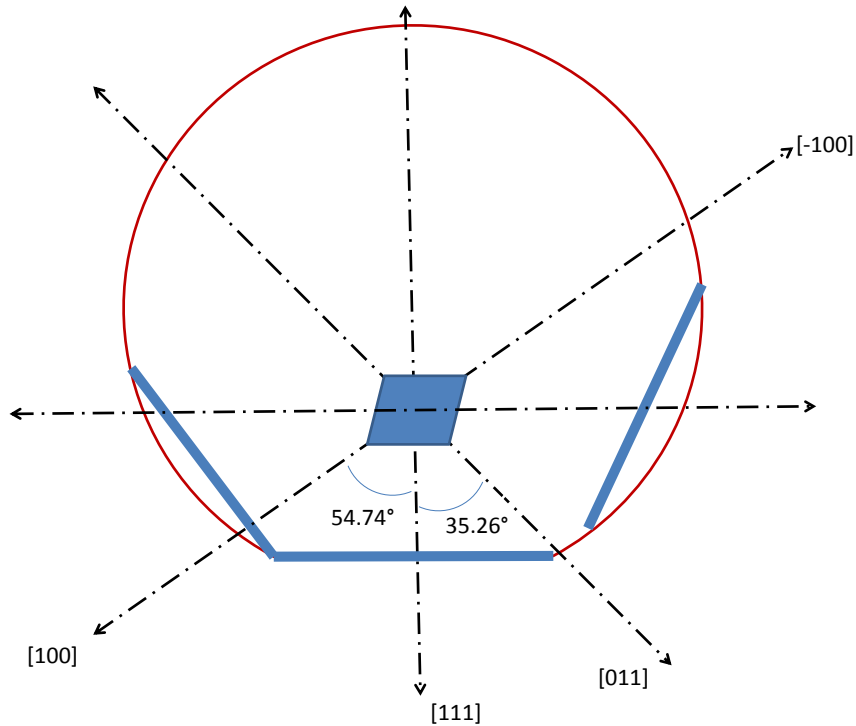
Figure 7-2. Masks design sketch. As it can be seen from the image three flats are designed for the mask layout in order to be possibly able to make nanowires on different direction just rotating the wafer relatively to the mask.

The sample has been designed to be tested in a characterization station (Figure K-2 (a) and

(b)). For tensile stress the front and back mask layout of the samples is presented respectively

in Figure 7-3 (a) and (b).

As can be seen in the figure three flats are designed for the reason explained earlier,

moreover four mask aligner marks are designed in order to align the front and back mask (top

right in Figure 7-3). On the top left of Figure 7-3(a) it can be seen the design of three pairs of

contacts from which the silicon nanowires will be grown.
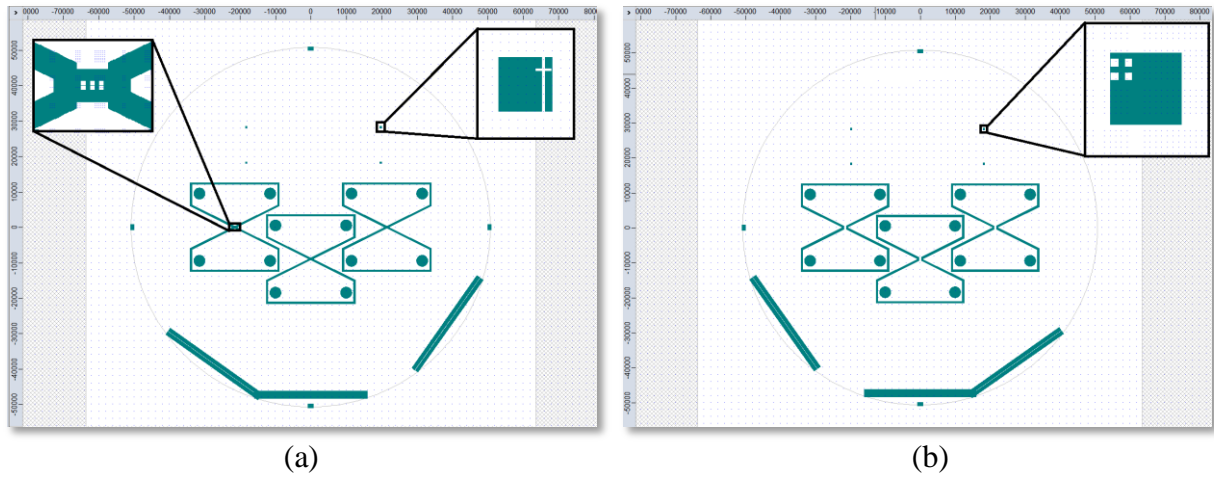
Figure 7-3. (a) Front mask design. In the inset on the left it can be seen the middle of the sample layout where the contacts are designed. On the inset on the right the mask aligner mark is shown. (b) Back mask design. The inset on the right shows the mask aligner mark.

The two masks, front and back, are designed mirroring each other in order to be perfectly aligned during photolithography.

Note that the SOI wafer used is a 4 inch wafer size but the space available for design is only the 3 inches in the centre because the mask aligner exposes only the three inches in the centre. After exposure both sides of the sample will be subject to plasma (DRIE) etching.

Each nanowire in the test-chip is designed to have 2 contacts. Each contact is designed to obtained an Ohmic contact in order to have a I-V curve more linear has possible in the region of usage and fulfil therefore the Ohm law. In order to obtain such contact the resistance change encountered by the current flow from the metal track to the nanowire itself must be as smooth as possible. This is possible by using a heavy doping dosage ($>1\times10^{19}$ cm^{-3}) on the contacts, on the other hand the nanowires will be lightly doped ($\sim5\times10^{16}$ cm^{-3}) during grow to get the resistivity required by the application.

The resistivity will affect the power dissipation of the entire sensor mainly by the Joule heating effect on the nanowires, therefore must be kept under control and designed in order to not exceed the limit of comfort for a human ear skin. The final sensor is designed to work

with power on for at least two hours of race and placed into the drivers' ears with direct contact to ear skin, therefore, the device temperature during the two hours race must be acceptable for the driver ergonomics condition and avoid any kind of dermal injury.

Special considerations are given into thermal conductivity of the surface, the geometry of the contact, and the duration of the contact which all determine whether dermal injury occurs in scenarios where conduction is the primary mode of heat transfer to the skin. The necrosis of the epidermal layer starts when the temperature of the epidermal cells reaches 44°C; this constitutes the threshold of pain. The human response to pain is rapid as it attempts to distance the part of body experiencing pain from the source of the heat. However, in many instances, the heat transfer rate is fast enough to cause irreversible damage in the short duration of the contact. In the race scenario, it is not possible for the body to distance itself, because the source of heat (device) covers the ear skin and the driver cannot prevents avoidance since focused on driving and covered by the helmet. In these case the skin temperature reaches and exceeds 44°C long enough to cause second or third degree burns. Thus, the time above a certain skin temperature constitutes the heat dose and determines the degree of the injury [57].

The maximum temperature to be reached by the device is then defined conservatively as less than 40°C, moreover considering the heat dissipation that occurs through the device packaging and the moulded earpiece material (plastic) before effectively reaching the driver ear skin, the temperature actually felt by the driver would drop to more or less the ear temperature one (37°C) therefore not affecting at all the driver comfortability. With this in mind the maximum current flowing into the piezoresistors has been estimated in the next section.

The electrical power dissipated by the resistor is defined by the Joule's Law as:

$$P_E = \frac{\Delta Q}{\Delta t} = \frac{V^2}{R} \tag{7.1}$$

For the Newton's law of cooling:

$$P_T = \frac{\Delta Q}{\Delta t} = h \cdot A \cdot [T(t = 2h) - T_{env}] \tag{7.2}$$

At equilibrium the two rates must be equal as:

$$P_E = P_T \tag{7.3}$$

Therefore the maximum power dissipated is:

$$P_E = P_T \implies \frac{V^2}{R} = h \cdot A \cdot [T_{max} - T_{env}] \tag{7.4}$$

The radiative heat transfer coefficient of human body is fixed to the generally accepted whole-body value of 4.7 W/m^2 per K [159]. The surface area of the device in contact to the inner ear is calculated approximately as a cylindrical shape of the ear canal, which is 7mm of diameter and 26 mm of total length, therefore if we assume the length of the earpiece that goes deep inside the ear canal is about 10 mm, we obtain:

$$A = 2 \cdot \pi \cdot r \times L = 6.28 \cdot 0.0035 \times 0.010 = 2.199e - 4 \, m^2 \tag{7.5}$$

The maximum temperature has been set less than 40°C and the temperature of the ear canal is around 37°C. The bias voltage is set to 5 V for the device, but a single nanowire will be powered by 2.5 V due to the measurement circuit (Wheatstone bridge).

The value of the power is then:

$$P_E = \frac{V^2}{R_{tot}} = h \cdot A \cdot [T_{max} - T_{env}] = 4.7 \cdot 2.199 \cdot 10^{-4}(40 - 37) = 0.0031 \, W =$$

$$3.1 \, mW \tag{7.6}$$

The maximum total current is therefore calculated as:

159

$$I_{tot} = \frac{P_E}{V} = \frac{0.0031}{5} = 0.00062 \; A = 0.62 \; mA \qquad (7.7)$$

This is the current that would put the device into the limit temperature of 40°C, which is not desirable. This current flow will split into the three Wheatstone bridges.

Following, the value of a single nanowire resistance is calculated based on the selected light doping concentration of approximately 5×10^{16} cm^{-3}. The correspondent resistivity is 0.35 $\Omega \cdot$cm.

The electrical resistance of a piezoresistor is defined by the resistivity and piezoresistor geometry like follows:

$$R = \rho \cdot \frac{l}{w \times t} \qquad (7.8)$$

where ρ is the resistivity that depends on the doping concentration and l, w, t are respectively length, width and thickness of the piezoresistor. Estimating the ratio l/t of 50 and a nanowire width of 20 nm the resistance is easily calculated as:

$$R = 0.341 \times 10^{-2} \cdot \frac{50}{20 \times 10^{-9}} = 8525000 \; \Omega = 8.5 \; M\Omega \qquad (7.9)$$

The correspondent current flow is then:

$$I_{piezo} = \frac{V_{piezo}}{R_{piezo}} = \frac{2.5}{8525000} = 0.2932 \cdot 10^{-6} A = 0.3 \; \mu A \qquad (7.10)$$

thus,

$$I_{tot} \gg I_{piezo} \qquad (7.11)$$

I_{piezo} is three orders of magnitude smaller than the maximum total current calculated previously. Therefore, the doping concentration selected for the nanowires is a safe choice.

7.3 Experiments

The following sections will bring the reader through the mechanical properties of the material used in the experiments, and then the fabrication of the samples.

7.3.1   Materials

The material selected for the sensing element was single crystal silicon, mainly chosen for its mechanical properties (good stress tensile strength and high gage factor). Furthermore micromachining of this material allows for batch production.   Different directions are indicated with respect to crystal basis using Miller indexes. The Miller convention is summarized in the Appendix J.

In the design of piezoresistors the crystallographic orientation affects the piezoresistive sensitivity. For instance a <111> oriented piezoresistor in a (110) plane will have the highest piezoresistive sensitivity. More commonly <110> aligned piezoresistors on (100) wafers are used because of their high equal and opposite longitudinal and transverse piezoresistive coefficients.

The stiffness matrix of an orthotropic linear elastic material like silicon can be written as:

$$\underline{C} = \begin{bmatrix} C_{11} & C_{12} & C_{13} & 0 & 0 & 0 \\ C_{21} & C_{22} & C_{23} & 0 & 0 & 0 \\ C_{31} & C_{32} & C_{33} & 0 & 0 & 0 \\ 0 & 0 & 0 & C_{44} & 0 & 0 \\ 0 & 0 & 0 & 0 & C_{55} & 0 \\ 0 & 0 & 0 & 0 & 0 & C_{66} \end{bmatrix} \tag{7.12}$$

Because silicon is such an important economic material, these values have been investigated thoroughly, and the three independent stiffness coefficients of principal crystallographic orientations <100>, <010> and <001>, gives the following stiffness matrix [52]:

$$C = \begin{bmatrix} 1.66 & 0.64 & 0.64 & 0 & 0 & 0 \\ 0.64 & 1.66 & 0.64 & 0 & 0 & 0 \\ 0.64 & 0.64 & 1.66 & 0 & 0 & 0 \\ 0 & 0 & 0 & 0.80 & 0 & 0 \\ 0 & 0 & 0 & 0 & 0.80 & 0 \\ 0 & 0 & 0 & 0 & 0 & 0.80 \end{bmatrix} \cdot 10^{11} Pa \qquad (7.13)$$

To obtain Young's modulus and Poisson ratio in different directions see Appendix J for details.

The initial material used for the fabrication of the samples is a four inches p-type silicon-on-insulator (110)-oriented wafer, with 2 μm of device layer at 0.001-0.005 Ohm-cm, 1 μm of buried oxide layer and 300 μm of handle wafer at 1-20 Ohm-cm supplied by Ultrasil. The very low resistivity of the device layer has been selected in order to have Ohmic contacts for the nano-devices. Moreover, this type of oriented wafer is used in order to obtain nanowires devices on all three principal directions <111>, <110>, <100>, by simply rotating the wafer respect to the mask.

7.3.2 Fabrication

The two different approaches adopted in the fabrication process (FIB milling and bottom-up) of the silicon nanowires samples are addressed in the next sections.

FIB fabrication

Nanowires can be developed by a different approach than the conventional top-down approach by electron-beam lithography, by the use of FIB tool. The Focus Ion Beam tool allows a progressive direct milling of the material surrounding the nanowires and basically it shrinks the conventional piezoresistors into a nanoscale dimension.

This approach has been tested and the conventional piezoresistors can be enhanced by FIB tool processing. Figures 7-4 (a), (b) and (c) show the results of the processing. The structure is designed to shrink its dimension in order to have nanometre stress concentration region (NSCR).
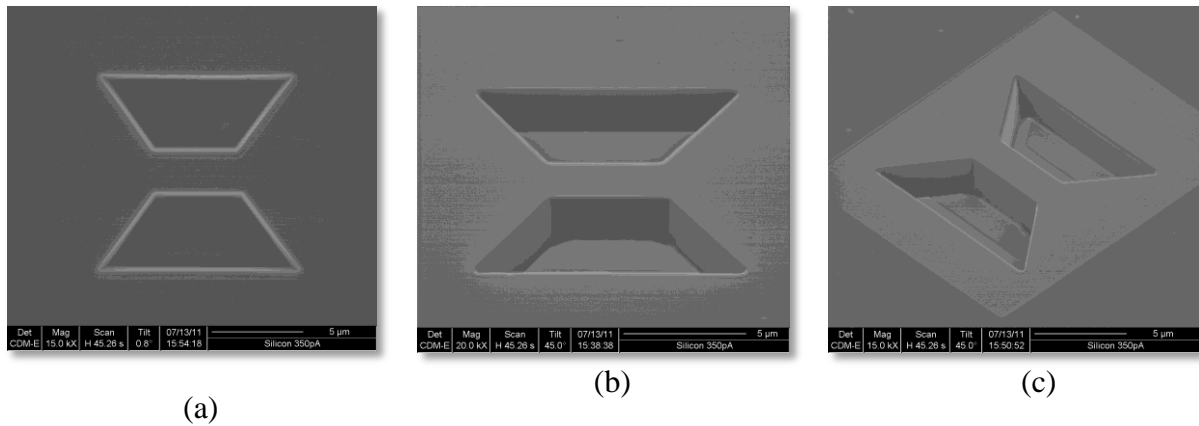
Figure 7-4. (a) FIB processing (top view). The thickness of the structure is around 1 micron. (b) FIB processing (side view). The sidewall of the structure is here visible with a thickness of around 2 microns. (c) FIB processing (isometric view). The isometric view is showing the entire stracture.

The fabrication process for obtaining the accelerometer with nanowires by FIB tool represents the last step in the processing described in Appendix F for conventional piezoresistors (see Figures F-6 and F-7).

Bottom-up sample microfabrication

The masks for this processing have been designed in previous section (see Figures 7-3 and 7-4) therefore first step is the photolithography of front side with single mask alignment, second step is DRIE of front side, third step is photolithography of back side with double mask alignment and finally DRIE etching of back side to release the samples.

Front side processing

For the first step, the lamp used has a 5.4 mW/cm^2 intensity, the photoresist adopted (S1818) has been distributed on the surface evenly by a spinning machine already programmed for the job (1.8μm thickness), after on the wafer has been pre-baked on a hot plate for 90 seconds. In order to stick properly the photoresist on the wafer surface the chemical hexamethyldisilazane (HMDS) has been used for 20 minutes before using the spin coating machine.

The first run of exposure was set to 22 seconds and the development time (developer AZ326 TMAH) to only 20 seconds, but due to the low profile of photolithography obtained the wafer has been cleaned up from the photoresist for reuse by acetone first and then isopropanol, finally on the hot plate for 1-2 minutes. Figure 7-5 (a) and (b) shows the gap between two contacts. Obviously as shown in the figures the development process didn't effectively remove the photoresist in between due to the low exposure time.

(a)   (b)
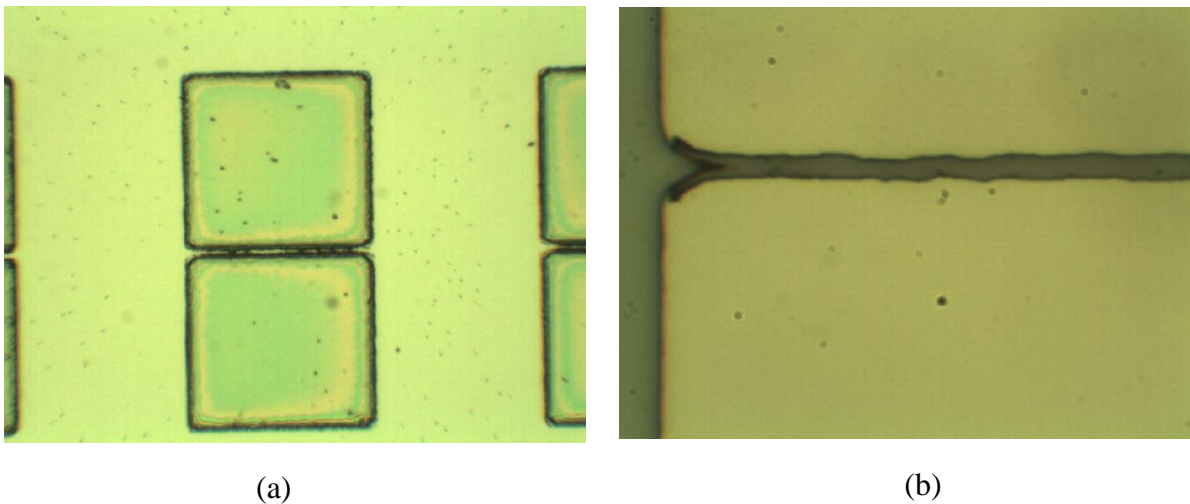
Figure 7-5. (a) Pair of contacts. The contacts shown in the picture are not completely separated. (b) Zoom on the gap between contacts not completely separated.

In the second run the hot plate time has been increased to 3 minutes and the exposure time has been increased to 27 seconds. In this case the development time was 20 seconds and then the microscopy check was undertaken, plus 5 seconds of development and checked again, another 5 seconds and checked again and then the plasma etching has been used at 12 W for 3 minutes to remove the unwanted photoresist on the surface by O_2. Since the results was not satisfactory due to debris between the contacts, other 10 seconds of development were added plus a total of 10 minutes (5 + 5 minutes) of plasma etching at 20 W is used. Finally the silicon wafer is ready for the DRIE etching. The Figure 7-6 (a) and (b) shows the final result. As it can be seen the two contacts are completely separated one another by 3 µm gap, ensuring after the DRIE etching a completely electrically isolated contacts.

(a)   (b)
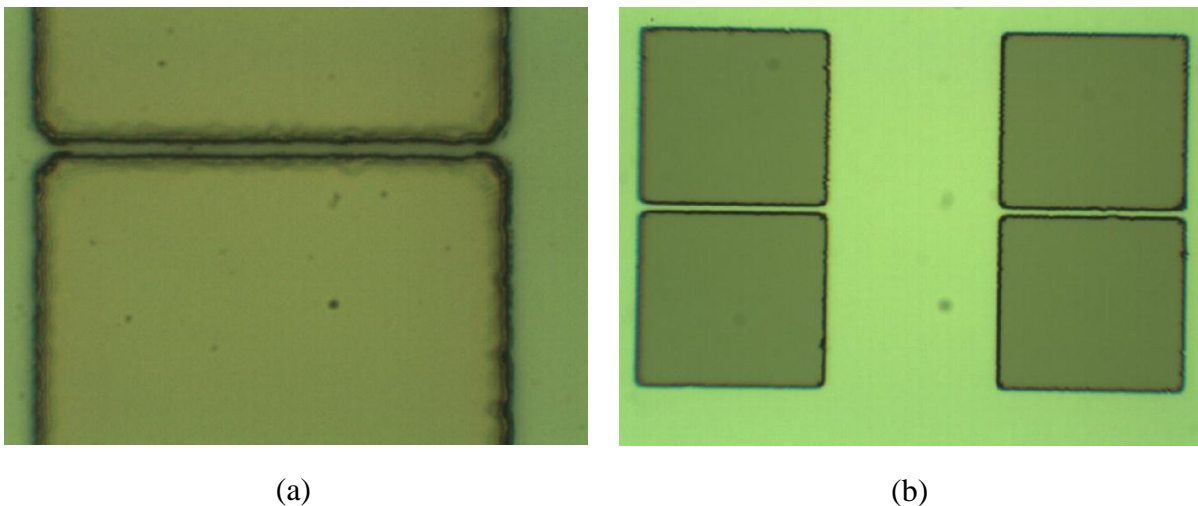
Figure 7-6. (a) Gap between contacts. As it can be seen from the image the gap is completely separated. (b) Two pairs of contacts perfectly separated.

First of all a test has been undertaken by loading a dummy wafer on the DRIE chamber, with 13 seconds of etching and 8 seconds of passivation cycle. All the checks of the machine were made to check that: i) the "fingers" that keep the wafer loaded were in the right location inside the chamber, ii) the chamber lid temperature was ofaround 45°C, iii) the cooler

temperature was ofaround 20°C, iv) the pressure was ofaround 0 mTorr. After all checks have been made the recipe for the test is loaded for processing (YASKAWA4.SET) with bias power of 15 W which is a deep standard process. Once the process is activated is required to check that the helium leakage is around 5-10 mT/min and then resume the processing. During the processing all the values obtained should match the values as set in the recipe. Another check to be made was to check in the chamber that the colour of the plasma was purple. Before to unload the wafer last check was to see that there is no plasma in the chamber, then unload.

After the DRIE test has been run, the machine was ready to process the wafer using a shallow recipe with 7 seconds of etching and 5 seconds of passivation cycle, the bias power is 12 W. The etching speed was between 1.8 μm per minutes to 2.2 μm per minutes, therefore 3 minutes were more than sufficient to etch 2 μm of the wafer device layer. In order to avoid a passivation layer at the end of the processing the machine processing was interrupted at the end of an etching cycle before passivation. During the processing some cycle were skipped and finally the chamber was unloaded.

At the end of the DRIE processing the thickness has been measured to be between 4.18 μm to 4.22 μm, which was reasonable considering a 1.5-1.8 μm of resist thickness.

Finally in order to clean up the surface from debris the wafer was subjected to O_2 in the chamber. Therefore the recipe was changed to O_2 skin for 2 minutes. The resist was then completely removed and the thickness obtained was of around 2.4 μm, close to the actual thickness of the device layer (2 μm), therefore the etching was successful.

Back side processing

Following the processing of the wafer front side, the processing on the back side is carried out. First of all the wafer back side was placed on the hot plate with a temperature of 93℃ for 2-3 minutes in order to dry completely. The programme of the spin coater was set to programme 16 (2000 rpm for 90 sec.). Before coating the wafer back side with photoresist, the surface and the edges were cleaned thoroughly by acetone firstly and then with isopropanol. Then two steps were used for coating the back side surface for a total of 20 μm of photoresist (AZ4562): spinning first to form 10 μm of photoresist and then 2 mins on the heater, then adding photoresist and spinning again, finally on the heater for 4-5 minutes.

After the coating of photoresist the surface was ready for photolithography on the double sided mask aligner (MJB21). This machine for cooling is using just a fun, differently from the single mask aligner (MA56) that is using nitrogen gas. First of all the two masks were placed in the machine, front mask on the bottom and back mask on the top with the chrome sides facing together. The masks were then centralized by rotation and translation and the distance of the masks was set based on the wafer thickness plus the photoresist thickness (300 μm handle wafer + 1 μm BOX + 2 μm device layer + 20 μm photoreisist = 323 μm). After coarse alignment process of the mask on the top to the mask on the bottom (mask adjustment by eyes) the alignment marks were aligned using the microscope and after releasing the mask adjustment button the fixing of the wafer can start. Next fine adjustment of the masks relatively to the wafer is carried out and the gap between the masks was introduced.

Finally the exposure was set to 1 minute with a lamp of intensity of 13.2 mW/cm^2, of course only the lamp on the top side is used since the bottom side of the wafer has been already exposed by a single sided mask aligner. After exposure the wafer was immerged in the developer solution made up of 50 ml of developer (AZ400) and 3.5 times of water (175 ml)

for 2.5 minutes and then the wafer was washed under water; finally the wafer was immerged again in the developer for another 1.5 minutes. The wafer was then checked by microscope for photoresist residue and photoresist thickness measure (27.8 µm – 28.5 µm). Since the results were good the wafer back side is ready for DRIE etching (Figure 7-7).
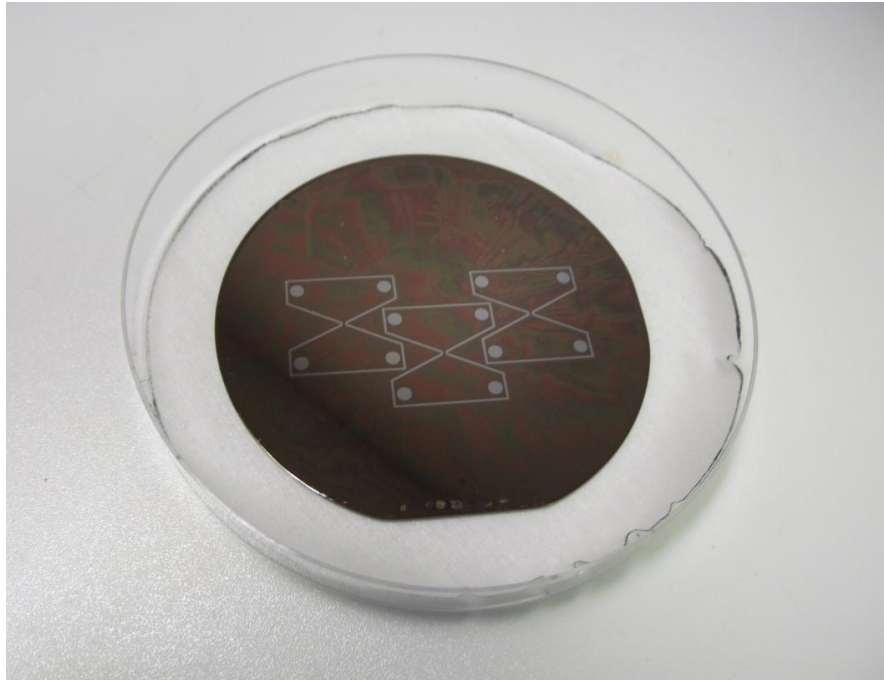
Figure 7-7. Back side ready for DRIE. Three samples are designed in a single wafer in order to efficiently exploit the available space of 3 inches.

The DRIE etching was then run for 60 minutes, where 80 microns of silicon were etched. Prior to the etching, the wafer was put in a hotplate at 90°C for 3 minutes to post-bake the resist. Next step was to put the wafer on a backing wafer (silicon wafer with one side of platinum) before completing the etching in order to better control the deep etching of the wafer and release the samples.

To backup the wafer, the wafer with the samples was firstly coated with photoresist (AZ4562) in order to stick the two wafers together. The spinning acceleration time was set to 3 minutes, the spinning time to 60 seconds, the spin speed to 1000 rpm and the deceleration time to 6.6 minutes. After the spinning the wafer was dried on the heater at 90°C for 5

minutes using pieces of glass to avoid contact to the heater. Then the backing wafer was coated by using the same resist on the wafer side without platinum and then spin it with acceleration time 3 minutes, spin time 15 seconds, spin speed 3000 rpm and deceleration time 6.6 minutes. Finally the backing wafer was put on the heater and immediately afterwards the other wafer with the samples was placed on top of it, from the device side, for a couple of minutes. Now that the two wafers were bonded together the next step can be carried out.

The final step was to etch completely the wafer till releasing the samples. Again the recipe was YASKAWA4.SET for a standard deep etching; the process time was set to two hours. In two hours of processing a total of around 260 µm of etch depth plus photoresist thickness was obtained. Since in the previous DRIE processing 103 µm of etch depth plus photoresist was obtained, this means that 160 µm were etched in 120 minutes, therefore the etch rate was 1.33 µm per minute. 50-60 µm were left to etch in order to release the samples therefore, given the etch rate, 45 minutes of DRIE etching were remained (see Figure 7-8 (a) and (b)). The processing was set to one hour and stopped when the etching was complete. To clean up the surface an oxygen skin recipe was then loaded for 3 minutes.

| (a) | (b) |
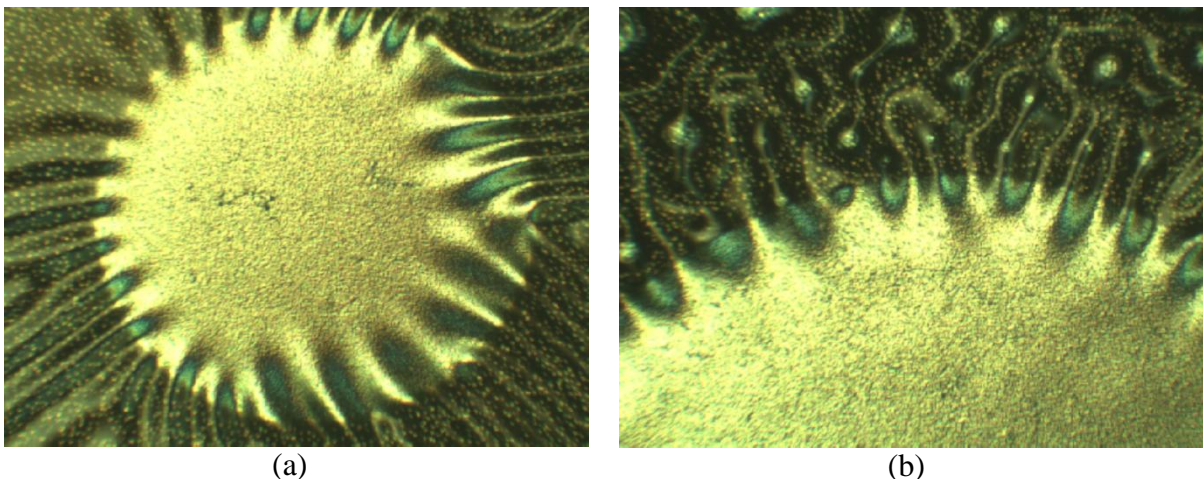
Figure 7-8. (a) Complete DRIE etching of a hole. The white color in the hole shows that the etching has reached the BOX. (b) The dark colour is the photoresist that remained after the DRIE etching.

Once the oxygen skin was stopped the wafer was unloaded from the ICP chamber. After a microscopy check the samples edges were cut with a cutter in order to allow the acetone to clean properly the SiO_2 gaps. Finally the wafer was put into acetone overnight in order to release the sample structures (Figure 7-9(a)).

The final result presents a misalignment of few microns (Figure 7-9 (b)).
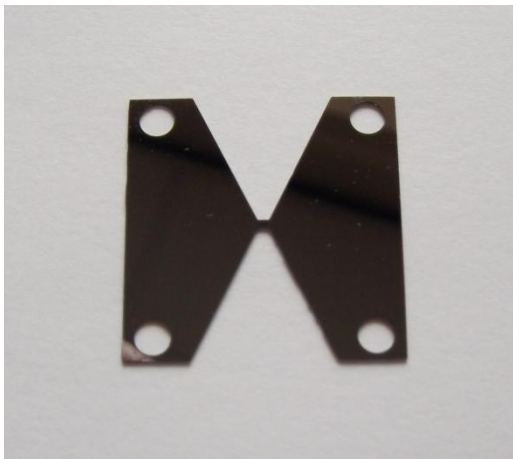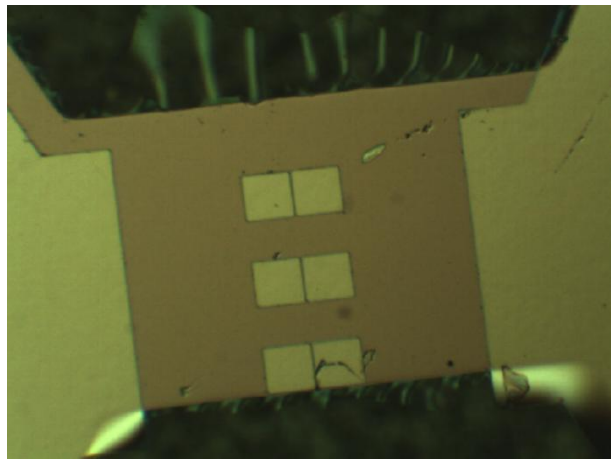
(a)   (b)

Figure 7-9. (a) Final released sample structure. (b) Misalignment of the central region with the contacts.

Nanowire growth

The nanowires were grown by Vapor-Liquid-Solid (VLS) synthesis using gold nanoparticles as metal catalyst and Silane mixture (2% SiH_4 in 98% He) as Si precursor at 100sccm, moreover they were grown in the <111> direction. The VSL is a 1D crystal growth that is assisted by a metal catalyst. This mechanism was suggested for wider use in the silicon industry by Wagner [153]. Figure 7-10 shows a schematic of the VLS mechanism where the metal catalyst forms liquid alloy droplets at high temperature by absorbing vapour components. The alloy is further supersaturated due to temperature or vapour pressure fluctuation. Basically the solution becomes with an actual components concentration higher

than the equilibrium concentration. Therefore it drives the precipitation of the component at the liquid-solid interface and the 1D crystal growth begins till the vapour components are supplied. The diameter and position of the 1D structure depends on the catalyst size and position [154]. The mechanism works at high temperature at which the metal catalyst forms a liquid alloy. In our chemical processing we used chemical vapour deposition (CVD) in conjunction with the mechanism.
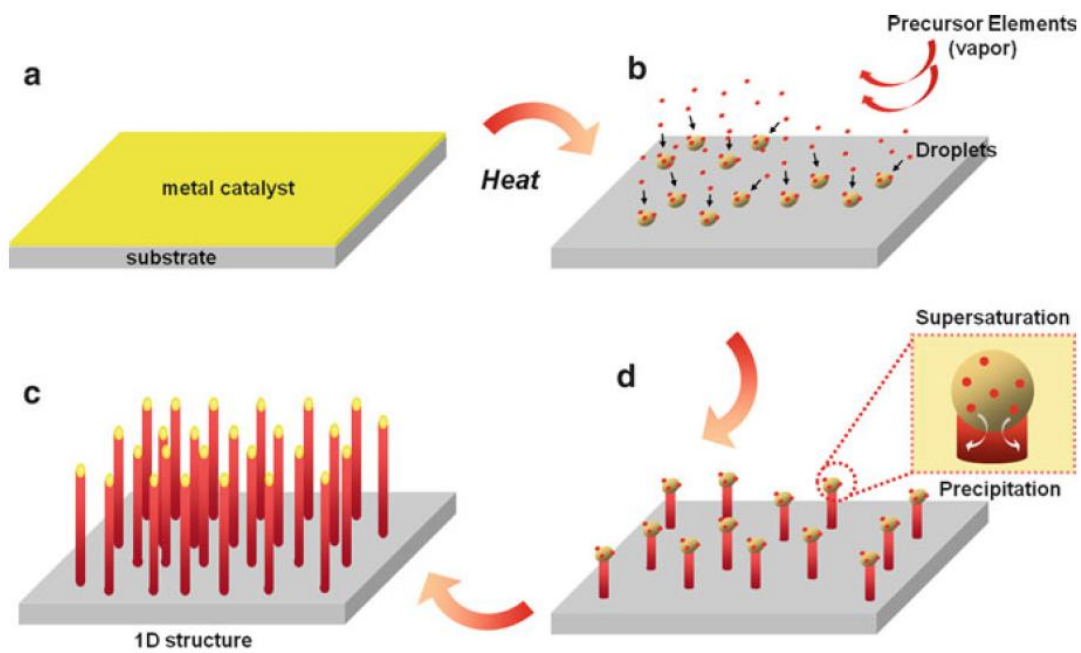
Figure 7-10. Growth of 1D structures by VLS mechanism [154]. (a) Metal catalyst thin-film deposition of Au catalyst by sputtering, (b) liquid alloy droplets formed by the metal catalyst by absorbing vapour components, (c-d) the alloy is supersaturated and precipitates at the liquid-solid interface growing the 1D structure.

To grow the nanowires between two of the three pairs of contacts (see Figure 7-9(b)), sample were firstly coated with photoresist. Three layers of resist were applied to the sample surface of a total of 3-5 µm; first layer was of 500 µm of AR30012 and AZ5214 with ratio 1:1, second and third layer were made up of only resist AZ5214. The spin coater was set to 35 sec. at 3000 rpm and after coating the sample was placed on hot plate at 100°C for one minute except after the last layer of coating where the sample was placed on hot plate at

100°C for 2 minutes. At the end of resist coating of the sample a microscopy check followed in order to verify the resist coating on the sample. Once the presents of resist on the sample has been ascertain the resist is ready to be patterned by laser in order to open windows for the gold deposition. Five windows were opened for each contact of 2×2μm in order to have more probability of success in the growing process (see Figure 7-10 (a) and (b)).

After laser pattering the sample was immersed in the developer solution AZ726 for 40 seconds and then the microscopy check was carried out. Since the windows were not completely opened the sample was developed for a total of 1 minute and 25 seconds. Once we were satisfied with the development the next step was to immerse the sample in HF for removing the native silicon oxide. The sample was then ready for gold deposition by sputtering with 50 W power for 3 seconds in order to deposit 5 nm thick gold film. To clean up the sample from the resist and leave only the gold on the patterned windows, lift off was carried out by immersing the sample in acetone and then in HF again. Finally the sample was ready for 2 hours of CVD process at high temperature (530°C) and partial pressure of 3 mbar in order to activate the VLS synthesis and then to allow the nanowires growing. As it can be seen in Figure 7-11(a) and (b) the nanowires growth in the five windows patterned by laser.
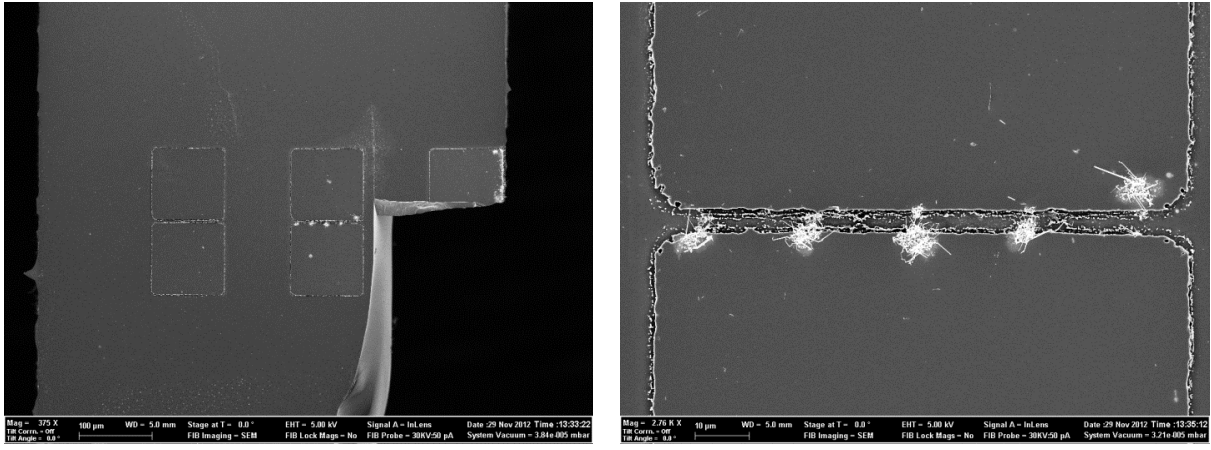
Figure 7-11. (a) Pairs of contacts with nanowires grown between them, see contacts in the middle. As it can be seen five different positions are chosen in contact gap to grow the nanowires. The sample broke during handling. (b) Five windows were opened in the contact gap and the nanowires grown in between.

7.4 Results and discussion

7.4.1 Focus Ion beams experiment results

When ion beam milling, the trench edges will generally not be sharp edged; using lower beam currents can reduce the effects. The degree is also influenced by the material being milled. See the two images 7-12(a) and (b) of a milled pattern in silicon.

(a)   (b)
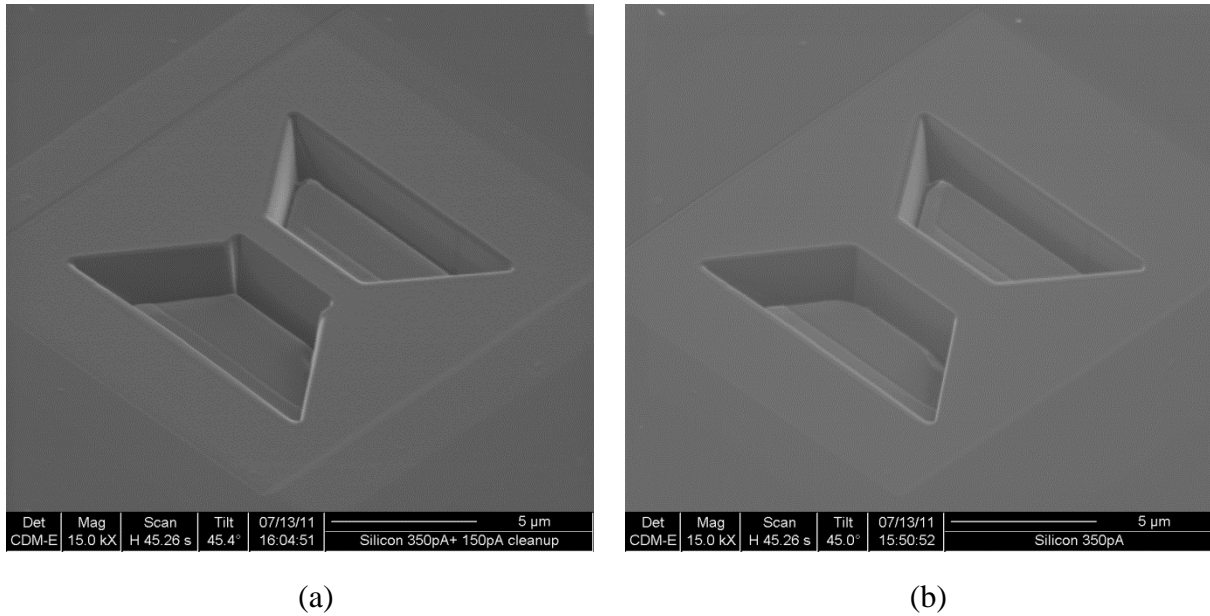
Figure 7-12. (a) Ion beam milling with higher current. (b) Ion beam milling with lower current. As it can be seen the trench edges were more sharp using lower beam current.

This is usually not a problem unless preparing transmission electron microscopy (TEM) thin sections or samples with thin or multiple layers on the surface. In both these instances it is enough to deposit a layer of platinum as a sacrificial layer over the site of interest, protecting the sample from milling damage and transferring any milling damage to the platinum layer.

In this case where the sensitive surface is a thin doped layer acting as a resistance, use of platinum is not possible. However some polymeric materials exhibit good resistance to the ion beam, and also mill cleanly, and it may be possible to use these instead.

The achievable line width on the present system would however seem to be about 100nm (Figure 7-13). This is constrained by the imaging resolution of the machine (50nm); the accuracy of the positioning of the milling pattern (drift due to sample charging); and the patterning parameters (essentially fixed on the current system). More modern systems which allow programming of the beam patterning (bit mapping) may allow better control of the milling [71].

The Figure 7-13 shows the best milling achieved. Note the top edge "rounding" and that the wall thickness is approx. three times the thickness of the measured (122 nm) undamaged top surface.
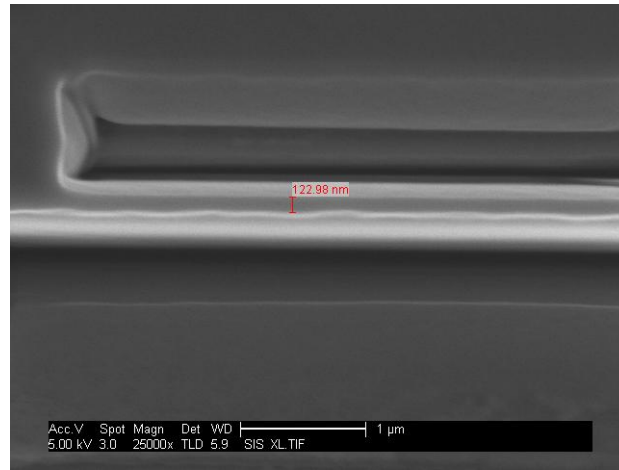
Figure 7-13. Best milling achieved. The maximum width achievable with the FIB is of around 100 manometers.

7.4.2 Nanowire growth experiment results

Few nanowires were able to actually create a bridge structure between the two contacts (see Figure 7-14). The main reason for that is related to the short gap width (3 µm) between contacts determining deposition of gold on both sidewalls and not on one side only as expected. Therefore the nanowires grow on both sides of the contacts and interfere with each other during the growth, allowing few nanowires to complete the growth in one direction (see Figure 7-14).

(a)   (b)
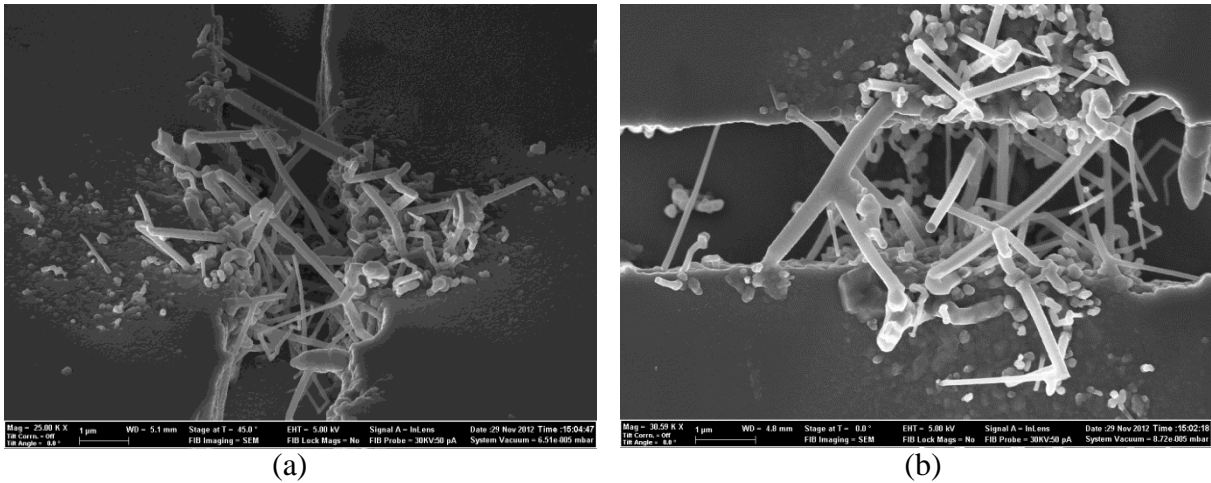
Figure 7-14. (a) Nanowires grown on both sides of the gap due to the short gap width that do not allow deposition of the gold on one side only. Therefore the nanowires grown from both sidewalls of the gap width interfering with each other during growth. (b) Due to the nanowires growth from both sidewalls only few nanowires are able to form a bridge structure.

As can be seen in Figure 7-15 the nanowire creates a bridge by crossing the entire gap width and then sticking on the opposite sidewall, finally forming a solid structure able to withstand high strain.
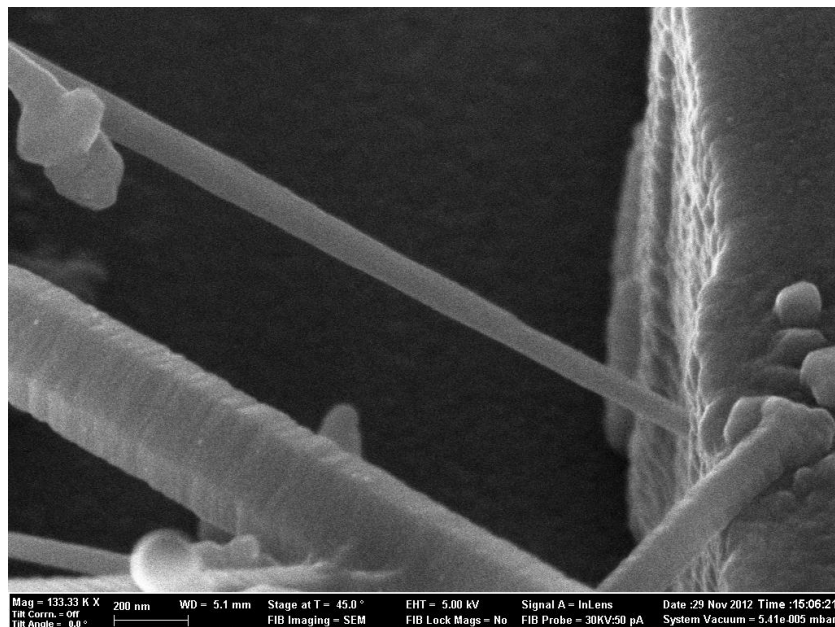
Figure 7-15. The nanowire grows and sticks on the opposite sidewall and finally forming a solid bridge structure that withstands high strain.

The length of the two nanowires structure visible in Figure 7-16 is of 2.10µm which is less than the gap width. This means that the gap initially designed as 3 µm width is actually shorter after the DRIE etching.
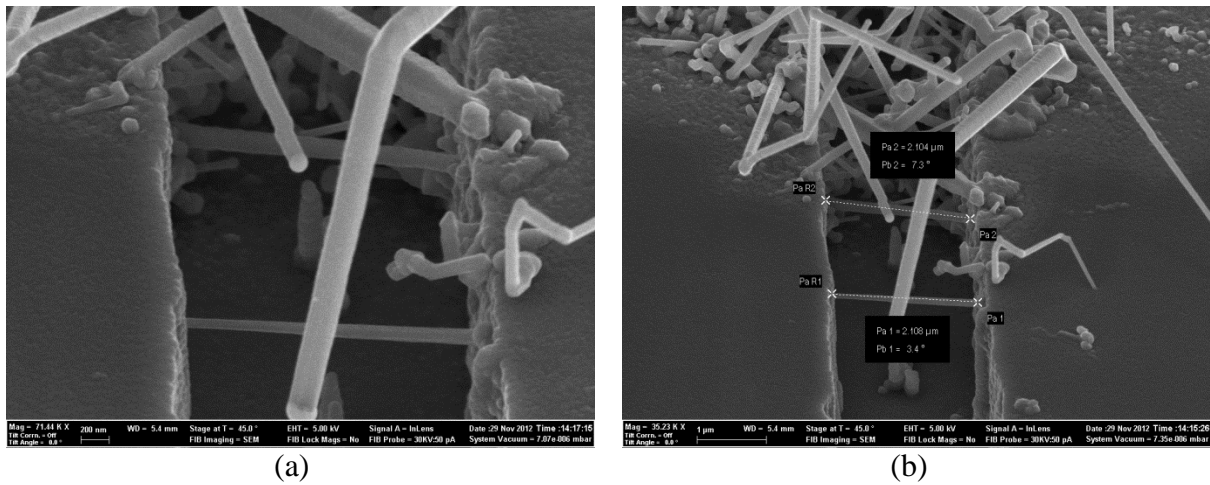
Figure 7-16. (a) Nanowires bridge structures between contacts gap. (b) The length of the two nanowires is of 2.10 µm which is smaller than the designed gap (3 µm).

The two nanowires bridges structures have diameter that changes during growth. The nanowire on the top in Figure 7-17 is 148.5 nm wide at the beginning and 128.2 nm at the end, on the other side of the gap. The second nanowire on the bottom is 106.7 nm wide at the beginning and 65.62 nm at the end (see Figure 7-17)).
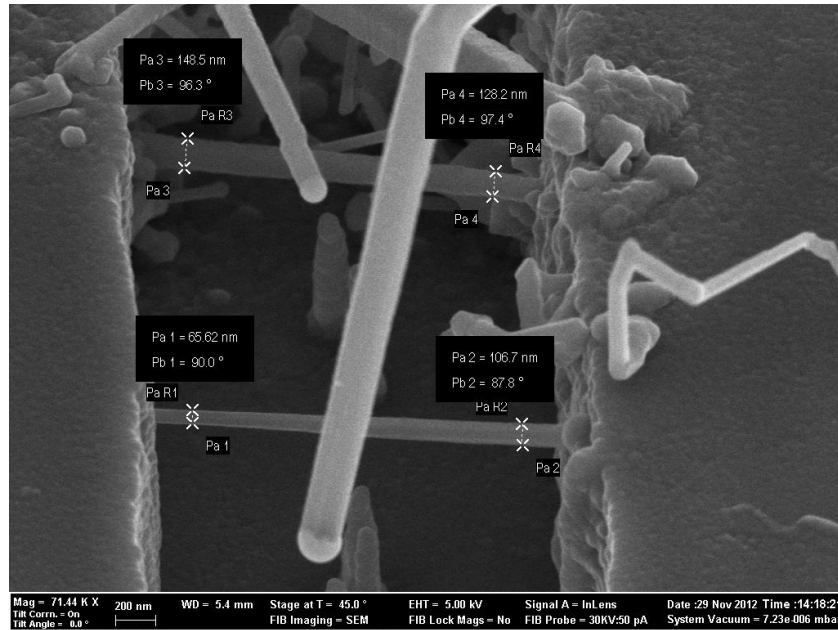
Figure 7-17. Two nanowires bridge structures. The nanowire width reduces during grow due to the change in size of the gold droplet.

A third nanowire was found creating a bridge structure but the direction of growth was not the <111> direction (see Figure 7-18). As it can be seen in the figure the nanowire did not grow straight from the sidewall. This nanowire starts growing 112.3 nm wide and then completes the growth on the other side of the gap 73.8 nm wide. Again the nanowire size changes during growth mainly because of the changes in the gold droplet size.
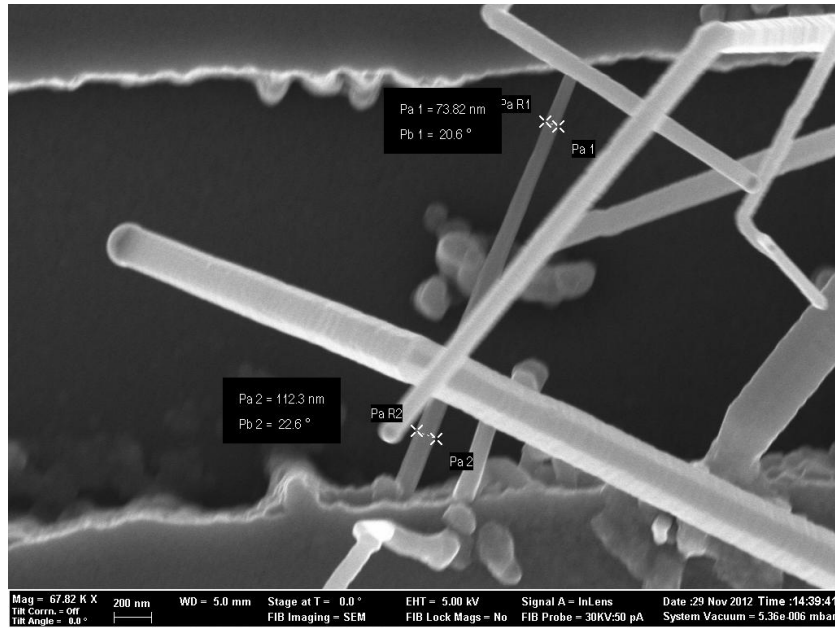
Figure 7-18. Nanowire bridge structure starting 112.3 nm wide and ending 73.8 nm wide in a direction different from <111>.

7.5 Conclusion

The feasibility study was undertaken to fabricate nanowires for piezoresistors using FIB tool and CVD process Nanowires of around 100 nanometers were successfully fabricated by both type of processes. To improve the FIB work results a deposition of a layer of platinum as a sacrificial layer over the site of interest is recommended, in order to protect the sample from milling damage and transfer the damage to the platinum layer. Regarding the results obtained by growth is it recommended to increase the gap width from 3 to 5 µm in order to avoid the overlapping growth of nanowires observed that limits the number of nanowires able to form a bridge.

In future work it would be possible to grow nanowires with reduced diameter by reducing the thickness of the gold sputtered on top surface of the device. This work represents a first step for future electromechanical characterization and testing of the silicon nanowires in order to ascertain their piezoresistive effect.

Chapter 8

8   CONCLUSION AND FUTURE WORK

The aim of this study was to advance the current state-of-art accelerometer design and optimization methodology by developing a novel accelerometer capable to measure head acceleration in case of an accident. The novel and enhanced accelerometer design has been developed, extensive finite element modelling and optimization has been conducted. Nine different shapes were studied with common feature of having highly symmetric mechanical structure. After the shape design, possible candidates have been selected for the final structure, and then the size optimization has been undertaken taking into account the packaging size (design for packaging). Two best microstructures were then selected and finally a design for manufacturing approach adjusted the device size accordingly. In the end of this first optimization process (DOE) overload end stops were introduced in the design. Silicon nanowires were also evaluated during the simulation of the earplug accelerometer, where both mechanical and electrical performance were analysed. Comparison of results between conventional microscale and nanoscale piezoresistors (nanowires) was performed showing that the nominal sensor sensitivity using nanowires is overall increased by more than 30 times.

The optimization of the device mechanical structure and the measurement circuit was further developed based on a mechanical principle that intended to extra enhance the electrical and mechanical performance of the accelerometer under study. The mechanical principle studied the influence of variation in the mass moment of inertia of the device proof mass by an optimization approach that progressively changed the beams and proof mass geometry in two steps of evolution. Two main different types of beams geometry were studied, i.e. curved and straight beams, and the proof mass changes from square geometry to octagonal geometry and then to circular geometry. The study highlights the potential of two different devices, one is with octagonal proof mass with curved beams and the other one is with circular proof mass with straight beams. The measurement circuits of this two types of devices were also compared and an enhanced geometry and correspondent measurement circuit was finally proposed as optimal device for the application studied (earplug accelerometer). The fabrication of the device is also further investigated by the development of the layout design and metallization. The analysis demonstrated that even mass moment of inertia not always improve measurement accuracy, but it dependent on the measurement circuit, the level of sensitivity of the sensing element (conventional vs. nanoscale piezoresistors) and on the beams geometry (straight or curved). The proposed optimal design, thanks to the mechanical principle that has led the optimization process, presents higher sensitivity and lower cross-sensitivity respect to the state-of-art design. For the first time during the optimization approach we are observing a progressively increment of the sensitivity and reduction of the cross-sensitivity.

The optimized design allows for an extreme miniaturization, a size of 2×2 mm is achieved through the implementation of current fabrication process and packaging technology even if with some fabrication issues and limitations (see Appendix F). Moreover the resolution that expresses the precision of the sensor response (minimum detectable acceleration that depends

181

on the noise level) has been improved respect to the initial performance specifications by one order of magnitude. The accuracy target has been also improved with a maximal total error less than 1% (cross-talk and nonlinearity).

Experimental work was also undertaken in order to ascertain our on capability of silicon nanowires fabrication. Nanowires have been fabricated by FIB tool and VLS process, demonstrating the feasibility of the fabrication process. Further work would be the metallization of the fabricated samples for characterization and testing purpose with the recommendation of increasing the contacts gap from 3 microns to 5 microns in order to avoid overlapping of silicon nanowires during the growth. Moreover the characterization and testing of nanodevice samples applying oscillating stress would ascertain the existence of the "Giant effect" on bottom-up silicon nanowires.

Figure 8-1 shows the developed experimental study for future work with the objective of acquiring new knowledge related to the "Giant piezoresistance effect" by characterization and testing of the fabricated bottom-up silicon nanowires. Moreover the results obtained would allow fabricating for the first time the designed novel accelerometer with bottom-up silicon nanowires.

Characterisation

Design and Fabrication of
Test-Chip

Data Collection & Analysis

Design and Fabrication of novel
Accelerometer
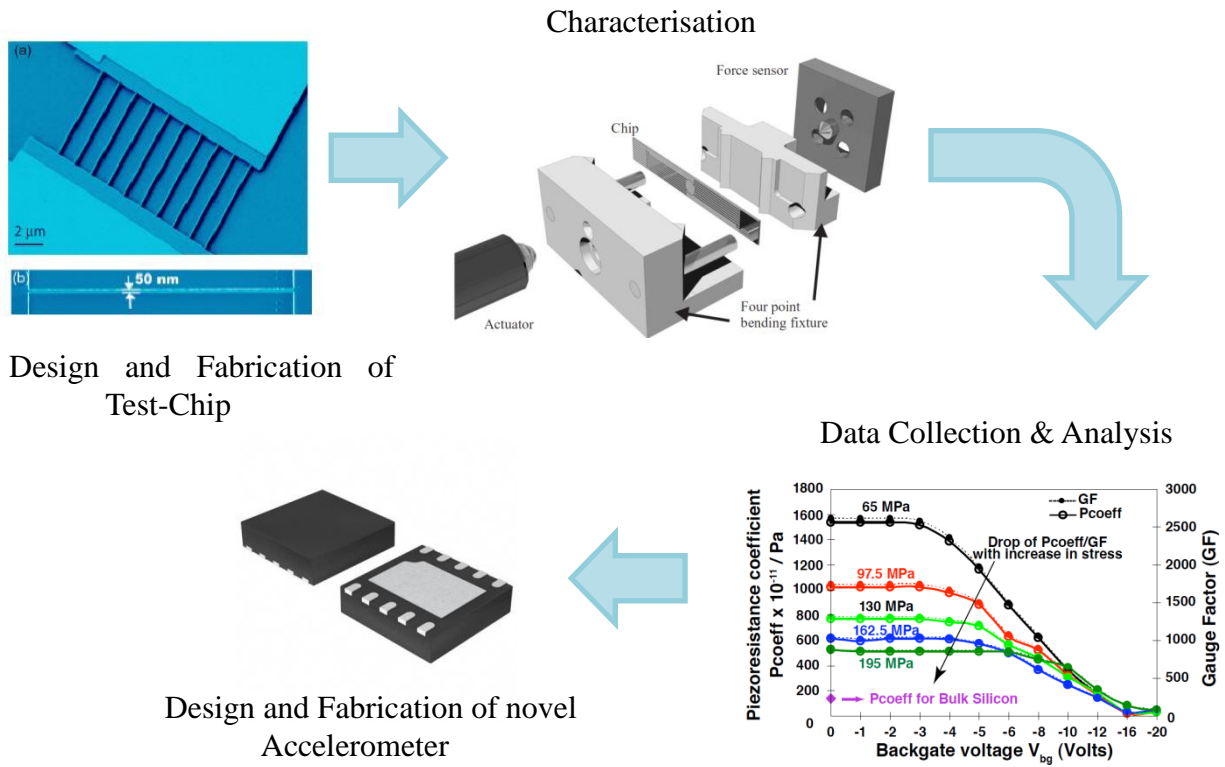
Figure 8-1. Diagram of the methodology adopted to address the first research aim. Notice that this work addresses only the first step of the research methodology that is the design and fabrication of test-chips in order to study the feasibility of sensor fabrication.

REFERENCES

[1] C. T. Huang, C. L. Hsin, K. W. Huang, C. Y. Lee, P. H. Yeh, U. S. Chen, and L. J. Chen, *Applied Physics Letters*, vol. 91, pp. 093133, 2007.

[2] D. V. Dao, T. Toriyama, and S. Sugiyama, "Noise and frequency analyses of a miniaturized 3-DOF accelerometer utilizing silicon nanowire piezoresistors," *IEEE*, vol. 3, pp. 1464–1467, 2004.

[3] R. He and P. Yang, "Giant piezoresistance effect in silicon nanowires," *Nat. Nano*, vol. 1, pp. 42–46, 2006.

[4] K. Reck, J. Richter, O. Hansen, and E. V. Thomsen, *"Piezoresistive effect in top-down fabricated silicon nanowires,"* in *MEMS 2008. IEEE 21st International Conference on Micro Electro Mechanical Systems*, 2008, pp. 717–720.

[5] T. Barwicz, L. Klein, S. J. Koester and H. Hamann , "Silicon nanowire piezoresistance: Impact of surface crystallographic Orientation," *Applied Physics Letters* , vol. 97, 2010.

[6] D. V. Dao, K. Nakamura, T. T. Bui and S. Sugiyama, "Micro/nano-mechanical sensors and actuators based on SOI-MEMS technology," *Advances in Natural Sciences: Nanoscience and Nanotechnology*, 2010.

[7] V. Passi, F. Ravaux, E. Dubois, J.-P. Raskin , "Backgate bias and stress level impact on giant piezoresistance effect in Thin silicon films and nanowires," in *IEEE MEMS 2010*, 2010, pp. 464 – 467.

[8] M. L. Lee, E. A. Fitzgerald, M. T. Bulsara, M. T. Currie and A. Lochtefeld, "Strained Si, SiGe and Ge channels for high-mobility metal-oxide–semiconductor field-effect transistors," *J. Appl. Phys.,* vol. 97, pp. 011101, 2005.

[9] B. M. Haugerud, L. A. Bosworth and R. E. Belford, "Mechanically induced strain enhancement of metal-oxide–semiconductor field-effect transistors," *J. Appl. Phys.*, vol. 94, pp. 4102–4107, 2003.

[10] L. J. Chen, "Silicon nanowires: the key building block for future electronic devices," *J. of Materials Chemistry*, vol. 17, pp. 4639–4643, 2007.

[11] S. Sasaki, T. Seki, K. Imanaka, M. Kimita, T. Toriyama, T. Miyano, and S. Sugiyama "Batteryless-Wireless MEMS Sensor System with a 3D Loop Antenna," in *Conference Proceeding at 6th Annual IEEE Conference on Sensors*, 2007.

[12] K. Nakamura, Y. Isono, and T. Toriyama, "First-Principles Study on Piezoresistance Effect in Silicon Nanowires," *Jpn. J. Appl. Phys.*, vol. 47, no. 6, pp. 5132–5138, 2008.

[13] A. Okamura, D. V. Dao, T. Toriyama and S. Sugiyama, "Fabrication of an Ultra Small Accelerometer Utilizing Si Nanowire Piezoresistors," in *Proceeding of the 22nd Sensor Symposium*, 2005, pp. 203-206.

[14] A. Sakai, D. V. Dao, A. Okamura, S. Sugiyama, "Fabrication of an Ultra Small 3-DOF Accelerometer Utilizing Small External Influence Structure and Si Nanoscale Piezoresistors," in *Proceeding of the 23rd Sensor Symposium*, 2006, pp. 270-273.

[15] V. R. Hodgson "Biomechanical study of football head impacts using a human head model: a final report prepared for NOCSAE". Overland Park, KS: NOCSAE, 1973.

[16] T. J. Myers, N. Yoganandan, A. Jr. Sances, F. A. Pintar, J. Reinartz, J. H. Battocletti, "Energy absorption characteristics of football helmets under low and high rates of loading," *Biomed. Mater. Eng.*, vol. 3, pp. 15-24, 1993.

[17] P. J. Bishop, R. W. Norman, M. Pierrynowski, J. Kozey, "The ice hockey helmet: how effective is it?," *Physician Sportsmed*, vol. 7, no. 2, pp. 97-106, 1979.

[18] E. S. Gurdjian, V. L. Roberts, L. M. Thomas, "Tolerance curves of acceleration and intracranial pressure and protective index in experimental head injury," *J. Trauma*, vol. 6, pp. 600-604, 1996.

[19] P. J. Bishop, R. W. Norman, R. Wells, D. Ranney, B. Sleryk, "Changes in the center of mass and moment of inertia of head form induced by a hockey helmet and face shield," *J. Appl. Sport Sci.*, vol. 8, pp. 19-25, 1983.

[20] P. J. Bishop, "Dynamic response criteria for ice hockey helmet design," in *Komi P.*, Ed. Biomechanics. vol. V-B. Baltimore, MD: University Park Press, 1976, pp. 299-305.

[21] R. Naunheim, A. Ryden, J. Standeven, "Does soccer headgear attenuate the impact when heading a soccer ball?," *Acad. Emerg. Med.*, vol. 10, pp. 85-90, 2003.

[22] L. M. Lewis, R. S. Naunheim, C. J. Richter, J. W. Standeven, "Are helmets protective in high impact collisions?," *Acad. Emerg. Med.,* vol. 7, pp. 437, 2000.

[23] L. M. Lewis, R. S. Naunheim, J. Standeven, C. Lauryssen, C. Richter, B. Jeffords, "Do football helmets reduce acceleration of impact in blunt head injuries?," *Acad. Emerg. Med.*, vol. 8, pp. 604-609, 2001.

[24] E. S. Gurdjian, H. R. Lissner, F. G. Evans, L. M. Patrick, W. G. Hardy, "Intracranial pressure and acceleration accompanying head impacts in human cadavers," *Surg. Gynecol. Obstet.,* vol. 113, pp. 185-190, 1961.

[25] M. Higgins, P. D. Halstead, L. Snyder-Mackler, D. Barlow, "Measurement of impact acceleration: mouthpiece accelerometer versus helmet accelerometer," *J. Athl. Train.* vol. 42, no. 1, pp. 5-10, 2007.

[26]   T. Knox, "Validation of earplug accelerometers as a means of measuring head motion," presented at the 2004 SAE Motorsport engineering Conference and Exhibition, Dearborn, Mi., 2004.

[27]   O. E. Stephen, T. Knox, C. A. Kelly, "The development of a method to measure head acceleration and motion in high-impact crashes," *Neurosurgery,* vol. 54, pp. 672-677, 2004.

[28]   G. D. N. Legg. (2003). *Gear for the ear* [Online]. Available: http://www.designnews.com/article/1088-MEMS_Sensors_Rev_Their_Engines.php?text=mems+accelerometers+bruce+natvig

[29]   P. C. Begeman, M. W. John, T. B. Tara, A. Mellor, "Frequency Response and Coupling of Earpiece Accelerometers in the Human Head," in Motorsports Engineering Conference and Exhibition, December 2006, © SAE International.

[30]   R. S. Salzar, B. R. 'Dale' Cameron, P. A. Joseph, "Improving Earpiece Accelerometer Coupling to the Head," *SAE Int. J. of Passenger Cars- Mechanical Syst.,* vol. 1, no. 1, pp. 1367-1381. 2009.

[31]   T. Knox, P. Joseph, P. Chris, J. Plaga and J. Bonfeld, "New Sensors to Track Head Acceleration during Possible Injurious Events," *SAE Int. J. of Passenger Cars - Electronic and Electrical Syst.*, vol. 1, no. 1, pp. 652-663, April 2009.

[32]   J. S. Wilson and Knovel, *Sensor technology handbook*, Elsevier, Amsterdam; Boston, 2005.

[33]   PCB Piezotronics. (2009). *Introduction to piezoelectric accelerometer* [Online]. Available: http://www.pcb.com/techsupport/tech_accel.

[34]   Honeywell Sensotec. (2003). *Frequently Asked Questions* [Online]. Available: http://www.alliantech.com/pdf/technique/questions_courantes_capteurs.pdf

[35] SENSR. (2010). *Practical guide to Accelerometers* [Online]. Available: http://www.sensr.com/pdf/practical-guide-to-accelerometers.pdf

[36] P. J. French and P. M. Sarro, "Surface versus bulk micromachining: the contest for suitable applications," *J. Micromech. Microeng.*, vol. 8, pp. 45–53, 1998.

[37] Endevco Corporation (2009). [Online]. Available at: http://www.endevco.com/.

[38] L. M. Roylance, "A miniature integrated circuit accelerometer for biomedical applications," Ph.D. dissertation, Electrical Engineering Dept., Stanford University, 1978.

[39] L. M. Roylance and J. Angell, "A Batch-fabricated silicon accelerometer," *IEEE Trans. Electron Devices*, vol. 26, no. 12, pp. 1911–1917, Dec. 1979.

[40] A. A. Barlian, W.-T. Park, J. R. Jr. Mallon, A. J. Rastegar, and B. L. Pruitt, "Review: Semiconductor Piezoresistance for Microsystems," in *Proc. of the IEEE,* 2009, vol. 97, no. 3.

[41] M. E. Motamedi, *"MOEMS: micro-opto-electro-mechanical system",* SPIE, 2005.

[42] M.-W. Shao, Y.-Y. Shan, N.-B. Wong, and S.-T. Lee, "Silicon Nanowire sensors for bioanalytical applications: Glucose and hydrogen peroxide detection," *Advanced Functional Materials*, vol. 15, pp. 1478–1482, 2005.

[43] T. Toriyama, Y. Tanimoto, and S. Sugiyama, "Single crystal silicon nano-wire piezoresistors for mechanical sensors," *J. of Microelectromech. Syst.*, vol. 11, pp. 605–611, 2002.

[44] T. Toriyama, D. Funai, and S. Sugiyama, "Piezoresistance measurement on single crystal silicon nanowires," *J. of Applied Physics*, vol. 93, pp. 561–565, 2003.

[45] K. Nakamura, Y. Isono, T. Toriyama, and S. Sugiyama, "First-Principles Simulation on Orientation Dependence of Piezoresistance Properties in Silicon Nanowires," *Jpn. J. Appl. Phys.*, vol. *48*, pp. 06FG09-1-06FG09-5, 2009.

[46] J. X. Cao, X. G. Gong, and R. Q. Wu, "Giant piezoresistance and its origin in Si(111) nanowires: First-principles calculations," *Phys. Rev. B, Condens. Matter*, vol. 75, no. 23, pp. 233-302, 2007.

[47] A. C. H. Rowe, *"Silicon nanowires feel the pinch," Nature Nanotechnology,* vol. 3, pp. 311, 2008.

[48] C. S. Smith, "Piezoresistance effect in germanium and silicon," *Physics Review,* vol. 94, pp. 42-49, 1954.

[49] S. Sugiyama, T. Toriyama, K. Nakamura and D. V. Dao, "Evaluation and Analysis of Physical Properties of Nanomaterials for Highly Sensitive Mechanical Sensing Devices," *IEEJ Transactions on Sensors and Micromachines*, vol. 130, no. 5, pp. 146-151, 2010.

[50] Y. S. Chou, P. R. Krauss, W. Zhang, L. Guo, and L. Zhuang, "Sub-10 nm Imprint Lithography and Applications", *J. of Vacuum Science Technology B*, vol. 15, no. 6, pp. 2897-2904, 1997.

[51] C. Vieu, F. Carcenac, A. Pepin, Y. Chen, M. Mejias, A. Lebib, L. Manin-Ferlazzo, L. Couraud, H. Launois, "Electron Beam Lithography: resolution limits and applications," *Applied Surface Science*, vol. 164, pp. 111-117, 2000.

[52] V. Kaajakari, "Silicon as an anisotropic mechanical material," in *Practical MEMS: Analysis and design of microsystems, MEMS sensors, electronics, actuators, rf mems, optical mems, and microfluidic systems,* Small Gear Publishing, 2009.

[53] J. A. Harley and T. W. Kenny, "1/f noise considerations for the design and process optimization of piezoresistive cantilevers," *J. of Microelectromech. Syst.,* vol. 9, pp. 226-235, 2000.

[54] J. J. Wortman and R. A. Evans, "Young's modulus, shear modulus, and Poisson's ratio in silicon and germanium," *J. Applied Physics,* vol. 36, no. 1, pp. 153-156, 1965.

[55] A. P. Boresi, R. J. Schmidt and O. M. Sidebottom, *Advanced Mechanics of Materials.* Wiley, 1993.

[56] Freescale Semiconductor. (2007). *Accelerometer Terminology Guide* [Online]. Available:

http://cache.freescale.com/files/sensors/doc/support_info/SENSORTERMSPG.pdf

[57] ASTM C1055 – 03. (2009). *Standard Guide for Heated System Surface Conditions That Produce Contact Burn Injuries* [Online]. Available:

http://www.exponent.com/scalds_burn_injuries/.

[58] S. Middelhoek, "Micro mechanical transducers", in *Handbook of sensors and actuator,* M. -H. Bao, Ed., Elsevier, 2000.

[59] H. Nyquist, "Thermal agitation of electric charge in conductors," *Phys. Rev.,* vol. 32, pp. 110-113, 1928.

[60] J. P. Lynch, A. Partridge, K. H. Law, T. W. Kenny, A. S. Kiremidjian, and E. Carryer , "Design of Piezoresistive MEMS-Based Accelerometer for Integration with Wireless Sensing Unit for Structural Monitoring," *J. of Aerospace Engineering*, vol. 16, no. 3, pp. 108-114, 2003.

[61] F. N. Hooge, "1/f noise is no surface effect," *Physical letters A,* vol. 29, pp. 139-140, 1960.

[62] L. K. J. Vandamme and S. Oosterhoff , "Annealing of ion-implanted resistors reduces the 1/f noise," *J. Appl. Phys.,* vol. 59, pp. 1-74, 1986.

[63] L. K. J. Vandamme, "Is the 1/f noise constant?," in *Noise in Physical Systems and 1/f noise,* Elsevier, Amsterdam, 1983, pp. 183-192.

[64] J. A. Harley, "Advances in piezoresistive probes for atomic force microscopy," Ph.D dissertation, Stanford University, 2002.

[65] H. Chen, M. Bao, H. Zhu, S. Shen, "A piezoresistive accelerometer with a novel vertical beam structure," *J. Sens. Actuators Phys.*, vol. 63, pp. 19-25, 1997.

[66] M. Tacano, J. Pavelka, N. Tanuma, S. Yokokura, S. Hashiguchi, "Dependence of Hooge constant on mean free paths of materials," in *Proc. SPIE,* 2004, vol. 5469, pp. 310-319.

[67] P. Gonzales, S. Severi, S. Lenci, P. Merken, A. Witvrouw, K. D. Meyer, "Evaluation of piezoresistivity and 1/f noise of polycrystalline SiGe for MEMS sensor application," in *Proc. Eurosens XXII,* 2008, pp. 881.

[68] J. A. Harley, "Advances in piezoresistive probes for atomic force microscopy," unpublished Dissertation at the department of Mechanical Engineering thesis, Stanford University, 2000.

[69] O. N. Tufte and E. L. Stelzer , "Piezoresistive properties of silicon diffused layers," *J. Appl. Phys.*, vol. 34, no. 2, pp. 313-318, 1963.

[70] W. P. Mason, J. J. Forst and L. M. Tornillo , "Recent developments in semiconductor strain transducers," in *15th Annual Conference of The Instrument Society of America,* New York, 1960, pp. 110–120.

[71] R. Amarasinghe, D. V. Dao, V. T. Dau, B. T. Tung and S. Sugiyama, "Sensitivity Enhancement Of Piezoresistive Micro Acceleration Sensors With Nanometer Stress Concentration Regions On Sensing Elements," in *Transducers 2009*, Denver, CO, USA, June 21-25.

[72] Y. Kanda, *"*A graphical representation of the piezoresistance coefficients in silicon," *IEEE Trans. Electron Devices,* vol. ED-29, no. 1, pp. 64-70, 1982.

[73] N. Maluf, *An Introduction to Microelectromechanical Systems Engineering.* 2nd ed. Boston: Arttech House, 2004.

[74] G. L. Bir and G. E. Pikus, in *Symmetry and Strain-Induced Effects in Semiconductors,* Ed. New York: Wiley, 1974, pp. 369–391.

[75] D. R. Kerr and Milnes A. G., "Piezoresistance of diffused layers in cubic semiconductors," *Appl. Phys.,* vol. 34, no. 4, pp. 727-731, 1963.

[76] E. Nassiopoulos and J. Njuguna, "An assessment of the side impact protection systems (SIPS) for racing drivers in motorsport rallying championships," unpublished.

[77] M. Unser, "Motorsports Accidentology," MSc thesis, School of Applied Sciences, Cranfield University, Cranfield, UK, 2009.

[78] P. Gkotsis, "Development of Mechanical Reliability Testing Techniques with films and piezo MEMS components," Ph.D dissertation, School of Applied Sciences, Cranfield University, Cranfield, UK, 2009.

[79] J. S. Milne, A. C. H. Rowe, S. Arscott and Ch. Renner, "Giant Piezoresistance Effects in Silicon Nanowires and Microwires," *Phys. Rev. Lett.*, vol. 105, no. 22, 2010.

[80] A. Koumela, D. Mercier, C. Dupre', G. Jourdan, C. Marcoux, E. Ollier, S. T. Purcell and L. Duraffourg, "Piezoresistance of top-down suspended Si Nanowires," *Nanotechnology,* vol. 22, 2011.

[81] Lipták and G. Béla, "Instrumentation Engineers' Handbook," in *Process Measurement and Analysis*. CRC Press. HB, 2003.

[82] K. Miller, A. Cowen, G. Hames and B . Hardy, "SOIMUMPs Design Handbook a MUMPs® process", MEMScAP., 2004.

[83] K. Sooriakumar, W. Chan, T. S. Savage and C. Fugate, "A comparative study of wet vs. dry isotropic etch to strengthen silicon micro-machined pressure sensor," *Electrochemical Soc. Proc.,* vol. 95, no. 27, 1995.

[84] K. E. Petersen, "Silicon as a mechanical material," in *Proc. IEEE,* 1982, vol. 70, no. 5.

[85] S. H. Christie, "The Bakerian Lecture: Experimental Determination of the Laws of Magneto-electric Induction in different masses of the same metal, and its intensity in different metals.," *Philosophical Transactions of the Royal Society of London*, vol. 123, pp. 95-142, 1833.

[86] X. L. Feng, R. He, P. Yang, and M. L. Roukes, "Very High Frequency Silicon Nanowire Electromechanical Resonators," *Nano Lett.*, vol. 7, no. 7, pp 1953–1959, 2007.

[87] H. Ren and P. Kazanzides, "Investigation of attitude tracking using an integrated inertial and magnetic navigation system for hand-held surgical instruments," *IEEE/ASME Trans. Mechatron.*, vol. PP, no. 99, Dec. 2010.

[88] J. Fang, S. Zheng, B. Han, "Amb vibration control for structural resonance of double-gimbal control moment gyro with high-speed magnetically suspended rotor," *IEEE/ASME Trans. Mechatron.*, vol. 18, no. 1, pp. 32-43, Feb. 2013.

[89] P. Liljeback, K. Y. Pettersen, O. Stavdahl, J. T.Gravdahl, "Snake robot locomotion in environments with obstacles," *IEEE/ASME Trans. Mechatron.*, vol. 17, no. 6, pp. 1158-1169, Dec. 2012.

[90] E. Lawrence, K. F. Navarro, J. Riudavets, M. Messina, "Macroscopic Sensor Networks: Application Issues in the Healthcare Industry", *J. of Computational Methods in Sciences and Engineering,* vol. 6, no. 5, 6, supplement 2, pp. 309 - 319, 2006.

[91] M. Messina, E. Lawrence, K. F. Navarro, E. Lubrin, "Towards Assistive Healthcare: prototyping advances in wireless sensor network (WSN) system integration and application" in *IADIS International Conference - Wireless Applications and Computing* Lisbon, Portugal, 2007, pp. 43-54.

[92] M. Messina, Y. Y. Lim, E. Lawrence, D. Martin, F. Kargl, "Implementing and Validating an Environment and Health Monitoring System" in *5th International*

Conference on Information Technology: New Generation ITNG 2008 , Las Vegas, USA, 2008, pp. 994-999.

[93] D. V. Dao, S. Okada, V. T. Dau, T. Toriyama and S. Sugiyama, "Development of a 3-DOF Silicon Piezoresistive Micro Accelerometer," in *Proc. of the 2004 Int. Symp. on Micro -Nanomechatronics and Human Science, 2004 and The Fourt Symp. Micro-Nanomechatronics for Information-Based Society*, 2004.

[94] D. Weiland, A. Chaehoi, S. Ray, D. O'Connell, M. Begbie and C. Wang, "BCB-Based Wafer-Level Packaging of Integrated CMOS/SOI Piezoresistive MEMS Sensors," in *EMPC'09,* Rimini, Italy, 15th - 18th June, 2009, pp. 1-5.

[95] G. Liu, B. Zhang and K. Zhang, "Design and fabrication of a GaAs/Al0.4Ga0.6As microaccelerometer based on piezoresistive effect," in *Symposia D, E and F from MRS International Materials Research Conference, Journal of Physics: Conference Series* 152, 2009.

[96] J.-H. Sim, C.-S. Cho, J.-S. Kim, J.-H. Lee and J.-H. Lee, "Eight-beam piezoresistive accelerometer fabricated by using a selective porous-silicon etching method," *Sensors and Actuators* A, vol. 66, pp. 273-278, 1998.

[97] R. Mukhiya, A. Adami, A. Bagolini, M. Zen and S. Kal, "FEM Based Design and Simulation of Bulk Micromachined MEMS Accelerometers with Low Cross Axis Sensitivity," in *7th. Int. Conf. on Thermal, Mechanical and Multiphysics Simulation and Experiments in Micro-Electronics and Micro-Systems, EuroSimE,* 2006.

[98] H. Dong and W. Zhang, "Micro inertial measurement system from China," *IEEE Instrumentation & Measurement Magazine,* 2002.

[99] Fujitzu. (2012). *Mems 3-axis Accelerometer – FAR-S2AB series*. [Online]. Available: http://www.lbenchindia.com/finalyearprojectdatasheets/Accelometer.pdf

[100] J.-H. Sim and J.-H. Lee, "A piezoresistive Silicon Accelerometer using Porous Silicon micromachining and Flip-Chip bonding," *Jpn. J. Appl. Phys.*, vol. 38, pp. 1915-1918, 1999.

[101] V. Ferrari, A. Ghisla, D. Marioli and A. Taroni, "Mems Accelerometer With Multiaxial Response By Dynamic Reconfiguration Of Piezoresistive Bridges," in *Proceedings of the Eurosensors XX Conference*, Göteborg, Sweden, 17-20 September, 2006.

[102] C. Lowrie, M. P. Y. Desmulliez, L. Hoff, O. J. Elle and E. Fosse, "MEMS Three-Axis Accelerometer: Design, Fabrication and Application of Measuring Heart Wall Motion," in *DTIP of MEMS & MOEMS 2009,* Rome, Italy, 1-3 April, 2009.

[103] R. P. van Kampen and R. F. Wolffenbuttel, "Modeling the mechanical behavior of bulk-micromachined silicon accelerometers, " *Sensora and Actuators A*, vol. 64, pp. 137-150, 1998.

[104] T. D. Tran, D. V. Dao, T. T. Bui, L. T. Nguyen, T. P. Nguyen and S. Susumu, "Optimum design considerations for 3-DOF micro accelerometer using nanoscale piezoresistors," in *Proceeding of the 3rd IEEE Int. Conf. on Nano/Micro Engineered and Molecular Systems,* Sanya, China, 6-9 January, 2008.

[105] R. Amarasinghe, D. V. Dao, T. Toriyama and S. Sugiyama, "Simulation, fabrication and characterization of a three-axis piezoresistive accelerometer," *Smart Mater. Struct.*, vol. 15, pp. 1691–1699, 2006.

[106] R. Amarasinghe, D. V. Dao, V. T. Dau and S. Sugiyama, "Ultra Miniature Novel Three-Axis Micro Accelerometer," in *IEEE SENSORS 2009 Conference*.

[107] M. B. Panzer, C. R. 'Dale' Bass, R. S. Salzar, J. Pellettiere, B. Myers, "Evaluation of Ear-mounted Sensor for Determining Impact Head Acceleration," in *IRCOBI Conferenc,* York (UK), September 2009.

[108] L. J. Currano, C. R. Becker, G. L. Smith, B. Isaacson, and C. J. Morris, "3-axis Accelerometer Switch for Traumatic Brain Injury Early Warning,," in *MEMS 2012,* Paris, France, 2012.

[109] J. F. Mullaney, "Optical properties and electronic structure of solid silicon," *Phys. Rev.,* vol. 66, pp. 326–339, 1944.

[110] C. Herring, "Transport properties of a many valley semiconductor," *Bell Syst. Tech. J.,* vol. 34, pp. 237–290, Mar. 1955.

[111] C. Herring, "Transport and deformation potential theory for many-valley semiconductors with anisotropic scattering," *Phys. Rev.,* vol. 101, p. 944, 1956.

[112] D. Long, "Stress dependence of the piezoresistance effect," *J. App. Phys.,* vol. 32, pp. 2050–2051, 1961.

[113] M.-S. Lin, "A better understanding of the channel mobility of Si MOSFETs based on the physics of quantized subbands," *IEEE Trans. Electron Devices*, vol. 35, pp. 2406–2411, 1988.

[114] K. Matsuda, "Strain-dependent hole masses and piezoresistive properties of silicon," in *IWCE-10 10th International Workshop on Computational Electronics*, 2004, pp. 173–174.

[115] M. V. Fischetti, Z. Ren, P. M. Solomon, M. Yang, and K. Rim, "Six-band k-p calculation of the hole mobility in silicon inversion layers: Dependence on surface orientation, strain, and silicon thickness," *J. App. Phys.,* vol. 94, pp. 1079–1095, 2003.

[116] R. Oberhuber, G. Zandler, and P. Vogl, "Subband structure and mobility of two-dimensional holes in strained Si/SiGe MOSFET's," *Phys. Rev. B*, vol. 58, pp. 9941–9948, 1998.

[117] T. Toriyama and S. Sugiyama, "Analysis of piezoresistance in p-type silicon for mechanical sensors," *J. Microelectromech. Syst.,* vol. 11, pp. 598–604, 2002.

[118] T. Kwa, G. Pender and J. Letterneau, "Triaxial accelerometer for placement inside the ear canal," in *NSTI-Nanotech 2010,* vol.2, 2010.

[119] N. Yazdi, F. Ayazi, and K. Najafi, "Micromachined inertial sensors," in *Proc. IEEE*, 1998, vol. 6, pp. 1640–1659.

[120] W. Riethmuller, "A smart accelerometer with on-chip electronics fabricated by a commercial CMOS process," *Sensors and actuators. A: Physical*, vol. 31, p. 121, 1992.

[121] H. Seidel, U. Fritsch, R. Gottinger, J. Schalk, J. Walter, and K. Ambaum, "A piezoresistive silicon accelerometer with monolithically integrated CMOS-circuitry," in *Solid-State Sensors and Actuators, 1995 and Eurosensors IX. Transducers '95. The 8th International Conference on,* 1995, pp. 597–600.

[122] W.-T. Park, K. O'Connor, K.-L. Chen, J. Mallon, T. Maetani, P. Dalal, R. Candler, V. Ayanoor-Vitikkate, J. Roberson, S. Puria, and T. Kenny, "Ultraminiature encapsulated accelerometers as a fully implantable sensor for implantable hearing aids," *Biomedical Microdevices*, vol. 9, pp. 939–949, 2007.

[123] K. Kwon and S. Park, "A bulk-micromachined three-axis accelerometer using silicon direct bonding technology and polysilicon layer," *Sensors and Actuators A: Physical*, vol. 66, pp. 250–255, 1998.

[124] A. Partridge, J. K. Reynolds, B. W. Chui, E. M. Chow, A. M. Fitzgerald, L. Zhang, N. I. Maluf, and T. W. Kenny, "A high-performance planar piezoresistive accelerometer," *J. Microelectromech. Syst.,* vol. 9, pp. 58–66, 2000.

[125] W.-T. Park, A. Partridge, R. N. Candler, V. Ayanoor-Vitikkate, G. Yama, M. Lutz, and T. W. Kenny, "Encapsulated submillimeter piezoresistive accelerometers," *J. Microelectromech. Syst.,* vol. 15, pp. 507–514, 2006.

[126] J. P. Lynch, A. Partridge, K. H. Law, T. W. Kenny, A. S. Kiremidjian, and E. Carryer, "Design of piezoresistive MEMS-based accelerometer for integration with wireless

sensing unit for structural monitoring," *J. of Aerospace Engineering*, vol. 16, pp. 108–114, Jul. 2003.

[127] Delphi Earpiece Sensor System. (2013). [Online]. Available: http:\\www.Delphi.com.

[128] MX2125. (2013). [Online]. Available:

http://www.parallax.com/dl/docs/prod/compshop/SICMemsicTut.pdf

[129] MOEMS University of Oulu. (2013). [Online]. Available:

http://www.infotech.oulu.fi/Annual/2002/OPME.html

[130] M. S. Sanders, and E. J. McCormick, *Human factors in engineering and design.* 7th Ed., McGraw-Hill, New York, 1993.

[131] C. D. Wickens, J. D. Lee, Y. Liu, and S. E. Gordon-Becker, *An Introduction to Human Factors Engineering.* Sec. Ed., Pearson Education, Upper Saddle River, NJ, 2004.

[132] B. S. Liu, "Incorporating anthropometry into design of ear-related products," *Applied Ergonomics,* vol. 39, no. 1, pp. 115-121, 2008.

[133] H. S. Jung, and H. Jung, "Surveying the dimensions and characteristics of Korean ears for the ergonomic design of ear-related products," *Int. J. of Industrial Ergonomics,* vol. 31, no. 6, pp. 361-373, 2003.

[134] M. Messina, James Njuguna, V. Dariol, C. Pace, and G. Angeletti, "Design and Simulation of a Novel Biomechanic Piezoresistive Sensor With Silicon Nanowires," *IEEE/ASME Transactions on Mechatronics*, vol. PP, no. 99, pp. 1-10, 2012.

[135] Nonlinearities. (2013). [Online]. Available at:

http://www.sensorland.com/HowPage026.html

[136] M. Messina and J. Njuguna, "Potential of silicon nanowires structures as nanoscale piezoresistors in mechanical sensors," in *International Conference on Structural Nano Composites (NANOSTRUC 2012)* 2–4 July 2012, Cranfield University, Bedfordshire, UK.

[137] K. Nakamura, T. Toriyama, S. Sugiyama, "First-principles simulation on thickness dependence of piezoresistance effect in silicon nanosheets," *Jpn. J. Appl. Phys.* vol. 49, pp. 06GH01, 2010.

[138] K. Nakamura, Dz.V. Dao, B. Th. Tung, T. Toriyama, S. Sugiyama, "Piezoresistive effect in silicon nanowires - a comprehensive analysis based on first-principles calculations," in *International Symposium on Micro-NanoMechatronics and Human Science,* pp. 38–43, 2009.

[139] K. Nakamura, T. Toriyama, S. Sugiyama, "First-principles simulation on piezoresistive properties in doped silicon nanosheets," *IEEJ Trans. Electr. Electron. Eng.,* vol. 5, pp. 157–163, 2010.

[140] Y. Yang, X. Li, "Giant piezoresistance of p-type nano-thick silicon induced by interface electron trapping instead of 2D quantum confinement," *Nanotechnology,* vol. 22, 2011.

[141] P. Neuzil, C. C. Wong, J. Reboud, "Electrically controlled giant piezoresistance in silicon nanowires," *Nano Lett*., vol. 10, pp. 1248–1252, 2010.

[142] C. Pramanik, S. Banerjee, H. Saha, C. K. Sarkar, "Piezoresistivity of silicon quantum well wire," *Nanotechnology,* vol. 17, pp. 3209–3214, 2006.

[143] C. Min, T. Nishida, X. Lv, N. Mohta, S. E. Thompson, "Comparison between high-field piezoresistance coefficients of Si metaloxide-semiconductor field-effect transistors and bulk Si under uniaxial and biaxial stress," *J. Appl. Phys.,* vol. 103, 2008.

[144] J.-H. Zhang, Q.-A. Huang, H. Yu, S.-Y. Lei, "Theoretical study of electromechanical property in a p-type silicon nanoplate for mechanical sensors," *Chin. Phys. B*, vol. 17, no. 11, pp. 4292-4299, 2008.

[145] J.-H. Zhang, Q.-A. Huang, H. Yu, J. Wang, S.-Y. Lei, "Effect of temperature and elastic constant on the piezoresistivity of silicon nanobeams," *J. Appl. Phys.,* vol. 105, 2009.

[146] K. Nakamura, T. Toriyama, S. Sugiyama, "First-principles simulation on thickness dependence of piezoresistance effect in silicon nanosheets," *Jpn. J. Appl. Phys.,* vol. 49, pp. 06GH01, 2010.

[147] K. Nakamura, Dz.V. Dao, B. Th. Tung, T. Toriyama, S. Sugiyama, "Piezoresistive effect in silicon nanowires - a comprehensive analysis based on first-principles calculations," in *International Symposium on Micro-NanoMechatronics and Human Science,* pp. 38–43, 2009.

[148] K. Nakamura, T. Toriyama, S. Sugiyama, "First-principles simulation on piezoresistive properties in doped silicon nanosheets," *IEEJ Trans. Electr. Electron. Eng.,* vol. 5, pp. 157–163, 2010.

[149] V. Aubry-Fortuna, K. Huet, T. T. Trang Nghiêm, A. Bournel, J. Saint-Martin, P. Dollfus, "Strain effects in p-type devices using full-band Monte Carlo simulations," in *Applications of Monte Carlo Methods in Biology, Medicine and Other Fields of Science,* Mode, C.J., Ed., 2011.

[150] S. I. Kozlovskiy, N. N. Sharan, "Piezoresistive effect in p-type silicon classical nanowires at high uniaxial strains," *J. Comput. Electron.,* vol. 10, pp. 258–267, 2011.

[151] W. B Langdon. and A. Qureshi, "Genetic Programming : Computers using 'Natural Selection' to Generate Programs," Technical Report, RN/95/76, London, UK, 1995.

[152] S. Guroglu, "An evolutionary methodology for conceptual design," Ph.D dissertation, Graduate School of Natural and Applied Sciences, Middle East Technical University, July 2005.

[153] R. S. Wagner, W.C. Ellis, "Vapor-liquid-solid mechanism of single crystal growth," *Appl. Phys. Lett.,* vol. 4, no. 89, 1964.

[154] H.-J. Choi, "Vapor-Liquid-Solid growth of semiconductor nanowires," in *Semiconductor Nanostructures for Optoelectronic Devices: Processing, Characterization and Applications.* By G.-C. Yi, Ed. Springer, 2012.

[155] Ear. (2013). [Online]. Available: http://www.virtualmedicalcentre.com/anatomy/ear/29.

[156] Earpiece. (2013). [Online]. Available: http://www.sensaphonics.com/?p=349.

[157] J. Bardeen, W. Shockley, "Deformation potentials and mobilities in non-polar crystals," *Phys Rev.,* vol. 80, pp. 72-80, 1950.

[158] Physicworld.com. (2010). *Question raised about giant piezoresistance* [Online]. Available: http://physicsworld.com/cws/article/news/2010/dec/01/questions-raised-about-giant-piezoresistance.

[159] R. J. de Dear, E. Arens, Z. Hui, M. Oquro, "Convective and radiative heat transfer coefficients for individual human body segments," *Int. J. Biometeorol.,* vol. 40, no. 3, pp. 141-156, 1997.

[160] M. Blejan, I. Ilie, B. Lupu, M. Comes, "Signal conditioner for piezoelectric sensors," in *31st International Spring Seminar on Electronics Technology 2008*, pp. 343 – 347, 2008.

[161] K. Yamada, M. Nishihara, S. Shimada, M. Tanabe, M. Shimazoe, Y. Matsuoka, "Nonlinearity of the Piezoresistance Effect of p-type Silicon Diffused Layers," *IEEE Transactions on Electron Devices*, vol. 29, no. 1, pp. 71 – 77, 1982.

[162] D. R. Kerr and A.G. Milnes, "Piezoresistance of Diffused Layers in Cubic Semiconductors," *Journal of Applied Physics*, vol. 34, pp. 727–731, 1963.

[163] S. D. Senturia, "Microsystem Design," Kluwer Academic Publishers, 2001.

APPENDIX A.   TECHNICAL SPECIFICATIONS OF THE ACCELERATION SENSOR

The main technical specifications of an accelerometer are: measurement range, electrical sensitivity, frequency response (bandwidth), shock survivability, resolution, cross-sensitivity, nonlinearity, thermal sensitivity, power consumption and physical characteristics. Each of them is described next.

Measurement Range

The measurement range is defined by the maximum and minimum absolute acceleration magnitude that the sensor can measure.

Electrical Sensitivity

The sensor electrical sensitivity is defined as the ratio of a change in the static response (output/input), measured in mV/g, to a change in an undesirable or secondary input, generally to a unit of power supply voltage change [34].

Of course higher sensitivity is preferable since a better signal to noise ratio is obtained, therefore a much simpler signal conditioning is required.

Frequency Response

The frequency response of a sensor is the signal time span covered for the measurement, the flat part of the dynamic transfer function (Figure 3) is the usable frequency range (dynamic range). In this region the sensor sensitivity keeps mostly linear except for some static inherent

nonlinearity (e.g. large deflection). Moreover the frequency response affects the speed of the measurement (dynamic response).

Frequency response and measurement range are the signal characteristics that can be detected by the sensor, these characteristics must match the characteristics of the phenomenon measured (i.e. shock measurement) in order to design a proper sensor.

The product of sensor electrical sensitivity and frequency response is sometimes called performance factor of the accelerometer, since both values are critical for the static and dynamic accelerometer performance. In designing an accelerometer the most of the effort is to maximize the performance factor that is the best trade-off between both values.

Shock Survivability

The shock survivability is simply the higher acceleration the sensor can withstand before breaking (i.e. failure of the mechanical structure). The stiffer is the sensor the higher is the acceleration the sensor can withstand.

Resolution

The resolution reflects for an analog system the ratio between noise level and sensor sensitivity. It is measured in g-force and defined by the minimum detectable acceleration.

Cross-Sensitivity

The cross-sensitivity is the undesirable signal output from other acceleration axes, also called transversal sensitivity and is measured as percentage of the output.

Nonlinearity

The nonlinearity may be described as percentage of the entire range of the sensor (full-scale output, FSO) or half of it (full-scale, ±FS). It represents a measure of the relative maximum deviation of the static response from the simple straight line (End Point Linearity Method, EPL), the best fit straight line (BFSL) or the least square best fit straight line.

Thermal Sensitivity

The thermal sensitivity is typically given as the sensitivity to operating temperature, specified as worst case value over the full operating temperature range. It is expressed as the change of the sensitivity per degree of temperature change, typically in ppm/°C for sensitivity. This index is useful for predicting maximum sensitivity error with temperature [34].

Power Consumption

The power consumption is the sensor consumption of electrical energy typically expressed by the Joule's Law as the product of the power supply (bias voltage) and the electrical current that flows in the measurement circuit. Low power consumption devices have better thermal performance, which is critical for sensors particularly sensitive to high temperature.

Physical Characteristics

The physical characteristics as sensor dimension and weight are in general important for an accelerometer since their mass loading effects on the sample measured. It is undesirable to place a large or heavy accelerometer on a small or light-weight structure. Mass loading will affect the accuracy of the results and skew the data. As a rule-of-thumb, in order to avoid mass loading the accelerometer's weight should be less than 10% of the test article [37].

APPENDIX B. ACCELEROMETER MECHANICAL STRUCTURE - SHAPES STUDY RESULTS

SHAPE 1. Cross-beams

The shape of the accelerometer with four cross- beams and a single mass is represented in the figure below.
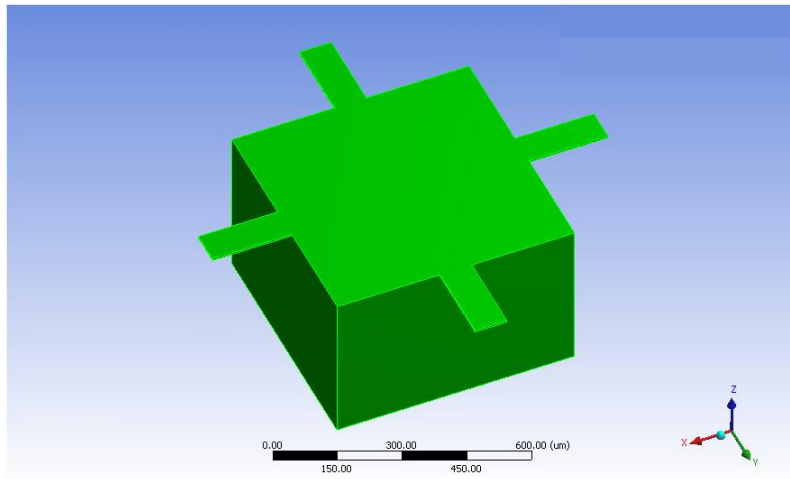
Figure B-1. Cross-beam Single-mass Accelerometer

The picture below shows the deformed shape under the out-of-plane acceleration and the maximum equivalent stress.
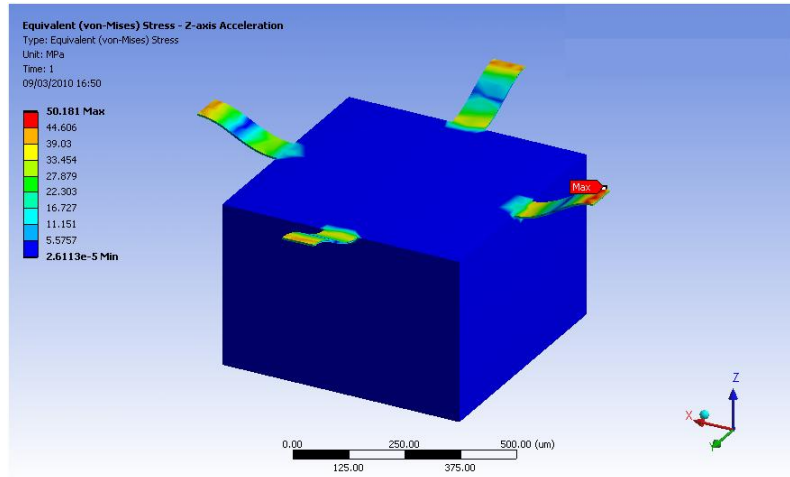
Figure B-2. Deformed structure Z-axis Acceleration

From the deformed structure above it is clear the identical deflection of the four beams that simply translate the proof mass along the Z-axis of a quantity equal to the total deformation. The results obtained with FEM analysis of the structure (single-crystal silicon) under an acceleration of 250g on the Z-axis are as follows:

Table B-1. FEA results shape 1 under Z-axis acceleration

Equivalent Stress (MPa)	Maximum Principal Stress (MPa)	Maximum Shear Stress (MPa)	Equivalent Elastic Strain (Dimensionless)	Maximum Principal Elastic Strain (Dimensionless)	Total Deformation (μm)
39.8	50.28	21.91	2.15e-004	2.27e-004	0.80

The Figure B-3 shows the deformed shape under the in-plane acceleration and the maximum equivalent stress.

206
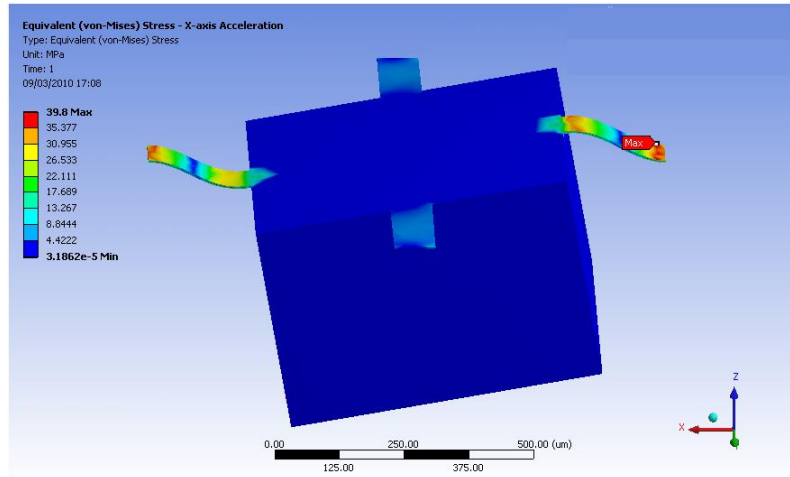
Figure B-3. Deformed structure X-axis Acceleration

The deformed structure under in-plane acceleration shows the main deformation of the two beams of the same axis of the applied acceleration, where the maximum stress is present, while the other two beams twist in a torsion deformation since the proof mass rotate relatively to the axis orthogonal to the applied acceleration (see Figure B-3).

Under the in-plane acceleration (X or Y-axis) of the same amplitude (250g) the data obtained are:

Table B-2. FEA results shape 1 under X- or Y-axis acceleraiotn

Equivalent Stress (MPa)	*Maximum Principal Stress (MPa)*	*Maximum Shear Stress (MPa)*	*Equivalent Elastic Strain (Dimensionless)*	*Maximum Principal Elastic Strain (Dimensionless)*	*Total Deformation (µm)*
39.8	50.28	21.91	2.15e-004	2.27e-004	0.80

The natural frequency and the correspondent total deformation obtained via the modal analysis for the first three modes of operation of the accelerometer are:

Table B-3. Mode of operation shape 1

Mode of Operation	Natural Frequency (kHz)
1st Mode (Y-axis)	8.99
2nd Mode (Z-axis)	9.14
3rd Mode (X-axis)	9.96

SHAPE 2. Surrounded-beams Picture-frame

Figure B-4. Picture-frame Accelerometer

Figure B-5. Deformed structure Z-axis Acceleration

Table B-4. FEA results shape 2 under Z-axis acceleration

Equivalent Stress (MPa)	Maximum Principal Stress (MPa)	Maximum Shear Stress (MPa)	Equivalent Elastic Strain (Dimensionless)	Maximum Principal Elastic Strain (Dimensionless)	Total Deformation (μm)
53.46	52.42	29.04	2.89E-04	2.84E-04	1.20

Figure B-6. Deformed structure X-axis Acceleration

Table B-5. FEA results shape 2 under X- or Y-axis acceleration

Equivalent Stress (MPa)	Maximum Principal Stress (MPa)	Maximum Shear Stress (MPa)	Equivalent Elastic Strain (Dimensionless)	Maximum Principal Elastic Strain (Dimensionless)	Total Deformation (μm)
48.69	50.73	26.91	2.63E-04	2.64E-04	1.52

Table B-6. Mode of operation shape 2

Mode of Operation	Natural Frequency (kHz)
1st Mode (Y-axis)	6.95
2nd Mode (X-axis)	7.16
3rd Mode (Z-axis)	7.41

SHAPE 3. Surrounded-beams Picture-frame type 2
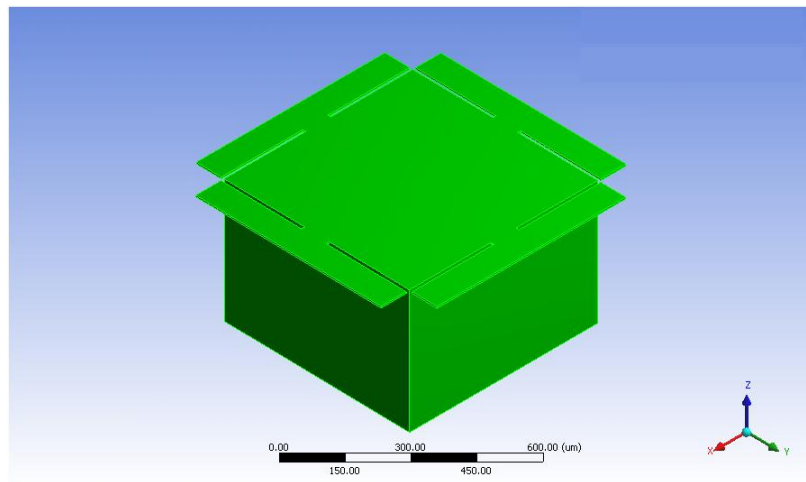

Figure B-7. Picture-frame Accelerometer type 2

Figure B-8. Deformed structure Z-axis Acceleration

Table B-7. FEA results shape 3 under Z-axis acceleration

Equivalent Stress (MPa)	Maximum Principal Stress (MPa)	Maximum Shear Stress (MPa)	Equivalent Elastic Strain (Dimensionless)	Maximum Principal Elastic Strain (Dimensionless)	Total Deformation (µm)
77.12	109.30	42.74	4.17E-04	4.80E-04	1.86

Figure B-9. Deformed structure X-axis Acceleration

Table B-8. FEA results shape 3 under X- or Y-axis acceleration

Equivalent Stress (MPa)	Maximum Principal Stress (MPa)	Maximum Shear Stress (MPa)	Equivalent Elastic Strain (Dimensionless)	Maximum Principal Elastic Strain (Dimensionless)	Total Deformation (µm)
61.04	86.58	32.44	3.30E-04	3.89E-04	1.98

Table B-9. Mode of operation shape 3

Mode of Operation	Natural Frequency (kHz)
1st Mode (Y-axis)	5.78
2nd Mode (X-axis)	6.44
3rd Mode (Z-axis)	6.62

211

SHAPE 4. Surrounded-beams Picture-frame type 3
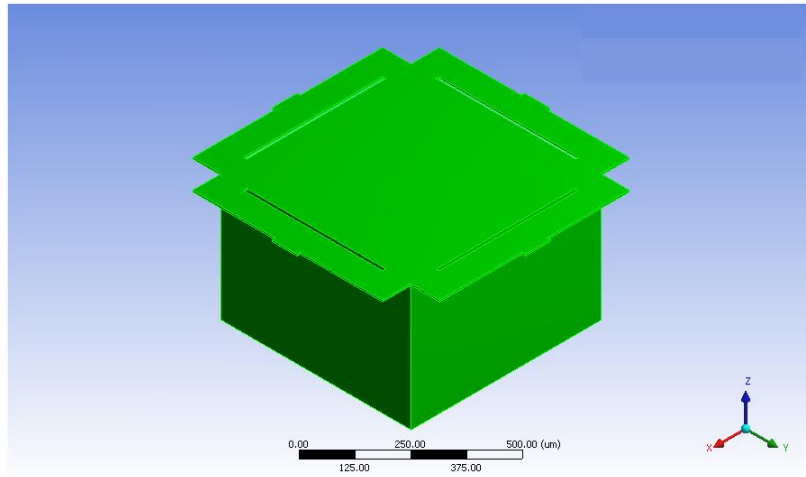
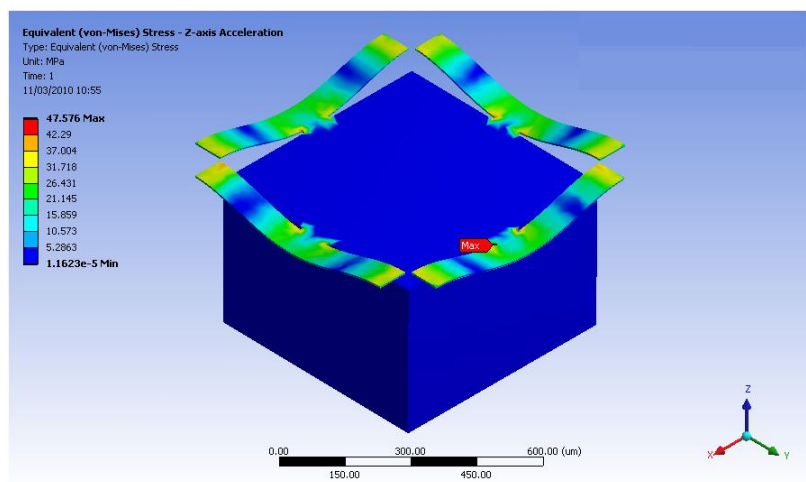**Figure B-10. Picture-frame Accelerometer type 3**
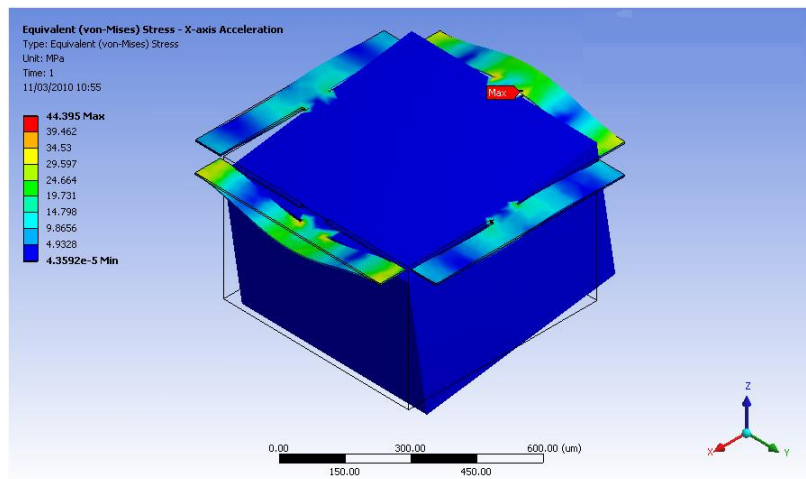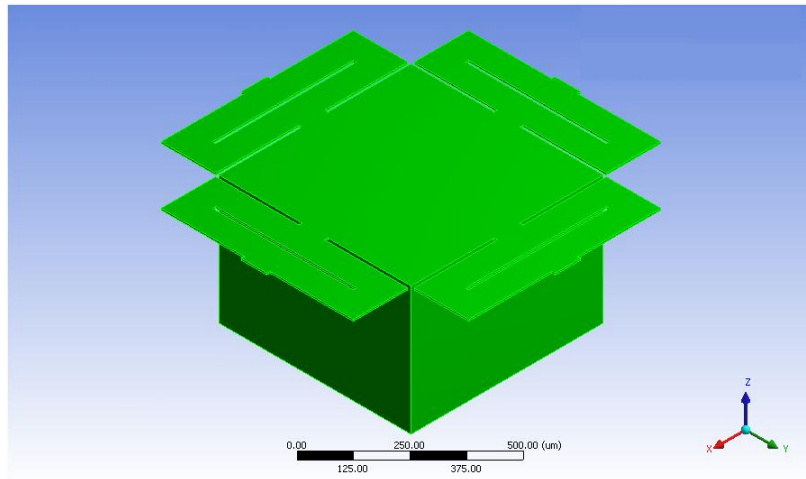

Figure B-11. Deformed structure Z-axis Acceleration

Table B-10. FEA results shape 4 under Z-axis acceleration

Equivalent Stress (MPa)	Maximum Principal Stress (MPa)	Maximum Shear Stress (MPa)	Equivalent Elastic Strain (Dimensionless)	Maximum Principal Elastic Strain (Dimensionless)	Total Deformation (µm)
71.30	97.82	38.43	3.85E-04	4.46E-04	0.70

Figure B-12. Deformed structure X-axis Acceleration

Table B-11. FEA results shape 4 under X- or Y-axis acceleration

Equivalent Stress (MPa)	Maximum Principal Stress (MPa)	Maximum Shear Stress (MPa)	Equivalent Elastic Strain (Dimensionless)	Maximum Principal Elastic Strain (Dimensionless)	Total Deformation (µm)
62.94	74.00	34.02	3.40E-04	3.52E-04	0.92

Table B-12. Mode of operation shape 4

Mode of Operation	Natural Frequency (kHz)
1st Mode (Y-axis)	8.93
2nd Mode (X-axis)	9.39
3rd Mode (Z-axis)	9.92

SHAPE 5. Cross-inset beams

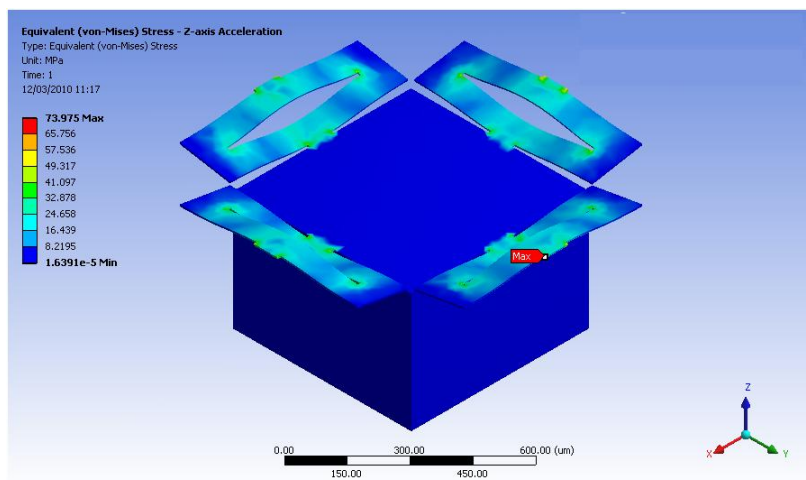**Figure B-13. Cross-inset beams Accelerometer**

Figure B-14. Deformed structure Z-axis Acceleration

Table B-13. FEA results shape 5 under Z-axis acceleration

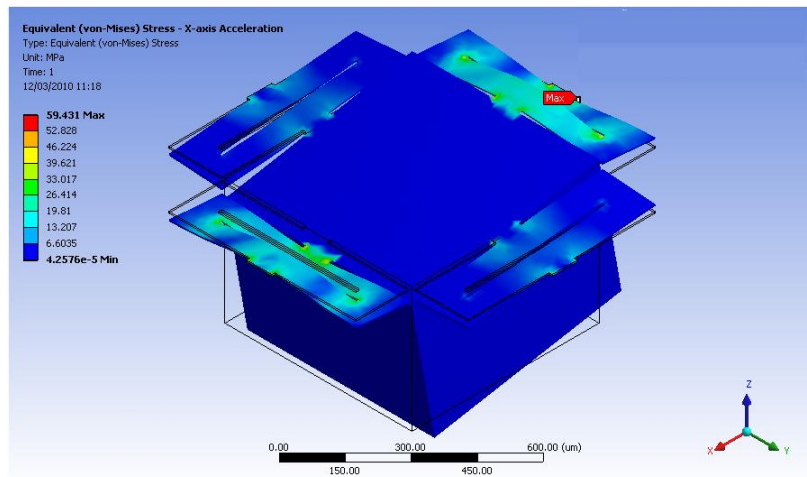| Equivalent Stress (MPa)	Maximum Principal Stress (MPa)	Maximum Shear Stress (MPa)	Equivalent Elastic Strain (Dimensionless)	Maximum Principal Elastic Strain (Dimensionless)	Total Deformation (µm)
51.40	69.32	28.71	2.78E-04	2.96E-04	0.85

Figure B-15. Deformed structure X-axis Acceleration

Table B-14. FEA results shape 5 under X- ot Y-axis acceleraiotn

Equivalent Stress (MPa)	Maximum Principal Stress (MPa)	Maximum Shear Stress (MPa)	Equivalent Elastic Strain (Dimensionless)	Maximum Principal Elastic Strain (Dimensionless)	Total Deformation (µm)
85.52	85.41	47.68	4.62E-04	4.37E-04	2.44

Table B-15. Mode of operation shape 5

Mode of Operation	Natural Frequency (kHz)
1st Mode (Y-axis)	5.28
2nd Mode (X-axis)	5.55
3rd Mode (Z-axis)	8.95

215

*SHAPE 6. Surrounded-cross inset beams Picture-frame*
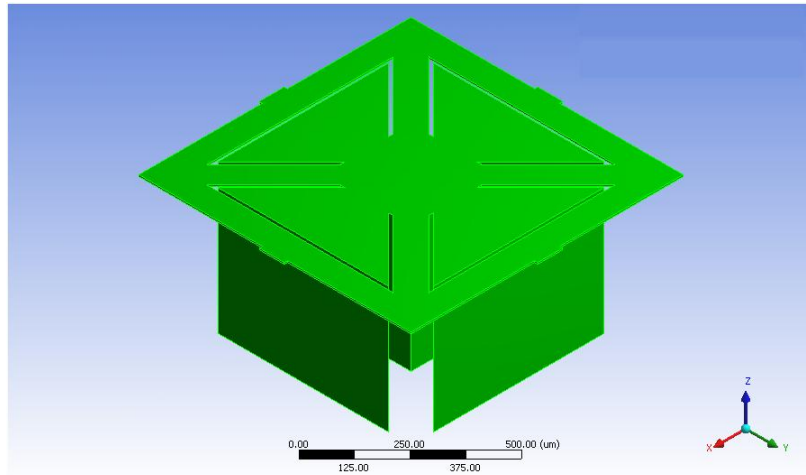
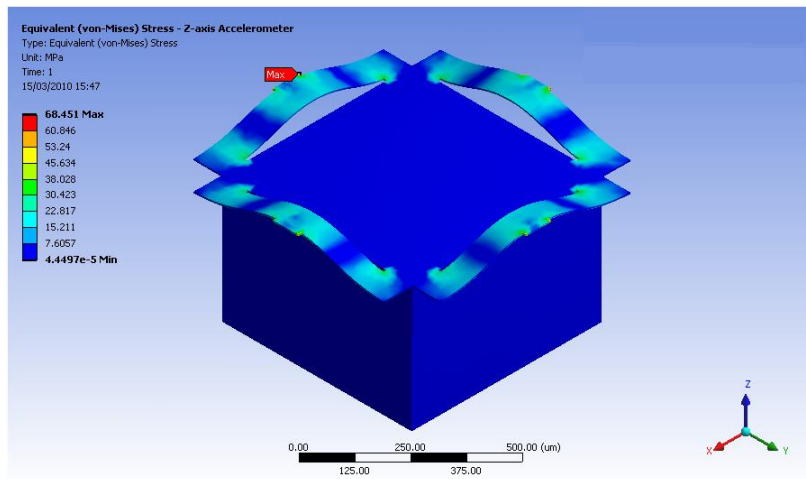**Figure B-16. Surrounded-cross inset beams Accelerometer**

Figure B-17. Deformed structure Z-axis Acceleration

Table B-16. FEA results shape 6 under Z-axis acceleration

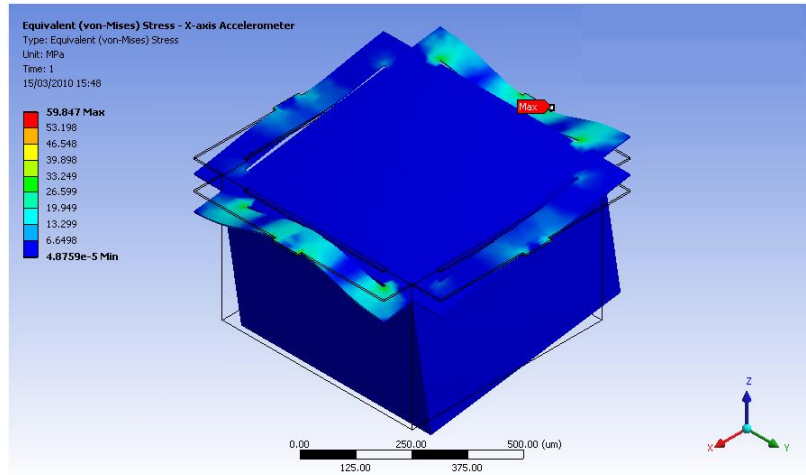| Equivalent Stress (MPa)	Maximum Principal Stress (MPa)	Maximum Shear Stress (MPa)	Equivalent Elastic Strain (Dimensionless)	Maximum Principal Elastic Strain (Dimensionless)	Total Deformation (μm)
78.52	101.77	42.69	4.24e-004	4.59e-004	3.62
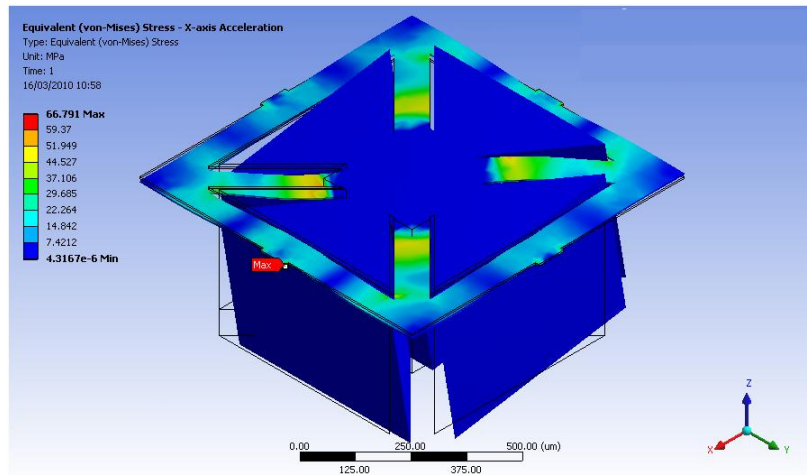
Figure B-18. Deformed structure X-axis Acceleration

Table B-17. FEA results shape 6 under X- or Y-axis acceleration

Equivalent Stress (MPa)	Maximum Principal Stress (MPa)	Maximum Shear Stress (MPa)	Equivalent Elastic Strain (Dimensionless)	Maximum Principal Elastic Strain (Dimensionless)	Total Deformation (μm)
66.79	71.22	36.06	3.61e-004	3.41e-004	5.06

Table B-18. Mode of operation shape 6

Mode of Operation	Natural Frequency (kHz)
1st Mode (X-axis)	3.83
2nd Mode (Y-axis)	3.86
3rd Mode (Z-axis)	4.23

217

SHAPE 7. Surrounded-cross inset beams Picture-frame type 2
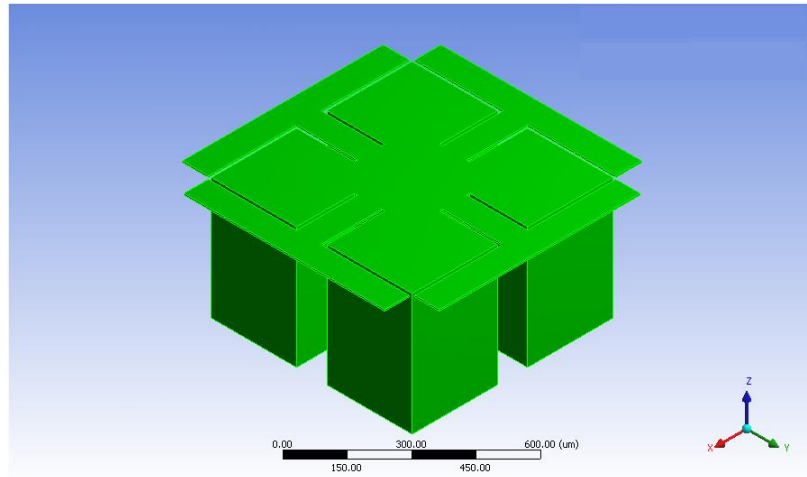
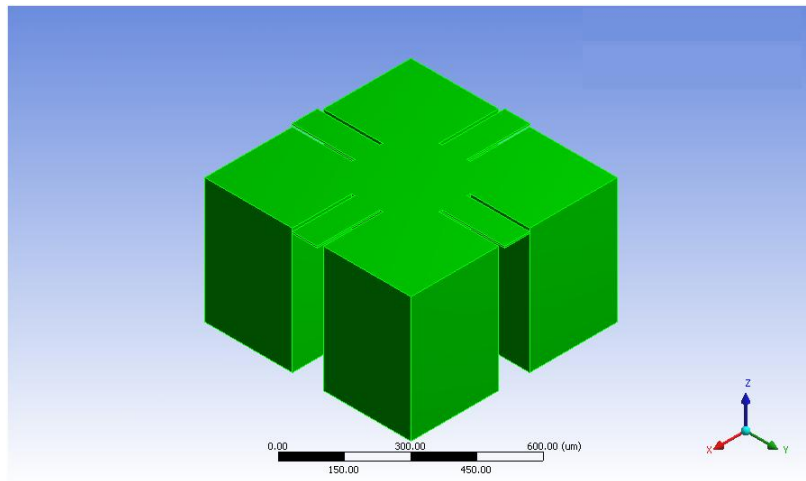

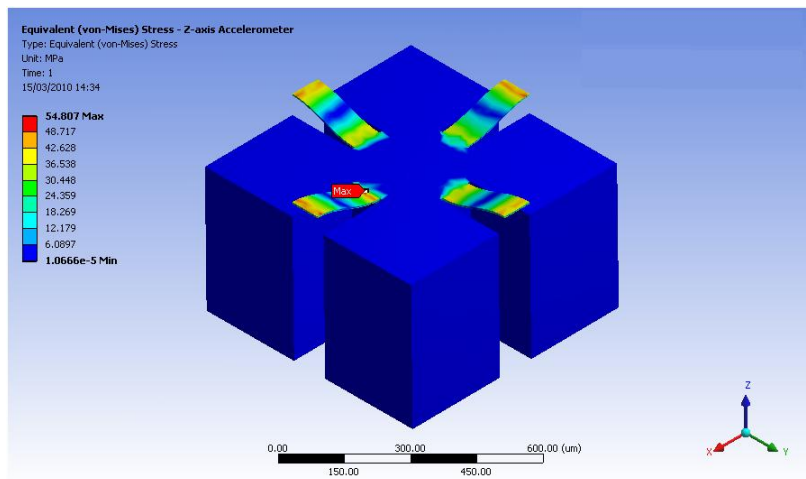**Figure B-19. Surrounded-cross inset beams Accelerometer type 2**

Figure B-20. Deformed structure Z-axis Acceleration

Table B-19. FEA results shape 7 under Z-axis acceleration

Equivalent Stress (MPa)	Maximum Principal Stress (MPa)	Maximum Shear Stress (MPa)	Equivalent Elastic Strain (Dimensionless)	Maximum Principal Elastic Strain (Dimensionless)	Total Deformation (µm)
74.78	80.91	40.97	4.04e-004	4.09e-004	3.82
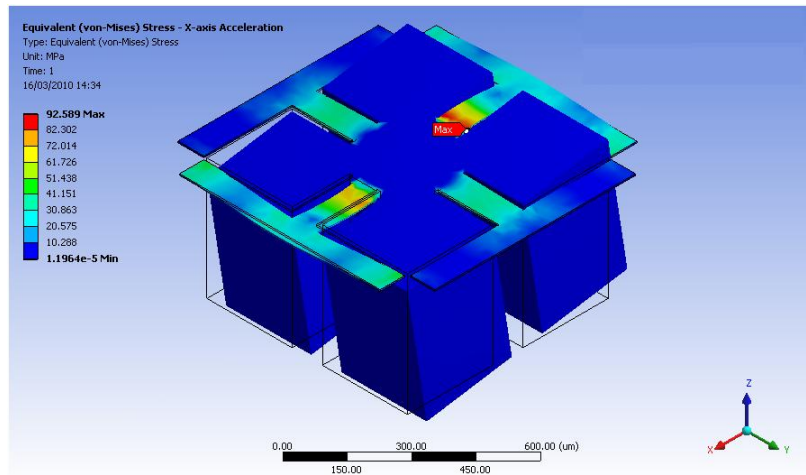
Figure B-21. Deformed structure X-axis Acceleration

Table B-20. FEA results shape 7 under X- or Y-axis acceleration

Equivalent Stress (MPa)	Maximum Principal Stress (MPa)	Maximum Shear Stress (MPa)	Equivalent Elastic Strain (Dimensionless)	Maximum Principal Elastic Strain (Dimensionless)	Total Deformation (µm)
92.58	99.35	50.61	5.00e-004	5.13e-004	6.64

Table B-21. Mode of operation shape 7

Mode of Operation	Natural Frequency (kHz)
1st Mode (X-axis)	3.26
2nd Mode (Y-axis)	3.28
3rd Mode (Z-axis)	4.12

SHAPE 8. Surrounded-cross inset beams Picture-frame type 3
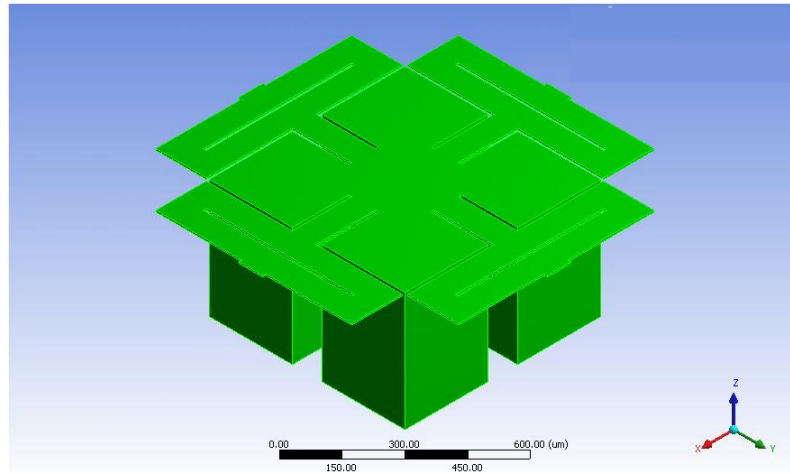
Figure B-22. Surrounded-cross inset beams Picture-frame Accelerometer type 3
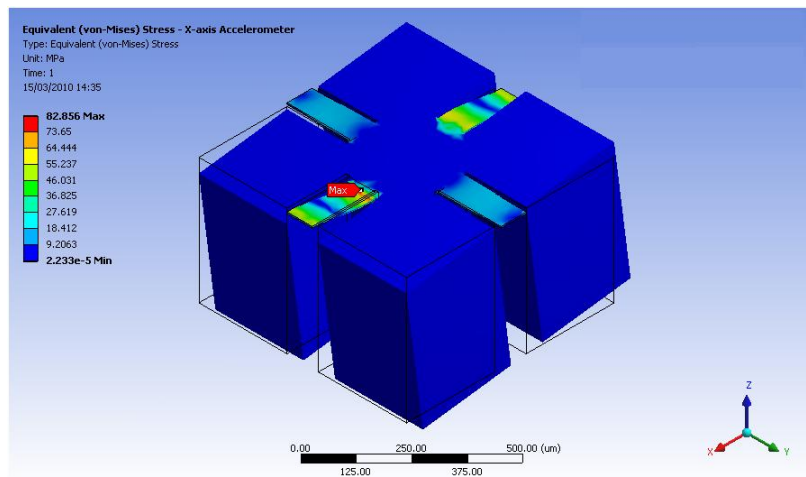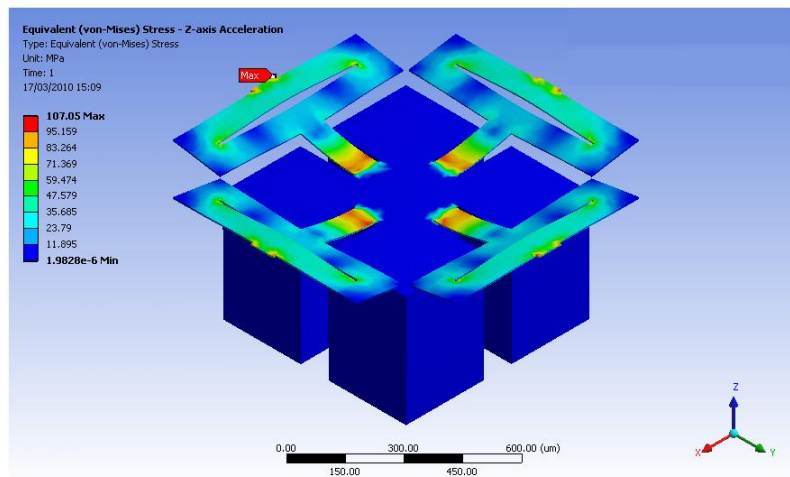

Figure B-23. Deformed structure Z-axis Acceleration

Table B-22. FEA results shape 8 under Z-axis acceleration

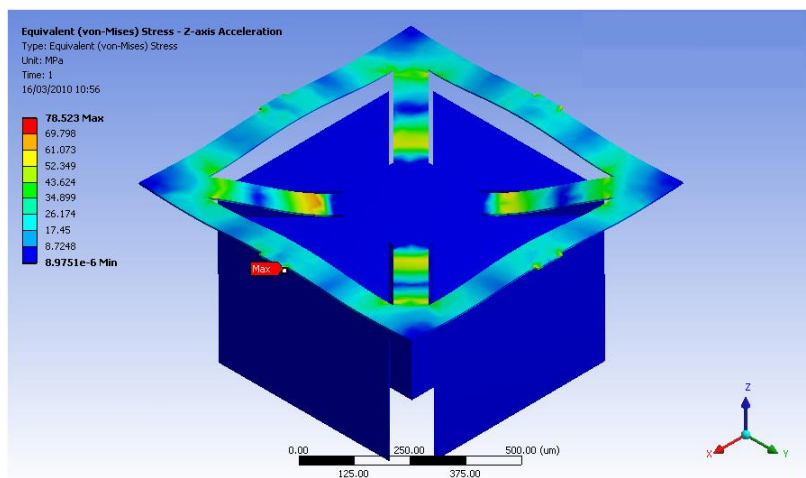| Equivalent Stress (MPa)	Maximum Principal Stress (MPa)	Maximum Shear Stress (MPa)	Equivalent Elastic Strain (Dimensionless)	Maximum Principal Elastic Strain (Dimensionless)	Total Deformation (μm)
107.05	149.28	59.16	5.78e-004	6.47e-004	7.88
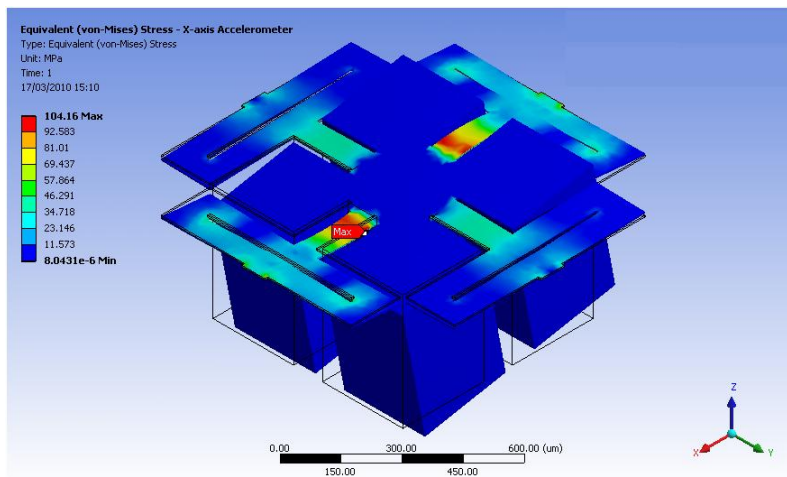
Figure B-24. Deformed structure X-axis Acceleration

Table B-23. FEA results shape 8 under X- or Y-axis acceleration

Equivalent Stress (MPa)	Maximum Principal Stress (MPa)	Maximum Shear Stress (MPa)	Equivalent Elastic Strain (Dimensionless)	Maximum Principal Elastic Strain (Dimensionless)	Total Deformation (μm)
104.16	110.58	57.06	5.63e-004	5.71e-004	9.85

Table B-24. Mode of operation shape 8

Mode of Operation	Natural Frequency (kHz)
1st Mode (Y-axis)	2.65
2nd Mode (X-axis)	2.67
3rd Mode (Z-axis)	2.82

SHAPE 9. Surrounded beams Picture-frame type 4
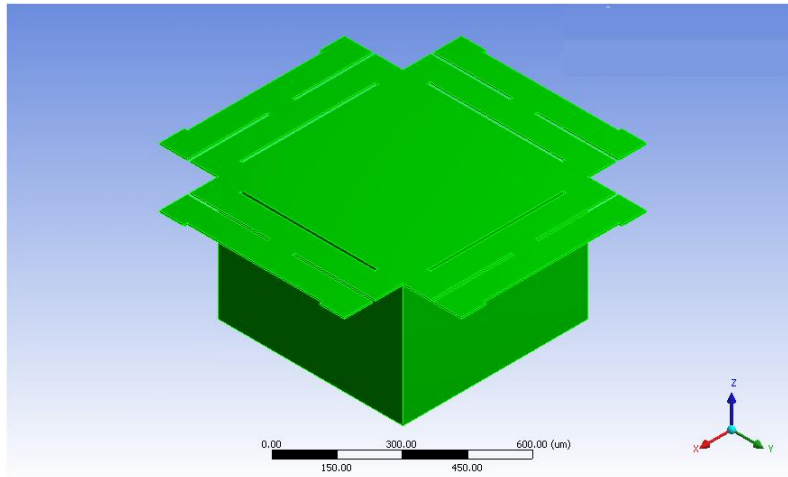
**Figure B-25. Surrounded beams Picture-frame Accelerometer type 4**
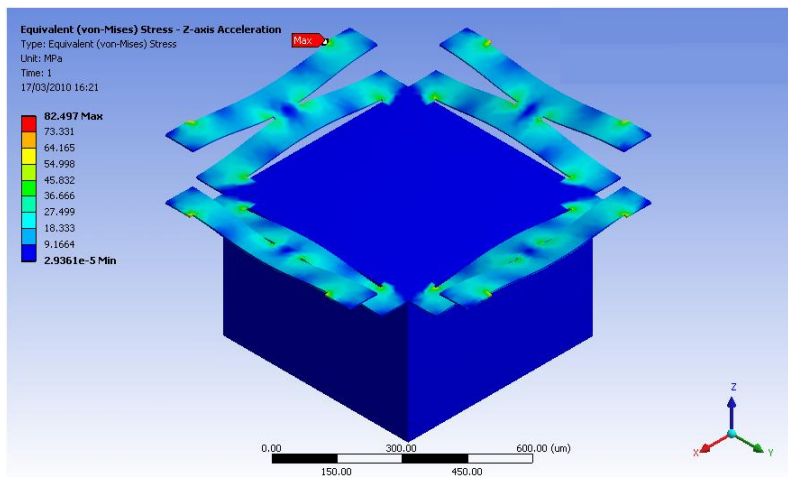
Figure B-26. Deformed structure Z-axis Acceleration

Table B-25. FEA results shape 9 under Z-axis acceelration

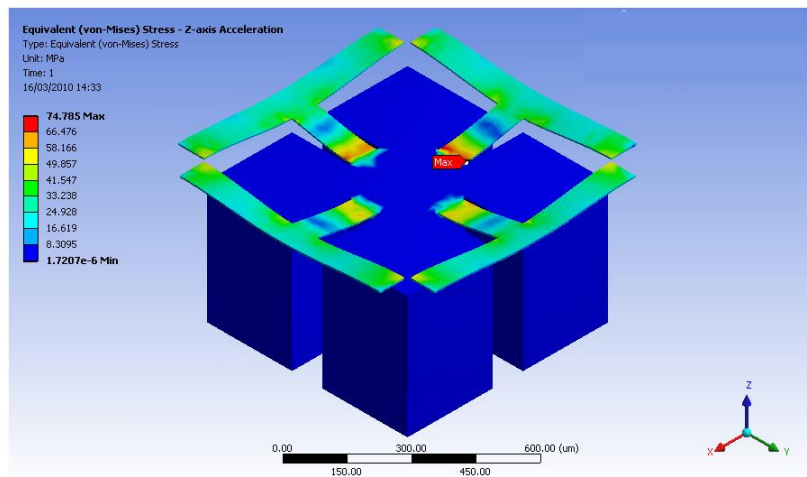| Equivalent Stress (MPa)	Maximum Principal Stress (MPa)	Maximum Shear Stress (MPa)	Equivalent Elastic Strain (Dimensionless)	Maximum Principal Elastic Strain (Dimensionless)	Total Deformation (µm)
82.49	122.41	44.95	4.46E-04	5.40E-04	1.93
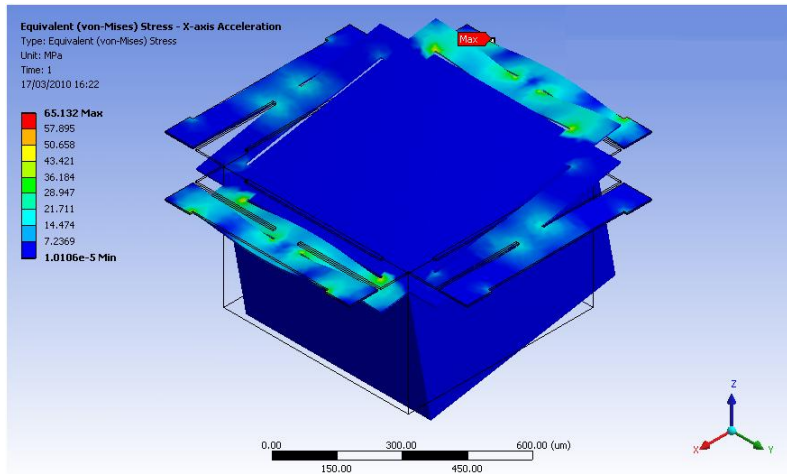
Figure B-27. Deformed structure X-axis Acceleration

Table B-26. FEA results shape 9 under X- or Y-axis acceleration

Equivalent Stress (MPa)	Maximum Principal Stress (MPa)	Maximum Shear Stress (MPa)	Equivalent Elastic Strain (Dimensionless)	Maximum Principal Elastic Strain (Dimensionless)	Total Deformation (µm)
65.13	92.66	35.02	3.52E-04	4.16E-04	2.00

Table B-27. Mode of operation shape 9

Mode of Operation	Natural Frequency (kHz)
1st Mode (Z-axis)	5.70
2nd Mode (X-axis)	6.06
3rd Mode (Y-axis)	6.13

223

APPENDIX C. SIZE OPTIMIZATION RESULTS OF ACCELEROMETER MECHANICAL STRUCTURES

Here are presented for each shape selected the charts obtained from the optimization process as design points (maximum equivalent stress vs. natural frequency under X- and Z-axis acceleration) and a table listing only the 3 best optimized design points. As it can be seen from the design of experiment optimizations results a Pareto frontier is drawn that describes the boundary of the feasible points region.

Shape n. 2 - size optimization

Figure C-1. Optimization Shape n. 2, Z-axis acceleration
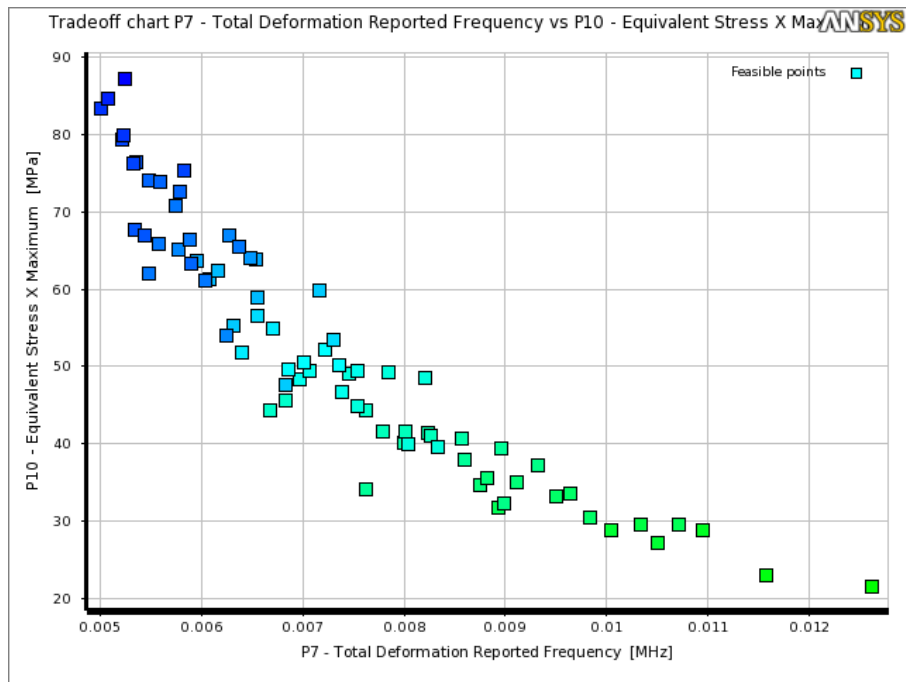
Figure C-2. Optimization Shape n. 2, X-axis acceleration

Table C-1. Optimized design points candidate shape 2

Sample Set 1	Mass_Width (µm)	Beam_Width (µm)	Beams_Thickness (µm)	Mass_Thickness (µm)	Total Deformation Reported Frequency (MHz)	Equivalent Stress Z Maximum (MPa)	Total Deformation Z Maximum (µm)	Equivalent Stress X Maximum (MPa)	Total Deformation X Maximum (µm)
Candidate A	550	60	5	400	0.0052	91.06	1.8605	87.16	2.7647
Candidate B	600	60	6	450	0.0050	87.80	1.8840	84.78	2.9822
Candidate C	650	80	6	450	0.0052	83.25	2.0118	79.87	2.7357
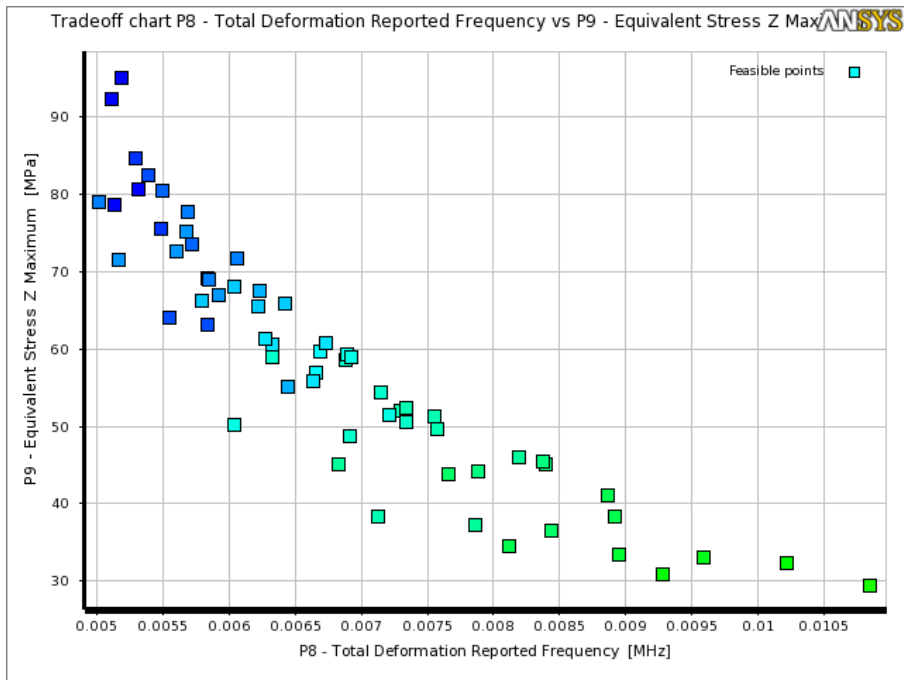
Figure C-3. Optimization Shape n. 3, Z-axis acceleration
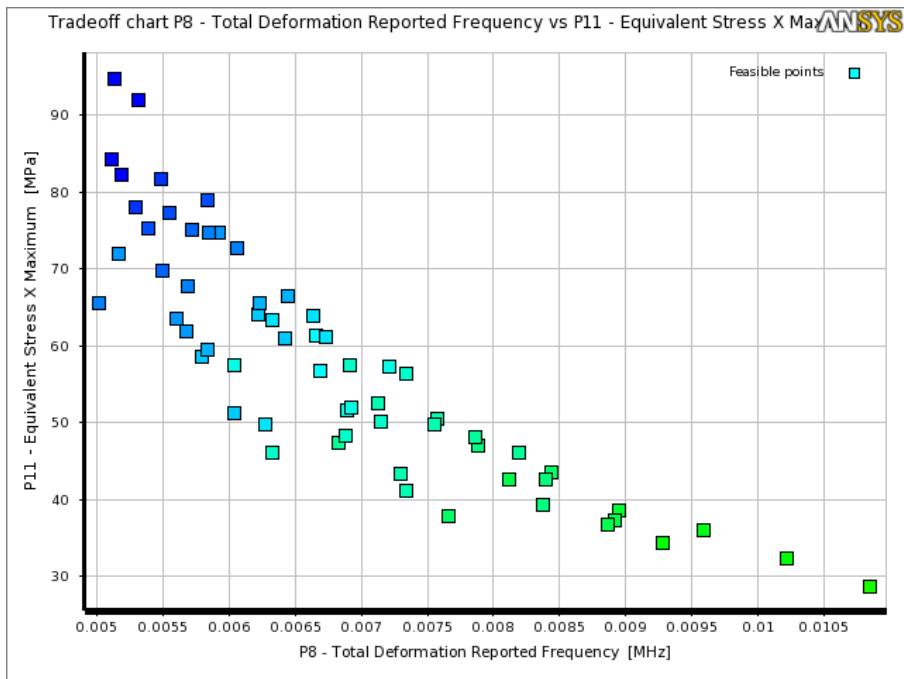
Figure C-4. Optimization Shape n. 3, X-axis acceleration

Table C-2. Optimized design points candidate shape 3

Sample Set 1	Beam_ Width (μm)	Mass_T hickness (μm)	Beams_ Thicknes s (μm)	Mass_W idth (μm)	Total Deforma tion Reporte d Frequen cy (MHz)	Equivale nt Stress Z Maximu m (MPa)	Total Deforma tion Z Maximu m (μm)	Equivale nt Stress X Maximu m (MPa)	Total Deforma tion X Maximu m (μm)
Candidate A	60	400	7	650	0.0051	95.08	2.4311	82.29	2.4023
Candidate B	80	500	7	650	0.0051	92.39	2.1327	84.44	2.9630
Candidate C	70	500	6	550	0.0051	78.75	1.7392	94.75	3.0830

Shape n. 4 - size optimization
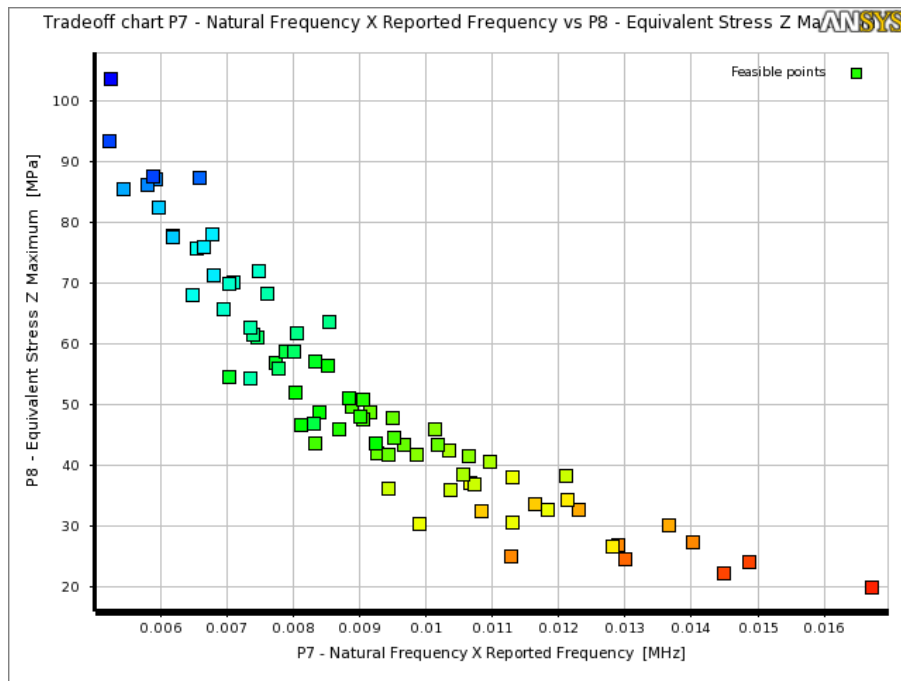
Figure C-5. Optimization Shape n. 4, Z-axis acceleration
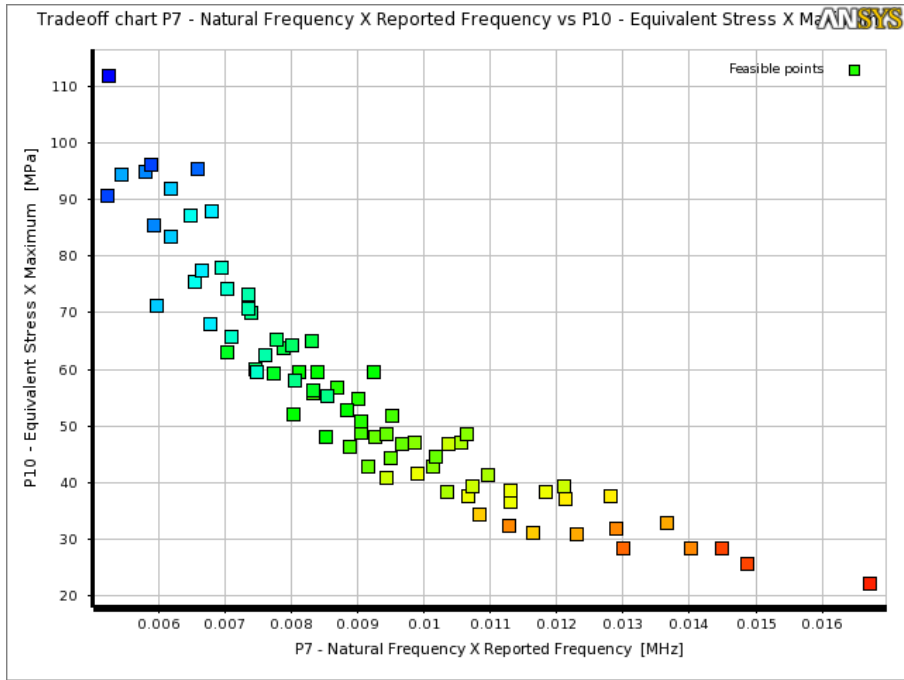
Figure C-6. Optimization Shape n. 4, X-axis acceleration

Table C-3. Optimized design points candidate shape 4

Sample Set 1	Mass_ Width (µm)	Beam_ Width (µm)	Mass_T hickness (µm)	Beams_ Thicknes s (µm)	Total Deforma tion Reporte d Frequen cy (MHz)	Equivale nt Stress Z Maximu m (MPa)	Total Deforma tion Z Maximu m (µm)	Equivale nt Stress X Maximu m (MPa)	Total Deforma tion X Maximu m (µm)
Candidate A	650	70	500	6	0.0052	103.5	1.6372	111.9	2.8169
Candidate B	650	60	450	6	0.0052	93.48	1.8717	90.74	2.7334
Candidate C	650	80	500	6	0.0058	87.53	1.3178	96.40	2.2377

Shape n. 5- size optimization
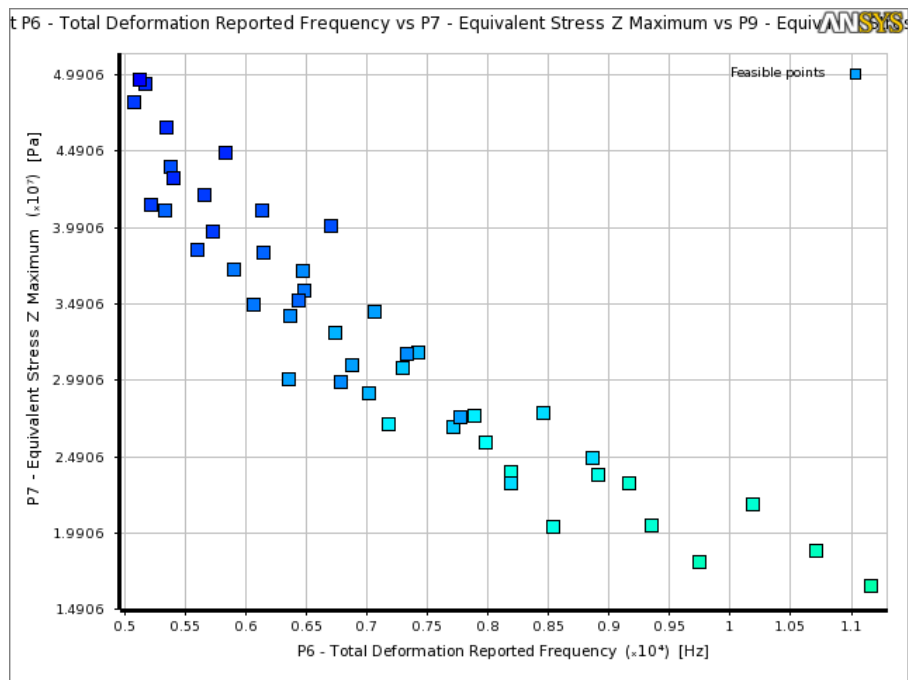
Figure C-7. Optimization Shape n. 5, Z-axis acceleration
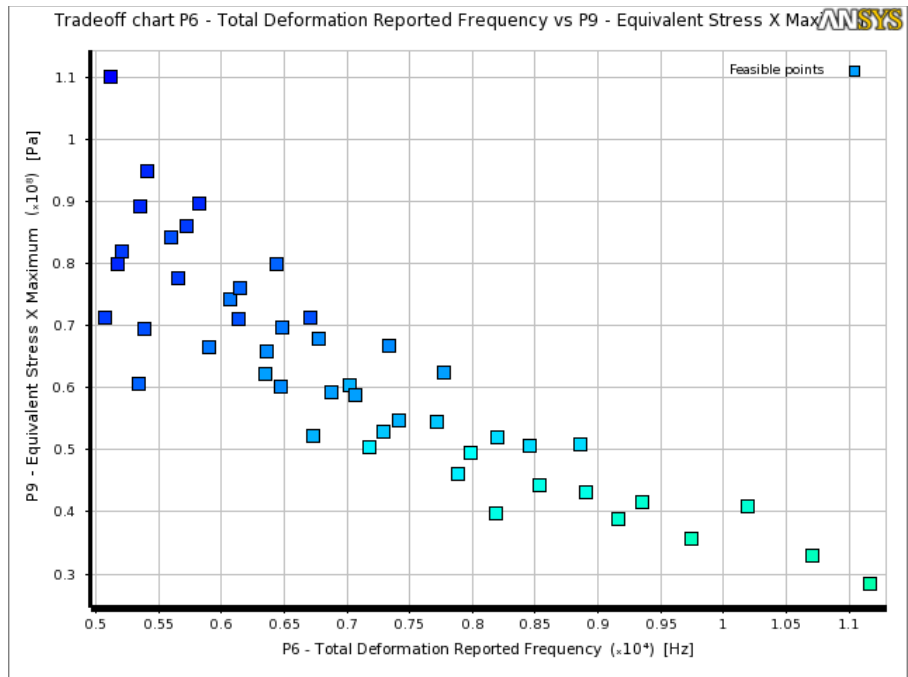
Figure C-8. Optimization Shape n. 5, X-axis acceleration

Table C-4. Optimized design points candidate shape 5

Sample Set 1	Beam_Width (µm)	Mass_Width (µm)	Mass_Thickness (µm)	Beams_Thickness (µm)	Total Deformation Reported Frequency (MHz)	Equivalent Stress Z Maximum (MPa)	Total Deformation Z Maximum (µm)	Equivalent Stress X Maximum (MPa)	Total Deformation X Maximum (µm)
Candidate A	50	250	500	6	0.0051	49.56	0.573	110.05	3.05
Candidate B	50	280	450	7	0.0053	46.48	0.672	89.30	2.60
Candidate C	60	250	500	6	0.0054	43.17	0.525	95.05	2.72

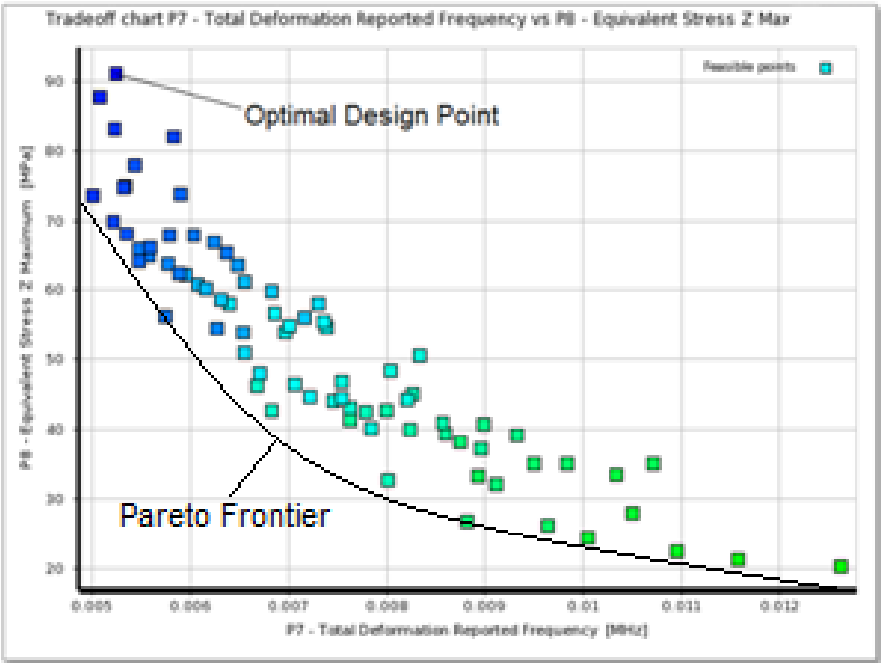## Shape n. 9 - *size optimization*
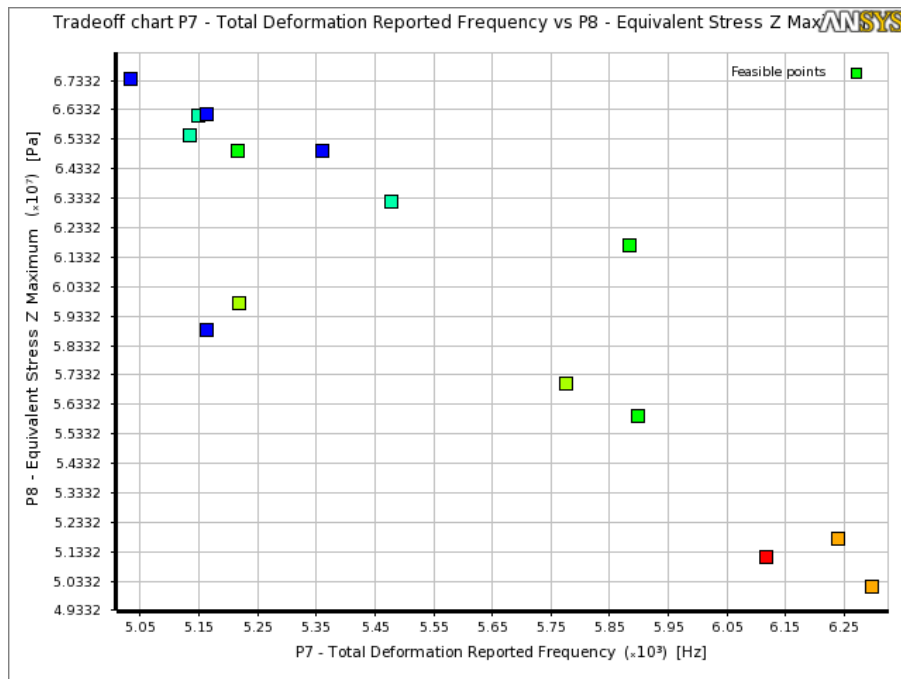
Figure C-9. Optimization Shape n. 9, Z-axis acceleration
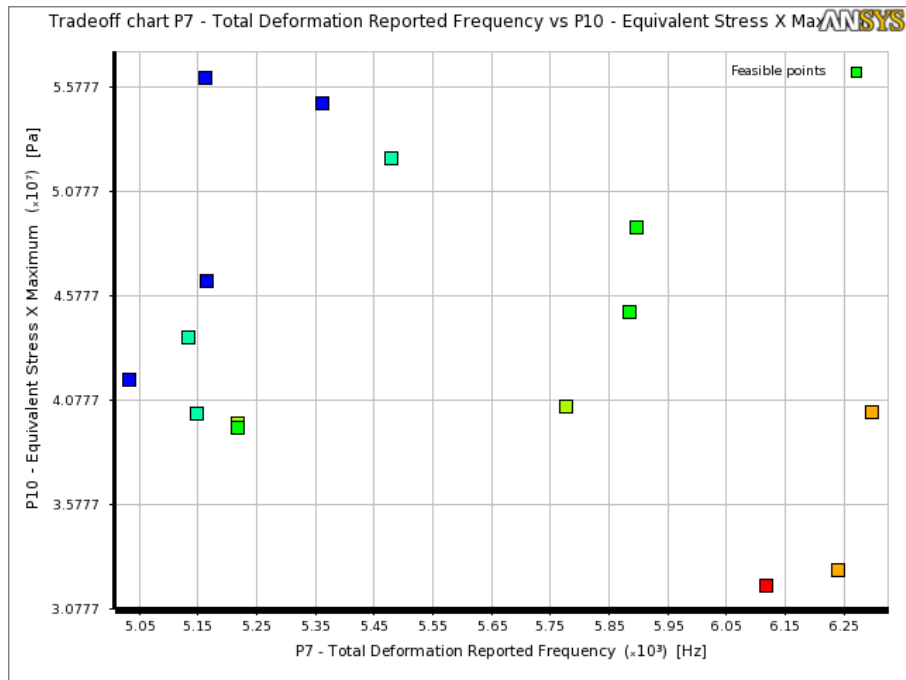
Figure C-10. Optimization Shape n. 9, X-axis acceleration

Table C-5. Optimized design points candidate shape 9

Sample Set 1	Beam_ Width (μm)	Mass_W idth (μm)	Mass_T hickness (μm)	Beams_ Thicknes s (μm)	Total Deforma tion Reporte d Frequen cy (MHz)	Equivale nt Stress Z Maximu m (MPa)	Total Deforma tion Z Maximu m (μm)	Equivale nt Stress X Maximu m (MPa)	Total Deforma tion X Maximu m (μm)
Candidate A	70	550	500	8	0.0053	64.97	2.017	55.00	2.806
Candidate B	60	550	500	8	0.0051	58.86	1.977	56.20	3.030
Candidate C	80	550	500	8	0.0054	63.22	2.091	52.40	2.640

231

APPENDIX D. PROBE STRESS ANALYSIS RESULTS UNDER 250g ACCELERATION

Stress comparison on the 16 locations of piezoresistors without NSCR –

X-, or Y-axis and Z-axis 250g acceleration

STRESS	RZ1 Probe 1		RZ2 Probe 2		RZ3 Probe 3		RZ4 Probe 4	
	X-axis	Z-axis	X-axis	Z-axis	X-axis	Z-axis	X-axis	Z-axis
Normal - X Axis	2.2663e-003 MPa	3.9592e-002 MPa	1.9856e-003 MPa	3.845e-002 MPa	-1.2142e-002 MPa	5.4542e-002 MPa	-4.8329e-005 MPa	5.124e-002 MPa
Normal - Y Axis	-41.971 MPa	64.797 MPa	41.993 MPa	64.85 MPa	-41.72 MPa	64.464 MPa	41.891 MPa	64.709 MPa
Normal - Z Axis	5.5754e-002 MPa	-8.4352e-002 MPa	-5.5448e-002 MPa	-9.3768e-002 MPa	8.9818e-002 MPa	-0.15333 MPa	-7.2517e-002 MPa	-0.11542 MPa
XY Shear	-1.3723 MPa	0.54391 MPa	-1.4527 MPa	-0.59355 MPa	1.3253 MPa	-0.49144 MPa	1.4034 MPa	0.57331 MPa
YZ Shear	0.62315 MPa	5.5453e-002 MPa	-0.64268 MPa	2.8401e-002 MPa	-0.61491 MPa	-6.114e-002 MPa	0.61852 MPa	-6.3307e-002 MPa
XZ Shear	2.5239e-003 MPa	-3.6187e-003 MPa	8.7742e-003 MPa	1.2822e-002 MPa	3.2831e-003 MPa	3.7757e-003 MPa	5.2838e-003 MPa	7.0955e-003 MPa
Equivalent (von-Mises)	**42.081 MPa**	**64.826 MPa**	**42.11 MPa**	**64.885 MPa**	**41.836 MPa**	**64.52 MPa**	**42.011 MPa**	**64.749 MPa**
Maximum Principal	7.5964e-002 MPa	64.801 MPa	42.053 MPa	64.855 MPa	0.10247 MPa	64.468 MPa	41.947 MPa	64.714 MPa
Middle Principal	3.6092e-002 MPa	3.5163e-002 MPa	-4.0834e-002 MPa	3.435e-002 MPa	2.6298e-002 MPa	5.0847e-002 MPa	-4.1146e-002 MPa	4.6519e-002 MPa
Minimum Principal	-42.025 MPa	-8.4539e-002 MPa	-7.2634e-002 MPa	-9.5116e-002 MPa	-41.771 MPa	-0.15344 MPa	-8.7479e-002 MPa	-0.11584 MPa
Intensity	42.101 MPa	64.886 MPa	42.126 MPa	64.95 MPa	41.874 MPa	64.621 MPa	42.034 MPa	64.83 MPa
STRESS	RZ5 Probe 5		RZ6 Probe 6		RZ7 Probe 7		RZ8 Probe 8	
	X-axis	Z-axis	X-axis	Z-axis	X-axis	Z-axis	X-axis	Z-axis
Normal - X Axis	0.49139 MPa	-0.34712 MPa	-0.52093 MPa	-0.39084 MPa	0.43857 MPa	-0.3271 MPa	-0.41094 MPa	-0.29538 MPa
Normal - Y Axis	44.517 MPa	-66.485 MPa	-44.675 MPa	-66.74 MPa	44.695 MPa	-66.709 MPa	-44.464 MPa	-66.533 MPa
Normal - Z Axis	1.2565e-002 MPa	-7.8245e-004 MPa	8.3224e-003 MPa	-1.9201e-003 MPa	-1.7854e-002 MPa	-1.0011e-002 MPa	3.3552e-002 MPa	5.4593e-002 MPa
XY Shear	-2.8903 MPa	1.2351 MPa	-3.0048 MPa	-1.2854 MPa	3.117 MPa	-1.2224 MPa	2.7417 MPa	1.1814 MPa
YZ Shear	0.55795 MPa	0.69619 MPa	-0.75843 MPa	0.57461 MPa	-0.83245 MPa	-0.51622 MPa	0.53389 MPa	-0.6188 MPa
XZ Shear	1.1285e-002 MPa	-0.17094 MPa	-5.7743e-002 MPa	-7.9503e-003 MPa	-5.4222e-002 MPa	4.9946e-002 MPa	5.7904e-002 MPa	0.17628 MPa
Equivalent (von-Mises)	**44.559 MPa**	**66.358 MPa**	**44.744 MPa**	**66.589 MPa**	**44.837 MPa**	**66.581 MPa**	**44.541 MPa**	**66.454 MPa**
Maximum Principal	44.713 MPa	6.9866e-002 MPa	2.1326e-002 MPa	4.0038e-003 MPa	44.929 MPa	5.3649e-003 MPa	6.6639e-002 MPa	0.12821 MPa
Middle Principal	0.30992 MPa	-0.38736 MPa	-0.3175 MPa	-0.36693 MPa	0.22018 MPa	-0.316 MPa	-0.26778 MPa	-0.34213 MPa
Minimum	-1.8148e-003	-66.515	-44.891	-66.77	-3.3403e-	-66.735 MPa	-44.64 MPa	-66.559

Principal	MPa	MPa	MPa	MPa	002 MPa			MPa
Intensity	44.714 MPa	66.585 MPa	44.913 MPa	66.774 MPa	44.963 MPa	66.741 MPa	44.707 MPa	66.688 MPa

STRESS	RX1 Probe 9		RX2 Probe 10		RX3 Probe 11		RX4 Probe 12	
	X-axis	Z-axis	X-axis	Z-axis	X-axis	Z-axis	X-axis	Z-axis
Normal - X Axis	-0.26348 MPa	0.33812 MPa	0.19761 MPa	0.25009 MPa	-0.23757 MPa	0.30006 MPa	0.28208 MPa	0.34077 MPa
Normal - Y Axis	-49.076 MPa	65.165 MPa	49.363 MPa	65.512 MPa	-49.497 MPa	65.673 MPa	49.182 MPa	65.295 MPa
Normal - Z Axis	0.11218 MPa	-0.1418 MPa	-0.14985 MPa	-0.19811 MPa	0.12589 MPa	-0.17066 MPa	-0.15 MPa	-0.18886 MPa
XY Shear	-0.27051 MPa	-1.2125 MPa	-0.15167 MPa	1.2015 MPa	0.24062 MPa	1.2957 MPa	9.8363e-002 MPa	-1.2704 MPa
YZ Shear	-0.7235 MPa	-0.18626 MPa	0.54173 MPa	-0.17101 MPa	0.6711 MPa	0.22606 MPa	-0.61265 MPa	0.21 MPa
XZ Shear	-2.3458e-002 MPa	3.1554e-002 MPa	1.7249e-002 MPa	5.2298e-003 MPa	-2.4173e-002 MPa	2.3297e-002 MPa	4.7307e-002 MPa	4.7676e-002 MPa
Equivalent (von-Mises)	**49.02 MPa**	**65.102 MPa**	**49.35 MPa**	**65.521 MPa**	**49.458 MPa**	**65.649 MPa**	**49.129 MPa**	**65.259 MPa**
Maximum Principal	0.1238 MPa	65.188 MPa	49.369 MPa	65.535 MPa	0.13614 MPa	65.699 MPa	49.189 MPa	65.32 MPa
Middle Principal	-0.26297 MPa	0.31716 MPa	0.19815 MPa	0.22814 MPa	-0.23756 MPa	0.27518 MPa	0.28718 MPa	0.32118 MPa
Minimum Principal	-49.088 MPa	-0.14405 MPa	-0.15679 MPa	-0.19872 MPa	-49.508 MPa	-0.17223 MPa	-0.1629 MPa	-0.19477 MPa
Intensity	49.212 MPa	65.332 MPa	49.526 MPa	65.733 MPa	49.644 MPa	65.871 MPa	49.352 MPa	65.515 MPa

STRESS	RY2 Probe 13		RY4 Probe 14		RY1 Probe 15		RY3 Probe 16	
	X-axis	Z-axis	X-axis	Z-axis	X-axis	Z-axis	X-axis	Z-axis
Normal - X Axis	-13.726 MPa	65.192 MPa	13.672 MPa	64.932 MPa	-13.692 MPa	65.126 MPa	13.714 MPa	65.284 MPa
Normal - Y Axis	-5.3915e-002 MPa	0.2729 MPa	9.418e-002 MPa	0.40431 MPa	-8.9639e-002 MPa	0.43069 MPa	7.9071e-002 MPa	0.35221 MPa
Normal - Z Axis	3.0829e-002 MPa	-0.15181 MPa	-3.3108e-002 MPa	-0.17287 MPa	2.6953e-002 MPa	-0.13689 MPa	-2.7863e-002 MPa	-0.15539 MPa
XY Shear	0.36125 MPa	-1.1267 MPa	0.39875 MPa	1.2751 MPa	-0.39301 MPa	1.2697 MPa	-0.40089 MPa	-1.3002 MPa
YZ Shear	2.2258e-003 MPa	-2.6375e-002 MPa	1.1685e-002 MPa	5.7134e-002 MPa	-2.3582e-003 MPa	3.2671e-002 MPa	-8.5442e-003 MPa	-3.6806e-002 MPa
XZ Shear	-9.4849e-002 MPa	0.22013 MPa	-0.10138 MPa	-0.30089 MPa	-9.8287e-002 MPa	0.20906 MPa	-8.5417e-002 MPa	-0.26356 MPa
Equivalent (von-Mises)	**13.73 MPa**	**65.163 MPa**	**13.661 MPa**	**64.858 MPa**	**13.679 MPa**	**65.02 MPa**	**13.707 MPa**	**65.227 MPa**
Maximum Principal	3.1484e-002 MPa	65.212 MPa	13.685 MPa	64.959 MPa	2.7659e-002 MPa	65.152 MPa	13.726 MPa	65.311 MPa
Middle Principal	-4.4378e-002 MPa	0.2546 MPa	8.4297e-002 MPa	0.38622 MPa	-7.8296e-002 MPa	0.40728 MPa	6.8553e-002 MPa	0.32982 MPa
Minimum Principal	-13.737 MPa	-0.1538 MPa	-3.5669e-002 MPa	-0.18135 MPa	-13.704 MPa	-0.13906 MPa	-2.9649e-002 MPa	-0.16008 MPa
Intensity	13.768 MPa	65.366 MPa	13.72 MPa	65.14 MPa	13.732 MPa	65.291 MPa	13.756 MPa	65.471 MPa

233

Stress comparison of the 16 locations of piezoresistors with NSCR –

X-, or Y-axis and Z-axis 250g Acceleration

STRESS	RZ1 Probe 1		RZ2 Probe 2		RZ3 Probe 3		RZ4 Probe 4	
	X-axis	Z-axis	X-axis	Z-axis	X-axis	Z-axis	X-axis	Z-axis
Normal - X Axis	-2.1511e-004 MPa	6.6949e-004 MPa	3.578e-004 MPa	4.4011e-004 MPa	1.2024e-003 MPa	-1.7265e-003 MPa	-1.4012e-003 MPa	-2.6224e-003 MPa
Normal - Y Axis	-61.072 MPa	95.451 MPa	61.153 MPa	95.379 MPa	-61.419 MPa	95.919 MPa	61.42 MPa	95.912 MPa
Normal - Z Axis	-1.9341 MPa	3.0164 MPa	1.8979 MPa	2.9728 MPa	-1.9135 MPa	2.9986 MPa	1.9191 MPa	3.0027 MPa
XY Shear	1.5844e-002 MPa	-1.1807e-002 MPa	1.4712e-002 MPa	1.1662e-002 MPa	-1.3771e-002 MPa	1.0553e-002 MPa	-1.3834e-002 MPa	-1.0845e-002 MPa
YZ Shear	0.12441 MPa	0.60066 MPa	-0.21559 MPa	0.44709 MPa	-0.1414 MPa	-0.59102 MPa	0.11054 MPa	-0.63178 MPa
XZ Shear	-7.9472e-003 MPa	1.2444e-002 MPa	-6.2008e-003 MPa	-9.5424e-003 MPa	-4.5511e-003 MPa	8.0931e-003 MPa	-3.6926e-003 MPa	-6.4112e-003 MPa
Equivalent (von-Mises)	**60.129 MPa**	**93.985 MPa**	**60.228 MPa**	**93.93 MPa**	**60.486 MPa**	**94.462 MPa**	**60.484 MPa**	**94.454 MPa**
Maximum Principal	-1.786e-004 MPa	95.455 MPa	61.154 MPa	95.381 MPa	1.2162e-003 MPa	95.923 MPa	61.42 MPa	95.916 MPa
Middle Principal	-1.9339 MPa	3.0126 MPa	1.8971 MPa	2.9707 MPa	-1.9132 MPa	2.9949 MPa	1.9189 MPa	2.9984 MPa
Minimum Principal	-61.072 MPa	6.16e-004 MPa	3.3433e-004 MPa	4.0767e-004 MPa	-61.419 MPa	-1.7499e-003 MPa	-1.4114e-003 MPa	-2.6376e-003 MPa
Intensity	61.072 MPa	95.455 MPa	61.154 MPa	95.38 MPa	61.42 MPa	95.924 MPa	61.422 MPa	95.919 MPa
STRESS	RZ5 Probe 5		RZ6 Probe 6		RZ7 Probe 7		RZ8 Probe 8	
	X-axis	Z-axis	X-axis	Z-axis	X-axis	Z-axis	X-axis	Z-axis
Normal - X Axis	-8.6074e-004 MPa	1.4228e-003 MPa	9.3775e-004 MPa	1.5212e-003 MPa	1.9623e-003 MPa	-2.0007e-003 MPa	-5.3492e-004 MPa	-3.5019e-004 MPa
Normal - Y Axis	67.121 MPa	-100.53 MPa	-66.945 MPa	-100.37 MPa	67.098 MPa	-100.8 MPa	-66.942 MPa	-100.49 MPa
Normal - Z Axis	2.1551 MPa	-3.2604 MPa	-2.1581 MPa	-3.2568 MPa	2.2037 MPa	-3.3157 MPa	-2.1823 MPa	-3.2862 MPa
XY Shear	2.4433e-002 MPa	-1.49e-002 MPa	2.4624e-002 MPa	1.5292e-002 MPa	-2.3263e-002 MPa	1.2802e-002 MPa	-2.0992e-002 MPa	-1.0812e-002 MPa
YZ Shear	-0.94278 MPa	2.1075 MPa	0.89359 MPa	2.0431 MPa	0.88728 MPa	-2.0556 MPa	-1.0059 MPa	-2.1482 MPa
XZ Shear	7.4231e-003 MPa	-8.2401e-003 MPa	5.9149e-003 MPa	6.1567e-003 MPa	5.0374e-003 MPa	-6.3798e-003 MPa	7.9688e-003 MPa	1.0363e-002 MPa
Equivalent (von-Mises)	**66.091 MPa**	**99.013 MPa**	**65.911 MPa**	**98.843 MPa**	**66.041 MPa**	**99.243 MPa**	**65.901 MPa**	**98.957 MPa**
Maximum Principal	67.135 MPa	1.4478e-003 MPa	9.6496e-004 MPa	1.5365e-003 MPa	67.11 MPa	-1.9856e-003 MPa	-4.9667e-004 MPa	-3.1439e-004 MPa
Middle Principal	2.1414 MPa	-3.2148 MPa	-2.1458 MPa	-3.2138 MPa	2.1916 MPa	-3.2723 MPa	-2.1667 MPa	-3.2388 MPa
Minimum Principal	-8.9778e-004 MPa	-100.58 MPa	-66.958 MPa	-100.41 MPa	1.9412e-003 MPa	-100.84 MPa	-66.958 MPa	-100.54 MPa
Intensity	67.136 MPa	100.58 MPa	66.959 MPa	100.41 MPa	67.108 MPa	100.84 MPa	66.957 MPa	100.54 MPa
STRESS	RX1 Probe 9		RX2 Probe 10		RX3 Probe 11		RX4 Probe 12	
	X-axis	Z-axis	X-axis	Z-axis	X-axis	Z-axis	X-axis	Z-axis
Normal - X Axis	1.047e-003 MPa	-2.1554e-003 MPa	-1.0093e-003 MPa	-2.1023e-003 MPa	-7.1175e-004 MPa	1.0663e-003 MPa	-8.7477e-005 MPa	2.0189e-004 MPa
Normal - Y Axis	-73.993 MPa	98.108 MPa	73.007 MPa	97.097 MPa	-73.048 MPa	97.052 MPa	72.851 MPa	96.734 MPa

Normal - Z Axis	-2.3361 MPa	3.094 MPa	2.2966 MPa	3.0502 MPa	-2.2907 MPa	3.0528 MPa	2.2992 MPa	3.0603 MPa
XY Shear	-3.8872e-004 MPa	9.9615e-003 MPa	-4.1374e-003 MPa	-1.4729e-002 MPa	4.6983e-004 MPa	-1.0153e-002 MPa	3.7651e-003 MPa	1.4567e-002 MPa
YZ Shear	-1.1505 MPa	0.81582 MPa	1.0072 MPa	0.6434 MPa	1.1044 MPa	-0.75059 MPa	-1.0985 MPa	-0.743 MPa
XZ Shear	6.3516e-003 MPa	-8.2005e-003 MPa	5.9767e-003 MPa	7.8669e-003 MPa	5.8807e-003 MPa	-8.0614e-003 MPa	6.8694e-003 MPa	8.8738e-003 MPa
Equivalent (von-Mises)	72.881 MPa	96.61 MPa	71.908 MPa	95.616 MPa	71.955 MPa	95.571 MPa	71.754 MPa	95.249 MPa
Maximum Principal	1.0644e-003 MPa	98.115 MPa	73.022 MPa	97.101 MPa	-6.965e-004 MPa	97.058 MPa	72.868 MPa	96.74 MPa
Middle Principal	-2.3176 MPa	3.087 MPa	2.2823 MPa	3.0458 MPa	-2.2735 MPa	3.0468 MPa	2.2821 MPa	3.0545 MPa
Minimum Principal	-74.012 MPa	-2.1786e-003 MPa	-1.0255e-003 MPa	-2.1254e-003 MPa	-73.065 MPa	1.0435e-003 MPa	-1.0869e-004 MPa	1.7326e-004 MPa
Intensity	74.013 MPa	98.117 MPa	73.023 MPa	97.103 MPa	73.065 MPa	97.057 MPa	72.868 MPa	96.739 MPa

STRESS	RY2 Probe 13		RY4 Probe 14		RY1 Probe 15		RY3 Probe 16	
	X-axis	Z-axis	X-axis	Z-axis	X-axis	Z-axis	X-axis	Z-axis
Normal - X Axis	-20.663 MPa	96.497 MPa	20.627 MPa	96.231 MPa	-20.572 MPa	96.056 MPa	20.757 MPa	96.633 MPa
Normal - Y Axis	3.5633e-004 MPa	-1.3149e-003 MPa	2.1356e-004 MPa	9.9457e-004 MPa	-5.3247e-004 MPa	2.2413e-003 MPa	4.9485e-005 MPa	9.4275e-005 MPa
Normal - Z Axis	-0.64398 MPa	3.0067 MPa	0.64582 MPa	3.0142 MPa	-0.64473 MPa	3.0142 MPa	0.65804 MPa	3.0648 MPa
XY Shear	-3.4496e-003 MPa	1.1627e-002 MPa	-3.188e-003 MPa	-1.1053e-002 MPa	3.6683e-003 MPa	-1.2651e-002 MPa	3.6413e-003 MPa	1.2701e-002 MPa
YZ Shear	-2.3e-003 MPa	9.8136e-003 MPa	2.5057e-003 MPa	1.0742e-002 MPa	2.6027e-003 MPa	-1.0646e-002 MPa	-2.4837e-003 MPa	-1.0661e-002 MPa
XZ Shear	0.15537 MPa	-0.54465 MPa	0.16822 MPa	0.65891 MPa	0.16879 MPa	-0.64453 MPa	0.17626 MPa	0.67773 MPa
Equivalent (von-Mises)	20.35 MPa	95.034 MPa	20.314 MPa	94.766 MPa	20.259 MPa	94.59 MPa	20.439 MPa	95.145 MPa
Maximum Principal	3.6532e-004 MPa	96.5 MPa	20.628 MPa	96.236 MPa	-5.2103e-004 MPa	96.06 MPa	20.759 MPa	96.638 MPa
Middle Principal	-0.64278 MPa	3.0036 MPa	0.64441 MPa	3.0096 MPa	-0.64331 MPa	3.0097 MPa	0.6565 MPa	3.06 MPa
Minimum Principal	-20.664 MPa	-1.3488e-003 MPa	2.0312e-004 MPa	9.5441e-004 MPa	-20.574 MPa	2.2013e-003 MPa	3.9214e-005 MPa	5.4838e-005 MPa
Intensity	20.664 MPa	96.501 MPa	20.628 MPa	96.235 MPa	20.573 MPa	96.058 MPa	20.759 MPa	96.638 MPa

APPENDIX E.   PACKAGING, 8 LEAD 2X2 DFN-EP

Mechanical Dimensions

DFN-2x2-8   Unit: mm(inch)

APPENDIX F. ACCELEROMETER FABRICATION

For the fabrication of the enhanced final accelerometer design, some design and fabrication challenges have been identified after a thorough discussion with the IZM company part of the Fraunhofer Institute in Germany.

The design and fabrication challenges are as follows:

Design issue n.1: *Stability issues and risk of breaking during dicing.*

- Beams design: 10 µm beams thickness

Action taken: Since the design of the beams with 10 µm thickness represent a risk of breaking of the beams during dicing the thickness has been increased to 20 µm to ensure stability. Moreover dicing protection is considered.

Design issue n.2: *Minimum metal track width achievable from the process is 5 µm.*

- Metallization design: 2 µm width Aluminium traces

Action taken: The metal traces have been designed below the minimum permitted by the IZM equipment; therefore an increase of the metal traces width to the minimum permitted (5 µm) is necessary.

Design issue n.3:

- Dicing protection:

a. Anodic bonding of glass on the top side of the device: The top glass is 300 µm thick

b. Use of material for covering the top side: Residual of material after removal

Action taken: The anodic bonding of glass is preferred to the material covering because the glass bonding represents also a wafer level packaging itself.

Design issue n.4: *Passive or active thermo-compensation maybe required.*

- Piezoresistors design: 2-5 kΩ resistance of piezoresistors

Action taken: the use of 2-5 kΩ resistance of piezoresistors increases significantly the temperature of the device for self-heating of piezoresistors, therefore changing the behaviour of the piezoresistors. A thermo-compensation is a possible solution.

Design issue n.5:

- Self-heating of piezoresistors.

Action taken: The self-heating of the device can be reduced by the use of current instead of voltage for powering the device.

Design issue n.6:

- Wire bonding design: *Long wires could break due to contact to the micro-structure.*

Action taken: In order to avoid possible braking of the wires it is preferred to use flip chip interconnection by bumps.

Design issue n.7:

- Bond pads design: *Minimum area 100 × 100 μm2.*

Action taken: The bond pads have been designed following the minimum area feature suggested by IZM.

Accelerometer layout design and fabrication

This section illustrates the sensor layout design and fabrication process of the two design selected for possible fabrication with conventional and nanoscale piezoresistors (Design A2 and B3).

In order to complete the sensor design of the sensor selected from geometries type A (octagon – Design A2) and B (circle – B3) the masks layout for the fabrication of the sensor have been designed with commercial software CleWin that gives as output a .GDS file, see figure F-1and F-3.
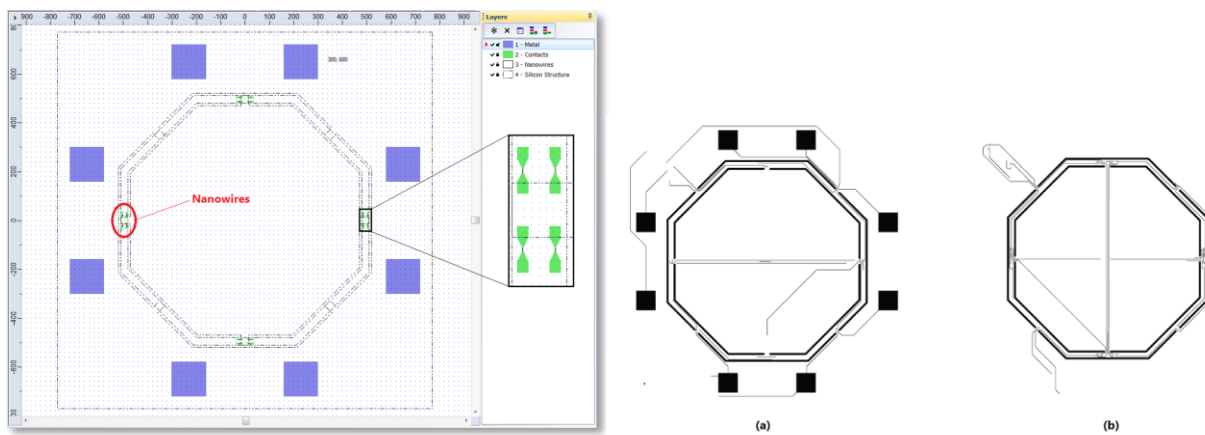

Figure F-1. .GDS file of the octagonal geometry sensor. **Figure F-2. Metallization layers. (a) Layer 1, (b) Layer 2.**

Moreover, the metallization has been developed with commercial EDA software. The metallization has been developed in 2 layers due to the traces complexity (Figure F-2).
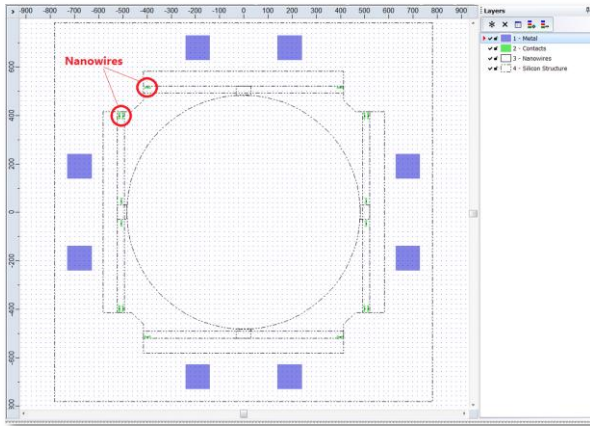
239

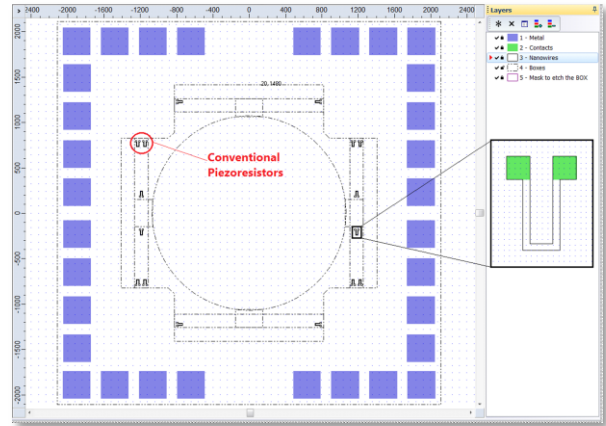**Figure F-3. .GDS file of the circular geometry sensor with nanowires**

Figure F-4. .GDS file of circular geometry sensor with conventional piezoresistors

Finally, a further design and sensor development has been undertaken with conventional piezoresistors with the purpose of comparing the performance of conventional and nanoscale piezoresistors. It should be noted that the bond pads surrounding the sensor are one for each piezoresistor contact, Figure F-4 shows the masks layout of the sensor. This design has been chosen in order to complete the measurement circuit connections beside the sensor and not overlapping it in different layers, as designed in the octagon type A sensor (Figure F-1). This choice makes the sensor fabrication more simple and convenient.

The conventional piezoresistors have been designed by Fraunhofer IZM, see Figure F-5.
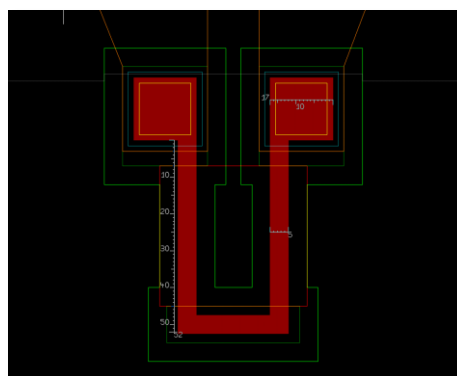
Figure F-5. Conventional piezoresistor design (Fraunhofer IZM)

The process flow for the conventional piezoresistors fabrication is illustrated in the figure F-6 and F-7.
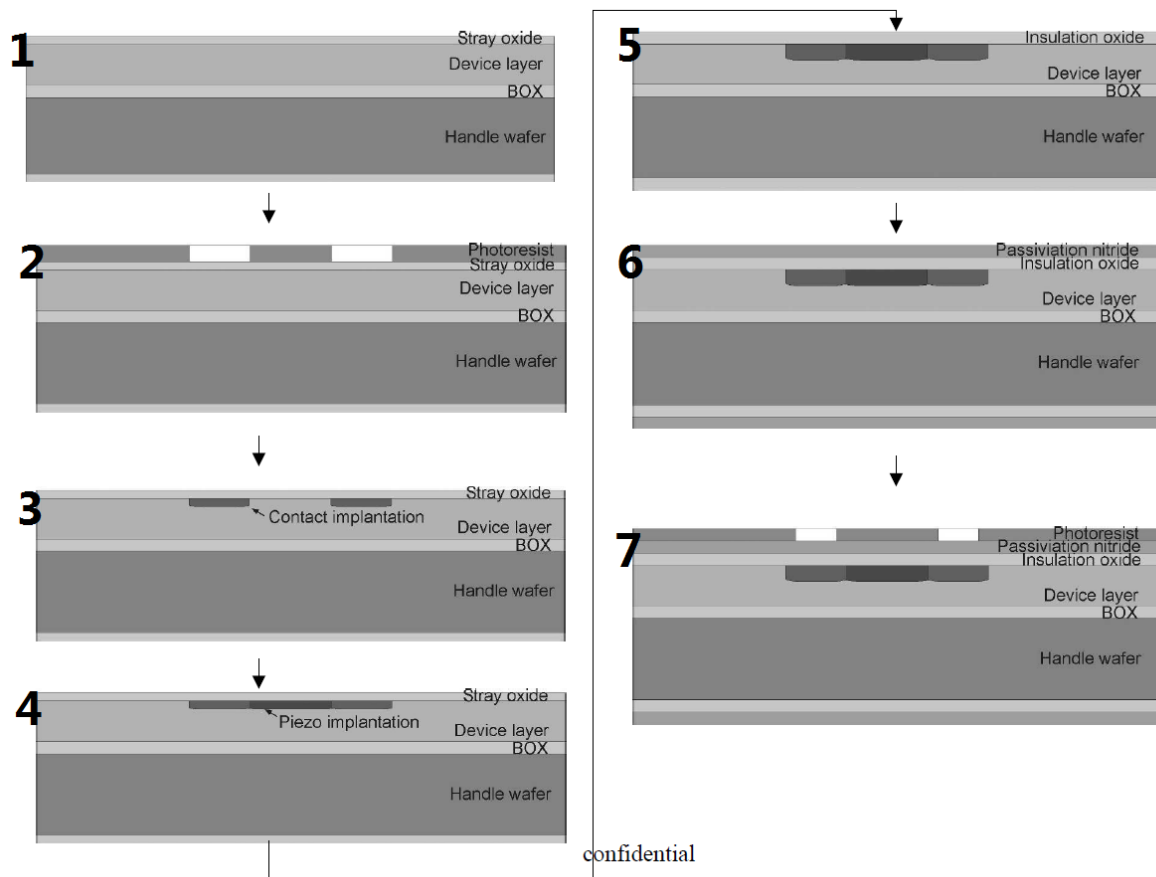
Figure F-6. Conventional piezoresistor process flow (Fraunhofer IZM)

The initial wafer (step 1) is exposed by photolithography that patterns the windows for contacts (step 2). Afterwards the contacts are doped by boron ion implantation (step 3) and the piezoresistors are also formed by boron ion implantation (step 4). Next step is the deposition of oxide for insulation (step 5) and the deposition of nitride for passivation (step 6). Then the metallization is prepared by photolithography of windows (step 7).

241
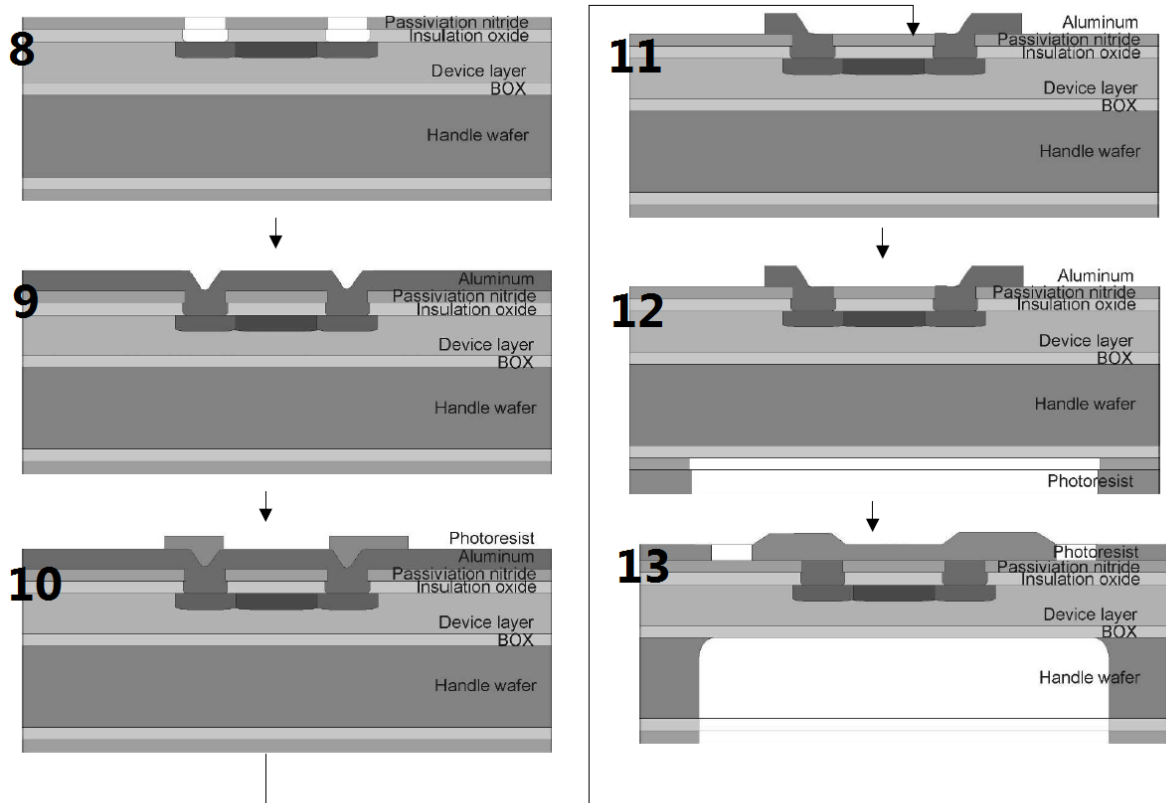
Figure F-7. Conventional piezoresistor process flow part 2 (Fraunhofer IZM)

The windows previously formed are etched; nitride and oxide layers are removed (step 8). Deposition of aluminium for metallization is performed (step 9) and photolithography for etching of metal is undertaken (step 10). Finally the aluminium is etched (step 11). To complete the processing the backside of the wafer is exposed to photolithography (step 12) and then etched. Last step to release the proof mass and beams is etching the wafer front side (step 13).

The final sensor element before and after wafer level packaging is illustrated in the Figure F-8.
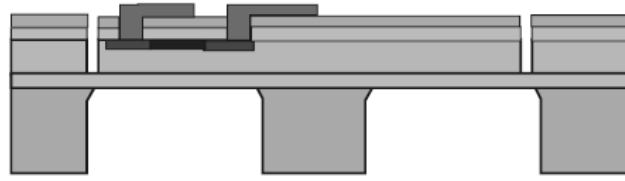
Silicon sensor element
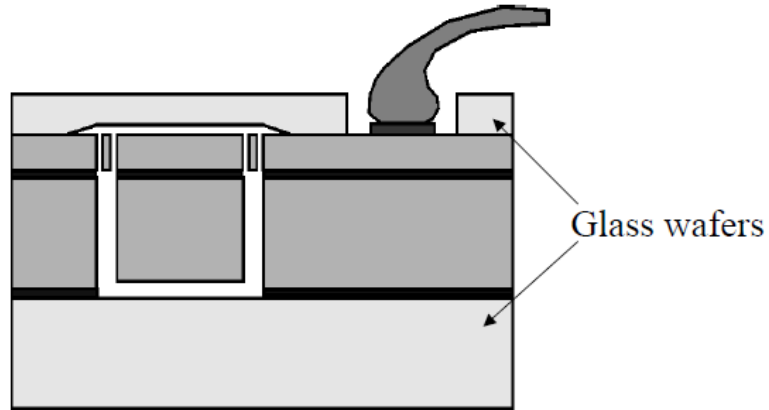
Sensor after packaging

Glass wafers

confidential

Figure F-8. Sensor before and after packaging (Fraunhofer IZM)

APPENDIX G. PIEZORESISTIVE ACCELROMETER MEASUREMENT CIRCUITS

Some of the most common sensors are the resistive elements. They are inexpensive to manufacture and relatively easy to interface with signal conditioning circuits. Resistive elements can be made sensitive to temperature, strain (by pressure or by flex as in the piezoresistive accelerometer), and light. Typically incorporated into force, pressure and acceleration sensors are the bridge circuits. Strain gages present a significant measurement challenge because the typical change in resistance over the entire operating range of a strain gage may be less than 1% of the nominal resistance value. Therefore is critical when applying resistive sensors to accurately measuring small resistance changes [32].

Attractive alternative for measuring small resistance changes accurately are offered by the bridges. The basic Wheatstone bridge [85] (see Figure G-1) consists of four resistors connected to form a quadrilateral, a source of excitation (voltage or current) connected across one of the diagonals, and a voltage detector connected across the other diagonal. The difference between the outputs of two voltage dividers connected across the excitation is measured by the detector [32].
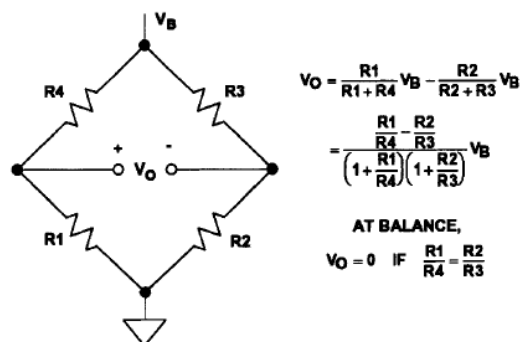

Figure G-1. Wheatstone bridge and equations [32]

In most of sensor applications employing bridges the deviation from an initial value of one or more resistors in a bridge is an indication of the magnitude or a change in the variable that has been measured. In this particular case, the output voltage change is an indication of the resistance change. Typically the resistance changes are very small, therefore the output voltage change may be as small. In many bridge applications, there may be two, or even four, elements that vary (see Figure G-2). In each case, the value of the fixed bridge resistor, R, is chosen to be equal to the nominal value of the variable resistor(s). The variable resistor(s) deviation about the nominal value is proportional to the quantity being measured, such as strain as in the piezoresistive accelerometers [32].
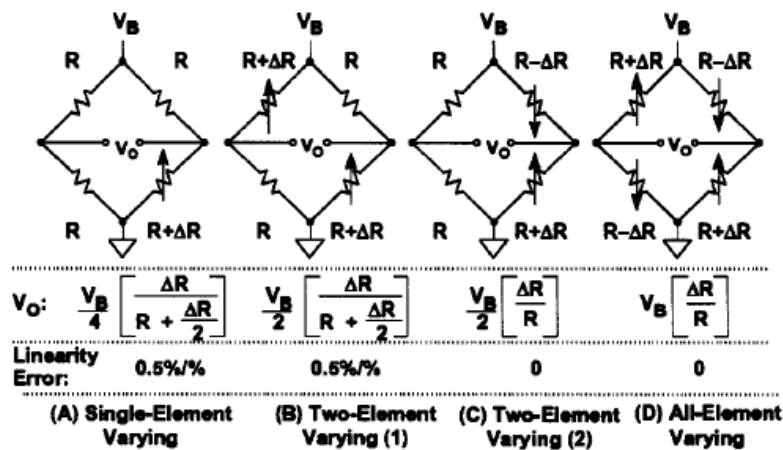
Figure G-2. Output voltage and linearity error for constant voltage drive bridge configuration [32]

The ratio of the maximum expected change in the output voltage to the excitation voltage is defined as *sensitivity* of a bridge.

The *single-element varying* bridge comprises a single resistive strain gage. All the resistances are nominally equal, but one of them is variable by an amount ΔR (see Figure 11). As the strain gauge is either compressed or tensed, its resistance will decrease or increase, respectively, thus unbalancing the bridge and producing a proportional output voltage, V_O.

This arrangement, with a single element of the bridge changing resistance in response to the measured variable (mechanical force), is known as a *quarter-bridge* circuit (Figure 11).

As the indicated in the equation, the relationship between the bridge output and ΔR is not linear. Depending on the applications, the bridge nonlinearity may be acceptable or not, but there are various methods available to linearize bridges. Software can be used to remove the linearity error in digital systems, since there is a fixed relationship between the bridge resistance change and its output (shown in the equations). To directly linearize the bridge output circuit techniques can also be used. Bridges may also be driven from constant current [32].

The *all-element varying* bridge or *full-bridge* circuit produces the highest signal (more sensitive) for a given resistance change, moreover is inherently linear. It is an industry-standard configuration for load cells which are constructed from four identical strain gages or can be applied for a piezoresistive accelerometer with four identical gages (2 tension and 2 compressed) (see Figure …). The type of measurement circuit adopted for the design of the ear-plug accelerometer related to this work is a full-bridge circuit, in order to obtain the highest sensitivity possible.

In summary, there are many design issues relating to bridge circuits. After selecting the basic configuration, the excitation method must be defined and then the value of the excitation voltage or current must be determined. Although large excitation voltages determine proportionally larger full-scale output voltages, they also result in higher power dissipation and therefore self-heating errors. On the other hand, the sensitivity to noise may increase with low values of excitation voltage that require more gain in the conditioning circuits [32].

APPENDIX H. DOPING CONCENTRATION AND ORIENTATION OF

PIEZORESISTORS

Doping type and concentration affects the piezoresistive coefficients (π, longitudinal and transverse) that define the ability of the piezoresistor to change resistivity once a stress is applied (sensitivity of piezoresistor depends to piezoresistive effect). The higher is the doping density the lower are the piezoresistive coefficients (lower sensitivity) and resistivity but the temperature dependence of sensitivity decreases (Figure H-7). However, the temperature coefficient of sensitivity drops off faster than sensitivity. The piezoresistive coefficients depend also on the crystal orientation of the piezoresistor. For {100} wafers, that have been chosen for fabrication due to fabrication convenience, the piezoresistive coefficients for *p*-type elements (boron doping) are maximal in the <110> directions and nearly vanish along the <100> directions (see Figure H-1). Smith [48] measured the piezoresistive coefficients for (100) samples along the <100> and <110> crystal directions. Longitudinal and transverse coefficients for the fundamental crystal axes were determined directly. Shear piezoresistive coefficients were inferred. By these measurements and considering the crystal symmetry, Smith fully characterized the piezoresistive tensor of 7.8 Ω-cm at low p-Si concentration as [48]:

$$[\pi_{\omega\lambda}] = \begin{bmatrix} \pi_{11} & \pi_{12} & \pi_{12} & 0 & 0 & 0 \\ \pi_{12} & \pi_{22} & \pi_{12} & 0 & 0 & 0 \\ \pi_{12} & \pi_{12} & \pi_{33} & 0 & 0 & 0 \\ 0 & 0 & 0 & \pi_{44} & 0 & 0 \\ 0 & 0 & 0 & 0 & \pi_{44} & 0 \\ 0 & 0 & 0 & 0 & 0 & \pi_{44} \end{bmatrix} =$$

$$\begin{bmatrix} 6.6 & -1.1 & -1.1 & 0 & 0 & 0 \\ -1.1 & 6.6 & -1.1 & 0 & 0 & 0 \\ -1.1 & -1.1 & 6.6 & 0 & 0 & 0 \\ 0 & 0 & 0 & 138.1 & 0 & 0 \\ 0 & 0 & 0 & 0 & 138.1 & 0 \\ 0 & 0 & 0 & 0 & 0 & 138.1 \end{bmatrix} \cdot 10^{-11} Pa^{-1} \qquad (H.1)$$

At light concentrations $(1.7 \times 10^{15}$ cm$^{-3})$, Smith [48] found the p-type longitudinal piezoresistive coefficient in the [110] direction for bulk silicon to be relatively constant at 72×10^{-11} Pa^{-1} $[(\pi_{11}+\pi_{12}+\pi_{44})/2]$. His results have been showed graphically by Kanda [72] (see Figure H-1):
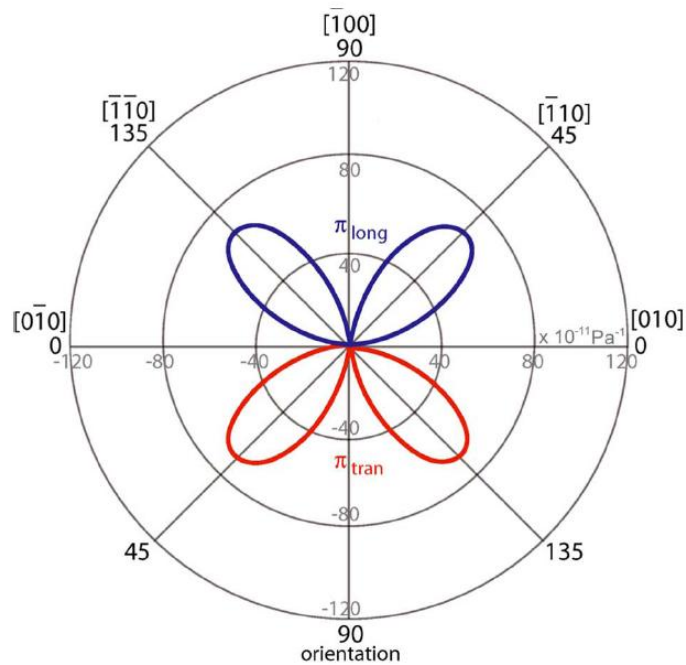

Figure H-1. Room temperature piezoresistive coefficients in the (100) plane of p-type silicon. This graphic predicts piezoresistive coefficients very well for low doses. After Kanda [72]

In other words, *p*-type piezoresistors must be oriented along the <110> directions to measure stress and thus should be either aligned or perpendicular to the wafer primary flat (see Figure H-2) [73].
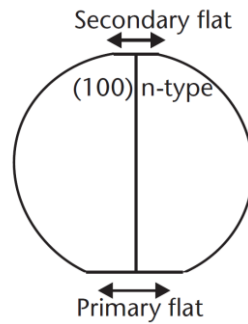
Figure H-2. n-type (100) oriented wafer showing the primary and secondary flats [73]

In our device the piezoresistors are *p*-type silicon and they are oriented on the <110> directions (Young's modulus E = 169 GPa) for *n*-type {100} wafer (parallel or perpendicular to the primary flat, see Figure H-2 and H-3) because they provide high sensitivity on this directions and is a convenient crystallographic orientation from a fabrication standpoint [53].

It should be noted that saying that the surface of a wafer has a particular orientation such as (100) is arbitrary; any orientation within the equivalent {100} group of planes, such as (001), can alternatively be selected (see Figure H-3).

Figure H-3. Illustration identifying various planes in a wafer of {100} orientation (the wafer thickness is exaggerated) [73]

All piezoresistors are arranged on the <110> directions along the four beams directions for both X and Y-axis direction. When referred to the crystallographic coordinate system of the silicon crystal, the coordinate transformation matrix (R) of the piezoresistor in <110> directions of the coordinate system are [58]:
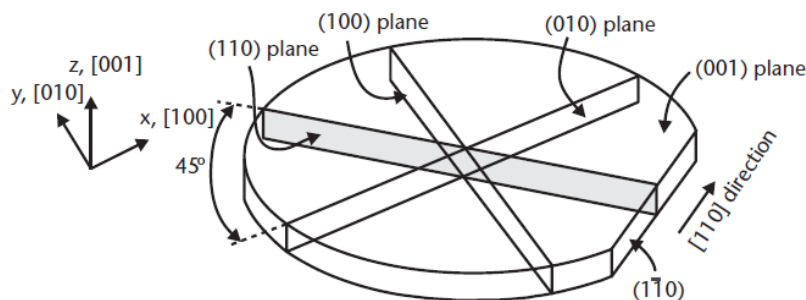
$$(R) = \begin{bmatrix} l_1 & m_1 & n_1 \\ l_2 & m_2 & n_2 \\ l_3 & m_3 & n_3 \end{bmatrix} \equiv \begin{bmatrix} \frac{\sqrt{2}}{2} & \frac{\sqrt{2}}{2} & 0 \\ -\frac{\sqrt{2}}{2} & \frac{\sqrt{2}}{2} & 0 \\ 0 & 0 & 0 \end{bmatrix} \tag{H.2}$$

And then the longitudinal and transverse piezoresistive coefficients are calculated by the Mason and Thurston [70] general formula (2.2), (2.3) and (2.4).

After substitution the formulae that express both coefficients for <110> directions and the circuit configuration are as follow [40]:

$$\pi_{<110>}^{I\|V} = \pi_l = \frac{1}{2}(\pi_{11} + \pi_{12} + \pi_{44}) \tag{H.3}$$

$$\pi_{<110>}^{I\perp V} = \pi_t = \frac{1}{2}(\pi_{11} + \pi_{12} - \pi_{44}) \tag{H.4}$$

The Figure H-4 shows the different test configuration for piezoresistive coefficient measurements.
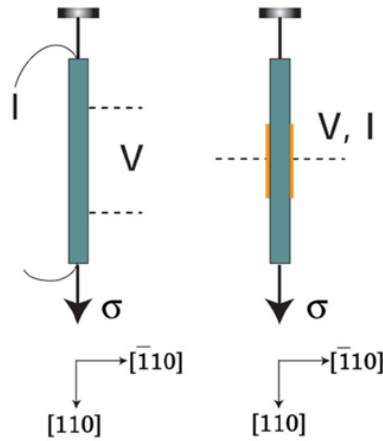
Figure H-4. Notation for Smith's test configurations [48]

The longitudinal and transverse piezoresistive coefficients for <110> directions are then calculated (see Figure 13) and the approximation is sometimes made that for *p*-Si $\pi_{11} = \pi_{12} = 0$ and then:

$$\pi_{<110>} = \pm\frac{\pi_{44}}{2} \tag{H.5}$$

where π_{44} is the shear coefficient. π_{44} originates from the change in mobility through carrier transfers and effective mass changes when the band structures of Si are modified by strains [74].

Therefore the fractional resistance change is simply given by:

$$\frac{\Delta R}{R} = \sigma_l \cdot \frac{\pi_{44}}{2} - \sigma_t \cdot \frac{\pi_{44}}{2} = \frac{\pi_{44}}{2} \cdot (\sigma_l - \sigma_t) \tag{H.6}$$

Generally, the value of the shear piezoresistive coefficient π_{44} depends on boron concentration and temperature of measurement.

The piezoresistance coefficient magnitude decreases significantly with the doping concentration and the temperature. The first systematic experimental study on piezoresistance over a broad temperature range (-90°C to 100°C) and doping concentration levels was carried

251

out by Tufte and Stelzer [69] in the early 1960's. Subsequent studies by many investigators have generally confirmed the trend of their results. Figure H-5 shows the dependence of π_{44} on the doping level at room temperature and Figure H-6 shows the temperature coefficient of π_{44} for a p-Si material [58].
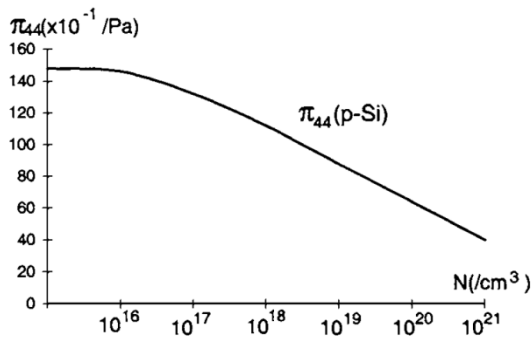
Figure H-5. Dependence of π_{44} on the doping level at room temperature
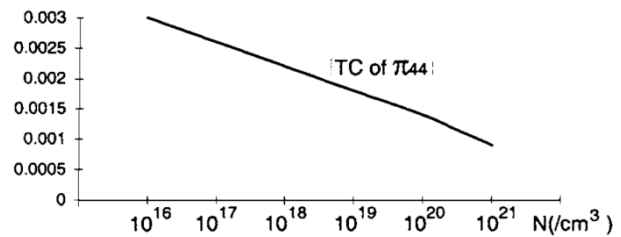
Figure H-6. Temperature coefficient of $\pi 44$ for a p-Si material.

The temperature coefficient of sensitivity is estimated as 0.0025 (0.25%/°C) for a concentration of around 10^{17} cm^{-3} (Figure 15).

Piezoresistive Coefficient

Kanda [72] has theoretically discussed the dependence of the piezoresistive coefficient on the impurity concentration and temperature. He concluded that the piezoresistive coefficient with a doping concentration of N at a temperature T, $\Pi(N, T)$, can be generally expressed as:

$$\Pi(N,T) = P(N,T)\Pi(300K) \hspace{2cm} (H.7)$$

where $\Pi(300K)$ is the piezoresistive coefficient at 300K for low doped material of the same conductive type and $P(N,T)$ is a factor indicating the dependence of the piezoresistive coefficient on the doping level and temperature. Based on the multi-valley theory of

semiconductor energy bands, the factor *P(N, T)* has been calculated. Some of his results are given in the Figure H-7 to show the trends for p-Si. It was claimed that the discrepancy between the theoretical results and the experimental results are within 15% for a temperature range o f - 50°C to +150°C and a doping level up to $5 \cdot 10^{18}$ cm^{-3}.
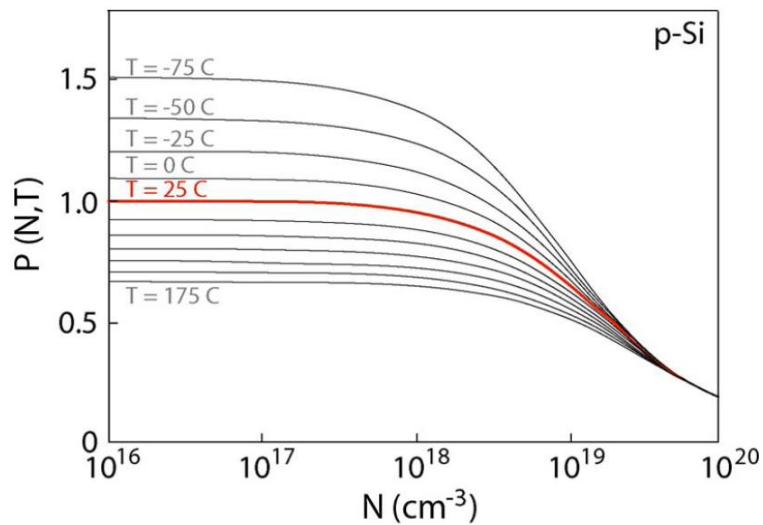
Figure H-7. Piezoresistive Factor vs. p-Si concentration at different temperatures

The calculated values of the *P(N,T)*, agree well with the experimental values obtained by Mason [70] for doping concentrations less than 1×10^{17} cm^{-3}, over the temperature range of 50°C to 150 °C, but differ by 21% at a concentration of 3×10^{19} cm^{-3} at room temperature. The error was attributed to dopant ions scattering for high dopant concentrations, whereas the calculation only considered lattice scattering. Harley and Kenny [53] later evaluated data from several researchers (see Figure 17) and provided an empirical fit of piezoresistance vs. concentration that better estimates the sensitivity for higher concentration devices.
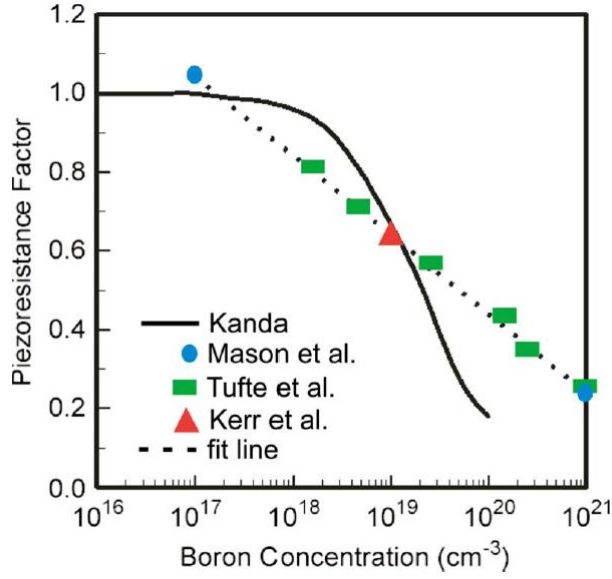
Figure H-8. Piezoresistive Factor comparison at room temperature [53]

The figure above shows room-temperature data from Mason *et al.* [70], Tufte and Stelzer [69], and one point from Kerr and Milnes [75] is shown along with the theoretical curve from Kanda [72].

The fitting function for room temperature is applied for doping densities above 1×10^{17} cm^{-3}. For doping concentrations below 1×10^{17} cm^{-3} the piezoresistive factor is set to 1. For concentrations in the range of interest (above 1×10^{17} cm^{-3}), this data is well approximated by a straight line on the semilog plot. The complete fitting function of the piezoresistive factor is shown in the Figure H-9 and given by:

$$P(p) = \begin{cases} \log\left(\frac{1.53\times10^{22}}{p}\right)^{0.2014} & (p > 1 \times 10^{17}) \\ 1 & (p \leq 1 \times 10^{17}) \end{cases} \tag{H.8}$$

Figure H-9. Fitting Function at room temperature [53]

This section has introduced the piezoresistance effect and how to calculate the fractional resistance change in conventional microscale piezoresistors.

Table I-1. Sensitivity and cross-sensitivity of three designs type A with nanowires

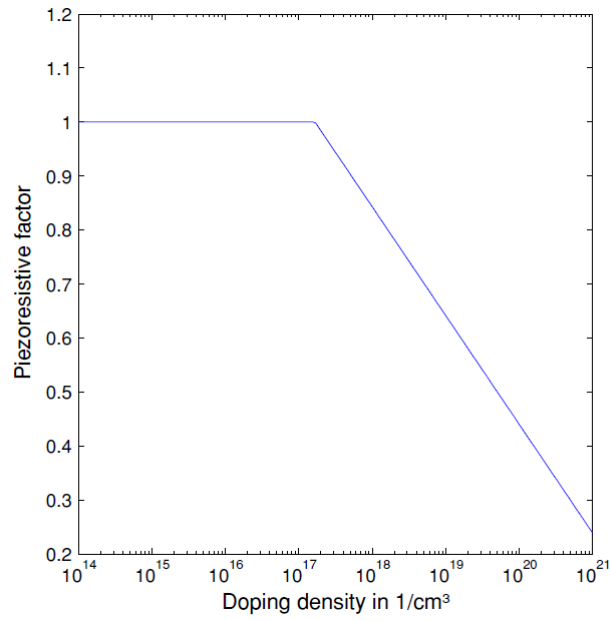|	X-axis ACCELERATION (500g)			Y-axis ACCELERATION (500g)			Z-axis ACCELERATION (500g)			X, Y-axis ACCELERATION (500g)		
	X-axis (V/G)	Cross-Y (%)	Cross-Z (%)	Y-axis (V/G)	Cross-X (%)	Cross-Z (%)	Z-axis (V/G)	Cross-X (%)	Cross-Y (%)	X-axis (V/G)	Y-axis (V/G)	Cross-Z (%)
SQUARE A1	1.11E-02	0.0611	2.7794	1.11E-02	0.0521	2.7576	3.77E-02	0.0058	0.0139	1.57E-02	1.57E-02	2.8421
OCTAGON A2	1.19E-02	0.1699	0.0463	1.19E-02	0.1154	0.0294	6.06E-02	0.0011	0.0374	1.49E-02	1.49E-02	0.0403
CIRCLE A3	1.15E-02	0.0105	0.6393	1.15E-02	0.0964	0.6117	3.84E-02	0.0227	0.0352	1.43E-02	1.44E-02	0.7327

Table I-2. Sensitivity and cross-sensitivity of three designs type B with nanowires

	X-axis ACCELERATION (500g)			Y-axis ACCELERATION (500g)			Z-axis ACCELERATION (500g)			X, Y-axis ACCELERATION (500g)		
	X-axis (V/G)	Cross-Y (%)	Cross-Z (%)	Y-axis (V/G)	Cross-X (%)	Cross-Z (%)	Z-axis (V/G)	Cross-X (%)	Cross-Y (%)	X-axis (V/G)	Y-axis (V/G)	Cross-Z (%)
SQUARE B1	1.10E-02	0.1474	2.1946	1.10E-02	0.0904	0.0043	1.48E-02	0.0220	0.1154	1.22E-02	1.22E-02	0.0118
OCTAGON B2	1.06E-02	0.0274	2.1716	1.06E-02	0.0339	0.1683	1.48E-02	0.1794	0.2275	1.16E-02	1.16E-02	0.0809
CIRCLE B3	1.05E-02	0.0106	1.5536	1.06E-02	0.0005	0.1152	1.48E-02	0.0228	0.1090	1.15E-02	1.15E-02	0.1283

Table I-3. Sensitivity and cross-sensitivity of three designs type A and final design with nanowires

	X-axis ACCELERATION (500g)			Y-axis ACCELERATION (500g)			Z-axis ACCELERATION (500g)			X, Y-axis ACCELERATION (500g)		
	X-axis (V/G)	Cross-Y (%)	Cross-Z (%)	Y-axis (V/G)	Cross-X (%)	Cross-Z (%)	Z-axis (V/G)	Cross-X (%)	Cross-Y (%)	X-axis (V/G)	Y-axis (V/G)	Cross-Z (%)
SQUARE A1	1.11E-02	0.0611	2.7794	1.11E-02	0.0521	2.7576	3.77E-02	0.0058	0.0139	1.57E-02	1.57E-02	2.8421
OCTAGON A2	1.19E-02	0.1699	0.0463	1.19E-02	0.1154	0.0294	6.06E-02	0.0011	0.0374	1.49E-02	1.49E-02	0.0403
CIRCLE A3	1.15E-02	0.0105	0.6393	1.15E-02	0.0964	0.6117	3.84E-02	0.0227	0.0352	1.43E-02	1.44E-02	0.7327
FINAL	1.29E-02	0.0630	0.0557	1.29E-02	0.1036	0.0524	1.92E-01	7.55E-05	0.0072	1.71E-02	1.71E-02	5.35E-02

Table I-4. Sensitivity and cross-sensitivity of three designs type A, final design and two new geometries with conventional microscale piezoresistors

	X-axis ACCELERATION (500g)			Y-axis ACCELERATION (500g)			Z-axis ACCELERATION (500g)			X, Y-axis ACCELERATION (500g)		
	X-axis (V/G)	Cross-Y (%)	Cross-Z (%)	Y-axis (V/G)	Cross-X (%)	Cross-Z (%)	Z-axis (V/G)	Cross-X (%)	Cross-Y (%)	X-axis (V/G)	Y-axis (V/G)	Cross-Z (%)
SQUARE	5.35E-04	0.094	2.626	5.34E-04	0.010	2.606	3.54E-04	0.016	0.040	5.37E-04	5.36E-04	3.7
OCTAGON	5.18E-04	0.074	0.044	5.18E-04	0.065	0.027	3.85E-04	0.005	0.197	5.19E-04	5.19E-04	0.049
CIRCLE	5.15E-04	0.009	0.631	5.15E-04	0.043	0.604	3.55E-04	0.066	0.104	5.16E-04	5.16E-04	0.887
FINAL	5.61E-04	0.005	0.054	5.61E-04	0.065	0.050	4.28E-04	1.83E-03	0.138	5.61E-04	5.62E-04	7.04E-02
CURVED+CIRCLE	5.62E-04	0.031	0.252	5.61E-04	0.067	0.269	4.36E-04	0.072	0.164	5.63E-04	5.62E-04	0.385
CURVED+CIRCLE2	5.98E-04	0.008	0.528	5.98E-04	0.047	0.510	5.08E-04	0.004	0.029	5.99E-04	5.99E-04	0.733
DOUGHNUT	4.57E-04	0.0007	0.063	4.58E-04	0.63	0.137	3.57E-04	1.010	0.193	4.55E-04	4.57E-04	0.189

APPENDIX J.   SINGLE CRYSTAL SILICON MATERIAL PROPERTIES

Miller convention:

Use the [ ] notation to identify a specific direction,

Use the < > notation to identify a family of directions with equivalent properties, for example:

1. <100> has equivalent directions [100], [010], [001] or

2. <110> has equivalent directions [110], [011], [101], [$\overline{1}\overline{1}$0], [0$\overline{1}\overline{1}$], [$\overline{1}$0$\overline{1}$], [$\overline{1}$10], [0$\overline{1}$1], [$\overline{1}$01], [1$\overline{1}$0], [01$\overline{1}$], [10$\overline{1}$] or

3. <111> has equivalent directions [111], [$\overline{1}$11], [1$\overline{1}$1], [11$\overline{1}$]

Use the ( ) notation to identify a specific plane,

Use the { } notation to identify a family of planes with equivalent properties.

The line on top of the axis

In cubic crystal such as silicon the [100], [010] and [001]-directions are chosen to coincide with x, y, and z-axes, the (100)-plane showed in the figure below is orthogonal to the [100] direction.
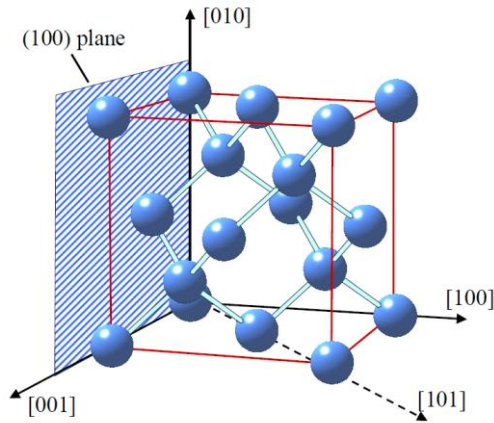
Figure J-1. Silicon crystal structure: Different crystal orientations are indicated with Miller indexes with [100] coinciding with x-axis. Also shown is (100)-plane (that is plane orthogonal to [100] direction) and crystal unit cell (red box) [52].

Figure J-1 is an introduction to the crystallographic notation. As a crystal is periodic, there exist families of equivalent directions and planes. Notation allows for distinction between a specific direction or plane and families of such.

In the design of piezoresistors the crystallographic orientation affects the piezoresistive sensitivity. For instance a <111> oriented piezoresistor in a (110) plane will have the highest piezoresistive sensitivity. More commonly <110> aligned piezoresistors on (100) wafers are used because of their high equal and opposite longitudinal and transverse piezoresistive coefficients.

The cubic nature of the single crystal silicon (SCS) lattice, leads to orthotropic material properties. For an orthotropic material such as silicon the Young's modulus and Poisson's ratio depends on which crystal direction the material is being stretched. An orthotropic material has two or three mutually orthogonal two-fold axes of rotational symmetry so that its mechanical properties are, in general, different along the directions of each of the axes.

Orthotropic materials are thus anisotropic; their properties depend on the direction in which they are measured.

To account for anisotropy tensor formalism is required. The general relationship between stress and strain is:

$$\begin{bmatrix} T_1 \\ T_2 \\ T_3 \\ T_4 \\ T_5 \\ T_6 \end{bmatrix} = \begin{bmatrix} C_{11} & C_{12} & C_{13} & C_{14} & C_{15} & C_{16} \\ C_{21} & C_{22} & C_{23} & C_{24} & C_{25} & C_{26} \\ C_{31} & C_{32} & C_{33} & C_{34} & C_{35} & C_{36} \\ C_{41} & C_{42} & C_{43} & C_{44} & C_{45} & C_{46} \\ C_{51} & C_{52} & C_{53} & C_{54} & C_{55} & C_{56} \\ C_{61} & C_{62} & C_{63} & C_{64} & C_{65} & C_{66} \end{bmatrix} \cdot \begin{bmatrix} \varepsilon_1 \\ \varepsilon_2 \\ \varepsilon_3 \\ \varepsilon_4 \\ \varepsilon_5 \\ \varepsilon_6 \end{bmatrix} \tag{J.1}$$

where C is the stiffness matrix.

The stiffness matrix C of single crystal silicon (SCS) is simplified due to the requirement that the elastic properties of a continuum are invariant under an orthogonal transformation. This means that the stiffness matrix C satisfies a given symmetry condition if it does not change when subjected to the corresponding orthogonal transformation. The orthogonal transformation may represent symmetry with respect to a point, an axis, or a plane. Orthogonal transformations in linear elasticity include rotations and reflections, but not shape changing transformations. The above symmetry requirement can be satisfied only if:

$$C_{14} = C_{15} = C_{24} = C_{25} = C_{34} = C_{35} = C_{46} = C_{56} = 0 \tag{J.2}$$

$$C_{16} = C_{26} = C_{36} = C_{45} = 0$$

Therefore, the stiffness matrix of an orthotropic linear elastic material like silicon can be written as:

$$\underline{C} = \begin{bmatrix} C_{11} & C_{12} & C_{13} & 0 & 0 & 0 \\ C_{21} & C_{22} & C_{23} & 0 & 0 & 0 \\ C_{31} & C_{32} & C_{33} & 0 & 0 & 0 \\ 0 & 0 & 0 & C_{44} & 0 & 0 \\ 0 & 0 & 0 & 0 & C_{55} & 0 \\ 0 & 0 & 0 & 0 & 0 & C_{66} \end{bmatrix} \tag{J.3}$$

Because silicon is such an important economic material, these values have been investigated thoroughly, and the three independent stiffness coefficients of principal crystallographic orientations <100>, <010> and <001>, gives the following stiffness matrix [52]:

$$C = \begin{bmatrix} 1.66 & 0.64 & 0.64 & 0 & 0 & 0 \\ 0.64 & 1.66 & 0.64 & 0 & 0 & 0 \\ 0.64 & 0.64 & 1.66 & 0 & 0 & 0 \\ 0 & 0 & 0 & 0.80 & 0 & 0 \\ 0 & 0 & 0 & 0 & 0.80 & 0 \\ 0 & 0 & 0 & 0 & 0 & 0.80 \end{bmatrix} \cdot 10^{11} Pa \tag{J.4}$$

To obtain Young's modulus in [100] direction just set all other stresses to zero and solve for $Y_{[100]} = T_1/\mathcal{E}_1$. This gives

$$Y_{[100]} = C_{11} - 2\frac{C_{12}}{C_{11}+C_{12}} \cdot C_{12} = 130 \, GPa \tag{J.5}$$

The Poisson's ratio can similarly be obtained as:

$$v_{[100]} = \frac{C_{12}}{C_{11}+C_{12}} = 0.28 \tag{J.6}$$

The expressions and values for Young's modulus to [110]- and [111]-direction are given in Table J-1:

Table J-1. Young's modulus in [100], [110] and [111] direction [54]

Direction	Expression	Value [GPa]
[100]	$C_{11} - 2\dfrac{C_{12}}{C_{11} + C_{12}} \cdot C_{12}$	130
[110]	$4\dfrac{(C_{11}^2 + C_{12}C_{11} - 2C_{12}^2)C_{44}}{2C_{44}C_{11} + C_{11}^2 + C_{12}C_{11} - 2C_{12}^2}$	170
[111]	$3\dfrac{C_{44}(C_{11} + 2C_{12})}{C_{11} + 2C_{12} + C_{44}}$	189

APPENDIX K.   CHARACTERIZATION AND TESTING OF SAMPLES

Characterization

Data collection is carried out on each nanowires of each test-chip through measurement instruments (source/measure). Figure K-1 below shows a single nanowire with 2 contacts, required to measure the change in resistance due to stress at various temperature. A constant electrical current is applied and the change in voltage output represents a measure of the resistance change, according to the Ohm law.
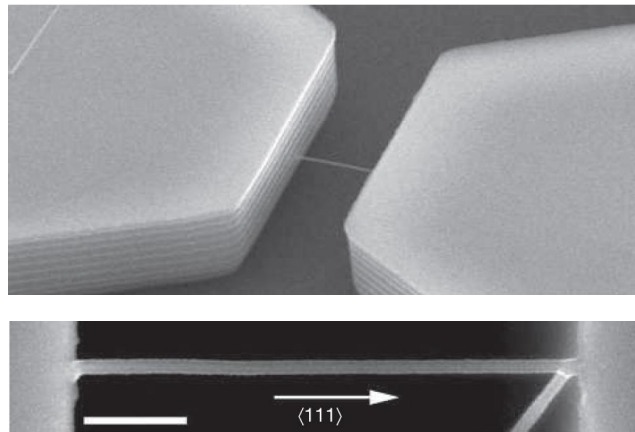

Figure K-1. Nanowire 2-points contacts [3]

The analysis of the data collected is based on the longitudinal piezoresistive coefficient that is calculated for each nanowire from the following equation:

$$\pi_l = \frac{\frac{\Delta R}{R_0}}{\sigma_l} \qquad (K.1)$$

where R_o is the resistance of the unstressed nanowire and σ_l the longitudinal stress.

The gauge factor will be calculated as follows:

$$GF = \frac{\frac{\Delta R}{R_0}}{\epsilon_l} \qquad (K.2)$$

where ϵ_l is the longitudinal strain.

From the data analysis a curve piezoresistive coefficient and/or gauge factor vs. stress is obtained. This curve represents the electro-mechanical behaviour of each nanowire. Moreover this curve varies based on the parameters under investigation (cross sectional area, aspect ratio, carrier density, irregularity of wire wall, temperature and crystallographic orientation).

Testing

The testing is carried out with a characterization station (see Figure K-2(a) for uniaxial test and Figure K-2(b) for bending test) that comprises probes for source/measure, microscope and a tensile kit equipped with an extra temperature controlling unit. The tensile kit established at Cranfield, was based on the 200N commercial model by DEBEN UK modified for the testing of micro- components by the addition of a new piezo- electric motor. The specific motor, model P-840 from Physik Instrument, is capable of high accuracy movement resolution of 2 nm, making it ideal for the particular application.

There are two available options for the load cell, a 2 N and a 20 N. The force resolution of the kit is equal to 1000:1 so the minimum resolved force with the second cell fitted is 0.02 N. The station is designed to fit in a Philips XL 30 SEM chamber. The applied strain rate is variable with a minimum value equal to 4 nm/sec. The station is controlled by an external controlling unit (DEBEN UK) which is connected to a personal computer with win XP platform through RS 232 interface.
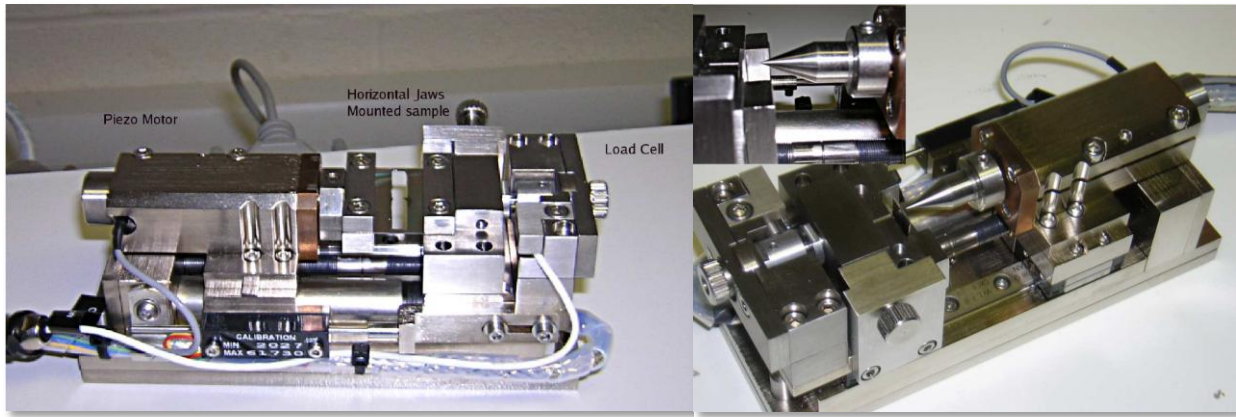
(a)   (b)

Figure K-2. (a) Prototype tensile kit, equipped with horizontal gripping jaws for conventional tensile testing [78]. (b) Prototype tensile stage kit, equipped with vertical gripping jaws and point tip for bending experiment. In the inset the pushing tip is shown in contact with a metal sample [78].

A 200 N load cell was used for the experiment due to the relatively high stress of around 100MPa required for the experiment. Notice that single crystal silicon has fracture strength of around 7 GPa [84]. The sample features have been specifically designed to reach this stress level because it is a typical stress applied to the beams of medium-G miniature inertial sensors.

The experiment consists of applying uniaxial stress (tensile and compressive) at different temperatures along the longitudinal axis of the nanowires through a prototype tensile stage. In the meanwhile a constant electrical current (~μA) is applied to each nanowire and electrical measurement of the potential drop (~100 nV) on the contacts electrodes will allow to calculate the change of resistance compared to the unstressed condition. Moreover for each nanowire the contact characteristic (I-V) is drawn. Finally the gauge factor and piezoresistive coefficient for each nanowire at different temperature are obtained.

ACHIEVEMENTS

List of Publications and patents from this Thesis:

M. Messina, J. Njuguna, V. Dariol, C. Pace, and G. Angeletti, "Design and Simulation of a Novel Bio-Mechanic Piezoresistive Sensor with Silicon Nanowires," *IEEE/ASME Transaction on Mechatronics*, vol. PP, n. 99, 2012.

M. Messina, J. Njuguna, "Potential of silicon nanowires structures as nanoscale piezoresistors in mechanical sensors" in *IOP Conf. Ser.: Mater. Sci. Eng.* vol. 40 012038, 2012.

M. Messina, J. Njuguna, "Design, Modelling and Optimization of a Bio-Mechanic Piezoresistive Accelerometer," *ASME Journal of Mechanical Design*. Under review.

M. Messina, J. Njuguna, "Influence of Variation in the Mass Moment of Inertia into the Performance of a Tri-axial Piezoresistive Accelerometer," *Journal of Micromachines.* Under review.

M. Messina, J. Njuguna, "Silicon Piezoresistance and Giant Piezoresistance in Silicon Nanowires," *Journal of Micromachines.* In preparation.

M. Messina, J. Njuguna, "High performance tri-axial piezoresistive accelerometer." Patent Application Number EP12195830.0